Controls of bedrock properties, climate, and biota on hillslope and fluvial denudation in the Coastal Cordillera of Chile

Dissertation

zur Erlangung des Grades eines

Doktors der Naturwissenschaften (doctor rerum naturalium)

am Fachbereich Geowissenschaften

der Freien Universität Berlin

vorgelegt von

Emma Lodes

Berlin 2024

Erstgutachter: Prof. Dr. Dirk Scherler

Freie Universität Berlin

Zweitgutachter: Prof. Dr. Taylor Schildgen

Universität Potsdam

Tag der Disputation: 29 April 2024

Eidesstattliche Erklärung

Hiermit erkläre ich, dass ich die Dissertation selbstständig und ohne unerlaubte fremde Hilfe verfasst habe. Ich habe keine anderen Hilfsmittel, Quellen oder Literatur verwendet als die, die im Text erläutert oder in der Referenzliste aufgeführt sind. Im Vorwort (Preface) dieser Arbeit habe ich alle Beiträge von Co-Autoren zu Manuskripten aufgeführt, die veröffentlicht wurden oder in Vorbereitung sind. Ich bestätige außerdem, dass die elektronische Version dieser Arbeit mit der gedruckten Version übereinstimmt. Ich habe mich nicht an einem anderen Fachbereich oder an einer anderen Universität für ein Promotionsverfahren beworben oder eingeschrieben. Die Dissertation ist in keinem früheren Promotionsverfahren angenommen oder abgelehnt worden.

Potsdam, 05. März, 2024

_____

Emma Lodes

Dedication

To Edeltraut Bilger, for showing me that everything is possible.

Acknowledgements

Many people played a role in the completion of this doctoral thesis. The first person I would like to thank is my supervisor, Dirk Scherler, who spent many hours describing geomorphological processes to me through conversations and drawings in Chile and in Potsdam, demonstrated incredible patience teaching me how to use MATLAB, and let me expand the topics of this thesis beyond the original plan. Perhaps most importantly, Dirk's enthusiasm about geomorphology and science has kept my enthusiasm up and kept me inspired through COVID lockdowns, lab work, and all the ups and downs of working on a doctoral thesis.

My research would not exist without the funding, training, and network of the DFG-funded priority program "EarthShape", which was led and coordinated by Friedhelm von Blanckenburg, Todd Ehlers, Kirstin Übernickel, and Leandro Paulino. Thanks to all of you for initiating and managing very interesting scientific projects in beautiful field sites in Chile. Being part of the EarthShape community was a great experience and I am very grateful for the opportunity to do field work in such spectacular settings with an interdisciplinary and international network of scientists. Field work would not have been possible without the support of Renee van Dongen, Iris Eder, Müge Yazici, and Adam Ossowicki, who helped me as field assistants and made the field work experience very enjoyable.

I would like to thank Friedhelm von Blanckenburg and my current and former colleagues of Section 3.3 (Earth Surface Geochemistry). I felt very welcome in the 3.3 group from the beginning and am honored to have been part of such an intelligent, hardworking and fun group. I especially would like to thank Hella Wittmann and Cathrin Schulz for their help in the laboratory, and for their patience, as learning cosmogenic radionuclide analysis was a steep learning curve for me.

I would also like to thank Donovan Dennis and Katharina Wetterauer for being such good friends to me and for their huge amount of support and help with administration, lab work, scientific and life problems, and for all the good times and laughter. I would also like to thank Richard Ott for the scientific discussions and good times climbing and playing music. In the last months of my doctoral thesis process, Donovan Dennis, Helen Werner, Katharina Wetterauer, Laura Krone, Renee van Dongen and Adam Ossowicki were especially helpful and supportive and deserve heartfelt thanks. Of course, I also want to thank my family for supporting me and believing me during the research process.

Summary

The surface of the earth is shaped by interactions between tectonics and climate on long timescales. Tectonic uplift supplies earth material, and the climate regime shapes the landscape through agents of weathering and erosion such as insolation, precipitation, streamflow, wind, glaciers, or frost. The local climate also influences biota, which plays a role in shaping the landscape as well. For example, plant roots can influence rainwater infiltration, fallen trees can uproot soil and enhance erosion, and grazing animals can compact soils. When tectonic uplift is held constant, another factor becomes important in controlling erosion rates and shaping landscapes: bedrock properties such as lithology and mineralogy, fracture density, and particle size. Bedrock properties interact with climate and biota in several ways. Rain can infiltrate into bedrock fractures and promote chemical weathering, the conversion of bedrock to regolith, and vegetation growth. Such chemical weathering also reduces the size of sediment on the earth's surface, facilitating its transport from hillslopes to streams. Certain minerals weather more quickly than others, and therefore lead to faster weathering rates and soil formation. Bedrock composition can also influence surficial particle size and vegetation growth due to the presence or absence of plant-essential elements, both of which can influence erosional patterns and stream incision.

In this thesis, I investigated the effects of bedrock properties, climate, and biota on erosion, weathering, and landscape morphology, along the Coastal Cordillera of Chile. I focused on three field sites in three different climate zones, a semi-arid, mediterranean, and humid site, all underlain by granitoid lithology. All three field sites have a similar tectonic setting; this allowed me to investigate the effects of climate, biota, and bedrock heterogeneities within and between field sites, such as fracture density, grain size, and mineralogy. I used *in situ* ^{10}Be cosmogenic radionuclide analysis to measure erosion and weathering rates of bedrock, boulders, soils, and stream sediment in each field site. ^{10}Be is a cosmogenically produced isotope that is commonly used to estimate erosion rates over long timescales (thousands of years), because it is produced in the upper few meters of the earth's surface by cosmic rays, and the concentration of ^{10}Be nuclides in the earth's surface

is inversely proportional to the erosion rate of the sampled material. To compliment the isotopic data, I also used topographic analysis tools (Topotoolbox in MATLAB) to quantify topographic metrics such as slope and drainage density, and obtained data from field surveys including sediment and boulder grain size distributions, and bedrock geochemistry and mineralogy.

In the first study (Chapter 3), I investigated the effect of bedrock fractures on differential erosion, weathering, and soil formation within three field sites in Chile, with the hypothesis that high fracture density in bedrock reduces surficial particle sizes and leads to higher erosion rates. Using ^{10}Be cosmogenic radionuclide analysis as a tool, I measured erosion rates of unfractured bedrock, large boulders, and soil on hillslopes, and assessed differential erosion rates between boulders and soils using a model that considers measured protrusion heights of hillslope boulders to estimate soil erosion. I found that large hillslope boulders do erode more slowly than the surrounding soil in field sites with moderate slope angles, and that erosion rates between boulders and soil are most similar in the semi-arid field site, and are most variable in the mediterranean site, where slope angles are high. I also found that more highly fractured bedrock has higher erosion rates than non-fractured bedrock, and that streams follow the orientations of major fracture networks. These findings imply that fracture networks can control landscape morphology through enhancing erodibility and stream incision where fractures are dense. Therefore, fracture patterns in the investigated field sites likely influence the locations of ridges and valleys.

In the second study (Chapter 4), I estimated the relative residence times of large boulders in stream channels within the same three field sites. It is generally known that stream boulders can influence landscape morphology by blocking stream channels from erosion, but this has yet to be measured using isotopic methods. Therefore, I measured the ^{10}Be concentrations of stream boulders and sediment and applied a model that estimates the ^{10}Be concentrations of nearby hillslope boulders (considering self-shielding), to directly compare hillslope and stream boulder ^{10}Be concentrations. I also analyzed grain size distributions in streams and adjacent hillslopes in each field site. I found that delivery of boulders to stream channels occurs most rapidly in the mediterranean field site, where slopes are steep. Stream boulders have the longest residence times in small catchments within the semi-arid field site and the shortest residence times in the humid-temperate

climate zone, likely due to higher discharge, which suggests that stream boulders have a relatively smaller effect on landscape morphology in the humid-temperate site.

In the third study (Chapter 5), I investigated whether bedrock composition and vegetation cover can influence landscape morphology. To do this, I studied three granitoid plutons (a monzogranite and two diorites) which underly three distinct landscapes with contrasting drainage densities, vegetation cover, and grain size, all within the semi-arid field site. For each rock type, I measured drainage density, grain size, erosion and weathering rates, vegetation cover, channel width, and bedrock properties such as mineralogy and hydraulic conductivity, to understand the underlying mechanisms that control the different landscape morphologies. Results indicate that the monzogranite bedrock has a higher drainage density due to higher stream erosivity. This is caused by enhanced runoff, which stems from its sparse vegetation cover, and higher erodibility, which is due to the monzogranite's mineralogical composition and smaller particle size. Ultimately, this study shows that bedrock composition and vegetation can influence drainage density and landscape morphology.

In summary, this doctoral thesis contributes to our understanding of how bedrock properties, climate, and biota influence erosion, weathering, and landscape morphology in granitoid bedrock landscapes, as well as the complexity and interconnectedness of geomorphological properties that operate together over thousands of years to create the landscapes that we see today.

Zusammenfassung

Die Oberfläche der Erde wird durch die Wechselwirkungen zwischen Tektonik und Klima auf langen Zeitskalen geformt. Die tektonische Hebung sorgt für den Nachschub an Gesteinsmaterial, und Faktoren wie Sonneneinstrahlung, Niederschlag, Flüsse, Wind, Gletscher oder Frost formen die Landschaft durch Verwitterungs- und Erosionsprozesse. Das lokale Klima beeinflusst auch die Pflanzen- und Tierwelt (Biota), die ebenfalls eine Rolle bei der Gestaltung der Landschaft spielen. So können beispielsweise Pflanzenwurzeln die Infiltration von Regenwasser beeinflussen, umgestürzte Bäume den Boden mobilisieren und die Erosion verstärken, und Weidetiere den Boden verdichten. Wenn die tektonische Hebung konstant gehalten wird, wird ein weiterer Faktor für die Kontrolle der Erosionsraten und die Gestaltung der Landschaften wichtig: die Eigenschaften des Grundgesteins wie Lithologie und Mineralogie, Dichte der Gesteinsbrüche und Korngröße. Auf verschiedene Weisen stehen diese Gesteinseigenschaften in Wechselwirkung mit Klima und Biota. Regen kann in Tektonische Brüche eindringen und die chemische Verwitterung, die Umwandlung von Gestein in Regolith, und das Wachstum der Vegetation fördern. Durch chemische Verwitterung verringert sich zudem die Korngröße an der Erdoberfläche und erleichtert deren Transport von den Hängen in die Flüsse. Bestimmte Minerale verwittern schneller als andere und führen zu höheren Verwitterungsraten und einer schnelleren Bodenbildung. Die Gesteinszusammensetzung kann auch einen Einfluss auf die Korngröße an der Oberfläche haben sowie das Pflanzenwachstum durch die Bereitstellung von Nährstoffen beeinflussen, was sich wiederum auf Erosionsmuster und Flusseinschneidung auswirken kann.

In dieser Doktorarbeit habe ich die Auswirkungen von Gesteinseigenschaften, Klima und Biota auf Erosion, Verwitterung und Landschaftsmorphologie entlang der Küstenkordillere Chiles untersucht. Dabei habe ich mich auf drei Arbeitsgebiete in drei verschiedenen Klimazonen konzentriert: einen semi-ariden, einen mediterranen und einen humiden Standort, die alle von granitoiden Gesteinen unterlagert sind. Alle drei Feldstandorte weisen eine ähnliche tektonische Struktur auf, so dass ich die Auswirkungen des Klimas, der Biota und der Heterogenität des Gesteins innerhalb und zwischen den Feldstandorten (z. B. Bruchdichte, Korngröße und Mineralogie) untersuchen konnte. An allen Feldstandorten habe ich mit dem kosmogenen Radionuklid in situ ^{10}Be Erosions- und Verwitterungsraten von Grundgestein, Geröll, Böden und Flusssedimenten quantifiziert.

^{10}Be ist ein kosmogenes Isotop, das zur Abschätzung von Erosionsraten über lange Zeiträume (Tausende von Jahren) verwendet wird, da es in den oberen Metern der Erdoberfläche durch kosmische Strahlung produziert wird und die Konzentration von ^{10}Be-Nukliden in Gesteinen an der Erdoberfläche umgekehrt proportional zur Erosionsrate des beprobten Materials ist. Ergänzend zu den Isotopendaten habe ich auch topografische Analysewerkzeuge (Topotoolbox in MATLAB) eingesetzt, um topografische Parameter wie Neigung und Entwässerungsdichte zu quantifizieren. Weiterhin habe ich Daten aus Felduntersuchungen gewonnen, darunter die Korngrößenverteilung von Sedimenten und Felsblöcken sowie die Geochemie und Mineralogie des Grundgesteins.

In der ersten Studie (Kapitel 3) habe ich die Auswirkungen von Gesteinsbrüchen auf Erosions-, Verwitterungs- und Bodenbildungsraten an den drei Feldstandorten in Chile untersucht. Dabei ging ich von der Hypothese aus, dass eng zusammenlegende Brüche im Gestein die Korngröße von Sedimenten an der Oberfläche verringern und zu höheren Erosionsraten führen. Um diese Hypothese zu testen, habe ich mit Hilfe der Analyse des kosmogenen Radionuklids ^{10}Be die Erosionsraten von intaktem Felsgestein, große Felsblöcke und Böden an Hanglagen gemessen und die unterschiedlichen Erosionsraten zwischen Felsblöcken und Böden mit Hilfe eines Modells berechnet, das die gemessenen Höhen von Felsblöcken an Hanglagen berücksichtigt, um die Bodenerosion zu schätzen. Durch diese Untersuchung fand ich heraus, dass große Felsblöcke in Hanglagen mit mäßigen Neigungswinkeln langsamer erodieren als der umgebende Boden. Außerdem sind die Erosionsraten zwischen Felsblöcken und Boden am semi-ariden Feldstandort am ähnlichsten, während sie am mediterranen Standort am stärksten variieren, wo die größten Neigungswinkel auftreten. Weiterhin habe ich festgestellt, dass stärker zerklüftetes Gestein höhere Erosionsraten aufweist als nicht zerklüftetes Gestein, und dass der Wasserfluss den Ausrichtungen der großen Kluftsysteme folgt. Diese Ergebnisse deuten darauf hin, dass Brüche im Grundgestein die Landschaftsmorphologie steuern können, indem sie die Erodierbarkeit und die Flusseinschneidung an Orten mit eng zusammenlegenden Gesteinsbrüchen verstärken. Daher beeinflussen die Bruchmuster in den untersuchten Gebieten wahrscheinlich die Lage von Bergrücken und Tälern.

In der zweiten Studie (Kapitel 4) habe ich die relativen Verweilzeiten von großen Felsblöcken in den Bachläufen an denselben drei Standorten abgeschätzt. Grundsätzlich

können Felsblöcke in Flüssen die Landschaftsmorphologie beeinflussen, indem sie die Felsblöcken das Flussbett vor Erosion schützen. Bisher wurde dies aber noch nicht mit Isotopenmethoden gemessen. Daher habe ich die ^{10}Be-Konzentrationen von Felsblöcken und Sedimenten in Flüssen gemessen und ein Modell angewandt, das die ^{10}Be-Konzentrationen von nahe gelegenen Felsblöcken an Hängen (unter Berücksichtigung der Selbstabschirmung) abschätzt, um die ^{10}Be-Konzentrationen von Felsblöcken in Bächen und an Hängen direkt zu vergleichen. Weiterhin habe ich die Korngrößenverteilungen in Bächen und angrenzenden Hängen an jedem Standort analysiert. Dabei fand ich heraus, dass der Eintrag von Felsblöcken in die Fließgewässer am schnellsten im mediterranen Gebiet erfolgt, wo die Hänge steil sind. In kleinen Einzugsgebieten am semi-ariden Standort haben Felsblöcke in Bächen die längste Verweildauer; in der humid-gemäßigten Klimazone ist die Verweildauer dagegen am kürzesten, was wahrscheinlich auf einen höheren Abfluss zurückzuführen ist. Dies deutet darauf hin, dass Flussblöcke einen relativ geringen Einfluss auf die Landschaftsmorphologie im humid-gemäßigten Gebieten haben.

In der dritten Studie (Kapitel 5) untersuchte ich, wie die Zusammensetzung des Grundgesteins und die Vegetationsbedeckung die Landschaftsmorphologie beeinflussen können. Dazu untersuchte ich drei granitoide Plutone (einen Monzogranit und zwei Diorite) in der semi-ariden Klimazone, die drei verschiedenen Landschaften mit unterschiedlichen Entwässerungsdichten, Vegetationsbedeckungen und Korngrößen zugrunde liegen. Für jeden Gesteinstyp habe ich die Entwässerungsdichten, die Korngröße, die Erosions- und Verwitterungsraten, die Vegetationsbedeckung, die Rinnenbreite und die Gesteinseigenschaften wie Mineralogie und hydraulische Leitfähigkeit gemessen, um die zugrunde liegenden Mechanismen zu verstehen, die die verschiedenen Landschaftsmorphologien steuern. Die Ergebnisse zeigen, dass das Monzogranit-Grundgestein eine höhere Entwässerungsdichte aufweist wegen einer höheren Erosivität der Flüsse. Dies ist auf den verstärkten Abfluss zurückzuführen, der sich aus der spärlichen Vegetationsdecke ergibt, sowie auf die höhere Erodierbarkeit, die auf die mineralogische Zusammensetzung des Monzogranits und die geringere Korngröße der Sedimente zurückzuführen ist. Letztlich zeigt diese Studie, dass die Gesteinszusammensetzung und die Vegetation die Entwässerungsdichte und die Landschaftsmorphologie beeinflussen können.

Die vorliegende Doktorarbeit trägt zu unserem Verständnis darüber bei, wie Erosion, Verwitterung und Landschaftsmorphologie in granitoiden Gesteinslandschaften von Gesteinseigenschaften, Klima und Biota beeinflusst sind, und deckt die Komplexität und die Verflechtung geomorphologischer Prozesse auf, die über Tausende von Jahren zusammenwirken und die Landschaften schaffen, die wir heute sehen.

Preface

This doctoral thesis contains 6 chapters, including an introductory chapter, a study area description, three scientific studies and a discussion chapter. The three scientific studies were written as manuscripts to be submitted to scientific journals.

Chapter 1 is the general introduction and includes an introduction to the main topics in this thesis, as well as the research gaps and objectives.

Chapter 2 contains a description of the study area, the Chilean Coastal Cordillera, and includes a description of the climatic setting, and a description of the tectonic setting.

Chapter 3 presents the first scientific study, "The story of a summit nucleus: hillslope boulders and their effect on erosional patterns and landscape morphology in the Chilean Coastal Cordillera." This study was published in Earth Surface Dynamics in 2023 (vol. 11, pp. 305–324), and includes the co-authors Dirk Scherler, Hella Wittmann, and Renee van Dongen. Dirk Scherler conceived the initial idea for this project. Emma Lodes, Dirk Scherler, and Renee van Dongen performed fieldwork. Emma Lodes performed the laboratory work, with support from Hella Wittmann. Dirk Scherler designed the model used to calculate boulder and soil denudation rates. Emma Lodes, Dirk Scherler, and Hella Wittmann analyzed the data. Emma Lodes wrote the text with support from Dirk Scherler, Hella Wittmann, and Renee van Dongen.

Chapter 4 presents the second scientific study, "Estimating stream boulder residence times through cosmogenic nuclide analysis along a climate gradient in Central Chile." This study is in preparation for submission to a journal. Dirk Scherler and Emma Lodes conceived the initial idea for this project. Emma Lodes and Dirk Scherler performed fieldwork. Emma Lodes performed the laboratory work. Dirk Scherler designed the model used to calculate hillslope boulder denudation rates. Emma Lodes analyzed the data and wrote the text with support from Dirk Scherler.

Chapter 5 presents the third scientific study "Lithological controls on drainage density through bedrock erodibility and advection: a case study in Central Chile". This study has been submitted to the Journal of Geophysical Research: Earth Surface. Coauthors include Dirk Scherler, Hella Wittmann, Anja Schleicher, Jessica Stammeier, Martín Andrés Loyola

Lafuente, and Paulina Grigusova. Dirk Scherler and Emma Lodes conceived the initial idea for this project. Field work was conducted by Emma Lodes (sample collection, grain size surveys, and vegetation surveys), Martín Andrés Loyola Lafuente (hydrological conductivity measurements) and Paulina Grigusova (vegetation surveys). Laboratory work was performed by Emma Lodes (in situ ^{10}Be measurement, bedrock hydraulic properties, and thin section point counting), Hella Wittmann (sequential chemical extractions and meteoric ^{10}Be measurements), and Anja Schleicher (XRF and XRD measurements). Data analysis was conducted by Emma Lodes (analysis of all field and laboratory results and topographic analysis), Dirk Schlerler (topographic analysis), Hella Wittmann (sequential chemical extraction and meteoric ^{10}Be analysis) and Paulina Grigusova (vegetation cover from remote sensing). Emma Lodes wrote the text with support from Dirk Scherler and Hella Wittmann.

Chapter 6 is a discussion and synthesis of all the previous chapters of the thesis.

Table of Contents

List of Tables

List of Supplementary and Appendix tables

List of Figures

List of Supplementary Figures

Chapter 1

Introduction

1.1 Influence of bedrock properties, climate and biota on erosion and weathering

On long (million year) timescales, the earth's surface is shaped by the interactions of tectonics and climate, where tectonic uplift brings bedrock into the atmosphere where it can be attacked by agents of weathering and erosion. However, when tectonic uplift is held constant, bedrock properties such as fracture density and mineralogical composition become important in shaping the landscape through setting grain size (e.g., Sklar et al., 2017), influencing the rates of weathering and erosion (e.g., Eggleton et al., 2017) on hillslopes and in streams, and setting the locations of ridgetops and valleys (e.g. Attal et al., 2015; Glade et al., 2017). Bedrock properties can also control where vegetation grows (Hahm et al., 2019; Callahan et al., 2022), and climate and biota interact with these bedrock properties by i.e., enhancing weathering rates where dense fractures exist (Drever, 1994; Lebedeva and Brantley, 2017) or modulating infiltration rates (e.g., Ibarra et al., 2019). In these ways, bedrock properties, climate, and biota all interact to influence weathering and erosion, and to shape landscapes. However, the relative importance of bedrock properties on landscape morphology and the mechanisms of their interactions with climate and biota remain incompletely understood.

1.1.1 Processes of erosion and weathering on hillslopes and in streams

Most landscapes on earth consist of hillslopes bound by stream channels. Hilltops and ridges form drainage divides between basins, or catchments, that collect rainwater and sediment that is transported downslope and into streams, and eventually, oceans. Processes of weathering and erosion sculpt ridges and valleys, form soil from bedrock, and transfer

solutes and nutrients into streams. Rates of weathering and the thickness of soil cover are influenced by tectonic uplift rates (e.g., Heimsath et al., 2000; Braun et al., 2016), climate conditions and vegetation cover (Amundson et al., 2007; Hayes et al., 2020), and bedrock properties (e.g., Lebedeva and Brantley, 2017). On hillslopes, erosion is dominated by diffusive hillslope processes, which include soil creep, (Culling, 1960; 1963), rainsplash (Sweeney et al., 2015), frost heave (e.g., Schumm, 1967), and biogenic processes such as burrowing or bioturbation and tree throw (e.g., White et al., 2015). These processes are directly controlled by the hillslope angle and lead to convex-upward shaped hillslopes. When hillslopes are very steep (>30 degrees), other processes become important, such as landslides and debris flows.

Often, landscapes are partially soil mantled with outcrops of bedrock and large boulders on hillslopes. Bedrock emerges on hillslopes when the rate of soil erosion is higher than the rate of soil production from bedrock, and typically occurs when stream incision rates or tectonic uplift rates are high or when the soil production rate is low (e.g., Dietrich et al., 2003). Diffusive hillslope processes such as soil creep are well-described, and transport laws are established for soil-mantled landscapes (e.g., Dietrich et al., 2003; Perron, 2011); however, the movement of soil downslope becomes more complicated when a hillslope also contains patchy bedrock outcrops or large boulders, which erode more slowly than the surrounding soil and can block soil transport (e.g., Glade et al., 2017; Neely et al., 2019). Rates of soil transport in such landscapes have not yet been resolved with field data, and therefore it remains unknown if, and to what extent, boulders block soil transport on hillslopes. To answer this question, denudation rates of hillslope boulders and the surrounding soil must be measured.

Hillslopes provide sediment and water to stream channels through erosion, overland flow, and groundwater, and streams transport the water and sediment down channel. Generally, the amount of discharge in a stream increases down channel and the slope decreases, which leads to a quantifiable relationship between slope and upstream area, or discharge, for streams. When a landscape is in topographic steady state, meaning tectonic uplift matches fluvial incision, a scaling relationship known as Flint's Law applies (e.g., Hack, 1973; Flint, 1974; Howard and Kerby, 1983; Whipple et al., 2013):

$$S = k_s A^{-\theta} \quad (1),$$

where S is the channel slope, A is the upstream area, k_s is the steepness index and θ is the concavity index. The steepness and concavity index vary between streams and sometimes within streams, and hold important information about the tectonic regime of the area through which the river flows, as well as bedrock properties such as erodibility. For example, the steepness index has been shown to increase with uplift rate (Tarboton et al., 1989; Kirby et al., 2003, 2007; Kirby and Whipple, 2012) and decrease with bedrock erodibility (Hack, 1973; Hack and Hack, 1957; Cyr et al., 2014), and the concavity index has been shown to vary with climate (Chen et al., 2019). If the runoff in a stream doesn't scale with upstream area, it can influence the concavity of the stream.

The incision of streams into bedrock depends on shear stress exerted by the flowing water onto the channel bed (e.g., Bagnold, 1977; Howard and Kerby, 1983; Whipple, 2004), the slope of the channel, the climate, and the erodibility of the bedrock. Bedrock river incision is commonly expressed by the stream power model (e.g., Whipple and Tucker, 1999; Lague, 2014):

$$I = KA^m S^n \quad (2),$$

where I is long-term bedrock river incision, m and n are scaling exponents, and K includes climate, biota and bedrock erodibility (Figure 1.1). Climate and biota influence processes of fluvial incision by setting surface runoff and river discharge through modulating the degree of rainwater infiltration into the regolith; soils and vegetation store and delay runoff, buffering the peak of river discharge after a precipitation event, while arid and sparsely vegetated landscapes tend to experience flashier discharge that often produces a larger geomorphic impact (Molnar et al., 2006; Rossi et al., 2015; Deal et al., 2017). In addition, hillslopes control river discharge by modulating overland flow through the presence or absence of soil and vegetation cover, and by controlling the size of grains transported into streams (Sklar et al., 2017). Bedrock erodibility is affected by the lithology and weathering extent of the bedrock (e.g., Anderson et al., 2023), the presence of bedrock fractures (Dühnforth et al., 2010; Neely et al., 2019), the grain size of sediment that is being transported by the stream (e.g., Turowski et al., 2007), and the presence of large boulders

on the stream channel bed that can shield it from erosion (e.g., Shobe et al., 2016). However, due to the difficulty in parsing apart erodibility parameters in models and the sparsity of field and laboratory data, the way in which these factors influence bedrock erodibility remains unresolved.

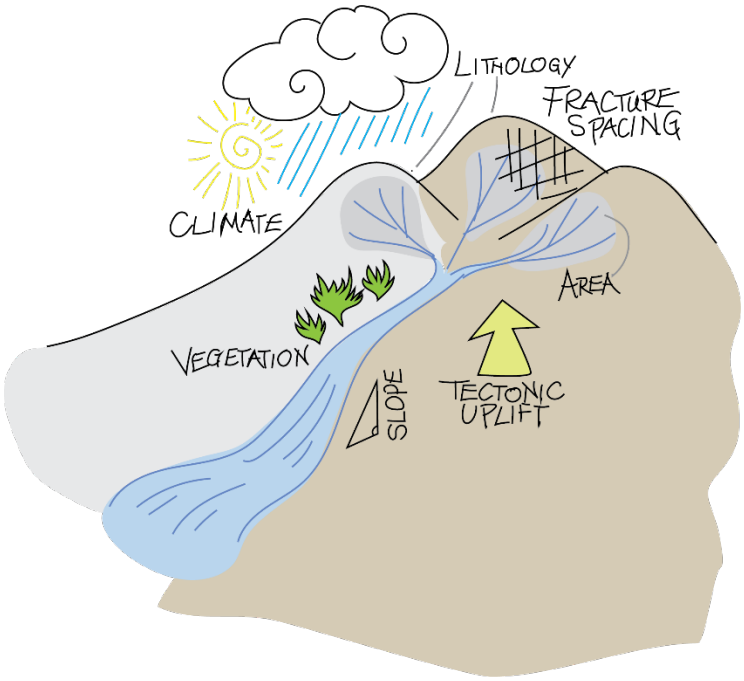

Figure 1.1. Schematic image of the landscape components that influence erosion and weathering on hillslopes and in streams, and that can be incorporated into versions of the stream power model.

1.1.2 How can bedrock fractures and lithology shape landscapes?

Bedrock fractures can form at depth from tectonic stresses (Molnar et al., 2007; Luo et al., 2019), and from shallower topographic stresses (St. Clair et al., 2015) as the bedrock is exhumed. Fractures set the preliminary grain sizes on hillslopes, and once bedrock is exhumed, longer residence times in the weathering zone (i.e., when tectonic uplift rates are low) allow sufficient time for bedrock to convert to regolith, while shorter times in the weathering zone can lead to the exposure of fresh bedrock on hillslopes and in streams, and larger surficial grains (boulders) whose sizes are set by the spacing between bedrock

fractures (e.g., Attal et al., 2015; Sklar et al., 2017; Roda-Boluda et al., 2018; Verdian et al., 2021). Climate and biota also interact with bedrock fractures to increase chemical weathering: rainwater can infiltrate into fractures carrying acids, which promote chemical weathering, and further reduces particle size, speeding up the conversion from bedrock to regolith (Lebedeva and Brantley, 2017; Hayes et al., 2020). The retention of moisture encourages plant growth, and vegetation further enhances chemical weathering through producing humic acids (Amundson et al., 2007). However, the extent to which bedrock fractures, climate, and biota interact to sculpt landscapes remains an open question. In order to solve this open question, it is necessary to measure denudation rates from fractured and non-fractured bedrock, in areas with differences in climate and vegetation cover.

Dense fracturing in bedrock eases the removal and transportation of grains on hillslopes and in streams, and as a result, increases physical erosion rates (Buss et al., 2013; Roy et al., 2016; Sklar et al., 2017; Tofelde et al., 2018; Sklar et al 2020; Neely and DiBiase 2020; Verdian et al., 2021; Figure 1.2). Within stream channels, fractured bedrock makes plucking processes (the removal of bedrock blocks and clasts by flowing water) much easier (e.g., Scott and Wohl, 2019; Chilton and Spotlia, 2020). In addition, streams have been shown to preferentially flow through highly fractured bedrock (Roy et al., 2016), and large-scale fracture orientations can influence stream orientations (Roy et al., 2015). It is not known, however, how broadly these observations can be extrapolated to larger spatial scales and to different climates. To answer this question, it is necessary to compare bedrock fracture orientations with stream orientations in different climate zones.

Fractures can also indirectly affect erodibility by reducing grain size (Buss et al., 2013; Verdian et al., 2021). Smaller grains are easier to transport (e.g., Paola et al., 1992) and can be used as tools to abrade and incise streambeds (Turowski et al., 2007; Lamb et al., 2008; Scheingross et al., 2014). On the other hand, large and stable boulders can shield hillslopes from the erosion of underlying soil (Glade et al., 2017), and stream channels from incision (Shobe et al., 2016; 2018). In this way, large boulders with long residence times can theoretically lower local erosion rates on hillslopes and in streams and therefore influence the morphology of landscapes by steepening local slopes (e.g., Seidl et al., 1994; Thaler and

Covington, 2016; Shobe et al., 2016; Cook et al., 2018). However, such relationships between boulder residence times and landscape morphology have only been reported in modelling studies (Carretier and Regard, 2011; Mackey and Lamb, 2013; Shobe et al., 2016; 2018; Glade et al., 2017), and field and laboratory data is needed to establish the impact of boulder residence time on landscapes. Several open questions remain, including how stream boulder residence times are impacted by boulder size, local climate and discharge, and hillslope and channel gradients. And what are the implications for landscape morphologies? In order to answer these questions, the residence times of large boulders in stream channels must be measured alongside topographic metrics, in different climates.

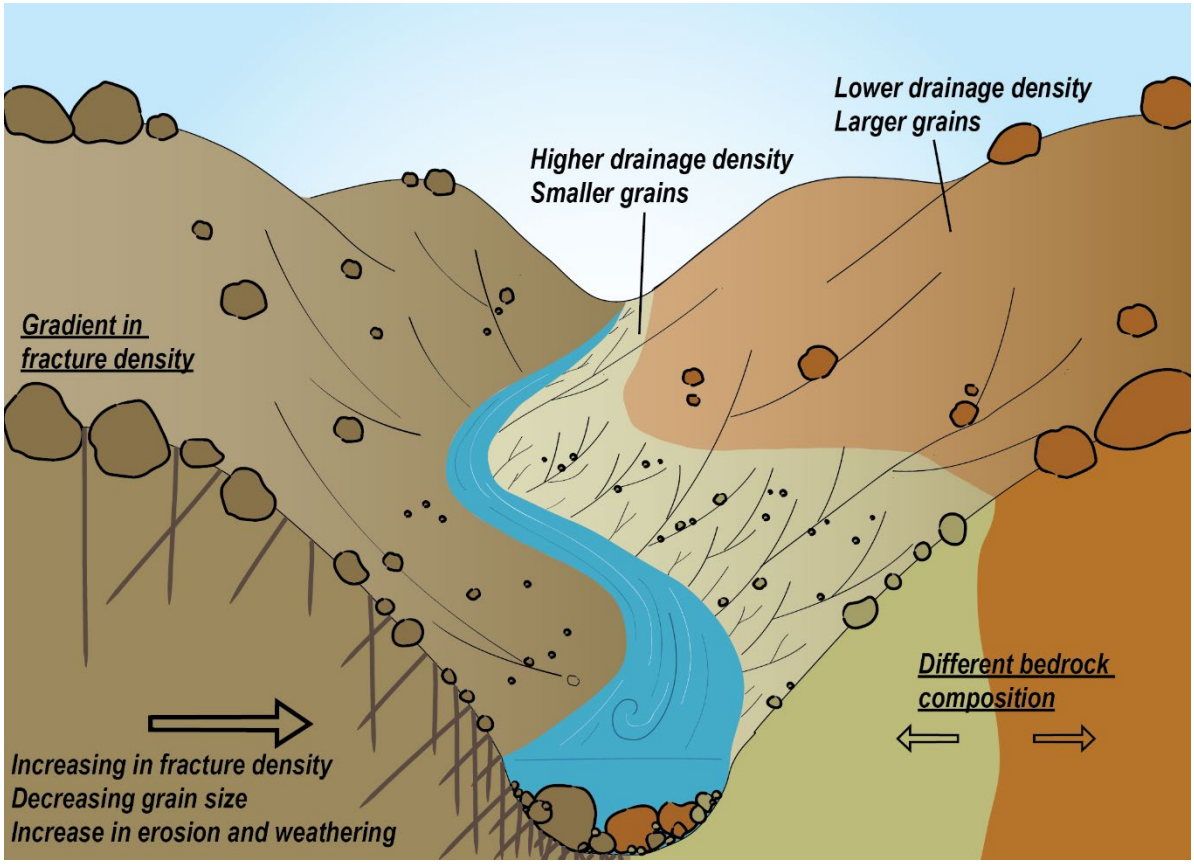

Figure 1.2. Schematic illustration of how fractures set grain size, showing fractured bedrock and blocks exhumed at the surface, with their size dictated by the spacing of fractures at depth.

Bedrock composition, or lithology, also interacts with climate and biota to shape landscapes through influencing erosion and weathering rates on hillslopes (e.g., Eggleton et al., 2017) and streams (e.g., Bursztyn et al 2015). Various properties of a given lithology can make it more resistant, including the thickness of bedding planes (Anderson et al., 2023), individual mineral sizes (Eppes and Griffing, 2010), cement that holds together mineral grains (Marshall and Roering, 2014), or the dissolution rate of the constituent minerals (e.g., White et al., 2001). For example, in granitoid lithologies, the first weathering reactions have been shown to occur in plagioclase feldspar or biotite (Banfield and Eggleton, 1990; Hayes et al., 2020). Biotite is also known to be one of the first minerals to weather in granitic rocks and can instigate positive feedback of weathering by producing iron III bearing clays and oxyhydroxides, whose crystallization inflicts pressure that can lead to cracks, increasing porosity and further weathering (e.g. Anovitz et al., 2021). These processes are more rapid in climates with higher rainfall rates and with warmer temperatures, where chemical reactions proceed at a faster rate and vegetation is denser (e.g., Riebe et al., 2004; Dixon et al., 2016).

On hillslopes, parts of a landscape underlain by more resistant bedrock often become topographic highs (e.g., Marshall and Roering, 2014; Eggleton et al., 2017; Glade et al., 2017). Lithology can set the steepness of a stream channel (Darling and Whipple, 2015; DiBiase et al., 2018); for example, a change in lithology along a fluvial channel can instigate a knickpoint, where the river changes steepness as it encounters more resistant bedrock (Wohl et al., 1994). Rivers have also been shown to narrow in reaches underlain by harder rock, such as in the Grand Canyon (Bursztyn et a., 2015). In addition, resistant lithologies can produce larger and/or more competent grains, which can reduce erosion locally, and when transported downhill and downstream, can also influence erosion beyond the outcrop of resistant rock (e.g., Marshall and Roering, 2014; Anderson et al., 2023). Bedrock lithology also influences the infiltration rate of rainwater, and therefore surface runoff, which can influence the density of streams because higher rates of runoff tend to create denser stream networks (e.g., Melton, 1957; Carlston, 1963; Litwin et al. 2022). Climate and vegetation density can influence infiltration as well; landscapes with moderate to high rainfall and vegetation cover often experience higher rates of infiltration and reduced runoff (Ibarra et al., 2019), and therefore lower drainage density (Sangireddy et al., 2016). In

contrast, very dry and very wet climates experience increased runoff due to lack of infiltration and an already-saturated groundwater table, respectively, and therefore can produce very dense drainage networks (Sangireddy et al., 2016). Biota plays an additional role in creating macro porosity in soils, further promoting infiltration and reducing runoff (Gutiérrez-Jurado et al., 2006). Although it is known that bedrock lithology can influence infiltration, and that infiltration influences drainage density, attempts to assess whether bedrock lithology influences drainage density have yielded inconclusive results (Sangireddy et al., 2016; Perron et al., 2009). To understand how lithology, climate and biota interact to influence drainage density, it is necessary to use field and laboratory approaches to measure multiple parameters (e.g., bedrock composition, vegetation cover, infiltration rates, and grain size) in landscapes with differing drainage densities, and to investigate their complex interactions in detail.

1.2 Research gaps and the scope of this project

Whereas it is clear that climate, biota, bedrock fracturing, lithology and grain size all have an influence on landscape morphology (e.g., Bierman, 1994; Heimsath et al., 2000; Granger et al., 2001; Neely and DiBiase, 2020), to date most studies have utilized a modelling approach to investigate the open research questions mentioned above (e.g., Perron et al., 2008; 2009; Shobe et al., 2016; 2018; Neely et al., 2019; Litwin et al., 2022). To our knowledge, no study has directly investigated the residence times and differential denudation rates of large boulders and the surrounding fine sediment on hillslopes and streams using the ^{10}Be cosmogenic nuclide method, along with an analysis of how these boulders influence landscape morphology in landscapes with different climates and vegetation cover. In addition, no study has investigated the effect of lithology and biota on drainage density through directly measuring field parameters including vegetation cover, grain size, bedrock composition, infiltration, and denudation rates of different lithologies alongside an analysis of drainage density. The overarching goal of this thesis is to investigate the roles of climate, biota, and bedrock properties (fracturing and mineralogy) on grain size, erosion, weathering, and landscape morphology. We used the natural laboratory of the Chilean Coastal Cordillera (see Chapter 2) and the tool of ^{10}Be cosmogenic radionuclide

analysis (see Section 1.3) to provide the field and laboratory data needed to answer the following fundamental questions:

(1), how do bedrock fractures and large hillslope boulders interact with climate and biota to control differential denudation rates and landscape morphology? (Chapter 3),

(2), what is the residence time of large boulders in streams, and how do they affect fluvial incision in different climates? (Chapter 4),

and (3), what is the influence of lithology and biota on fluvial incision and drainage density? (Chapter 5).

For the first two projects, I worked in three field sites along a climate gradient in Chile, with semi-arid, mediterranean, and humid climates, all underlain by crystalline granitoid bedrock. The third project focused on the semi-arid field site alone, to resolve how differences in bedrock composition and biota affect landscape morphology while holding climate constant.

In the first study (Chapter 3), I present a study that has been published in Earth Surface Dynamics (Lodes et al., 2023). In the study, we hypothesized that bedrock fractures influence landscape evolution by setting the maximum grain size on hillslopes, and that unfractured bedrock and larger boulders erode more slowly than fractured bedrock and soil, which experiences enhanced rainwater infiltration and vegetation growth. Additionally, we hypothesized that bedrock fracture networks enhance fluvial incision because fractured bedrock is more easily eroded by water (e.g., Lamb et al., 2015; Sklar and Dietrich, 2001), and therefore streams follow the orientations of major fracture networks. We found that large hillslope boulders erode more slowly than the surrounding soils in field sites that do not have steep slopes and landslides, and that the sparsely vegetated semi-arid landscape experiences the most similar denudation rates between boulder and soils. We also found that stream orientations match regional fault orientations in our field sites, indicating that fault and fracture orientations guide fluvial incision. These findings imply that fracture networks can control the location of ridgelines and valleys through setting the grain size, and therefore erodibility, of the bedrock, and that differential erosion rates between

bedrock and soil are larger when denudation rates are higher, due to climate (high precipitation) and biota, or slope.

A follow-up study (Chapter 4) is in preparation for submission to a journal. In this study, we estimated the relative residence time of large boulders in stream channels in the same three climate zones along the Chilean Coastal Cordillera and considered the resulting effect on stream channel incision. Though large boulders in stream channels are known to reduce fluvial incision, the residence times of large boulders have not been measured via cosmogenic radionuclide analysis. We measured the ^{10}Be concentrations of amalgamated samples from stream boulders and sediment and modelled the effect of self-shielding on hillslope boulder ^{10}Be concentrations to compare stream and hillslope boulder concentrations. In addition, we analyzed sediment grain size distributions from hillslopes and streams in each climate zone. We found that residence times of stream boulders in the humid-temperate climate zone are relatively shorter than in the other climate zones, and that the delivery of boulders from the hillslopes to streams occurs relatively rapidly in the mediterranean climate zone due to steeper slopes. These findings indicate that stream boulders have a smaller effect on landscape morphology in humid climates due to higher discharge, in alignment with previous modelling studies.

The third and final study in this thesis (Chapter 5) has been submitted to the Journal of Geophysical Research: Earth Surface. In the study, we focused on how lithology and biota affect drainage density and landscape morphology by analyzing three plutons within the semi-arid field site, a monzogranite and two diorites, which have the same climatic and tectonic conditions but different drainage densities and vegetation cover. For each rock type, we measured drainage density and obtained estimates of morphological characteristics (i.e., channel steepness), and together with a non-linear advection-diffusion equation, estimated ratios of diffusion to advection. We also measured vegetation cover, grain size, denudation rates, weathering intensity, and infiltration. We found that the monzogranite has a higher drainage density due to higher stream erosivity, which is caused by enhanced runoff and erodibility. The enhanced runoff is likely due to sparser vegetation in the monzogranite, which we link to a lower abundance of plant-essential elements in the monzogranite bedrock, whereas the denser vegetation cover in the diorites enhances

infiltration. Higher erodibility in the monzogranite results from a higher degree of weathering intensity and smaller sediment grains, which are more easily transported by streams and act as tools for incision. As each of these characteristics are linked to the monzogranite's bedrock composition and mineralogy, this study implies that lithology does indeed impact stream erosivity and drainage density.

1.3 Cosmogenic radionuclide analysis as a tool to measure denudation rates

In this thesis, I hypothesized that heterogeneity in bedrock properties, such as gradients in fracture density or grain size, or differences in bedrock composition, result in differential erosion and weathering rates. Such an influence of bedrock properties on erosion and weathering has been estimated in modelling studies; however, to test whether model predictions truly represent geomorphological processes in nature, field and laboratory data is required. In situ ^{10}Be cosmogenic radionuclide analysis is an ideal tool to answer the above-mentioned research questions, as it is a well-established method that provides bedrock erosion and weathering rates on intermediate timescales (thousands of years) that span the production and transport of sediment and soil from bedrock (von Blanckenburg and Willenbring, 2014). ^{10}Be radionuclide analysis also allows the quantification of erosion and weathering or residence times of material on various spatial scales, including individual sediment grains or boulders, patches of soil, or entire catchments. This feature allows for the analysis of differential erosion of boulders and the surrounding soil on hillslopes (Chapter 3), the residence time of stream boulders and catchment average erosion rates from fine sediment (Chapter 4) and the erosion and weathering rates of different rock types (Chapter 5).

Cosmogenic radionuclides are isotopes that are produced in mineral grains within rocks and soil at known rates. Nuclide production attenuates at an exponential rate with depth, and therefore the concentration of a given nuclide within a mineral can be used to estimate the residence time or erosion rates of the rock, sediment, or soil of interest (Lal, 1991; Granger and Riebe, 2014). Since cosmogenic radionuclide analysis captures both the erosion of particles and chemical weathering together, the term "denudation" is used as it refers to

the combined effects of erosion and chemical weathering. ^{10}Be is a cosmogenic nuclide produced by the nuclear reactions of cosmic rays, which are energetic particles that continuously bombard the earth. Like other cosmogenic nuclides produced in mineral grains (which include ^{14}C, ^{26}Al, ^{36}Cl, among others), ^{10}Be is produced when primary cosmic rays interact with atoms in the upper atmosphere and trigger a secondary cascade of nuclides that reach the earth's surface and create spallation reactions (Lal and Peters, 1967). Nuclides produced in the atmosphere are called "meteoric" while nuclides produced in minerals are called "in situ"; in this thesis, I measured in situ-produced nuclides. At the earth's surface, the cosmic ray flux that produces cosmogenic nuclides consist of neutrons and muons (Rossi, 1948), but neutronic production is more abundant, consisting of ~98.5% of production, whereas muonic production is relatively more abundant at depth (>3m) (Granger and Riebe, 2014). In situ ^{10}Be is most commonly produced from silicon or oxygen within mineral grains when the kinetic energy of a nuclear spallation reaction breaks up the nucleus of an oxygen atom and produces the lighter nuclide of ^{10}Be. Quartz (SiO_2) is a useful mineral for cosmogenic nuclide analyses because the ratio of oxygen to other incipient elements in the mineral is high, therefore maximizing the potential for ^{10}Be production. The concentration of ^{10}Be in soil and rock at the earth's surface is a function of the nuclide's production rate, which is dependent on the latitude and altitude of the sample and how much the sample has been shielded from cosmic rays (i.e. from surrounding mountains), as well as the sample thickness and density. In this thesis, I measured ^{10}Be concentrations from bedrock, boulders, soil, and stream sediment in three field areas along the Coastal Cordillera of Central Chile. In the following section, I describe that field setting in more detail.

Chapter 2

Study area

The study area of this thesis is the central Chilean Coastal Cordillera, a series of granitoid batholiths in the forearc of the Andean subduction zone (Figure 2.1). The Coastal Cordillera hosts a dramatic, 1300 km long climate and vegetation gradient (from 26-38°S); the northernmost part is in the hyper-arid Atacama Desert, and the southernmost part lies in a humid-temperate climate. This thesis project is part of "EarthShape", a program with a goal of exploring how "biologic processes form soil, influence topography, and thereby shape the Earth surface" on a climate and vegetation gradient in the Chilean Coastal Cordillera (www.earthshape.net). Field work was conducted in study sites selected by the EarthShape network due to their granitoid bedrock lithology, similar effective uplift rates (>100 m Myr^{-1}; Melnick, 2016), absence of glaciation during the Last Glacial Maximum, and location on protected land away from major human influence such as mines, dams, and large infrastructure. This thesis focuses on three of the EarthShape sites: the semi-arid, mediterranean, and humid-temperate sites. Samples for the first two studies were collected within the EarthShape field sites, to compare denudation rates and landscape morphologies between the different climate zones, along with the bedrock properties and grain size. A regional investigation of fault and stream orientations was additionally conducted in the first project that expanded beyond the EarthShape sites. The third project takes place entirely within the semi-arid field sites and focuses on how subtle differences in granitoid lithology can sculpt landscapes while holding climate constant. The following chapters outline the climatic (2.1), and geological setting (2.2).

2.1 Climate and biota

Chile contains one of the driest deserts on the planet in the north, the Atacama Desert, and one of the wettest regions of the world outside the tropics in the south,

Patagonia (Garreaud et al., 2009; Figure 2.1). The extreme aridity in northern Chile began between ~14 and 9 Ma (Jordan et al., 2014), and is a result of a combination of several factors. The Southeast Pacific anticyclone hovers above the area; the Humboldt current brings cold water from depth to the surface offshore of Chile (Hartley et al., 2005), which cools down the air and decreases its water holding capacity (Diaz and Kiladis, 1995); and the Andean topographic barrier blocks moisture coming from the Amazon (Insel et al., 2010). In northern Chile, rainfall, discharge, and erosion occurs mainly in pulses associated with El Nino events, with extreme rainfall events occurring every ~100 years (e.g., Houston, 2006; Aguilar et al., 2015). Southern Chile is affected by the Southern Westerlies, which bring high precipitation rates throughout the year, and is covered by three major ice fields which were more prominent during the Last Glacial Maximum (e.g., Rabassa, 2008).

The field areas in this thesis are in Central Chile and sit between these two climate extremes, but still represent a major gradient in rainfall, temperature, and vegetation. Increasing precipitation and vegetation density toward the south both influence erosional patterns and hydrological dynamics. From the semi-arid to humid-temperate EarthShape site, there is an increase in rainfall from 88 to over 1200 mm yr^{-1} (Meyer-Christoffer et al., 2015), an increase in vegetation from 31% to 95% cover (Broxton et al., 2014), and an increase in the fine fraction of hillslope sediment with the clay fraction from 20% to 40-50% (Terweh et al., 2021). In general, denser vegetation cover is associated with thicker mobile regolith, increased evapotranspiration and increased infiltration rates, which leads to more modulated and delayed river discharge responses to precipitation events (e.g., Ibarra et al., 2019). In contrast, more arid and sparsely vegetated climates are typically characterized by flashy discharge and high surface runoff, which leads to more stochastic erosive events (e.g., Vargas et al., 2000; 2006; Aguilar et al., 2014). Although arid conditions have persisted in northern Chile for millions of years, central and southern Chile experienced a wetter climate and colder air temperatures during the Last Glacial Maximum (~20,000 years ago) and Mid Holocene (Werner et al., 2018). These fluctuations affected vegetation species distribution but did not have a major effect on vegetation density (Werner et al., 2018).

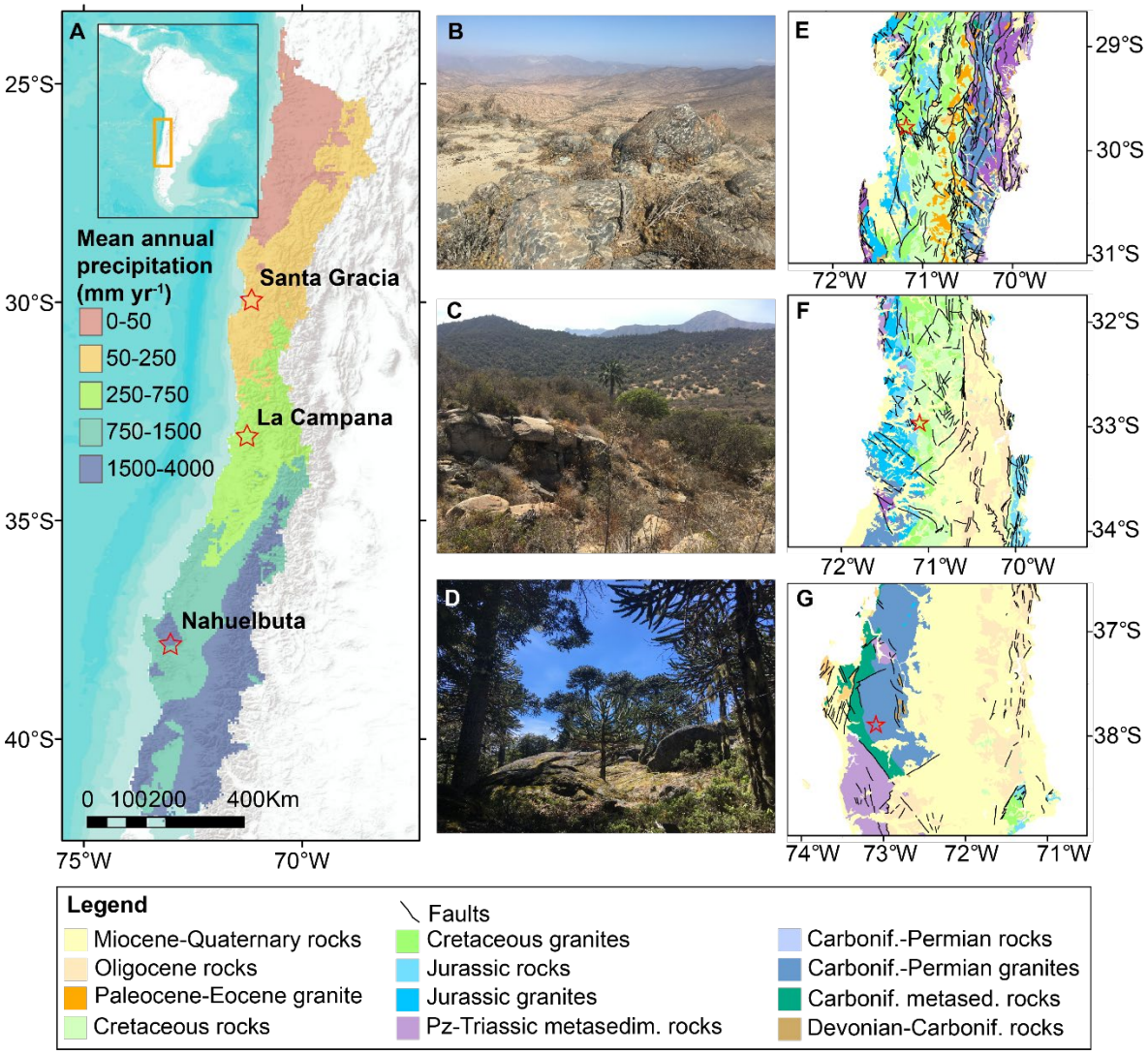

Figure 2.1. Overview of the field sites. A) Map of mean annual precipitation in Chile. Precipitation data from the CR2MET dataset, by the Center for Climate and Resilience Research (CR2) (Boisier et al., 2018), provides an average for the time period 1979-2019. World Terrain Base map sources are Esri, USGS, NOAA. B) Photo of Santa Gracia, the semiarid field area. C) Photo of La Campana, the mediterranean climate field site. D) Photo of Nahuelbuta, the humid-temperate field site. Geologic maps of E) Santa Gracia, F) La Campana and G) Nahuelbuta, showing major geologic units (legend below) and major faults. Field site locations are indicated with red stars. The geologic maps are from SERNAGEOMIN (2003).

2.2 Tectonic and geological setting

Central Chile is divided into three structural units, all parallel to the volcanic arc (from west to east): the Coastal Cordillera, the Central Depression, and the Andean pre-cordillera. The Coastal Cordillera of Central Chile is the oldest structural unit and is the focus of this thesis. It is comprised of a series of granitoid plutons whose ages range from Paleozoic in the south to Cretaceous in the north (Figure 2.1). The Coastal Cordillera was once the site of a volcanic arc; however, the arc has migrated eastward, and current volcanic activity occurs in the Andes. Now, the Coastal Cordillera consists of exhumed plutons that were once the magma chambers that fed the older volcanic arc.

The active Andean subduction zone lies directly to the west of the Coastal Cordillera and just offshore and hosts the subduction of the oceanic Nazca plate (formerly the Farallon Plate) under the continental South American plate, currently at a rate of ~6.5 cm yr^{-1} (Angermann et al., 1999; Kendrick et al., 2003). Subduction has been active since at least Jurassic times (e.g., Coira et al., 1982), and peaked at a rate of ~15 cm yr^{-1} during the Miocene (Pardo-Casas and Molnar, 1987; Somoza, 1998). Contact between the subducting Nazca plate and the overriding South American plate causes earthquakes to occur directly below the Coastal Cordillera, ~50 km below the subsurface (Husen et al., 1999, 2000; Buske et al., 2002). Earthquakes tend to occur in cycles of ~100-150 years; the Coastal Cordillera tends to uplift while the plate boundary is locked and stress builds; then stress is released when the boundary ruptures, and the Coastal Cordillera tends to subside (Comte and Pardo, 1991; Klotz et al., 1999; Pritchard et al., 2002; 2006; Chlieh et al., 2004). Earthquakes cause slip on faults within the Coastal Cordillera, and cause cracks to form (Allmendinger and Gonzales, 2010).

Faults cause the formation of smaller fractures which decrease the strength of bedrock and may increase rates of weathering and erosion in the Coastal Cordillera (Krone et al., 2021; Lodes et al., 2023; see Chapter 3 of this thesis). In addition, due to the complex magmatic processes involved in creating the plutons that now comprise the Coastal Cordillera, the cordillera consists of granitoid bedrock of diverse mineralogical makeup (Oeser et al., 2018). Compositionally heterogeneous plutons, which have been faulted and

fractured by subduction earthquakes over many millions of years (e.g., Allmendinger and Gonzalez, 2010), have given rise to a mountain range that is not entirely homogeneous but instead hosts bedrock with variable strength and susceptibility to weathering and erosion.

Indeed, there are granitoid plutons of different compositions and with varying fracture density within the field sites investigated in this thesis (see Chapters 3 and 5). These bedrock heterogeneities along the Chilean Coastal Cordillera provide a unique opportunity to study how subtle yet crucial differences in bedrock properties control landscape morphologies along a climate and vegetation gradient.

Chapter 3

The story of a summit nucleus: Hillslope boulders and their effect on erosional patterns and landscape morphology in the Chilean Coastal Cordillera

Emma Lodes[1], Dirk Scherler[1,2], Renee van Dongen,[3] and Hella Wittmann[1]

[1]GFZ German Research Centre for Geosciences, Earth Surface Geochemistry, Telegrafenberg, 14473 Potsdam, Germany

[2]Freie Universität Berlin, Institute of Geographical Sciences, 12249 Berlin, Germany

[3]International Centre for Water Resources and Global Change, 56068 Koblenz, Germany

This chapter is published in:

Earth Surface Dynamics Vol. 11, issue 12, pages 305-324, 2023
Emma Lodes, Dirk Scherler, Renee van Dongen, and Hella Wittmann
https://doi.org/10.5194/esurf-11-305-2023

Table S3.1 is published with GFZ Data Services as:
Lodes, Emma; Scherler, Dirk; van Dongen, Renee; Wittmann-Oelze, Hella (2022): Beryllium-10 erosion rate data for hillslope erosion in the Coastal Cordillera, Chile. GFZ Data Services. https://doi.org/10.5880/GFZ.3.3.2022.004

Abstract

While landscapes are broadly sculpted by tectonics and climate, on a catchment scale, sediment size can regulate hillslope denudation rates and thereby influence the location of topographic highs and valleys. In this work, we used *in situ* ^{10}Be cosmogenic radionuclide analysis to measure the denudation rates of bedrock, boulders, and soil, in three granitic landscapes with different climates in Chile. We hypothesize that bedrock and boulders affect differential denudation by denuding more slowly than the surrounding soil, where the null hypothesis is that no difference exists between soil and boulder or bedrock denudation rates. To evaluate denudation rates, we present a simple model that assesses differential denudation of boulders and the surrounding soil by evaluating boulder protrusion height against a two-stage erosion model and measured ^{10}Be concentrations of boulder tops. We found that hillslope bedrock and boulders consistently denude more slowly than soil in two out of three of our field sites, which have a humid and a semi-arid climate: denudation rates range from ~5 to 15 m Myr^{-1} for bedrock and boulders and from ~8 to 20 m Myr^{-1} for soil. Furthermore, across a bedrock ridge in the humid site, denudation rates increase with increasing fracture density. In our lower-sloping field sites, boulders and bedrock appear to be similarly immobile based on similar ^{10}Be concentrations. However, in the site with a mediterranean climate, steeper slopes allow for higher denudation rates for both soil and boulders (~40-140 m Myr^{-1}), while the bedrock denudation rate remains low (~22 m Myr^{-1}). Our findings suggest that unfractured bedrock patches and large hillslope boulders affect landscape morphology by inducing differential denudation in lower-sloping landscapes. When occurring long enough, such differential denudation should lead to topographic highs and lows controlled by bedrock exposure and hillslope sediment size, both a function of fracture density. We further examined our field sites for fracture control on landscape morphology by comparing fracture, fault and stream orientations, with the hypothesis that bedrock fracturing leaves bedrock more susceptible to denudation. Similar orientations of fractures, faults, and streams further supports the idea that tectonically-induced bedrock fracturing guides fluvial incision and accelerates denudation through reducing hillslope sediment size.

3.1 Introduction

Landscapes on Earth are shaped by tectonic uplift and climate, which dictate erosional and weathering regimes over geologic timescales. When uplift and climate are held constant sufficiently long, fluvial landscapes reach a steady state, in which the slopes of hills and stream channels adjust so that denudation rates match tectonic uplift rates (e.g. Burbank et al., 1996; Kirby and Whipple, 2012). Variations in bedrock strength and the grain size of hillslope sediment, however, exert additional control on the morphology of hills and valleys (e.g. Attal et al., 2015; Glade et al., 2017). Initially, hillslope sediment size is set by lithology and the density of fractures, which are formed due to tectonic and topographic stresses (e.g. Molnar et al., 2007; St. Claire et al., 2015; Roy et al., 2016; Sklar et al., 2017). Near the earth surface, water, often carrying biotic acids, infiltrates bedrock fractures and promotes chemical weathering that further reduces sediment size and converts bedrock to regolith (Lebedeva and Brantley, 2017; Hayes et al., 2020). Therefore, long residence times of sediment in the weathering zone (on a million-year timescale) may result in complete disintegration of bedrock and the formation of saprolite and soil, whereas rapid erosion and short residence times can lead to hillslope sediment size limited by fracture spacing (e.g. Attal et al., 2015; Sklar et al., 2017; Roda-Boluda et al., 2018; Verdian et al., 2021). A spectrum between these end-members can also exist within one catchment, especially where variations in lithology, fracture density or elevation cause spatial differences in the rate and/or extent of weathering (e.g. Sklar et al., 2020). Where weathering does not completely disintegrate the bedrock, boulders, or corestones, can be found embedded in hillslope sediment, with a maximum size set by the spacing of bedrock fractures (Fletcher and Brantley, 2010; Buss et al., 2013; Sklar et al., 2017). Here we focus on the effects of such boulders on differential denudation and landscape morphology on hillslopes with mixed cover of soil, boulders and bedrock.

Soil-mantled hillslopes are typically considered to be dominated by diffusive processes, for which conceptual models and geomorphic transport laws are relatively well-established (e.g., Dietrich et al., 2003; Perron, 2011). However, these models generally assume uniform hillslope material and do not account for the exhumation of larger boulders through the critical zone. Neely et al. (2019) recently addressed erosion and soil transport

on mixed bedrock and soil-covered hillslopes using a nonlinear diffusion model, but assumed the same denudation rate for bedrock and soil. Fletcher and Brantley (2010) modeled the reduction in the size of corestones due to chemical weathering as they are exhumed through the weathering zone, although this model does not consider the corestones' effect on differential erosion. Often, however, bedrock and large boulders protrude above the surrounding soil, indicating that they are eroding more slowly than the soil (Biermann and Caffee, 2002). Indeed, studies have shown that average denudation rates of bedrock outcrops and hillslope boulders are often lower than catchment average and soil denudation rates (e.g. Bierman, 1994; Heimsath et al., 2000; Heimsath et al., 2001; Granger et al., 2001; Portenga and Bierman, 2011).

Larger boulders require greater forces to be moved, which can be achieved by steepening slopes (Granger et al., 2001; DiBiase et al., 2018; Neely and DiBiase, 2020), or by lengthening residence time until subaerial weathering has decreased their size sufficiently to be transported downslope. During this prolonged residence time, boulders can shield hillslopes from erosion (Glade et al., 2017; Chilton and Spotlia, 2020), and stream channels from incision (Shobe et al., 2016; Thaler and Covington, 2016). In terrain where spatial gradients in bedrock fracture spacing result in spatial gradients of hillslope sediment size, it is thus reasonable to expect that the resistance of surface boulders to weathering and transport ought to retard erosion locally, resulting in spatially differential erosion. Moreover, fractured, and therefore weaker, bedrock facilitates erosion via both abrasion and plucking by streams (Lamb et al., 2015; Sklar and Dietrich, 2011), and smaller blocks are also more easily transported in fluvial systems (Shobe et al., 2016). Therefore, we would expect that rivers preferentially incise in zones of more intensely fractured rocks (Buss et al., 2013) that align with the orientation of faults (Molnar et al., 2007; Roy et al., 2016).

In this study we provide a new framework for measuring and assessing differential denudation of boulders and the surrounding fine-grained regolith on hillslopes, and also discuss the extent to which bedrock fracturing affects sediment size, denudation rates, and stream incision. We quantified bedrock, boulder, and soil denudation rates in three different areas along the granitic Coastal Cordillera of Chile with different climates and erosional regimes, using *in situ* cosmogenic ^{10}Be. By developing a simple model to convert

^{10}Be concentrations from boulders into soil and boulder denudation rates, we explored the hypothesis that on a hillslope, boulders affect differential erosion by eroding more slowly than the surrounding soil, with the corresponding null hypothesis that no difference exists between soil and boulder denudation rates. We make the simplifying assumption that soil denudation rates remain constant over the time period that a boulder is exhumed, and over long time periods, denudation rates throughout the landscape vary according to whether boulders or soil are exposed at the surface. Following the logic outlined above, we additionally examined our field sites for signs of fracture control on landscape morphology with the hypothesis that more highly fractured bedrock is more susceptible to denudation and stream incision than intact bedrock.

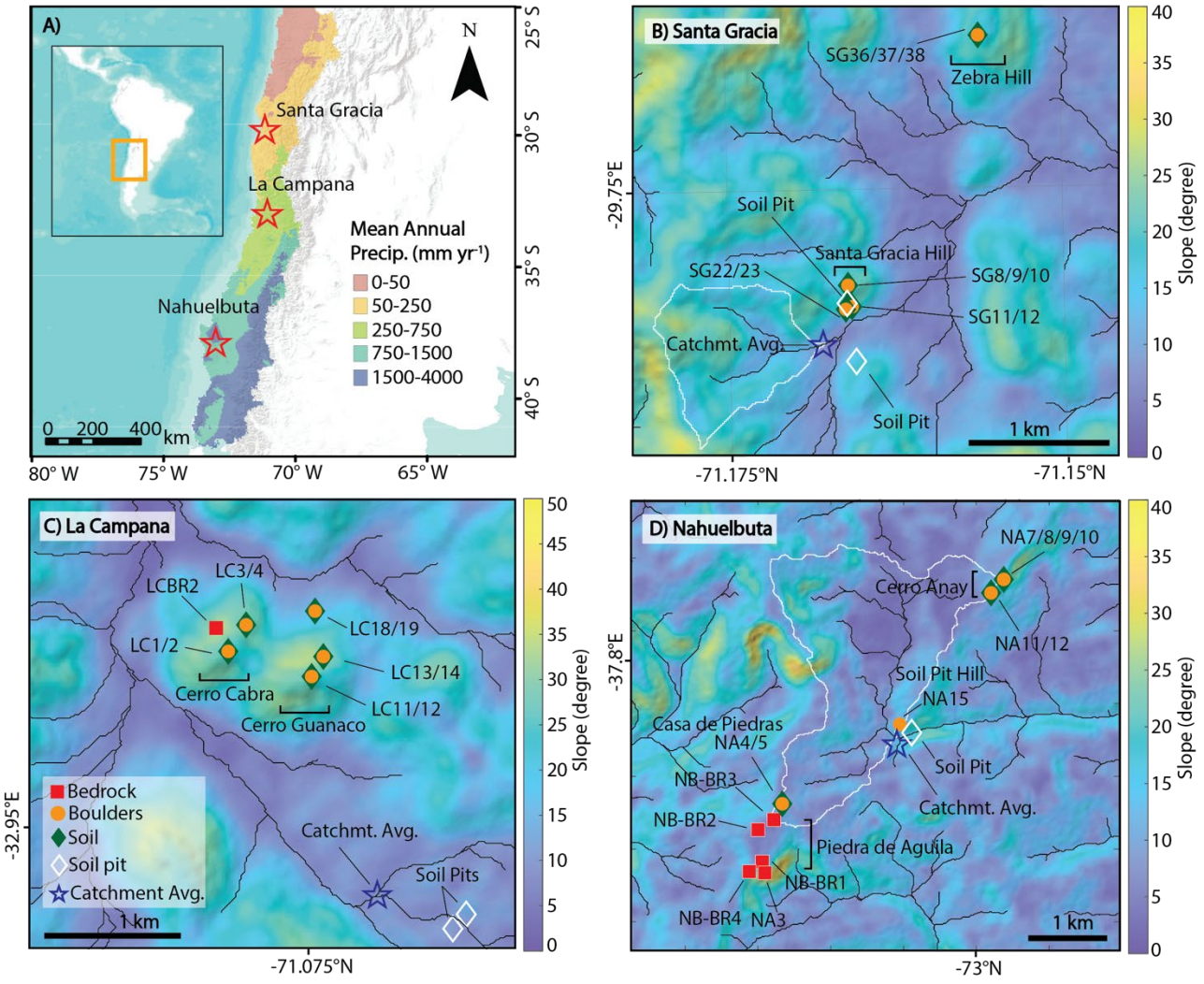

Figure 3.1. Field site locations and features. A) Map of mean annual precipitation in central Chile, with field sites marked by red stars. Precipitation data from the CR2MET dataset, by the Center for Climate and Resilience Research (CR^2) (Boisier et al., 2018), provides an average for the time period 1979-2019. World Terrain Base map sources are Esri, USGS, NOAA. B-D: Slope and hillshade maps from 12.5-m ALOS PALSAR digital elevation models, of B) Santa Gracia (SG), C) La Campana (LC), and D) Nahuelbuta (NA). Sample locations and sample names are shown, with symbol shape and color indicating the sample type (see legend in lower left panel). White outlines delineate the catchments from which the catchment average sample (star) was taken (the catchment from La Campana does not fit within the bounds of the map and therefore is not shown). Black lines indicate streams. Soil pit sample data are from Schaller et al. (2018), and catchment average sample data are from van Dongen et al. (2019).

3.2 Field sites

The Chilean Coastal Cordillera, a series of batholiths in the forearc of the Andean subduction zone, lies along a marked climate gradient with humid conditions in the south and hyper-arid conditions in the north (Figure 3.1). The Andean subduction zone, in which the Nazca Plate subducts under the South American Plate, has been active since at least Jurassic times (e.g., Coira et al., 1982). In this study we investigated three field sites along the Coastal Cordillera from south to north: Nahuelbuta National Park, (NA), with a humid-temperate climate, La Campana National Park (LC), with a mediterranean climate, and Private Reserve Santa Gracia (SG), with a semi-arid climate (Figure 3.1). NA and SG have more gently-sloping hillslopes with a lack of observed landslides, while hillslopes in LC are steeper and landslides have been observed (van Dongen et al., 2019; Terweh et al., 2021). All three sites are underlain by granitoid bedrock (Oeser et al., 2018), none show any signs of former glaciation, and all are located on protected land, away from major human influence, such as mines, dams, and large infrastructure. In all three sites, denudation rates from ^{10}Be cosmogenic radionuclide analysis have been reported by van Dongen et al. (2019) (catchment average rates), and Schaller et al. (2018) (soil pits).

NA is located on an uplifted, fault-bounded block (plateau), an unusually high part of the Coastal Cordillera with a mean elevation of ~1300 m above sea level. Tectonic uplift rates in NA increased from 0.03–0.04 to >0.2 mm year^{-1} at 4±1.2 Ma (Glodny et al., 2008), a

shift that appears to be also recorded by knickpoints in streams that drain the plateau. All of the measurements in this work are from the plateau (~9° mean slope), above knickpoints (see Figure S3.1). ^{10}Be-derived denudation rates are around 30 m Myr^{-1} (Schaller et al., 2018; van Dongen et al., 2019), indicating that denudation rates on the NA plateau have not yet adjusted to the higher uplift rates. The main catchment in LC has a mean elevation of 1323 m with a mean slope of 23°, and regional uplift rates are estimated to be <0.1 mm yr^{-1} (Melnick, 2016). Van Dongen et al. (2019) reported a catchment average denudation rate of ~200 m Myr^{-1} for a sub-catchment in LC, whereas Schaller et al. (2018) reported soil denudation rates of 40-55 m Myr^{-1}. In SG, the mean elevation is 773 m above sea level, the mean slope is 17.2°, and uplift rates are <0.1 mm year^{-1} (Melnick, 2016). Previously reported ^{10}Be-derived denudation rates are ~9-16 m Myr^{-1} (Schaller et al., 2018; van Dongen et al., 2019).

3.3 Methods

3.3.1 In situ ^{10}Be analysis

3.3.1.1 Sample collection

We collected samples for cosmogenic ^{10}Be analysis from bedrock, boulders, and soil to estimate denudation rates in our field sites, targeting hillslopes near previously-collected catchment average and soil pit samples from van Dongen et al (2019) and Schaller et al. (2020). All sample locations are shown in Figure 3.1. Bedrock samples were taken using a hammer and chisel from an area of up to ~20 m × 20 m (on ridge tops or hillslopes) and consist of an amalgamation of at least ten chips (~25 cm^2 and <2 cm thick), with which we aim to obtain representative mean values of denudation rates that are potentially variable due to episodic erosion by spalling rock chips (Small et al., 1997). Similarly, for boulder samples, one chip was taken from the top of each of at least ten similarly-sized boulders and amalgamated for an area of up to ~40 m × 40 m, depending on boulder abundance. Topsoil samples were also collected by amalgamation in the area surrounding the sampled boulders. In places with many various-sized boulders, we collected samples from different protrusion heights (~1-m tall boulders, ~0.5-m tall boulders, etc.). Each sampled boulder was measured along the a, b, and c axes, as far as discernible (see Table 3.1). We also

measured the protrusion height of each boulder from the center of the top of the boulder to the ground. Each protrusion height value in Table 3.1 consists of an average of at least ten boulders of similar protrusion heights that we sampled for one amalgamated sample. Boulders on sloping surfaces typically show varying protrusion heights, with higher values downslope and lower values upslope. In such cases, we measured protrusion at the sides of boulders. Occasionally, we observed that upslope protrusion was further reduced by sediment trapping upslope of boulders. We targeted boulders that appear to be in situ (essentially, exhumed corestones), based on the observation that they are tightly imbedded in the ground. We acknowledge that it is possible that some of the larger sampled boulders are connected to bedrock roots, and that it is also possible that some boulders are not in situ, despite our best efforts.

In NA, we collected five bedrock samples from an area called Piedra de Aguila from outcrops with different fracture densities, and measured fracture spacing (47 measurements) by stringing a measuring tape along the bedrock surface and measuring the distance between fractures that were at least 1 mm wide, and fracture orientations (41 measurements), using a Brunton compass (Figure 3.2A1 and Figure 3.2A2). We further collected six boulder samples and three soil samples from the ridge and hillslope of Cerro Anay (Figure 3.2A3), an area called Casa de Piedras, and a hillslope near the soil pits that were sampled by Schaller et al. (2018). We measured the dimensions of all boulders from which we took a sample chip (141 boulders). In LC and SG, we were not able to collect samples at variably fractured bedrock outcrops due to rarely exposed bedrock. In LC, we took one bedrock sample, two boulder samples and two soil samples from the ridge and slope of Cerro Cabra (Figure 3.2B1), and three boulder samples and three soil samples from the ridge, upper slope, and lower slope of Cerro Guanaco (Figure 3.2B3). In SG, we took four boulder samples and three soil samples from the ridge and slope of Santa Gracia Hill, which also hosts the soil pits of Schaller et al. (2018) (Figure 3.2C2 and 3.2C3), and two boulder samples and one soil sample from the ridge of Zebra Hill (Figure 3.2C1).

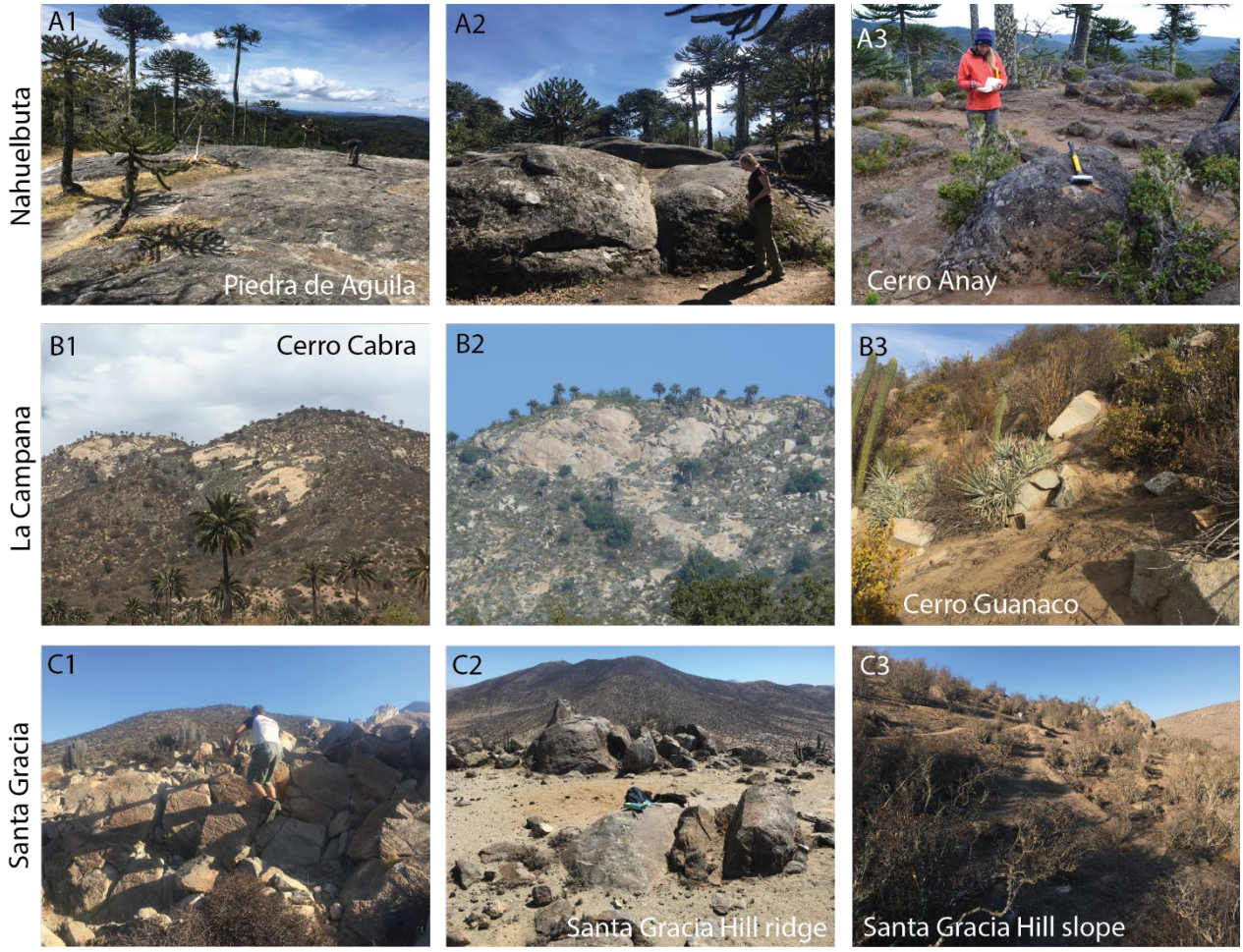

Figure 3.2. Field photos showing the various surfaces sampled, including bedrock, boulders and soil. Figure panels are grouped by field site. A: Nahuelbuta, A1) Bedrock (sample NB-BR1). A2) Fractured bedrock, in transition between unfractured bedrock and boulders (sample NB-BR2). A3) Smaller boulders surrounded by soil (sample NA7). B: La Campana, B1) Bedrock (sample LC-BR2). B2) Bedrock transitioning to large boulders and soil. B3) Boulders and soil on a hillside (samples LC13 and LC14). C: Santa Gracia, C1) Boulders on Zebra Hill delineated by fractures. C2) Large boulders on the ridge of Santa Gracia Hill (sample SG8). C3) Soil with minimal boulders on the slope of Santa Gracia Hill (samples SG22 and SG23).

3.3.1.2 Analytical methods

We dried, crushed, and sieved amalgamated bedrock and boulder samples for quartz mineral separation, and dried and sieved soils, each to 250-500 micrometer particle size, or to 250-1000 micrometers if the 250-500 micrometer sample amount wasn't sufficient. We used standard physical and chemical separation methods to isolate ~20 g of pure quartz from each sample. After spiking each sample with 150 µg of ^{9}Be carrier and dissolving the

quartz in concentrated hydrofluoric acid, we extracted Be following protocols adapted from von Blanckenburg et al. (2004). $^{10}Be/^{9}Be_{(carrier)}$ ratios were measured by accelerator mass spectrometry at the University of Cologne, Germany (Dewald et al., 2013). Sample ratios were normalized to standards KN01-6-2 and KN01-5-3 with ratios of 5.35×10^{-13} and 6.320×10^{-12}, respectively. Final ^{10}Be concentrations were corrected by process blanks with an average $Be^{10}/Be^{9}_{(carrier)}$ ratio of $(2.21\pm0.25)\times10^{-14}$.

3.3.1.3 Denudation rate calculations

In order to calculate denudation rates from the measured ^{10}Be concentrations, we evaluated bedrock, boulder, and soil samples differently. Bedrock samples present the simplest case, in which we assumed steady state erosion and calculated bedrock denudation rates (ϵ_{br}) using the CRONUS online calculator v2.3 (Balco et al., 2008). The steady state assumption is based on our amalgamated sampling, and follows the results of Small et al. (1997), who showed that an amalgamation of several individual bedrock samples is a reasonable approximation of the long-term average denudation rate in episodically eroding settings.

Boulder and soil samples require a more nuanced assessment. Boulders protrude above the ground surface, which implies that the lowering of the ground surface (i.e., the soil denudation rate, ϵ_s) is faster than the lowering of the boulder's surfaces (i.e., the boulder denudation rate, ϵ_b) (Figure 3.3). Thus, even while they are buried and covered by soil (or saprolite), boulders are exposed to cosmic rays for a significant amount of time prior to breaching the surface (Figure 3.3A). We refer to this time span as phase 1. When boulders breach the surface, they should have a concentration similar to that of the surrounding soil (Figure 3.3B). As boulders are exposed during phase 2, nuclide production and decay continues, but it takes time for the boulder surfaces to attain a ^{10}Be concentration that is in equilibrium with the slower boulder denudation rate. Thus, we expect that the measured concentrations from the tops of boulders are combinations of the two different phases in which ^{10}Be is accumulated at different rates (first a rate corresponding to the soil denudation rate, and after exhumation, a rate corresponding to the boulder denudation rate). Converting the ^{10}Be concentrations of soil samples collected from around the boulders to a denudation rate also requires a special approach, as these

samples include an unknown number of grains eroded off boulders, which ought to increase the ^{10}Be concentration, due to the slower denudation rate of boulders, as compared to soil.

Because of the above complications, we used an approach to estimate the soil and boulder denudation rates that considers the measured boulder protrusion heights and their measured ^{10}Be concentrations. We modelled ^{10}Be concentrations ($N_{modelled}$, in atoms g^{-1}) by approximating the production rate profile with a combination of several exponential functions (e.g., Braucher et al., 2011) during the two different phases:

$$N_{modelled} = \sum_i \frac{P_i(0)}{\lambda + \frac{\epsilon_s \rho}{\Lambda_i}} e^{-t_2 \lambda} + \sum_i \frac{P_i(0)}{\lambda + \frac{\epsilon_b \rho}{\Lambda_i}} \left[1 - e^{-t_2 (\lambda + \frac{\epsilon_b \rho}{\Lambda_i})}\right] \quad (3.1),$$

where i indicates different terms for the production by spallation, fast muons, and negative muons; $P_i(0)$ are the site-specific ^{10}Be surface production rates in atoms g^{-1} yr^{-1} for the different production pathways (Table 3.1); λ is the ^{10}Be decay constant (4.9975 ×10^{-7}); ϵ_b is the boulder denudation rate (cm yr^{-1}); and Λ_i is the attenuation length scale (160 g cm^{-2} for spallation, 4320 g cm^{-2} for fast muons, and 1500 g cm^{-2} for negative muons, respectively; Braucher et al., 2011). ρ is the bedrock and boulder density, and here we use a value of 2.6 g cm^{-3} for all samples; we discuss the impact of density changes in section 3.5.1. Surface production rates by spallation are based on a SLHL (sea level high latitude) reference production rate of 4.01 atoms g^{-1} yr^{-1} (Borchers et al., 2016) and the time-constant spallation production rate scaling scheme of Lal (1991) and Stone (2000) ('St' in Balco et al., 2008). Surface production rates by both fast and negative muons were obtained using the MATLAB-function 'P_mu_total.m' of Balco et al. (2008). Topographic shielding at each sampling site was calculated with the function 'toposhielding.m' of the TopoToolbox v2 (Schwanghart and Scherler, 2014) and 12.5-meter resolution ALOS PALSAR-derived digital elevation models (DEMs) from the Alaska Satellite Facility.

In equation 3.1, the first term represents phase 1 and the second term represents phase 2, with t_2 being the exposure time of the boulder, calculated from the height of the boulder (z) divided by the difference between the soil denudation rate and the boulder denudation rate:

$$t_2 = \frac{z}{(\epsilon_s - \epsilon_b)} \tag{3.2}$$

For each sample and associated average boulder protrusion height, we modelled ^{10}Be concentrations with equation 3.1 for different combinations of soil and boulder denudation rates that we allowed to vary between 5 and 50 m Myr^{-1} (NA), between 3 and 50 m Myr^{-1} (SG), and between 10 and 300 m Myr^{-1} (LC), guided by previously published denudation rate estimates (Schaller et al., 2018; van Dongen et al., 2019). We consider permissible denudation rates as those for which the difference between the modelled and observed ^{10}Be concentrations is less than the measured 2σ concentration uncertainty.

This idealized model rests on several assumptions; (1) the landscapes are in a long-term steady state where denudation is locally variable as boulders and bedrock are exhumed in different locations, but this variation is around a long-term stable average; (2) soil denudation rates remain steady over the course of boulder exhumation; (3) boulders are in situ and have not rolled downhill; (4) boulders have not been intermittently shielded during their exhumation; and (5) soil density is inconsequential and can be assigned the same value as bedrock. Assumption 3 has a higher chance of being violated on steep slopes or where boulders are tall, and assumption 4 is more likely violated where boulders are densely clustered. These assumptions are discussed in more detail in section 3.5.1.

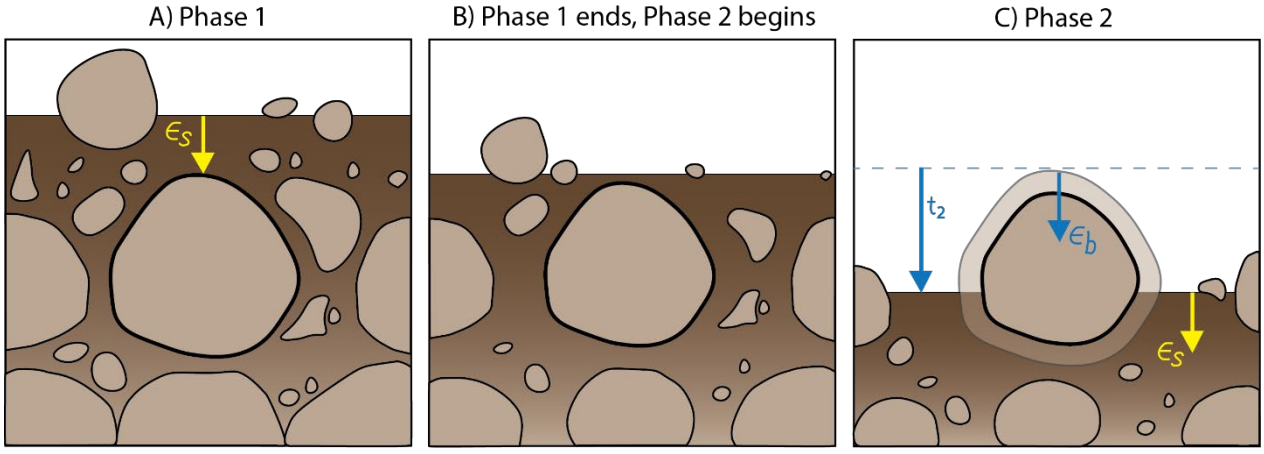

Figure 3.3. Schematic image showing the process of boulder exhumation. A) Overview of the setting: a mixed soil- and bedrock- covered hillslope where sediment size decreases with decreasing fracture spacing. B) During phase 1, the boulder is buried, and accumulates nuclides at a rate governed by the soil denudation rate, ϵ_s. C) Phase 1 ends when the boulder breaches the soil surface. D) During phase 2, the boulder itself is eroding at a rate of ϵ_b, and the surrounding soil continues to denude at a rate of ϵ_s. Phase 2 lasts for a time period t_2 that ends with our sampling.

3.3.2 Topographic analysis

To test if stream orientations in our field sites follow fault orientations, we analyzed the orientations of streams using one-meter resolution LiDAR DEMs (Kügler et al., 2022). Within each DEM, we first calculated stream networks based on flow accumulation area thresholds of 10^4, 10^5 and 10^6 m^2. The lowest threshold was determined based on the occurrence of incised channels visible in the DEMs. We then used the TopoToolbox function 'orientation' with a default smoothing factor (*K*) of 100, to obtain the orientation of each node in the stream network. Fractures in the field can only be seen where there are bedrock outcrops, which are generally scarce. Therefore, we decided to refer to the orientation of faults, as depicted in geological maps, with the assumption of similar orientation (Krone et al., 2021; Rodriguez Padilla et al., 2022). To obtain the orientation of mapped faults, we extracted faults within ~50 km of each sampling site from a 1:1,000,000-scale geological map from Chile's National Geology and Mining Service in ArcGIS (SERNAGEOMIN, 2003). Fault orientations were measured for straight fault segments with a length of 100 m. Because we are only interested in the strike of streams and faults, all orientations lie between 0° and 180°. For displaying purposes in rose diagrams, we mirrored these values around the diagram origin by duplicating values and adding 180°.

3.4 Results

3.4.1 ^{10}Be concentrations

Table 3.1. ^{10}Be cosmogenic nuclide sample data.

Sample ID	IGSN [a]	Sampling location [b]	Latitude (°N)	Longitude (°E)	Sample type [c]	^{10}Be conc. ±2σ (×10^5) (atoms g^{-1})	^{10}Be conc. normalized by SLHL ±2σ (×10^5) (atoms g^{-1}) [d]	^{10}Be production rate (spallation, atoms g^{-1} yr^{-1})	Site scaling factor [e]	Slope angle at sample location (°) [f]	Avg. boulder width / protrusion or fracture density [g]	No. chips taken for sample
Nahuelbuta												
NB-BR1	GFRD1002U	PdA ridge 1	-37.826	-73.035	BR	8.25±0.56	2.92±0.20	11.41	2.82	18	7.83	20
NB-BR2	GFRD1002V	PdA ridge 2	-37.821	-73.034	BR	6.92±0.48	2.43±0.18	11.44	2.85	4	4.75	15
NB-BR3	GFRD1002W	PdA ridge 3	-37.819	-73.032	BR	5.18±0.40	1.86±0.14	11.15	2.78	3	2	15
NB-BR4	GFRD10029	PdA ridge 4	-37.825	-73.034	BR	3.85±0.28	1.36±0.10	11.46	2.84	16	4.78	15
NA3	GFEL10002	PdA slope	-37.826	-73.034	BR	6.55±0.46	2.38±0.16	11.25	2.75	25	4.43	30
NA4	GFEL10003	CdP	-37.817	-73.031	B	9.08±0.64	3.49±0.24	10.43	2.60	5	1.70 / 0.68	30
NA7	GFEL10006	CA ridge	-37.789	-72.998	B	10.28±0.72	3.65±0.26	11.3	2.81	10	1.52 / 1.00	10
NA8	GFEL10007	CA ridge	-37.789	-72.998	B	8.94±0.62	3.18±0.22	11.3	2.81	10	3.30 / 2.43	10
NA9	GFEL10008	CA ridge	-37.789	-72.998	B	7.57±0.54	2.69±0.18	11.3	2.81	10	0.64 / 0.19	10
NA11	GFEL1000A	CA slope	-37.790	-72.999	B	7.67±0.54	2.76±0.18	11.18	2.78	14	1.90 / 1.60	10
NA15	GFEL1000E	SPH slope	-37.807	-73.013	B	2.84±0.14	1.12±0.06	10.24	2.53	18	0.96 / 0.76	12
NA5	GFEL10004	CdP	-37.817	-73.031	S	2.32±0.20	0.89±0.08	10.43	2.60	5	N/A	N/A
NA10	GFEL10009	CA ridge	-37.789	-72.998	S	5.04±0.36	1.79±0.12	11.3	2.81	10	N/A	N/A
NA12	GFEL1000B	CA slope	-37.790	-72.999	S	4.27±0.32	1.54±0.12	11.18	2.78	14	N/A	N/A
La Campana												
LC-BR2	GFRD1002X	CC slope	-32.938	-71.081	BR	1.83±0.22	1.38±0.16	5.75	1.33	39	N/A	15
LC2	GFEL1002J	CC ridge	-32.939	-71.081	B	0.92±0.18	0.59±0.12	6.25	1.55	9	0.95 / 0.54	10
LC4	GFEL1003V	CC slope	-32.938	-71.079	B	0.92±0.16	0.66±0.12	5.77	1.40	27	0.30 / 0.15	10
LC11	GFEL1000Q	CG ridge	-32.941	-71.074	B	1.21±0.14	0.76±0.08	6.42	1.59	13	1.32 / 0.70	10
LC13	GFEL1000S	CG upper slope	-32.94	-71.073	B	0.73±0.16	0.51±0.12	6.13	1.43	33	0.32 / 0.20	12
LC18	GFEL1000Z	CG lower slope	-32.937	-71.074	B	1.55±0.16	1.17±0.12	5.43	1.32	18	0.50 / 0.32	12
LC1	GFEL1002H	CC ridge	-32.939	-71.081	S	1.54±0.18	0.99±0.12	6.25	1.55	9	N/A	N/A
LC3	GFEL1003W	CC slope	-32.938	-71.079	S	1.03±0.18	0.74±0.12	5.77	1.40	27	N/A	N/A
LC12	GFEL1000R	CG ridge	-32.941	-71.074	S	0.88±0.08	0.55±0.06	6.42	1.59	13	N/A	N/A
LC14	GFEL1000T	CG upper slope	-32.940	-71.073	S	0.63±0.08	0.44±0.06	6.13	1.43	33	N/A	N/A
LC19	GFEL1000X	CG lower slope	-32.937	-71.074	S	1.84±0.14	1.39±0.10	5.43	1.32	18	N/A	N/A
Santa Grácia												
SG8	GFEL10017	SGH ridge	-29.756	-71.166	B	5.94±0.42	4.17±0.30	5.72	1.42	10	1.10 / 0.80	10
SG9	GFEL10018	SGH ridge	-29.756	-71.166	B	4.70±0.34	3.30±0.24	5.72	1.42	10	0.38 / 0.12	10
SG11	GFEL1001A	SGH slope 1	-29.758	-71.166	B	3.56±0.26	2.61±0.20	5.56	1.36	21	1.30 / 0.87	9
SG22	GFEL1001M	SGH slope 2	-29.758	-71.166	B	3.85±0.30	2.83±0.22	5.56	1.36	22	0.37 / 0.24	11
SG37	GFEL1002T	ZH ridge	-29.740	-71.156	B	11.46±0.88	8.21±0.62	5.64	1.40	28	1 / 0.90	10
SG38	GFEL1002S	ZH ridge	-29.740	-71.156	B	7.84±0.56	5.62±0.40	5.64	1.40	28	0.10 / 0.12	10

SG10	GFEL10019	SGH ridge	-29.756	-71.166	S	2.58±0.22	1.81±0.16	5.72	1.42	10	N/A	N/A
SG12	GFEL1001B	SGH slope 1	-29.758	-71.166	S	2.39±0.18	1.75±0.14	5.56	1.36	21	N/A	N/A
SG23	GFEL1001N	SGH slope 2	-29.758	-71.166	S	2.10±0.16	1.54±0.12	5.56	1.36	22	N/A	N/A
SG36	GFEL1002U	ZH ridge	-29.740	-71.156	S	5.40±0.50	3.87±0.36	5.64	1.40	28	N/A	N/A

[a]Open access metadata: http://igsn.org/[insert IGSN number here]
[b]Sample locations: PdA: Piedra de Aguila, CdP: Casa de Piedas, CA: Cerro Anay, SPH: Soil Pit Hill, CC: Cerro Cabra, CG: Cerro Guanaco, SGH: Santa Gracia Hill, ZH: Zebra Hill..
[c]Sample type abbreviations: BR: bedrock, B: boulders, S: soil.
[d]Concentrations were normalized to SLHL (sea level high latitude) using a SLHL production rate of 4.01 atoms g-1 yr^{-1} (Borchers et al., 2016) and the site's scaling factor.
[e]Time constant spallation production rate scaling scheme of Lal (1991) and Stone (2000) ('St' in Balco et al., 2008), calculated taking topographic shielding into account.
[f]Local hillslope angles were calculated using a 12.5m DEM and an 8-connected neighbourhood method.
[g]Fracture density for bedrock (in meters) and width and protrusion measurements (in meters) for boulders. Values are averages of >10 measurements per sample site.

Measured ^{10}Be concentrations span a wide range of values, and are generally lowest in LC and higher in NA and SG (Table 3.1). Within NA, we observe the lowest averaged ^{10}Be concentrations (normalized to SLHL) for soil samples ($\mu \pm 2\sigma = 1.41\times10^5\pm0.06\times10^5$ atoms g^{-1}), followed by bedrock samples ($2.19\times10^5\pm0.07\times10^5$ atoms g^{-1}) and boulder samples ($2.82\times10^5\pm0.08\times10^5$ atoms g^{-1}) (Figure 3.4A). In NA at Piedra de Aguila, where we were able to measure fracture spacing in areas with exposed bedrock, the ^{10}Be concentrations of samples from fractured bedrock decrease with increasing fracture density (Figure 3.5A). One boulder sample from the slope of Soil Pit Hill stands out with a concentration that is lower than most soil samples. Similar, but slightly higher average values as in NA are attained in SG, with soil samples ($2.24\times10^5 \pm 0.11\times10^5$ atoms g^{-1}) being lower than boulder samples ($4.22\times10^5 \pm 0.16\times10^5$ atoms g^{-1}) (Figure 3.4C). Only in LC are the differences between averaged soil ($0.82\times10^5 \pm 0.04\times10^5$ atoms g^{-1}) and boulder samples ($0.74\times10^5 \pm 0.05\times10^5$ atoms g^{-1}) small, and with 2σ error, within uncertainties (Figure 3.4B). In addition, at 3 out of 5 sampling locations in LC, boulders have lower concentrations than adjacent soil samples, inconsistent with the assumption that $\epsilon_s < \epsilon_b$ (see section 3.3.1.3). However, our single bedrock sample from LC has a higher concentration of $1.38\times10^5 \pm 0.16\times10^5$ atoms g^{-1}. In NA and SG, boulder samples from slope locations have lower average ^{10}Be concentrations compared to boulder samples from ridge locations. Again, in LC this pattern does not hold. Finally, we do not observe a significant trend between ^{10}Be concentration and protrusion height (Figure 3.5D); however, there is a relationship between protrusion height and slope for LC (Figure 3.5E).

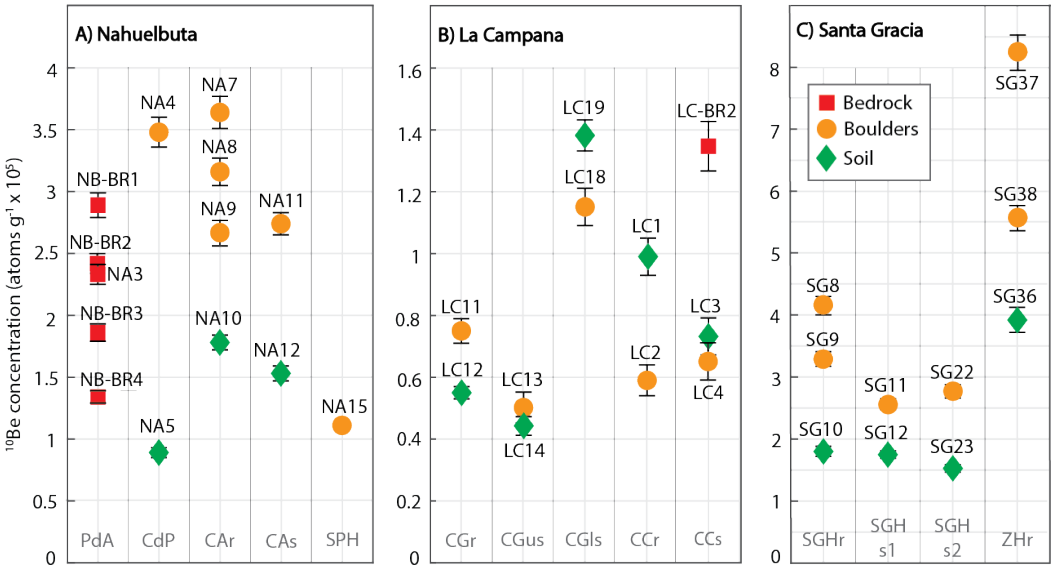

Figure 3.4. Measured ^{10}Be concentrations normalized to reference production rate at sea-level high latitude for A) Nahuelbuta, B) La Campana, and C) Santa Gracia; note different scales of y-axes. X-axes are not numerical but rather show the sampling locations, also reported in Table 3.1. Labels next to data points provide sample IDs, also reported in Table 3.1. Gray labels at the bottom of panels are the sample locations. PdA: Piedra de Aguila, CdP: Casa de Piedas, CAr: Cerro Anay ridge, CAs: Cerro Anay slope, SPH: Soil Pit Hill, CGr: Cerro Guanaco ridge, CGus: Cerro Guanaco upper slope, CGls: Cerro Guanaco lower slope, CCr: Cerro Cabra ridge, CCs: Cerro Cabra slope, SGHr: Santa Gracia Hill ridge, SGHs1: Santa Gracia Hill slope 1, SGHs2: Santa Gracia Hill slope 2, ZHr: Zebra Hill ridge.

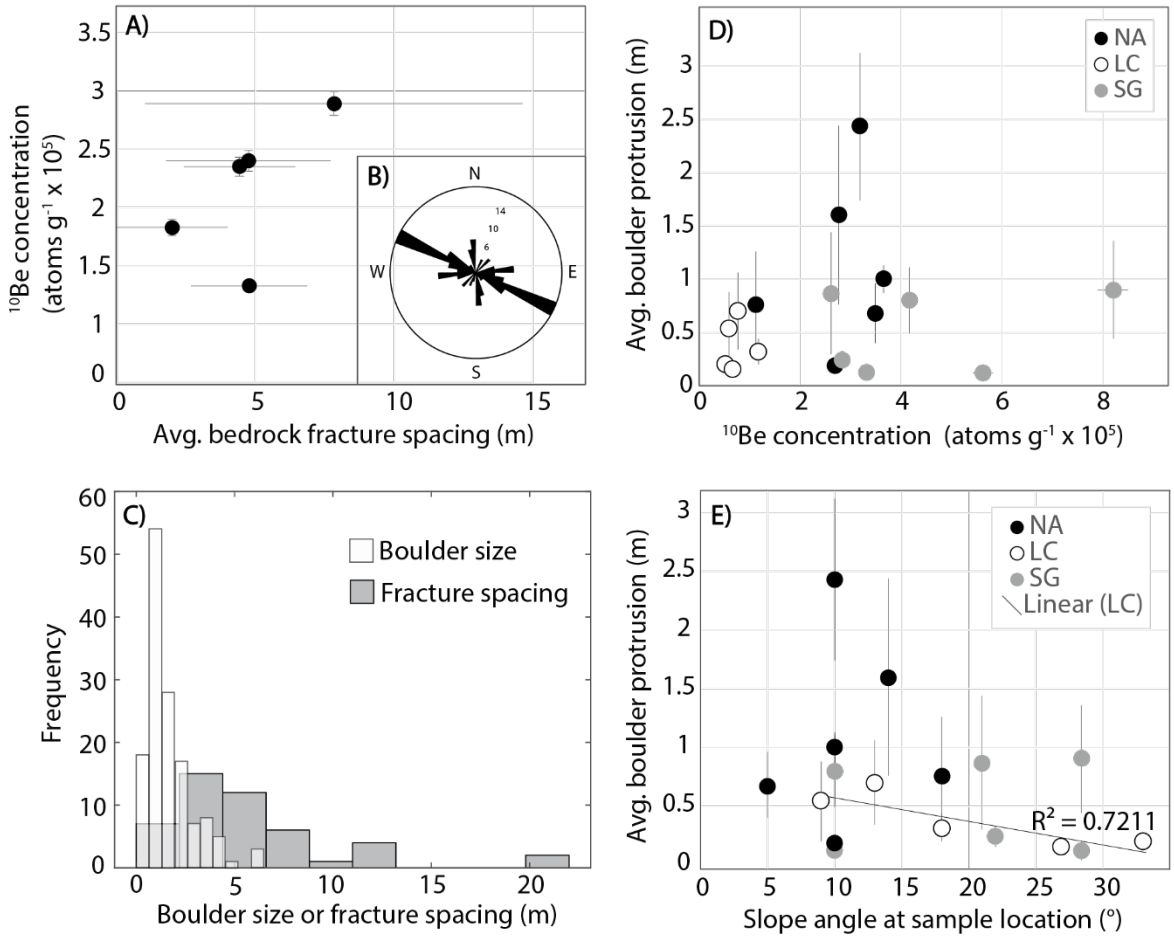

Figure 3.5. A) Average bedrock fracture spacing (NA only), plotted against measured ^{10}Be concentrations normalized to the reference production rate at sea-level high latitude. Error bars represent the standard deviation of all fracture spacing measurements for each location. B) Rose diagram showing bedrock fracture orientations measured in the field in NA (same fractures as panel A). C) Measurements of individual fracture spacing and individual boulder sizes, where boulder size is the average of the x and y axes of each boulder and the z axis is the protrusion height. D) Average boulder protrusion height plotted against measured ^{10}Be concentrations normalized to reference production rate at sea-level high latitude for each field site. Error bars represent the standard deviation of all boulder protrusion height measurements for each location. E) Average boulder protrusion height plotted against hillslope angle. A linear regression model is fit through LC datapoints.

3.4.2 Bedrock, boulder, and soil denudation rates

Bedrock denudation rates in NA range from 8.53±0.60 m Myr^{-1} to 18.64±1.40 m Myr^{-1}, and the LC bedrock sample yielded a denudation rate of 22.28±2.62 m Myr^{-1}. We modelled boulder (ϵ_s) and soil denudation rates (ϵ_s) using the approach described in section 3.3.1.3 for all boulder samples that have higher concentrations than the adjacent soil

concentrations. We address locations where ^{10}Be concentrations are higher in soil compared to boulder samples in the discussion (three locations in LC and one in NA). In contrast to the bedrock denudation rates, modelled boulder and soil denudation rates have no unique solution, and their ranges of possible denudation rates are more complex (Figure 3.6). The ranges of denudation rates, illustrated by the curves in Figure 3. 6, are comprised of values for which the difference between the measured and modelled ^{10}Be concentrations are less than the measured 2σ ^{10}Be concentration uncertainty, where modelled ^{10}Be concentrations are based on Eq. 3.1. Each colored band represents one amalgamated boulder sample (such as 1-meter-protruding boulders from the ridge of Cerro Anay). The x-axis shows the range of modelled boulder denudation rates, and the y-axis shows the range of modelled soil denudation rates. However, not every combination within the range plotted in Figure 3.6 is plausible. For example, the part of the colored bands in Figure 3.6 that is close to the 1:1-line (edge of the gray area) exists because at very low differential denudation rates (differences between soil and boulder denudation rates), phase 2 gets very long so that the boulder denudation rate dominates the resulting concentration and approaches the value one would obtain when neglecting the first term on the right side in Eq. 3.1. We argue that differential denudation rates of less than ~1 m Myr^{-1} are highly unlikely, as it would take ~1 Myr to exhume a boulder of only 1 m in height above the soil, while simultaneously eroding many times more soil and boulder material.

In NA, permissible modelled soil denudation rates range from ~13 to 37 m Myr^{-1} and permissible modelled boulder denudation rates range from ~5 to 20 m Myr^{-1} (Figure 3.6A). Three samples that were taken from the same ridge at Cerro Anay (Figure 3.2A3 and 3.4A) all overlap in denudation rate despite varying protrusion heights. These samples also overlap with a sample from Casa de Piedras, and together indicate a rather narrow range of soil and boulder denudation rates of ~15-20 m Myr^{-1} and ~10-15 m Myr^{-1}, respectively. Only the mid-slope sample from Cerro Anay has higher modelled soil and boulder denudation rates. In LC, modelled boulder and soil denudation rates that are consistent with the measured ^{10}Be concentrations extend to much higher values compared to the other field sites (40-140 m Myr^{-1}; Figure 3.6B) and the two solutions do not overlap. In SG, permissible modelled denudation rates are similar in magnitude to results from NA (Figure 3.6C); soil denudation rates range from ~7 to 28 m Myr^{-1} and boulder denudation rates range from ~4

to 23 m Myr^{-1}. Samples taken from the ridge of Santa Gracia Hill (Figure 3.2C2 and 3.4C) have permissible modelled soil and boulder denudation rates that overlap at values of ~12-15 m Myr^{-1} and ~10-12 m Myr^{-1}, respectively, whereas samples from the ridge of Zebra Hill overlap at ~4-5.5 m Myr^{-1} for boulders and ~6.5-7.5 m Myr^{-1} for soil. Samples from the slope of Santa Gracia Hill have higher modelled soil denudation rates, when considering very low differential denudation rates unlikely. We further discuss the most plausible ranges of denudation rates in sections 3.5.1 and 3.5.2.

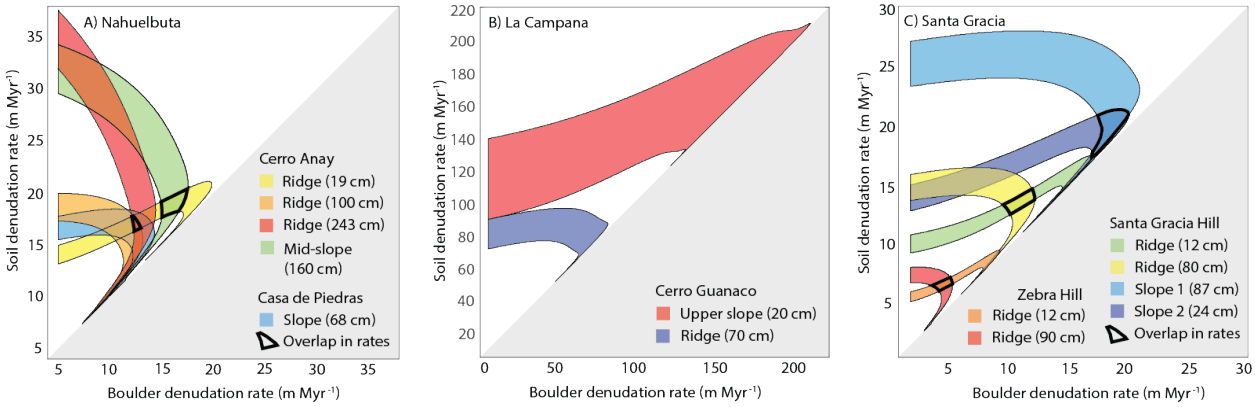

Figure 3.6. Range of best fitting combinations of modelled soil and boulder denudation rates in A) Nahuelbuta, B) La Campana, and C) Santa Gracia according to Eq. 3.1. Each color band corresponds to an amalgamated boulder sample, listed in the legend along with the average protrusion height of the boulders. Areas where best fitting denudation rates overlap for samples from the same location are highlighted by a black outline. The gray areas are forbidden fields, as by assumption, boulder denudation rates have to be lower than soil denudation rates, otherwise there would be no boulder protruding above the soil surface.

3.4.3 Fault and stream orientations

Fault orientations in our field sites, based on straight segments of 100 m (8,731 segments for SG, 6,572 segments for LC, and 6,214 segments for NA), generally have at least one dominant orientation that aligns with stream orientations (Figure 3.7). Stream orientations depend on the flow accumulation threshold: at smaller thresholds (10^4 m^2), abundant small streams yield a wide distribution of orientations that seems to reflect the shape of the catchment as a whole. At a high flow accumulation threshold (10^6 m^2), the

derived stream networks comprise only the largest channels and their orientation is strongly controlled by the orientation and tilt of the drainage basin. This can be seen clearly in NA, where the east-west oriented trunk stream is weighted heavily. In SG, faults and stream orientations match each other well, both trending north-south. In LC and NA, one of two regional fault orientations match stream orientations, and faults closest to the field sites more closely match dominant stream orientations (red faults in Figure 3.7). Specifically, in LC, the dominant orientations for the regional faults are roughly northeast and secondarily northwest, whereas streams are generally oriented northwest. In NA, faults generally have east-west and northwest-southeast orientations, and streams with an accumulation threshold above 10^4 follow an east-west orientation. Fracture orientations measured in the field (in NA) also generally agree with the larger fault and stream orientations, with mostly west-northwest – east-southeast orientations (Figure 3.5B). Our fracture spacing measurements are mostly in the range of 2-15 meters (Figure 3.5A), while our boulder width measurements are generally smaller (0-5 meters). When plotted together, the distribution of boulder sizes sits at the left tail of the distribution of the fracture spacing measurements (Figure 3.5C).

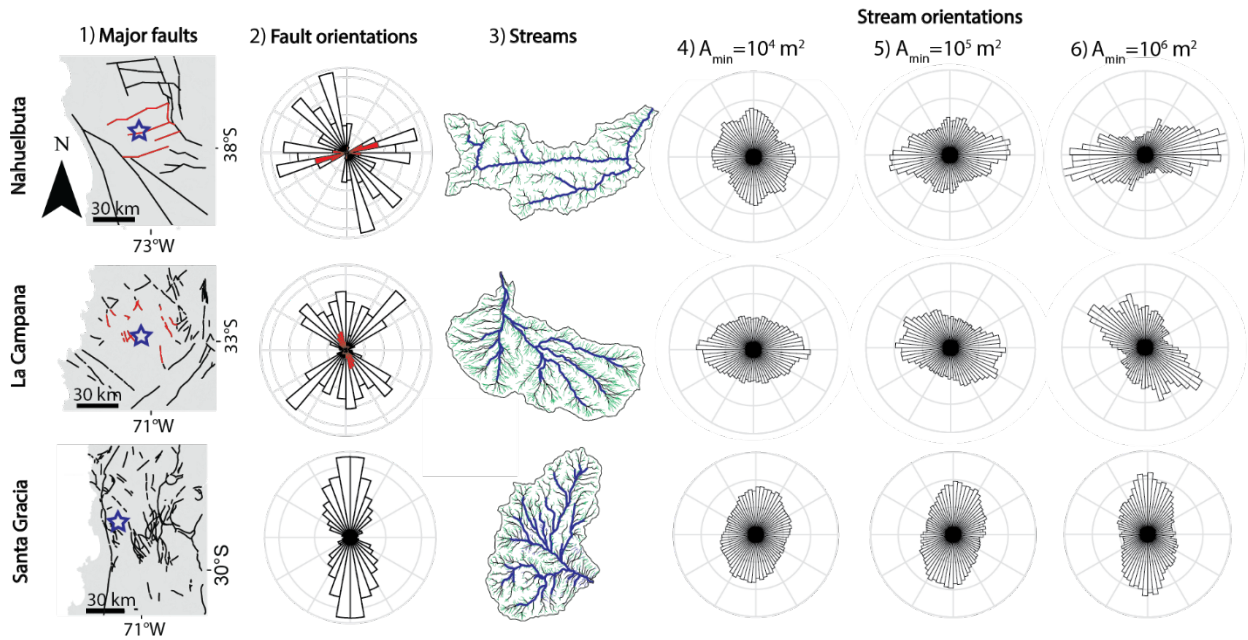

Figure 3.7. Rose diagram plots and maps showing fault and stream orientations for Nahuelbuta (top row), La Campana (middle row), and Santa Gracia (bottom row). For each

field site, the columns show from left to right: (1) major faults digitized from geological map (SERNAGEOMIN, 2003), within ~50 km (black) and ~25 km (red, NA and LC only) of the sampling site (blue star); (2) rose diagram of fault orientations from the maps in column 1, constructed using 100 m long, straight fault segments and 36 bins, with orientations of faults <25 km from NA and LC in red; (3) a map of the studied catchments and the drainage network, with green, black, and blue streams indicating minimum upstream areas (A_{min}) of 10^4, 10^5, and 10^6 m^2, respectively, derived from one-meter resolution LiDAR DEMs (Kügler et al., 2022).; (4-6) rose diagrams (72 bins) of stream orientations for different A_{min}. All maps and rose diagrams are oriented with the top being north.

3.5 Discussion

3.5.1 Deciphering the denudation rates of boulders and soil

Our model results show that there exists no unique combination of soil and boulder denudation rates for any particular site (Figure 3.6). Which, then, are the most plausible combinations of boulder and soil denudation rates? The answer depends on the characteristic exhumation histories of the boulders, and events that could have influenced the accumulation of ^{10}Be during the course of exhumation. In order to narrow down the ranges of denudation rates for boulders and soils investigated in this study, we address our model assumptions and complicating factors, such as shielding and toppling of boulders, and compare measured and modelled ^{10}Be concentrations of soils to each other.

Our model rests on five main assumptions outlined at the end of section 3.3.1.3. The first, long-term steady state of the landscape, is difficult to assess; however, the lack of knickpoints above our sampling locations (Figure S3.1) suggests this to be reasonable. With our dataset, it is also difficult to assess assumption two, whether soil denudation rates were steady or variable throughout boulder exhumation; however, we speculate on this possibility below. Assumptions 3 and 4, regarding boulder mobility and shielding, are discussed in depth in the next section. Assumption 5 is that the density of soil can be treated like the density of boulders and bedrock. Although the density of soil and saprolite layers is in reality lower, we assume a steady thickness of these layers through time, which means that the lowering of the bedrock-saprolite boundary occurs at the same rate as that of the soil surface. The actual thickness of the soil and saprolite layers is relatively

unimportant (Granger and Riebe, 2014), and thus one can consider the thickness to be zero. While this approach may appear unrealistic, it is important to note that the attenuation of cosmogenic nuclide production with depth depends on length times density, and a lower density soil layer can simply be viewed as inflated bedrock.

3.5.1.1 Shielding and toppling of boulders

There exist two scenarios that would lead to violations of our model assumptions 3 and 4, and would inadvertently introduce bias into our approach of determining boulder denudation rates: (1) sampling of boulders that have been previously shielded by soil or other boulders, and (2) sampling of boulders that have toppled or rolled downhill, and that are no longer in situ. In either case, the actual production rate for the sample would be lower than assumed, leading to an artificially high denudation rate estimate. Shielding by boulders is more likely in areas where there are tall, densely-clustered boulders, or at protruding bedrock outcrops such as Piedra de Aguila, where we measured a very low ^{10}Be concentration in sample NB-BR4 (Table 3.1; Figure 3.4A). This sample was taken from a bedrock knob close to a cliff in an area accessed by tourists; it is possible that the low concentration of our sample is due to shielding by boulders that toppled, or were manually moved from the sampled area.

Boulders in steeply sloping areas are more likely to be shielded by soil or topple downhill. In LC, where slopes are generally steeper than the other field sites, it is possible that some boulders were not in situ when we sampled them: they could have rolled or been overturned on the steep slopes, uncovering a side that was previously shielded. They could have also been transiently shielded by soil coming from upslope (Figure 3.2B3). In addition, there is a significant relationship between protrusion height and hillslope angle for LC boulders, indicating that boulders on steeper slopes are either smaller, or may be partially buried by upslope soil (Figure 3.5E). Indeed, three boulder samples from LC (LC2, LC4, and LC18; Table 3.1) have measured ^{10}Be concentrations that are lower than the surrounding soil, violating our model assumptions, and suggesting that the sampled boulder surfaces were shielded. Two of these amalgamated boulder samples (LC4 and LC18) were collected from slopes with rather high angles of 27° and 18°, respectively, and therefore could include toppled boulders. Boulder sample LC2 however was collected on a ridge with a relatively

lower slope of 9° (Table 3.1). In that case, the low ^{10}Be concentration could stem from shielding by stacked boulders (scenario 1). In NA, one boulder sample (NA15; Table 3.1) also has a very low ^{10}Be concentration and was not included in the model. We did not collect a soil sample near the boulder sample NA15, and instead compared its concentration to the adjacent surficial soil pit sample of Schaller et al. (2018). Because these samples were not taken exactly next to each other, there exists some ambiguity in this comparison. However, the relatively low ^{10}Be concentration of sample NA15 when compared to other boulder samples in NA suggests issues that could be related to shielding or toppling of boulders. Over long timescales, we expect all sampled boulders to be fully exhumed and either weather away completely in place or topple down the hill, eventually ending up in streams where they would be exported from the catchment. It is plausible that such a cycle of boulder exposure, exhumation, and transport has operated in the past and will continue into the future. In LC, due to higher hillslope angles and overall higher denudation rates, this cycle seems to be occurring at a faster rate, probably leading to a higher chance of sampling boulders that have more recently been exhumed and rolled downhill.

3.5.1.2 Plausible ranges for modelled denudation rates

For most of our soil samples, measured ^{10}Be concentrations agree well with modelled ^{10}Be concentrations (Table 3.2), suggesting that our model setup and assumptions are reasonable. Positive or negative deviations stemming from soil samples collected in the field are expected, however, because (1) our soil samples are most likely a mixture between lower concentration soil that is directly exhumed from below, and higher concentration grains eroded from the surrounding boulders, (2) soil surrounding boulders could be blocked from moving downslope by the boulders themselves (as shown in Glade et al., 2017), which could slow down soil transport and raise soil ^{10}Be concentrations, (3) we did not account for shielding of soil by the surrounding boulders, which would lower production rates, and (4), quartz could be enriched in weathered soils (Riebe and Granger, 2013). In most cases, the modelled soil concentrations are slightly lower than the measured soil concentrations, which suggests that cases 1, 2, or 4 are common in our field sites. The relevance of case 4 (quartz enrichment) depends on the degree of chemical weathering, and can lead to an overestimation of ^{10}Be concentrations. Work by Schaller and Ehlers (2022)

suggests that on average about half the mass loss in La Campana and Santa Gracia occurs by chemical weathering in soil and saprolite, but only about a quarter in Nahuelbuta. However, their data stem from meter-deep soil pits, whereas our soil samples were collected from areas in between boulders, where the soil depth is probably less deep, and also variable. In order to calculate a quartz enrichment factor, we would need additional geochemical data, such as zircon enrichment in soils and bedrock, which we do not have; therefore, we can only assume the possibility of some quartz enrichment leading to higher-than-expected ^{10}Be concentrations in our soil samples.

Sample location	Soil sample ID	Best-fitting modelled soil denudation range rate (ϵ_s) (m Myr^{-1})	Corresp. modelled range of ^{10}Be conc. ($\times10^5$) (atoms g^{-1}) for soil (N_m)	Measured ^{10}Be conc. $\pm2\sigma$ ($\times10^5$) (atoms g^{-1})	Boulder sample IDs	Best-fitting modelled boulder denudation rate range (ϵ_b) (m Myr^{-1})	Differential erosion rate (boulder vs. soil; m Myr^{-1})	Time needed for boulder exposure (Kyr)
Nahuelbuta								
CdP	NA5	15-20	3.61-4.75	2.32±0.20	NA4	10-15	5	136
CA ridge	NA10	15-20	3.89-5.12	5.04±0.36	NA7, NA8, NA9	10-15	5	200, 486, 38
CA slope	NA12	18-20	3.84-4.25	4.27±0.32	NA11	15-18	2.5	640
La Campana								
CG ridge	LC12	70-90	0.54-0.69	0.88±0.08	LC11	40-60	30	23
CG upper slope	LC14	120-140	0.32-0.37	0.63±0.08	LC13	80-120	30	7
Santa Gracia								
SGH ridge	SG10	12-15	2.77-3.41	2.58±0.22	SG8, SG9	10-12	2.5	320, 48
SGH slope 1	SG12	19-21	1.94-2.13	2.39±0.18	SG11	18-20	1	870
SGH slope 2	SG23	19-21	1.94-2.13	2.10±0.16	SG22	18-20	1	240
ZH ridge	SG36	6.5-7.5	4.78-5.45	5.40±0.50	SG37, SG38	4-5.5	2.25	400, 53

Table 3.2. Modelled denudation rates for soil and boulder samples using the first term of Eq. 3.1, and comparison of modelled and measured ^{10}Be concentrations for soil samples. Sample location abbreviations are described in the caption for Table 3.1.

In one sampling site (Casa de Piedras in NA), the measured soil ^{10}Be concentration is significantly lower than the modelled soil ^{10}Be concentration (Table 3.2). If the soil was eroding as fast as our measured soil samples indicate, the boulders should be protruding higher. However, Casa de Piedras has a high density of tall boulders. The observed discrepancy could be caused by boulders shielding the soil directly surrounding it from

cosmic rays, or by eroding chips with low ^{10}Be concentrations of shielded parts of the boulders, perhaps from the base, that fall directly into the soil.

Another discrepancy exists in the relationship between measured ^{10}Be concentrations and protrusion heights of our sampled boulders. No significant relationship exists between protrusion height and ^{10}Be concentration for all samples plotted together (Figure 3.5D); this is to be expected as each individual site has a unique local denudation rate. On the other hand, one would expect a relationship between protrusion and concentration for boulders sampled from the same site (i.e. at Cerro Anay ridge in NA, and Santa Gracia Hill and Zebra Hill in SG). At Santa Gracia Hill and Zebra Hill, taller boulders have a higher ^{10}Be concentration, as expected, but the highest-protruding boulder sample from Cerro Anay has a lower concentration than the second-tallest sample, perhaps due to toppling of pieces of the tallest boulders. The differential erosion rate between boulders and soil at Cerro Anay ridge is also one of the highest for NA at 5 m Myr^{-1} (Table 3.2), indicating relatively rapid exposure of boulders that may raise the risk of boulder toppling. However, there is an overlap in the modelled denudation rates of all three boulder and soil sample pairs from Cerro Anay ridge (Figure 3.6A).

The lack of a trend between boulder protrusion height and ^{10}Be concentration could also be due to changing soil denudation rates over time. Taller boulders and boulders with longer residence times (such as those on the slope of Cerro Anay Hill in NA and the slope of Santa Gracia Hill in SG; Table 3.2), were exhumed during one or more glacial-interglacial cycles; during such climatic transitions, soil denudation rates could have changed. Similarly, Raab et al. (2019) suggested that soil denudation rates surrounding tors in southern Italy shifted in conjunction with climate changes over the course of their exhumation (around 100 ka). However, our approach yields an average soil denudation rate over the time of boulder exhumation; therefore, we can only speculate whether soil denudation rates were variable. Carretier et al. (2018) analyzed denudation rate data for Chile averaged over decadal and millennial timescales, and found that millennial denudation rates are higher than decadal erosion rates, with the highest discrepancy between integration time periods being in the arid north. However, the authors suggest that this discrepancy is related to

increased stochasticity of erosion in arid regions; millennial erosion rates reflect many stochastically erosive events, such as 100-year floods, that decadal rates do not record.

Given the above caveats and uncertainties, we attempted to identify the most plausible range of denudation rates for each sample type and location for all modelled denudation rates. Specifically, we identified most plausible denudation rate ranges for samples on Cerro Anay ridge and Casa de Piedras based on their overlap with each other, for samples on Cerro Anay slope based on their overlap with sample NA9 on Cerro Anay ridge, and ranges for Santa Gracia hill ridge and slope and Zebra Hill ridge based on the overlap of modelled rates for each location, respectively (Figure 3.6). For LC we regard denudation rates near the center of the modelled curves in Figure 3.5 to be most plausible, based on reasonable expectations of differential erosion (section 3.4.2), and considering possible issues with shielding and toppling (section 3.5.1). These ranges are listed in Table 3.2 along with measured and modelled ^{10}Be concentrations of soil samples, and are displayed in Figure 3.8 along with previously published soil (Schaller et al., 2018) and catchment-average denudation rates (van Dongen et al., 2019). In the following section, we discuss the erosional processes that may account for the differences and similarities in denudation rates from bedrock, boulders, soil (this study and Schaller et al., 2018), and stream sediment (van Dongen et al., 2019) within each field site. We focus on the modelled denudation rates from this study that we regard to be most plausible.

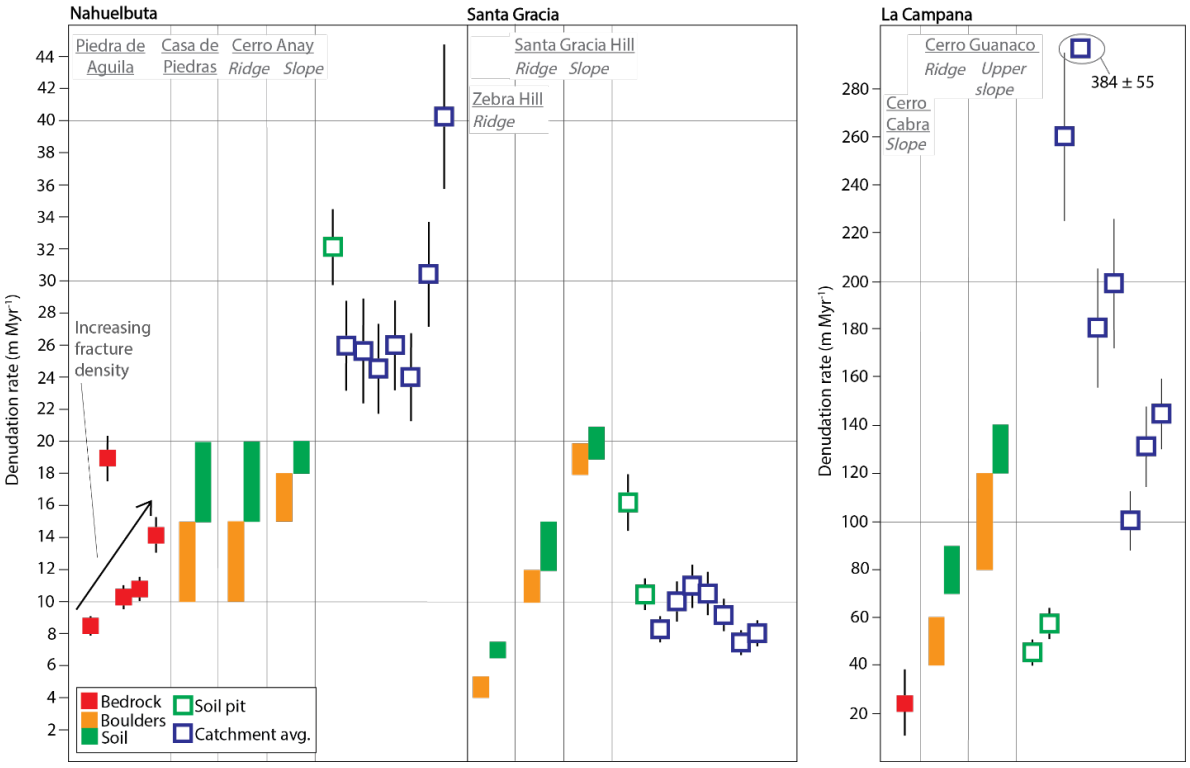

Figure 3.8. Overview of new and previously published denudation rates (data from this study are shown by solid symbols and previously-published data are shown by hollow symbols). Soil pit data is from Schaller et al. (2018), and catchment average data is from van Dongen et al. (2019). Catchment average denudation rates from various sediment grain sizes (from left to right for each field site: 0.5-1, 1-2, 2-4, 4-8, 8-16, 16-32, and 32-64 mm). Bedrock denudation rates are calculated using the CRONUS online calculator v2.3 (Balco et al., 2008). Boulder and soil denudation rates are estimated using our model and reflect the most plausible denudation rates as described in section 3.5.1.2. Denudation rates for each location within a field site are separated by thin gray bars, and locations are labeled at the top of the chart. Samples that were not included in the model (one sample from Nahuelbuta and 3 samples from La Campana) are also not included here.

3.5.2 Processes controlling differential erosion

3.5.2.1 Nahuelbuta (NA)

In NA, the slowest denudation rates occur on bedrock and boulders, likely because precipitation runs off quickly from exposed bedrock, limiting its chemical alteration (Eppes and Keanini, 2017) and weathering (Hayes et al., 2020), whereas soils denude faster. However, denudation rates for soil surrounding the sampled boulders are lower than denudation rates from the soil pit and the catchment average denudation rates. It is

possible that boulders physically block soil from being transported downslope: where a dense clustering of exhumed boulders exists, the regolith will be thinner, and the boulders may retard soil erosion throughout the area in which they are clustered (Glade et al, 2017). Considering boulder protrusion and modelled differential erosion rates, boulders in NA are exposed over a long period (up to 640 Kyr), allowing time to affect the long-term transportation of surrounding soil downslope. Although we did not measure sediment damming upslope of boulders in the field, we did note a small amount of sediment damming for boulders on slopes. Away from exhumed boulders, where soil is thicker and where slopes are steep enough, shallow landsliding can occur, as observed in NA by Terweh et al. (2021). In accordance with these observations, van Dongen et al. (2019) found that smaller grains in stream sediment were likely derived from the upper mixed soil layer, and the largest grains were likely excavated from depth, perhaps by shallow landsliding. The smaller grains have denudation rates similar to those presented in this study (Figure 3.8), while larger grains have denudation rates similar to deeper soil pit samples from Schaller et al. (2018).

Finally, in NA, where bedrock fracture density is higher, denudation rates are also higher (Figure 3.8), likely because precipitation infiltrates into fractures, accelerating chemical weathering, regolith formation (St. Claire et al., 2015; Lebedeva and Brantley, 2017), and subsequent vegetation growth, which introduces biotic acids that further accelerate chemical weathering (Amundson et al., 2007). We further speculate that large exhumed boulders in NA are also sites of less-fractured bedrock at depth, as boulders can only be as large as the local fracture spacing allows (e.g. Sklar et al., 2017). Based on the observed differences in soil, boulder, and fractured bedrock denudation rates in NA, and on previous studies that have correlated higher fracture density with more rapid erosion (e.g., Dühnforth et al., 2010; DiBiase et al., 2018; Neely et al., 2019), we suggest that bedrock fractures have an effect on NA's morphology through grain size reduction and differential erosion. Further, the thicker soil cover and shallow landsliding on NA slopes may increase the discrepancy between slowly-eroding bedrock and boulders versus more rapidly-eroding, vegetation-covered hillslopes, eventually causing bedrock and boulders to sit at topographic highs, as we observed in the field.

3.5.2.2 La Campana (LC)

In LC we observe the largest range of denudation rates between bedrock, boulders, soil, and stream sediment, and also the highest overall denudation rates of the three field sites. We suspect that both of these characteristics are related to slope angles, which are on average nearly twice as steep as in NA and SG (Table 3.1; van Dongen et al., 2019). It should be noted that the stream sediment samples were taken from an adjacent catchment that does not drain the hillslopes sampled in this study, and the generally low and wide-ranging ^{10}Be concentrations in the stream sediment have been related to relatively recent landslides observed in the upper headwaters (van Dongen et al., 2019; Terweh et al., 2021). However, steep slopes are pervasive throughout LC and lead us to suggest that shallow landslides are important erosional processes in this field site.

In LC we frequently observed boulder samples with lower ^{10}Be concentrations than adjacent soil samples (Table 3.1, section 3.5.1), which is inconsistent with our simple model of boulder exhumation (Figure 3.3), and is possibly because the sampled boulders were not exhumed in situ (section 3.5.1.1). Landslides as observed in LC can bring down boulders in the processes of downhill movement, and may cause the excavation of larger blocks from greater depth before their size is reduced in the weathering zone. More vigorous mass wasting is consistent with larger average hillslope grain sizes for LC, as compared to NA and SG (Terweh et al., 2021). In general, the high relief, steep slopes, and high denudation rates suggest that tectonic uplift rates in LC could be higher than assumed for the nearby coast (Melnick, 2016). Modelled differential denudation rates between boulders and soil are the highest of all field sites, and therefore the time needed to reach the measured boulder protrusion heights is the lowest (23 and 7 Kyr; Table 3.2), suggesting relatively rapid turnover of boulder exposure and movement downslope. However, we did note some sediment damming by boulders on LC slopes (Figure 3.2B3), and in all cases in LC the modelled soil denudation rates are lower than measured soil denudation rates, suggesting that boulders are locally suppressing soil denudation to some extent on LC slopes.

Finally, although the role that fracturing plays in LC is difficult to assess, note that our bedrock sample has a significantly lower denudation rate than boulders and soils (Figure 3.8), despite being on a steep slope (Table 3.1). Rolling and toppling processes that may be

relevant for LC boulders are not plausible for the bedrock patch, allowing its nuclide concentration to be high. Likewise, the boulder denudation rate from the ridge sample LC1, where the risk of toppling is likely the lowest, is similar to the bedrock denudation rate. Additionally, LC's mediterranean climate features frequent fires, which cause spalling of rock flakes off boulder surfaces. While LC boulders are surrounded by shrubs that occasionally burn, causing spalling of boulder surfaces, the extensive bedrock patch in LC is free of vegetation and therefore at a lower risk for fire-induced erosion.

3.5.2.3 Santa Gracia (SG)

In the semi-arid landscape of SG, as in humid-temperate NA, boulders are eroding more slowly than the surrounding soil, but the differences in boulder and soil denudation rates are subtle. This leads to a slow exposure of hillslope boulders, with exposure of current boulder protrusion (based on differential modelled denudation rates) taking up to 870 Kyr (Table 3.2). In addition, denudation rate differences between ridge and slope samples – possibly related to slope angle – are larger than the differences between boulders and soil. Furthermore, unlike in NA, our boulder and soil denudation rates are within the same range as the soil pit and catchment average denudation rates (Figure 3.8), suggesting that erosional efficiencies are similar across different sediment sizes. Van Dongen et al. (2019) also measured relatively constant catchment average ^{10}Be concentrations over seven grain size classes in SG (Figure 3.8), which suggests that all grain sizes have been transported from the upper mixed layer of hillslope soil and that deep-seated erosion processes are unlikely, in accordance with absent landsliding (Terweh et al., 2021). Thus, our results agree with previous findings that erosion in SG is likely limited to grain-by grain exfoliation of boulders and the slow diffusive creep of the relatively thin soil cover on hillslopes (Schaller et al., 2018). When bedrock is exhumed, its long residence time on hillslopes allows it to weather slowly in place and reduce in size, with minimal transportation of weathered material by runoff and a low degree of chemical weathering and soil production (Schaller and Ehlers, 2022).

Such a narrow range of relatively low denudation rates indicates that very long time periods are necessary to produce relief between hilltops and valleys. Note, however, despite low uplift rates in SG, the total mean basin slope in SG is 17° compared to 9° in NA (van

Dongen et al., 2019). This could be due to low MAP resulting in a low erosional efficiency in SG, which, in order to achieve denudation rates that match uplift rates, requires the slopes to be steeper (Carretier et al., 2018). Although the differences in denudation rates between grain sizes is subtle in SG, soils have higher denudation rates than the boulders they directly surround. Additionally, the measured denudation rates of soil surrounding boulders on SG slopes are lower than modeled soil denudation rates (Table 3.2), indicating that boulders may be prolonging the residence time of the surrounding soil by a small amount, either by blocking its movement downslope or by contributing grains through exfoliation.

3.5.3 Fracture control on larger-scale landscape evolution

We have shown that, in our field sites, bedrock denudes the slowest, followed by boulders, and finally soil. In each climate zone, and especially where chemical weathering plays a large role (NA), sediment size is likely controlled by the spacing of bedrock fractures. Once on the surface, on low or moderate slopes, large boulders initially delineated by fracture spacing are more difficult to transport than smaller sediment, and therefore locally retard denudation rates. On the landscape scale, such differential erosion should lead to landscape morphologies controlled by fracture spacing patterns. In NA, we were able to measure fracture density in several bedrock outcrops and found that average higher fracture density is correlated with higher denudation rates (Figure 3.5A). It is plausible that the measured fracture spacing in bedrock outcrops represents the parts of the landscape where bedrock fracture density is the lowest, and it is highest under the soil mantled parts of the landscapes, where fractures are not exposed. Fracture spacing in NA is generally larger than boulder width (Figure 3.5C), although there is overlap. If we assume that boulder width is initially delineated by fracture spacing at depth, our results indicate that boulders have reduced in size in the weathering zone prior to and during exhumation. If we further assume that hillslope sediment lies on a spectrum with unweathered blocks delineated by fractures on one end, and sediment that has been significantly reduced in size in the weathering zone on the other end (e.g. Verdian et al., 2021), boulders in NA seem to fall somewhere in the middle.

Bedrock fracture patterns also likely affect stream incision in a similar way, by dissecting bedrock and reducing sediment size, making it easier to be transported by flowing

water. This phenomenon may be visible in our field sites on a larger scale, through the similarity of fault and stream orientations. In NA, our fracture orientation measurements (Figure 3.5B) are similar to fault and stream orientations (Figure 3.7). In general, as tectonically-induced faults and fractures are products of the same regional stresses, we assume that regional faults have orientations consistent with fractures in our field sites (c.f., Krone et al., 2021). Regional faults and smaller fractures have been shown to be closely related: Rodriguez Padilla et al. (2022) mapped fractures resulting from the 2019 Ridgecrest earthquakes in bedrock and sediment-covered areas, and found that fracture density decreases from main faults with a power law distribution. They also found that the orientations of faults and fractures were closely matching. Fracture orientation has also been shown to influence stream orientation. Roy et al. (2015) modeled stream incision in a landscape dissected by dipping weak zones, meant to resemble fracture or fault zones, and found that in cases with a large contrast in bedrock weakness (>30x), channels migrated laterally to follow the shifting exhumation of the weak zone. In our field sites, we observe that stream channels ($A_{min} \geq 10^5$ m^2) generally follow fault orientations (Figure 3.7). This is especially clear in SG, where the north-south striking Atacama Fault System is reflected in the orientation of faults, streams, and also fractures measured in a nearby drill core (Krone et al., 2021; Figure 3.7). In LC and NA, despite more variety in fault and stream orientations, streams closest to the field sites tend to align with fault orientations (Figure 3.7). Especially in NA, the larger streams are often nearly perpendicular to each other, similar to rectangular drainage networks, which are often indicative of structural control on drainage patterns (e.g., Zernitz, 1932). These results suggest that within the same rock type, local fracture patterns induced by regional faults can induce differential denudation in landscapes.

In summary, we argue that in NA, and possibly also in SG and LC, bedrock fracturing influences landscape morphology by setting grain size and thus dictating patterns of denudation rates on hillslopes and in streams: in situ hillslope boulders likely originated as blocks set by fracture spacing, and after being exhumed, locally suppress denudation as described above. This interpretation is supported by work in Puerto Rico; Buss et al. (2013) studied corestones from two boreholes cutting through regolith in the Luquillo Experimental Forest, and found that corestones decreased in size with increased chemical weathering and exhumation through the regolith profile. They deduced that the corestones likely started as

bedrock blocks delineated by fractures. Further, they found that the borehole drilled near a stream channel contained more highly-fractured bedrock compared to the borehole drilled at a ridge, and inferred that corestone size was larger under the ridge due to lower bedrock fracture density. In accordance with Fletcher and Brantley (2010), they concluded that, if erosion and weathering increase with bedrock fracture density, then the ridges and valleys in their study area could be controlled by fracture density patterns.

We therefore offer the following conceptual model: in a landscape with fractured bedrock (Figure 3.9A), areas with higher fracture density should be sites of smaller hillslope sediment sizes (e.g. Sklar et al., 2017; Neely and DiBiase, 2020), where rainfall can easily infiltrate, conversion of bedrock to regolith is easiest (St. Claire et al., 2015; Lebedeva and Brantley, 2017), and denudation rates are highest. Over time, precipitation will divergently run off topographic highs and starve bedrock and larger boulders on high points while infiltrating into topographic lows, where streams eventually incise (Bierman, 1994; Hayes et al., 2020; Figure 3.9B). Bedrock and boulders on topographic highs denude more slowly than finer sediment and soil, accentuating any elevation differences. Regolith also promotes vegetation growth, which slows runoff, raises rates of infiltration, and enhances chemical weathering (Amundson et al., 2007; Figure 3.9B). In steeper landscapes, such as LC, boulders will be more mobile and may roll down the hillslopes, eventually ending up in stream channels where they may shield the channel bed from denudation (DiBiase et al., 2017; Shobe et al., 2016; Figure 3.9C). In addition, in such higher relief landscapes, fractures due to topographic stresses from exhumation may form at topographic highs as the topography emerges (St. Claire et al., 2015), countering this positive feedback loop (Figure 3.9C). Over longer timescales, bedrock with different patterns of fracture density may be exhumed, which can invert landscapes to reflect the new fracture patterns exposed at the surface (Roy et al., 2016). In this way, fracturing, climate, and residence time can operate in conjunction to set the sediment size and morphology of hillslopes and streams within landscapes.

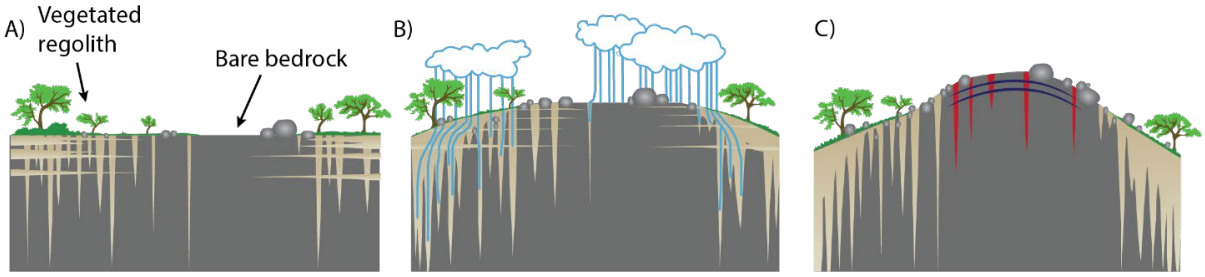

Figure 3.9. Schematic illustration showing influence of bedrock fractures on landscape evolution. (A) Bedrock with different fracture densities is to different degrees infiltrated by rain and ground water, which leads to differences in chemical weathering, soil formation and vegetation growth, resulting in different hillslope sediment sizes. (B) Differential denudation between highly fractured and less fractured areas induce relief growth under slow but persistent uplift, which further promotes spatial gradients in chemical weathering, hillslope sediment size, and denudation. (C) Growing relief increases topographic stresses and formation of new fractures (red) at topographically high positions (e.g. St. Clair et al., 2015) as well as non-topographic surface-parallel fractures (dark blue) (e.g. Martel, 2011), and steeper slopes allow for transportation of boulders, shown rolling down the slopes on either side.

3.6 Conclusions

In this study, we explored the ability of bedrock patches and large boulders to retard denudation and influence landscape morphology, in three relatively slowly-eroding landscapes along a climate gradient in the Chilean Coastal Cordillera. Based on *in situ* cosmogenic ^{10}Be-derived denudation rates of bedrock, boulders and soil, we find that in almost all cases across the three sites studied, soil denudation rates are by ~10-50% higher than the denudation rates of the boulders that they surround, which are more similar to bedrock denudation rates. This pattern is more complicated in La Campana, where some boulders have lower ^{10}Be concentrations than the surrounding soil, perhaps because they were overturned or covered with soil at some point due to steeper slopes. These results suggest that exposed bedrock patches and large hillslope boulders affect landscape morphology by slowing denudation rates, eventually forming the nucleus for topographic highs. On the other hand, our work also suggests that where slopes are close to the angle of repose and where landsliding is observed (as in La Campana), while bedrock patches denude

slowly and likely retard hillslope denudation, hillslope boulders may have a smaller or even negligible effect on suppressing denudation.

In addition, we found that bedrock fracturing and faulting accelerates hillslope denudation and stream incision in our field sites: hillslope denudation rates increase with fracture density in NA, and streams tend to follow the orientation of larger faults in all three sites. We infer that bedrock fracture patterns in our field sites set grain sizes on hillslopes, and bedrock patches and boulders represent locations where fracture density is lower, and thus weathering, erosion, and soil formation are suppressed. On a larger scale, our results imply that tectonic preconditioning in the form of bedrock faulting and fracturing influences landscape evolution by impacting the pathway of streams, as well as the migration of ridges, as landscapes denude through layers of bedrock preconditioned by tectonic fracturing over time, and encounter varying levels of resistance depending on the fracture density.

3.7 Acknowledgements

This work was supported by the German Science Foundation (DFG) priority research program SPP-1803 “EarthShape: Earth Surface Shaping by Biota” (grant SCHE 1676/4-2 to D. S.). We are very grateful to the Earthshape management, Friedhelm von Blanckenburg and Todd Ehlers, and the Earthshape coordinators Kirstin Übernickel and Leandro Paulino. We also thank the Chilean National Park Service (CONAF) for providing access to the sample locations and on-site support of our research. We also thank Iris Eder and David Scheer for their help in the field and in the laboratory, Cathrin Schulz for her help in the laboratory, and Steven A. Binnie and Stefan Heinze from Cologne University for conducting AMS measurements.

3.8 Data availability

Cosmogenic nuclide data and Matlab-scripts of the model presented in this paper will be made available as a GFZ Data Publication in accordance with FAIR principles. LiDAR data from the studied catchments is available in Krüger et al. (2022).

3.9 Supplementary tables

Table S3.1. Cosmogenic ^{10}Be data for denudation rates of hillslope bedrock, boulders, and soil.

Sample name	IGSN[a]	Latitude (°N)	Longitude (°E)	Sample type	Qtz mass in sample (g)	^{9}Be carrier mass added to sample (mg)	AMS ^{10}Be/^{9}Be x10^{-14} ± 1σ[b]	Blank[c]	^{10}Be conc. ±1σ (×10^{5}) (atoms g^{-1})	^{10}Be production rate (spallation, atoms g^{-1} yr^{-1})[d]	^{10}Be production rate (fast muons, atoms g^{-1} yr^{-1})[e]	^{10}Be production rate (negative muons, atoms g^{-1} yr^{-1})[e]	Topographic shielding[f]
Nahuelbuta													
NB-BR1	GFRD1002U	-37.826	-73.035	Bedrock	25.80508333	0.20905	199.1 ± 6.53	B3	8.25±0.28	11.41	0.0502	0.0695	0.9927
NB-BR2	GFRD1002V	-37.821	-73.034	Bedrock	23.47923333	0.2094	152 ± 5.1	B3	6.92±0.24	11.44	0.0503	0.0696	0.9998
NB-BR3	GFRD1002W	-37.819	-73.032	Bedrock	25.18825	0.2039	132.1 ± 4.55	B4	5.18±0.20	11.15	0.0499	0.0686	0.9995
NB-BR4	GFRD1002 9	-37.825	-73.034	Bedrock	23.94115	0.20945	86.72 ± 2.98	B3	3.85±0.14	11.46	0.0503	0.0696	0.9942
NA3	GFEL10002	-37.826	-73.034	Bedrock	23.69081667	0.20965	145 ± 4.82	B3	6.55±0.23	11.25	0.05	0.0689	0.9995
NA4	GFEL10003	-37.817	-73.031	Boulders	23.80646667	0.2095	201.6 ± 6.75	B3	9.08±0.32	10.43	0.049	0.0662	0.9989
NA7	GFEL10006	-37.789	-72.998	Boulders	23.5065	0.2041	237.9 ± 7.59	B4	10.28±0.36	11.3	0.0501	0.0692	0.9984
NA8	GFEL10007	-37.789	-72.998	Boulders	23.199	0.2067	195.6 ± 6.36	B5	8.94±0.31	11.3	0.0501	0.0692	0.9984
NA9	GFEL10008	-37.789	-72.998	Boulders	23.6304	0.2039	178.3 ± 5.69	B4	7.57±0.27	11.3	0.0501	0.0692	0.9984
NA11	GFEL1000A	-37.79	-72.999	Boulders	24.0158	0.2025	177.5 ± 5.79	B5	7.67±0.26	11.18	0.05	0.0687	0.9965
NA15	GFEL1000E	-37.807	-73.013	Boulders	11.72845	0.204	31.9 ± 1.43	B6	2.84±0.069	10.24	0.0487	0.0655	0.9914
NA5	GFEL10004	-37.817	-73.031	Soil	23.64241667	0.2095	51.99 ± 2.02	B3	2.32±0.10	10.43	0.049	0.0662	0.9989
NA10	GFEL10009	-37.789	-72.998	Soil	28.3847	0.2053	137.3 ± 4.52	B1	5.04±0.18	11.3	0.0501	0.0692	0.9984
NA12	GFEL1000B	-37.79	-72.999	Soil	24.02616667	0.222	90.83 ± 3.24	B3	4.27±0.16	11.18	0.05	0.0687	0.9965
La Campana													
LC-BR2	GFRD1002X	-32.938	-71.081	Bedrock	16.91205	0.204	37.34 ± 1.59	B4	1.83±0.11	5.75	0.0426	0.0502	0.9259
LC2	GFEL1002J	-32.939	-71.081	Boulders	20.6192	0.2039	18.22 ± 0.9	B6	0.92±0.089	6.25	0.0436	0.0526	0.993
LC4	GFEL1003V	-32.938	-71.079	Boulders	20.70925	0.2041	18.38 ± 1.02	B6	0.92±0.083	5.77	0.0427	0.0503	0.9743
LC11	GFEL1000Q	-32.941	-71.074	Boulders	22.53805	0.2042	33.82 ± 1.33	B4	1.21±0.070	6.42	0.044	0.0534	0.9949
LC13	GFEL1000S	-32.94	-71.073	Boulders	23.47035	0.2039	19.6 ± 1.11	B4	0.73±0.080	6.13	0.0434	0.052	0.9381
LC18	GFEL1000Z	-32.937	-71.074	Boulders	21.53235	0.2041	39.7 ± 1.46	B4	1.55±0.079	5.43	0.042	0.0486	0.9764
LC1	GFEL1002H	-32.939	-71.081	Soil	20.3916	0.2041	30.01 ± 1.3	B6	1.54±0.092	6.25	0.0436	0.0526	0.993
LC3	GFEL1003W	-32.938	-71.079	Soil	19.8288	0.2044	19.62 ± 0.854	B6	1.03±0.086	5.77	0.0427	0.0503	0.993
LC12	GFEL1000R	-32.941	-71.074	Soil	24.8286	0.2049	22.53 ± 0.986	B1	0.88±0.044	6.42	0.044	0.0534	0.9949
LC14	GFEL1000T	-32.94	-71.073	Soil	26.5023	0.2051	17.41 ± 0.899	B2	0.63±0.037	6.13	0.0434	0.052	0.9381
LC19	GFEL1000X	-32.937	-71.074	Soil	30.6745	0.2049	55.05 ± 1.97	B2	1.84±0.071	5.43	0.042	0.0486	0.9764
Santa Gracia													
SG8	GFEL10017	-29.756	-71.166	Boulders	23.28445	0.2039	133.1 ± 4.53	B5	5.94±0.21	5.72	0.0433	0.0518	0.9984
SG9	GFEL10018	-29.756	-71.166	Boulders	24.07705	0.2033	109.6 ± 3.78	B5	4.7±0.17	5.72	0.0433	0.0518	0.9984
SG11	GFEL1001A	-29.758	-71.166	Boulders	24.3841	0.2025	83.94 ± 2.92	B5	3.56±0.13	5.56	0.0429	0.051	0.9828
SG22	GFEL1001M	-29.758	-71.166	Boulders	18.54665	0.2032	75.71 ± 2.72	B5	3.85±0.15	5.56	0.0429	0.051	0.9836
SG10	GFEL10019	-29.756	-71.166	Soil	11.2648	0.2033	36.96 ± 1.81	B4	2.58±0.11	5.72	0.0433	0.0518	0.9984
SG12	GFEL1001B	-29.758	-71.166	Soil	23.47785	0.2032	54.24 ± 1.91	B5	2.39±0.089	5.56	0.0429	0.051	0.9828
SG23	GFEL1001N	-29.758	-71.166	Soil	24.30125	0.2021	49.65 ± 1.87	B5	2.1±0.083	5.56	0.0429	0.051	0.9836

[a]Open access metadata: http://igsn.org/[insert IGSN number here]
[b]Measured by Accelerator Mass Spectrometry (AMS) at the University of Cologne.
[c]Process blank used to correct respective sample batches, where corresponding AMS ^{10}Be/^{9}Be ratios are B1 = 1.85±0.27×10^{-14}, B2 = 1.57±0.2×10^{-14}, B3 = 1.179±0.18×10^{-14}, B4 = 7.851±0.61×10^{-14}, B5 = 6.546±1.56×10^{-15}, B6 = 1.419±0.58×10^{-15}
[e]Surface production rates by muons were obtained using the MATLAB-function 'P_mu_total.m' of Balco et al. (2008). Without topographic shielding correction
[f]Calculated with the function 'toposhielding.m' of the TopoToolbox v2 (Schwanghart and Scherler, 2014) and 12.5-meter resolution DEMs from the Alaska Satellite Facility.

3.10 Supplementary figures

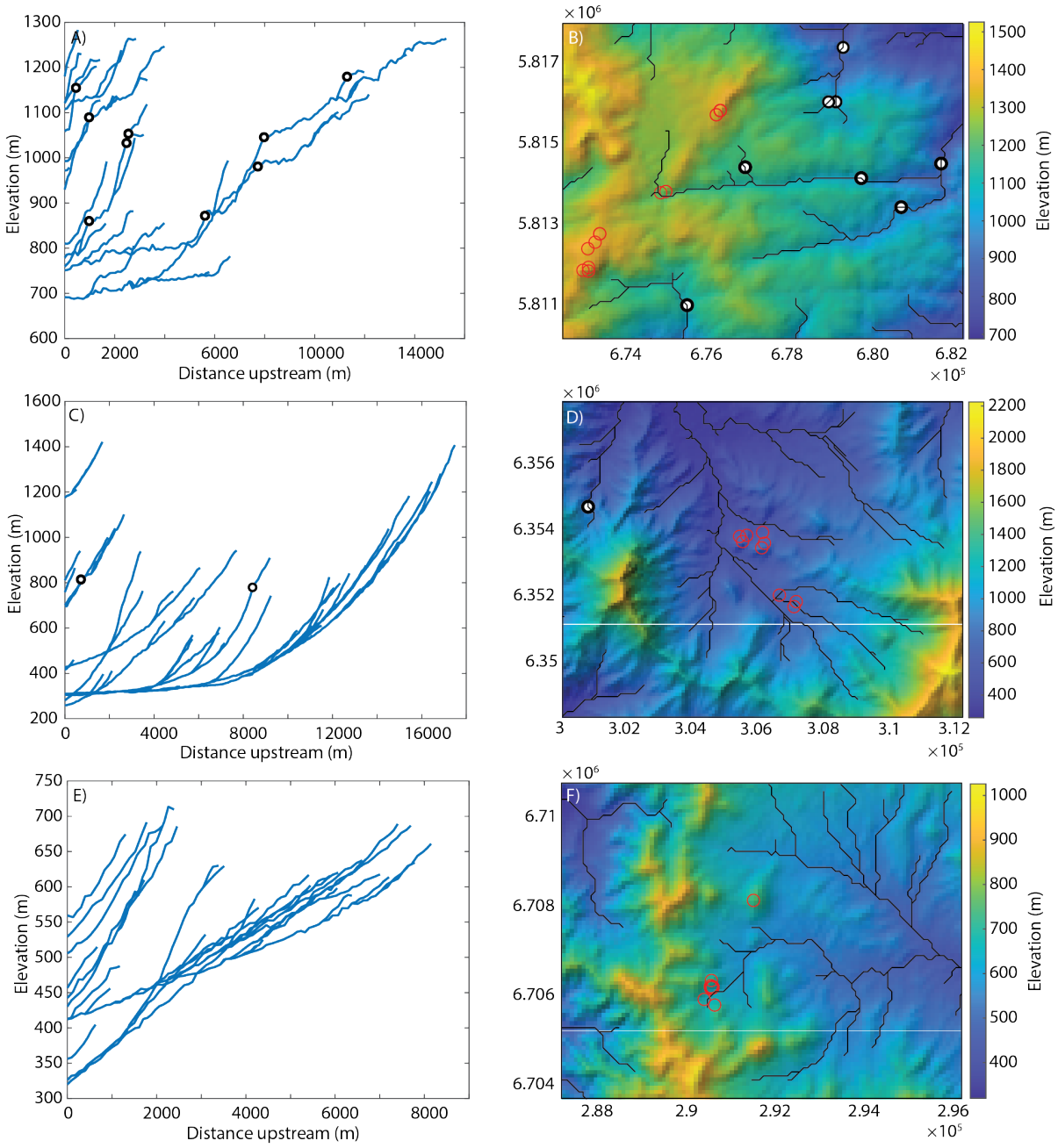

Figure S3.1. Knickpoints from all three catchments. Knickpoints (white circles) were identified with TopoToolbox's knickpoint finder function, using an elevation threshold of 30 m; streams are plotted with a minimum upstream area of 10^6 m2. A) Stream profiles and knickpoints from NA; B) map of NA showing knickpoints in white and all samples plotted in red; C) stream profiles and knickpoints from LC; D) map of LC showing samples in red and knickpoints in white; E) stream profiles from SG with no knickpoints; F) map of SG showing samples in red and no knickpoints.

Chapter 4

Estimating stream boulder residence times through cosmogenic nuclide analysis along a climate gradient in Central Chile

Emma Lodes[1] and Dirk Scherler[1,2]

[1]GFZ German Research Centre for Geosciences, Earth Surface Geochemistry, Telegrafenberg, 14473 Potsdam, Germany

[2]Freie Universität Berlin, Institute of Geographical Sciences, 12249 Berlin, Germany

Abstract

While it is known that large boulders within stream channels can influence landscape morphology by shielding channel beds from erosion, the residence times of stream channel boulders has only been estimated in modelling studies and has not been directly measured with cosmogenic radionuclide analysis. In this study, we estimated the residence times of stream boulders and sediment in three different climate zones (humid-temperate, mediterranean and semi-arid) along the Chilean Costal Cordillera, using ^{10}Be radionuclide dating. We also modelled ^{10}Be concentrations of hillslope boulders on adjacent hillslopes incorporating self-shielding to directly compare hillslope boulder ^{10}Be concentrations to stream boulder ^{10}Be concentrations, and measured grain size distributions on hillslopes and in streams in each field site. We found that the residence time for stream boulders is shortest in the humid-temperate site, likely due to higher discharge, and longest in small catchments within the semi-arid site, likely due to their lower discharge and smaller upstream areas. Modelling results show that hillslope boulders have longer residence times than stream boulders in the humid-temperate and semi-arid site, while in the mediterranean site hillslope boulders have shorter residence times, and are generally smaller, than stream boulders. Our results imply that hillslope boulders are delivered rapidly from hillslopes to stream channels in the mediterranean site due to steep hillslope angles, and that stream boulders have the smallest impact on landscape evolution in the humid-temperate climate zone, and the largest impact in small catchments within the semi-arid site.

4.1 Introduction

Boulders are ubiquitous in bedrock river channels. Large boulders remain stationary in channels for long periods of time, moving only when the discharge and slope are large enough to transport them (e.g., Cook et al., 2018), thereby retarding stream incision by blocking the erodible surface of the channel bed and enhancing form drag (e.g., Shobe et al., 2016; 2018). By raising the threshold for fluvial incision, boulders can cause large-scale increases in channel slope, retard the migration of knickpoints, and alter the overall

landscape morphology (Sklar and Dietrich, 2004; 2006; Turowski, 2009; Lague, 2010; Attal et al., 2015, Shobe et al., 2016; DiBiase et al., 2018).

The magnitude of the impact that boulders can have on stream morphology depends on their residence time in the channel. Once in the stream channel, flowing water can impact a boulder's residence time in two major ways. First, it can overturn or transport the boulder downstream (e.g. Turowski et al., 2009; Mackey and Lamb, 2013). Transportation of the largest boulders generally only occurs during large flood events that are difficult to observe (e.g., Cook et al., 2018; Huber et al., 2020); however, boulders can also experience gradual movement such as rolling or toppling (e.g. Turowski et al., 2009; Mackey and Lamb, 2013). Second, flowing water can cause increased chemical weathering and physical erosion of the boulder surface (Seidl et al., 1994; Wilson et al., 2013; Murphy et al., 2016). Chemical weathering reduces the physical strength of bedrock (Murphy et al., 2016), and can make boulders more vulnerable to erosion. In addition, exposed boulder surfaces can be abraded by moving bedload, whereby the resulting increase in erosion rates depends on the size and velocity of impacting clasts (Whipple et al., 2000; Sklar and Dietrich, 2004; 2008), and the downstream sides of boulders can be equally affected by moving bedload abrasion due to fluid recirculation (Wilson et al., 2013; Beer et al., 2017). If these processes quickly reduce the size of boulders, allowing lower discharge to transport them, boulders will have a shorter residence time in the channel and a smaller impact on landscape morphology (e.g., Carretier and Regard, 2011).

Despite the importance of understanding boulder residence times in stream channels, they are difficult to quantify. Previous work includes modelling surficial cosmogenic nuclide concentrations of rotating boulders to predict residence times (e.g., Carretier and Regard, 2011; Mackey and Lamb, 2013), and tracking boulder transport through the reconstruction of satellite images and photographs (e.g., Cook et al., 2018; Neely et al., 2023). As far as we know, no effort has been made to use field data and ^{10}Be concentrations to predict stream boulder residence times. Cosmogenic nuclides have been widely used to measure residence times and denudation rates of hillslope boulders (e.g., Small et al., 1997; Granger et al., 2001; Bierman and Caffee, 2002; Balco et al., 2011; Lodes et al., 2023). However, measuring the residence times of large boulders in streams presents complications: 1) measured

cosmogenic nuclide concentrations can be partially derived from the boulder's hillslope residence, and 2) concentrations can be artificially lowered by overturning and self-shielding of the boulder both on the hillslope and within the stream (Carretier and Regard, 2011; Mackey and Lamb, 2013). This can occur through rolling or toppling (e.g. Turowski et al., 2009; Mackey and Lamb, 2013), or due to the scouring of the surrounding or underlying sediment, whereby the boulder is repeatedly reoriented so that different faces are exposed to full cosmogenic nuclide production and the buried side of the boulder is shielded from nuclide production (Mackey and Lamb, 2013; Wilson et al., 2013).

In this work, we attempt to resolve the relative residence times of large and small boulders and fine sediment in streams using cosmogenic radionuclide analysis as a tool, in three different climate zones in the Chilean Coastal Cordillera. We address the complications listed above in two ways. First, we measured two sets of cosmogenic radionuclides with different integration time periods, ^{10}Be and ^{14}C, which should provide longer-term and shorter-term denudation rates (respectively) that may allow us to disentangle the longer-term denudation rates of the boulders on the hillslope from the more recent denudation rates of boulders in the stream (Hippe, 2017). However, we have experienced delays in obtaining the ^{14}C results, including two years of lab closure during the COVID pandemic, and therefore we provide a preliminary analysis of only ^{10}Be data here.

In addition, we provide preliminary results from a model similar to models by Balco et al. (2011) and Mackey and Lamb (2013) that predicts the impacts of boulder overturning and self-shielding on ^{10}Be concentrations, allowing us to directly compare between ^{10}Be concentrations of stream boulders from this work and hillslope boulders published in Lodes et al. (2023). Finally, we present a set of grain size data from channels and hillslopes. These datasets represent the first attempt to directly measure stream boulder residence times and mobilities in different climates using a combination of cosmogenic radionuclide analysis and modelling, and represent a step towards a full understanding of the impact of stream boulders on landscape morphology.

4.2 Field sites

The three field sites investigated in this work lie along the Chilean Coastal Cordillera, which runs north-south along the coast of Chile. The cordillera hosts a dramatic climate gradient, with arid conditions in the north and humid conditions in the south. Our three sites are, from south to north, Nahuelbuta National Park (Nahuelbuta), with a humid-temperate climate, La Campana National Park (La Campana), with a mediterranean climate, and Private Reserve Santa Gracia (Santa Gracia), with a semi-arid climate. Van Dongen (2021) estimated mean annual runoff values for the three field areas based on an empirical relationship with mean annual precipitation and reported values of 1020.6 mm yr^{-1} for Nahuelbuta, 182.2 mm yr^{-1} for La Campana, and 30.5 mm yr^{-1} for Santa Gracia. All three sites are underlain by granitoid bedrock (Oeser et al., 2018), are in national parks or reserves, are minimally affected by anthropogenic influence, and show no signs of recent glaciation. Nahuelbuta and Santa Gracia are characterized by gently sloping hillslopes, whereas in La Campana, slopes are steeper and debris flows have been noted (Terweh et al., 2021).

In Nahuelbuta, knickpoints indicate that denudation rates may have changed with time, and using thermochronology, Glodny et al. (2008) reported an increase in uplift from 0.03–0.04 to >0.2 mm $year^{-1}$ at 4 ± 1.2 Ma. However, all our measurements and field samples were taken from the plateau above the knickpoints. In the regions surrounding Santa Gracia and La Campana, Melnick (2016) reported relatively low uplift rates of <0.1 mm $year^{-1}$ based on modeled coastal elevation profiles. Santa Gracia's landscape hosts three different granitoid bedrock types (a monzogranite and two diorites) that have different bedrock properties that influence drainage density, grain size and vegetation cover (Lodes et al., submitted). Hillslope denudation rates are similar between the inner diorite and the monzogranite, but slightly higher for the outer diorite (Lodes et al., 2023; Lodes et al., submitted). Santa Gracia Hill and Santa Gracia Stream are within the outer diorite bedrock, Zebra Hill and Diorite Stream are within the inner diorite bedrock, and Cactus Hill, Cactus Stream, Flag Hill, and Flag Stream are within the monzogranite bedrock (Figure 4.1).

In all three sites, hillslopes contain scattered boulders that are likely the source for stream boulders measured in this work (e.g., Attal et al., 2015; Sklar et al., 2017). ^{10}Be-derived denudation rates have been measured locally for hillslope boulders and soils (Lodes et al., 2023), and in soil pits (Schaller et al., 2018), as well as for entire catchments based on stream sediment (van Dongen et al., 2019; Lodes et al., submitted). Differences between hillslope and catchment-averaged denudation rates vary between sites: in Nahuelbuta and La Campana, catchment average denudation rates from stream sediment are higher than hillslope denudation rates, whereas in Santa Gracia, catchment average and hillslope denudation rates are generally similar (van Dongen et al., 2019; Lodes et al., 2023; Lodes et al., submitted). In Nahuelbuta, denudation rates range between ~10 and 30 m Myr^{-1}, in La Campana between ~20 and 140, and in Santa Gracia between ~5 and 20 (Lodes et al., 2023). Lodes et al. (2023) modelled differential denudation rates of boulders and the surrounding soil in all three field sites, considering the protrusion of the hillslope boulders, and found that hillslope boulders are stable and have been steadily exhuming in Nahuelbuta and (more slowly) in Santa Gracia. However, results from La Campana indicate that boulders on steep hillslopes are more mobile. Eventually, these boulders are likely to roll or slide down into the streams, and our motivation for this work is to predict the subsequent residence time of these boulders once they sit in the stream channels.

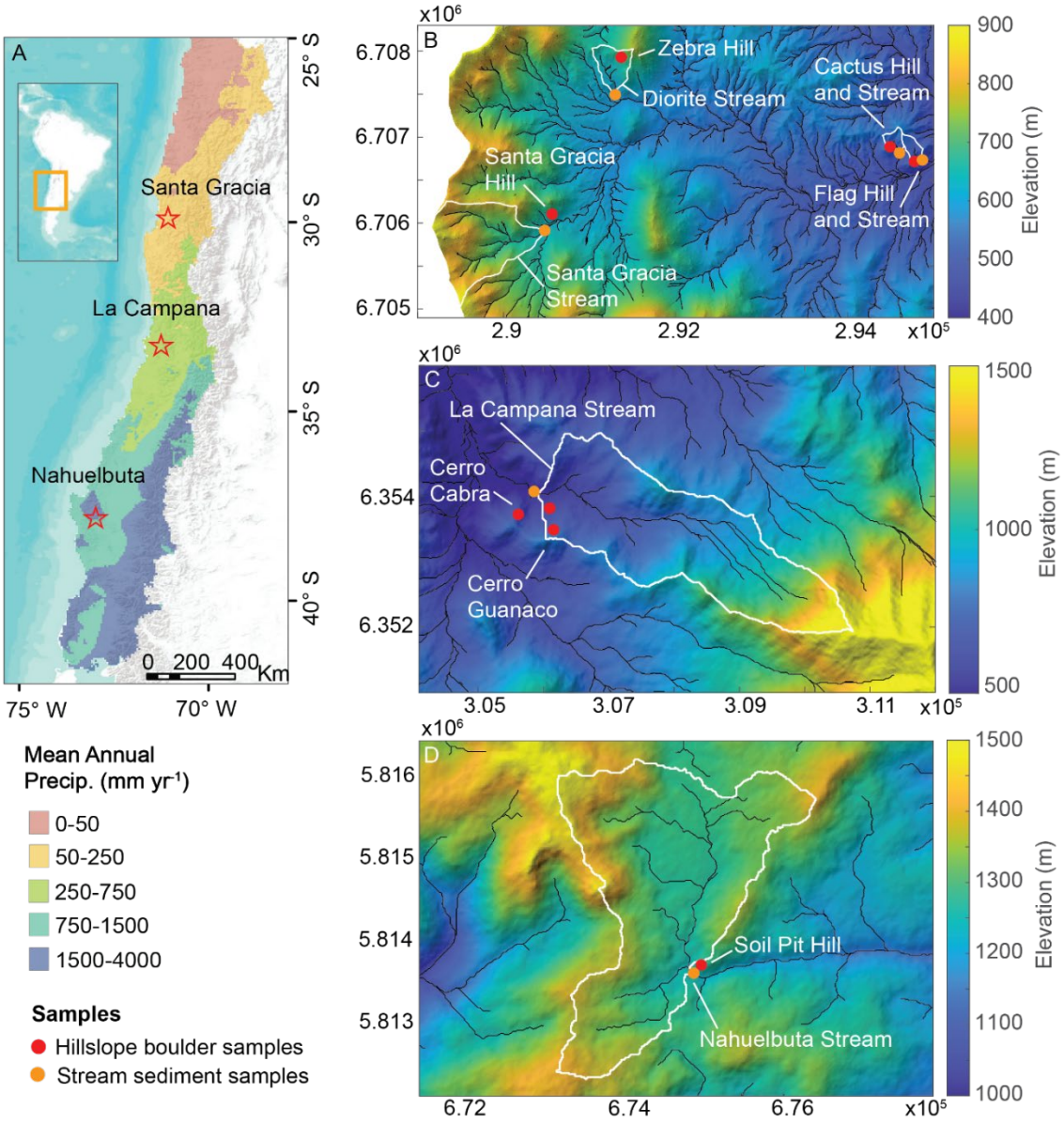

Figure 4.1. Field site locations and features. A) Map of mean annual precipitation in central Chile, with field sites marked by red stars. Precipitation data from the CR2MET dataset, by the Center for Climate and Resilience Research (CR2) (Boisier et al., 2018), provides an average for the time period 1979-2019. World Terrain Base map sources are Esri, USGS, and NOAA. B-D: Elevation maps of B) Santa Gracia, with a 1 m LiDAR DEM (Kügler et al., 2022), C) La Campana, with a 12.5-m DEM from the Alaska Satellite Facility Distributed Active Archive Center (2019), and D) Nahuelbuta, with a 12.5-m DEM from the Alaska Satellite Facility Distributed Active Archive Center (2011a). Sample locations and sample names are shown, with symbol shape and color indicating the sample type (see legend in lower left panel). White outlines delineate the catchments from which the stream sediment samples were taken. Black lines indicate streams. Hillslope boulder sample data was published in Lodes et al. (2023).

4.3 Methods

4.3.1 Field measurements

To estimate the residence times of stream boulders and sediment in each field area, we collected samples for in situ ^{10}Be cosmogenic radionuclide analysis from stream boulders and stream sediment from each catchment (Figure 4.1). In this work, we define a boulder as a grain with an intermediate axis length longer than 20 cm, which corresponds with the average intermediate axis length of our smallest stream boulder sample and is close in value to the classic sedimentological definition of a boulder (diameter greater than 25.6 cm; Udden, 1914; Wentworth, 1922). We define clasts as grains with an intermediate axis length between 2 and 6 cm. For each stream boulder sample, we amalgamated rock chips collected from the top surface of at least 10 different boulders (~25 cm^2 and <2 cm thick) along the stream channel and within ~10 meters from the fine sediment sampling point. As we assume that stream boulders have rotated within the channel, by amalgamating the samples we sampled boulder surfaces that have experienced varying amounts of self-shielding.

New stream boulder samples from Nahuelbuta Stream (Figure 4.1) consist of three samples of boulders with average intermediate axis lengths of 20, 44, and 87 cm, and new stream boulder samples from La Campana Stream consist of two samples of boulders with average intermediate axis lengths of 134 and 30 cm (Table 4.1). In Santa Gracia, we sampled one larger catchment (Santa Gracia Stream, which was also sampled by van Dongen et al., 2019), and three smaller catchments. We collected one stream boulder sample from Santa Gracia Stream with an average intermediate axis length of 38 cm, one stream boulder sample from Flag Stream with an average intermediate axis length of 36 cm; and clast samples from the other small catchments. We collected fine stream sediment samples by scooping stream sediment from inside channels, which were dry at the time of sampling in Santa Gracia and La Campana but contained water in Nahuelbuta (Figure 4.2). To quantify grain size distributions, we conducted Wolman pebble counts (Wolman, 1954) in all three field sites, on hillslopes and in streams where samples were collected. Counts were conducted with 1-meter intervals between measurements. We conducted separate grain

size counts for ridges, hillslopes, and stream channels. Bedrock was noted separately in the pebble count, and all grains <2mm were grouped together.

Figure 4.2. Field photos of hillslopes and streams. A) Casa de Piedras, a hillslope in Nahuelbuta close to Nahuelbuta Stream, B) Nahuelbuta Stream, C) Cerro Cabra Hill, D) La Campana Stream, E) Santa Gracia Hill, F) Santa Gracia Stream, G) Zebra Hill, H) Diorite Stream, I) Cactus Hill, J) Cactus Stream, K) Flag Hill, L) Flag Stream.

4.3.2 ^{10}Be cosmogenic radionuclide analysis

We measured ^{10}Be concentrations for three new stream boulder samples from Nahuelbuta, two new stream boulder and one new sediment samples from La Campana, and two new boulder samples and three clast-sized stream sediment samples from Santa Gracia. To process samples for the extraction of ^{10}Be, we dried, crushed (if necessary), and

sieved samples for quartz mineral separation to 250-500 µm particle size, or to 250-1000 µm if the 250-500 µm sample fraction wasn't sufficient. We isolated ~10-20 g of pure quartz from each sample using standard physical and chemical separation methods, spiked each sample with 150 µg of ^{9}Be carrier, and dissolved the quartz in concentrated hydrofluoric acid in order to extract beryllium, following protocols adapted from von Blanckenburg et al. (2004). ^{10}Be/^{9}Be ratios were measured by accelerator mass spectrometry at the University of Cologne, Germany (Dewald et al., 2013). Sample ratios were normalized to standards KN01-6-2 and KN01-5-3 with ratios of 5.35×10^{-13} and 6.320×10^{-12}, respectively. Final ^{10}Be concentrations were corrected by process blanks with an average ^{10}Be/^{9}Be ratio of $(1.70 \pm 0.16) \times 10^{-14}$.

4.3.3 Model to predict hillslope boulder concentrations with self-shielding

Because we assume that stream boulders rotate within the stream channel, we must assume that amalgamated stream boulder samples consist of faces that have experienced varying degrees of self-shielding, such that one amalgamated stream boulder sample represents the average surface concentration of one rotating stream boulder (Mackey and Lamb, 2013). In contrast, amalgamated hillslope boulder samples from Lodes et al. (2023) were taken from only the top of stable hillslope boulders, resulting in ^{10}Be concentrations that cannot be directly compared to stream boulder sample concentrations. To be able to directly compare hillslope boulder ^{10}Be concentrations to stream boulder ^{10}Be concentrations, we modelled the concentrations of artificial amalgamated samples taken from all sides of a hillslope boulder. In the model, we consider a spherical boulder of a certain initial radius (r_i) in the subsurface, where z_0 indicates the depth of a sample when the boulder reaches the surface (Figure 4.3A). Next, we let the boulder exhume according to a constant rate of soil denudation (ϵ_s) (Figure 4.3B). During the exhumation, we consider that the boulder is denuding at a constant rate (ϵ_b), and decreases in size until it reaches a final radius (r_f) and sampling height (z_1) (Figure 4.3C).

To estimate the average surficial ^{10}Be concentration of the modelled boulders, we computed the ^{10}Be concentration accumulated during two stages: 1) the subsurface stage, before the boulder breaches the soil surface, and 2) the exhumation stage. ^{10}Be concentrations for both stages were calculated using iterations of Eq. 4.1:

$$N = \sum_i \frac{P_i e^{-z\rho/\Lambda_i}}{\lambda + \frac{\epsilon_s \rho}{\Lambda_i}} \left(1 - e^{-t\left(\lambda + \frac{\epsilon_s \rho}{\Lambda_i}\right)}\right) \quad (4.1),$$

where i indicates different terms for the production by spallation, fast muons, and negative muons; $P_i(0)$ are the site-specific ^{10}Be surface production rates for the different production pathways in atoms g^{-1} yr^{-1}; λ is the ^{10}Be decay constant (5×10^{-7}), Λ_i represents the attenuation length scales for spallogenic and muonic production, which are based on values from Granger and Smith (2000) and Granger and Muzikar (2001) in stage 1 and are customized for self-shielding in stage 2, ρ is density (2.7 g cm^{-3}), and t is time (1×10^7 to approximate steady state denudation in stage 1, and time until present day in stage 2). For stage 1, we calculated cosmogenic nuclide depth profiles according to models by Granger and Smith (2000) and Granger and Muzikar (2001) using Eq. 4.1. For stage 2, we considered self-shielding using an approach similar to Balco et al. (2011). We simulated the cosmic-ray flux at the boulder surface, and calculated shielding factors by calculating the total length of each cosmogenic ray and computing an attenuation factor for each ray by dividing the ray lengths by the attenuation length of an individual ray, using the value 208 g cm^{-2} (Gosse and Phillips, 2001). We calculated a mean shielding factor for all rays and found that 2000 iterations were sufficient. For each stage of boulder exhumation, we fit a production rate model with two exponential terms based on best fit values for attenuation lengths. We found that two exponential functions for spallogenic production yielded good fits with calculated shielding factors. Finally, to obtain the total modelled concentration for the boulder, we added the nuclide concentrations calculated in stages 1 and 2, and artificially collected samples from the surfaces of the boulders (100 per boulder).

The expected concentration around the boulder depends on the initial and final boulder radii, the exhumation stage, and the soil and boulder denudation rates (Figure 4.3), which are estimated based on boulder size and ^{10}Be concentration data from Lodes et al. (2023) and Lodes et al. (submitted). We modelled hillslope boulder concentrations for boulder with initial radii of 1, 2, and 3 meters for Nahuelbuta and La Campana, and for 1 and 2 meters for Santa Gracia Stream and Flag Stream, for exhumation stages of 50%, 75%, and 100% for each boulder. We did not model hillslope boulder concentrations for Diorite Stream or Cactus Stream because we did not collect stream boulder samples there, and we

did not model ^{10}Be concentrations for large boulders (3 m initial radius) in Santa Gracia Stream and Flag Stream because of their generally smaller stream grain size distributions.

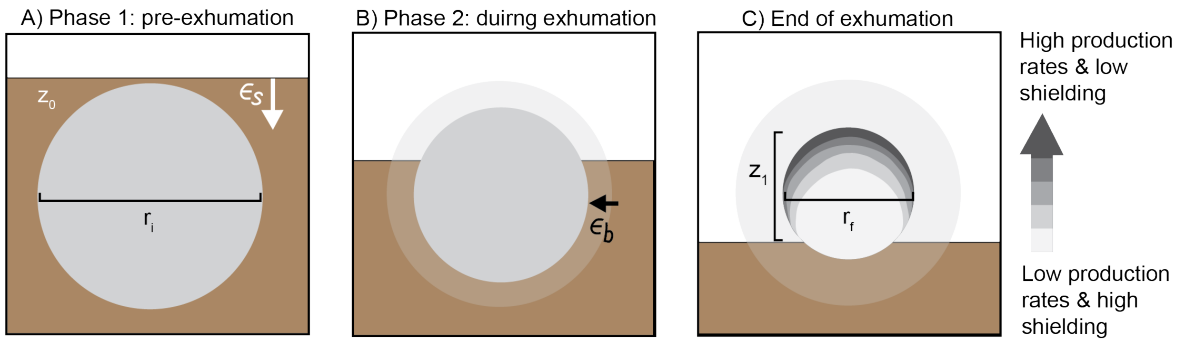

Figure 4.3. Schematic illustration of a boulder exposed to cosmic rays. The distribution of nuclide concentrations is shown by shades of gray (see scale on the right-hand side). A) During phase 1, the boulder is buried, and accumulates nuclides at a rate governed by the soil denudation rate, ϵ_s. B) During phase 2, the boulder itself is denuding at a rate of ϵ_b, and the surrounding soil continues to denude at a rate of ϵ_s. The transluscent sphere represents the original size of the boulder, and the opaque sphere represents the size of the boulder during the current stage, which has decreased due to denudation. C) The end of exhumation (100% exhumation). z_0 is the depth of the sample when the boulder reaches the surface and z_1 is the sample height at the boulder surface after exhumation; r_1 is the initial radius of the boulder and r_f is the final radius of the boulder.

4.3.4 Basin attributes

With the use of a 1m LiDAR DEM (Nahuelbuta and Santa Gracia), a 12.5m DEM from ALOS PALSAR (La Campana) and TopoToolbox V2 (Schwanghart and Scherler, 2014), we delineated the upstream river catchment at each sample location. Next, we calculated hillslope angles as the steepest downward gradient of an 8-grid cell-connected neighbourhood and the normalized channel steepness index with a reference concavity (ϑ_{ref}) of 0.3 based on average values from slope-area relationships of the catchments. We determined mean basin slope and mean basin channel steepness values as the arithmetic mean of all values within the catchment.

4.4 Results

4.4.1 Measured and modelled ^{10}Be concentrations

We report new ^{10}Be concentrations normalized to sea level high latitude production rates and compare our values with similarly normalized data published by van Dongen et al. (2019), Lodes et al. (2023), and Lodes et al. (submitted). Overall, stream boulder and sediment ^{10}Be concentrations are lowest in Nahuelbuta and highest in Santa Gracia, apart from Santa Gracia Stream's large boulders, which have a lower concentration that is similar to stream boulders in Nahuelbuta (Table 4.1). The relationship between ^{10}Be concentration and grain size varies between catchments. In the larger catchments (Nahuelbuta Stream, La Campana Stream, and Santa Gracia Stream), stream boulder sample ^{10}Be concentrations are lower for larger grain sizes (Figure 4.4A-C). However, samples from smaller catchments show the opposite pattern, where larger grain sizes have higher concentrations (Figure 4.4D-F).

Table 4.1. New ^{10}Be cosmogenic radionuclide sample data.

Sample ID	IGSN[a]	Sampling location[b]	Latitude (°N)	Longitude (°E)	Sample type / grain size (cm)[c]	No. boulders sampled	^{10}Be conc. ±2σ (×10^5 atoms g^{-1})	^{10}Be conc. ±2σ (×10^5 atoms g^{-1}) normalized to SLHL[d]	^{10}Be production rate (spallation) (atoms gr^{-1} yr^{-1})[e]	Site scaling factor
					Nahuelbuta					
EL19-NA14	GFEL1000D	NA Stream	-37.808	-73.014	113×87×51	20	1.51 ± 0.07	0.57 ± 0.03	10.59	2.64
EL19-NA13	GFEL1000C	NA Stream	-37.808	-73.014	60×44×31	19	1.23 ± 0.08	0.47 ± 0.03	10.59	2.64
EL19-NA6	GFEL10005	NA Stream	-37.808	-73.014	26×20×14	20	1.34 ± 0.08	0.51 ± 0.03	10.59	2.64
					La Campana					
EL19-LC15	GFEL1000U	LC Stream	-32.935	-71.076	172×134×102	13	1.67 ± 0.09	0.95 ± 0.05	7.06	1.76
EL19-LC16	GFEL1000V	LC Stream	-32.935	-71.076	38×30×22	10	2.26 ± 0.11	1.28 ± 0.06	7.06	1.76
EL19-LC17	GFEL1000W	LC Stream	-32.935	-71.076	Fine sediment	N/A	5.69 ± 0.22	3.23 ± 0.13	7.06	1.76
					Santa Gracia					
EL19-SG21	GFEL1001L	SG Stream	-29.759	-71.167	48×38×28	16	0.84 ± 0.08	0.56 ± 0.06	1.50	6.00
EL20-SG44	GFEL1002L	Diorite Stream	-29.745	-71.158	2-5cm clasts	N/A	13.35 ± 0.50	9.71 ± 0.36	1.38	5.51
EL20-SG7	GFEL1003N	Cactus Stream	-29.752	-71.124	2-5cm clasts	N/A	7.91 ± 0.33	6.33 ± 0.26	1.25	5.02
EL19-SG18	GFEL1001H	Flag Stream	-29.753	-71.122	45×36×32	12	8.18 ± 0.32	6.63 ± 0.26	1.23	4.95
EL19-SG19	GFEL1001J	Flag Stream	-29.753	-71.122	3-6cm clasts	N/A	4.76 ± 0.22	3.86 ± 0.18	1.23	4.95

Modelled hillslope boulder ^{10}Be concentrations are lowest in La Campana, intermediate in Nahuelbuta, and highest in Santa Gracia (Table 4.2). Similarly, modelled boulder exposure durations during exhumation (considering varying initial boulder sizes and exhumation stages; see Table 4.2) are highest for Flag Hill (with average duration of 221 kyr) intermediate for Santa Gracia Hill (with average duration of 111 kyr) and Nahuelbuta (with average duration of 118 kyr), and lowest for La Campana (with average duration of 23 kyr). However, soil denudation during boulder exposure is similar between field sites (~1-4 m; Table 4.2). Modelled concentrations are lower for boulders with a larger initial radius, as the amount of self-shielding increases with boulder size. Boulders with a 2 m or 3 m initial radius experience decreasing ^{10}Be concentrations with increasing percent exhumation, whereas boulders with a 1 m initial radius experience increasing ^{10}Be concentrations with percent exhumation, in all four sites (Table 4.2). On Nahuelbuta's hillslopes and on Santa Gracia Hill, modelled hillslope boulder concentrations are higher than measured stream boulder ^{10}Be concentrations from the adjacent stream, whereas on La Campana's hillslopes and on Flag Hill, modelled hillslope boulder concentrations are lower than measured stream boulder concentrations (Figure 4.4). In all cases, averaged measured hillslope boulder concentrations from Lodes et al. (2023) are higher than modelled hillslope boulder concentrations from this study. Modelled hillslope boulder concentrations are plotted alongside measured stream boulder concentrations in Figure 4.4.

Table 4.2. Modelled hillslope boulder concentrations for hillslopes adjacent to streams with stream boulder samples. Average soil and boulder denudation rates were estimated based on data from Lodes et al. (2023) and Lodes et al. (submitted).

Average soil denudation range rate (m Myr^{-1})	Average boulder denudation rate range (m Myr^{-1})	Boulder exhumation stage (%)	Boulder initial radius (m)	Boulder final radius (m)	Exposure duration (kyr)	Soil denudation during exposure (m)	Modelled boulder ^{10}Be conc. range ($\times10^5$) (atoms g^{-1})	Modelled boulder ^{10}Be conc. range ($\times10^5$) (atoms g^{-1}) normalized by SLHL production
Nahuelbuta								
20	10	100	3	1	200	4	2.88	1.13
20	10	75	3	1.2	180	3.6	3.29	1.29
20	10	50	3	1.5	149.99	3	3.84	1.51
20	10	100	2	0.67	133.33	2.67	3.79	1.48
20	10	75	2	0.8	120	2.4	3.79	1.48
20	10	50	2	1	100	2	3.94	1.54
20	10	100	1	0.33	66.67	1.33	4.21	1.65
20	10	75	1	0.4	60	1.2	4.06	1.59
20	10	50	1	0.5	50	1	3.81	1.49
La Campana								
100	60	100	3	0.75	37.5	3.75	0.40	0.29
100	60	75	3	0.92	34.61	3.46	0.43	0.32
100	60	50	3	1.2	30	3	0.47	0.35
100	60	100	2	0.5	25	2.5	0.47	0.35
100	60	75	2	0.62	23.08	2.31	0.48	0.35
100	60	50	2	0.8	20	2	0.49	0.37
100	60	100	1	0.25	12.5	1.25	0.49	0.36
100	60	75	1	0.31	11.54	1.15	0.49	0.36
100	60	50	1	0.4	10	1	0.46	0.34
Santa Gracia Hill (Santa Gracia)								
15	10	100	2	0.4	160	2.4	3.15	2.27
15	10	75	2	0.5	149.99	2.25	3.23	2.33
15	10	50	2	0.67	133.32	2	3.31	2.39
15	10	100	1	0.2	80	1.2	3.19	2.30
15	10	75	1	0.25	75	1.12	3.16	2.28
15	10	50	1	0.33	66.66	1	3.07	2.21
Flag Hill (Santa Gracia)								
8	4	100	2	0.67	333.33	2.67	4.95	3.57
8	4	75	2	0.8	299.99	2.4	5.19	3.74
8	4	50	2	1	249.99	2	5.39	3.89
8	4	100	1	0.33	166.67	1.33	5.59	4.03
8	4	75	1	0.4	150	1.2	5.52	3.98
8	4	50	1	0.5	125	1	5.32	3.83

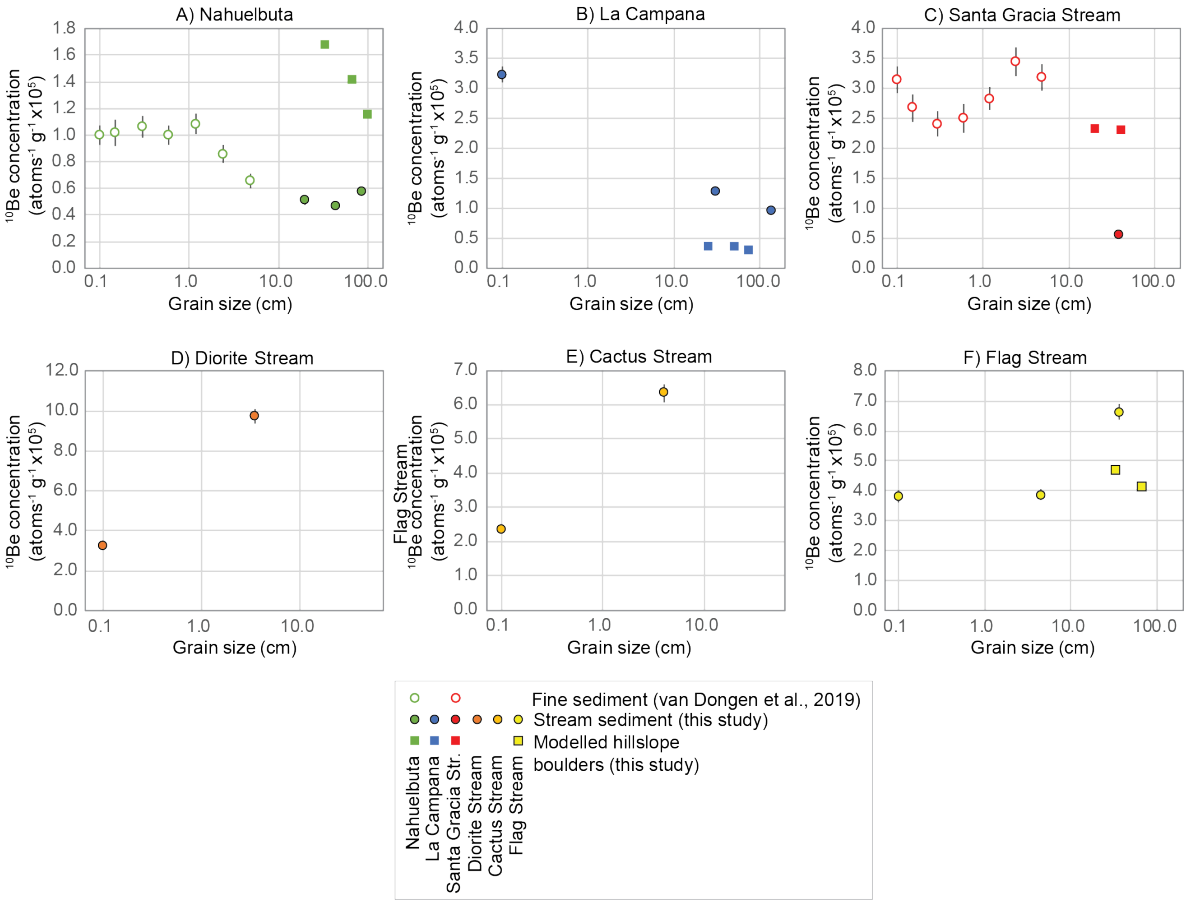

Figure 4.4. ^{10}Be concentrations from stream boulders, clasts and sediment and modelled hillslope boulder ^{10}Be concentrations in the final stage of exhumation (100%; see Table 4.2), all normalized to sea level high latitude production rates. Round markers with a black outline indicate stream sediment samples from this study as well as three fine sediment samples from Diorite Stream, Cactus Stream and Flag Stream from Lodes et al. (submitted). Hollow markers indicate catchment average stream sediment samples from van Dongen et al. (2019), and square markers indicate modelled hillslope boulder concentrations.

4.4.2 Grain size measurements

Grain size measurements from Wolman pebble count surveys are shown below in Table 4.3 and Figure 4.5. Grain size distributions between surveyed sites are relatively similar except for the sites in Santa Gracia's monzogranite lithology, which generally have smaller surficial grain sizes. For all sites except Nahuelbuta Stream, we collected data for a hillslope and stream pair, where the stream drains the connected hillslope; these connected sites are color coded in Figure 4.5. The D50 value is similar (~1-7 cm) for all surveyed areas except Nahuelbuta Stream, La Campana Stream and Diorite Stream, where it is larger, at

~20. D84 is between 40 and 80 for all sites except the streams in Santa Gracia's monzogranite, Flag Hill, and Santa Gracia Stream, where D84 values are lower at ~10 cm. In La Campana, the D50 grain size of La Campana Stream is larger than the connected Cerro Cabra Hill. For all hill and stream pairs in Santa Gracia, D50 values are higher in the stream than on the connected hillslope, whereas D84 values higher on hillslopes. In Nahuelbuta, we were not able to conduct pebble counts on the hillslopes.

Table 4.3. Sediment grain size data from Wolman pebble counts.

Grain size category (cm)	Nahuelbuta Stream (NA)	Cerro Cabra Hill (LC)	La Campana Stream (LC)	Santa Gracia Hill (SG)	Santa Gracia Stream (SG)	Zebra Hill (SG)	Diorite Stream (SG)	Flag Hill (SG)	Flag Stream (SG)	Cactus Hill (SG)	Cactus Stream (SG)
D16	1.88	<0.01	0.10	0.10	0.10	0.10	0.10	0.10	1.00	0.13	0.20
D50	22.00	<0.01	20.00	1.00	3.00	1.00	20.00	1.00	7.00	1.00	3.00
D84	40.00	50.00	53.00	45.64	18.52	70.00	59.20	22.00	14.00	40.00	20.00
Mean	25.64	19.79	26.81	20.11	8.44	31.17	27.06	10.15	8.43	13.76	9.72
SD	27.20	36.36	31.35	35.31	11.83	51.32	29.68	18.00	7.49	21.31	14.41

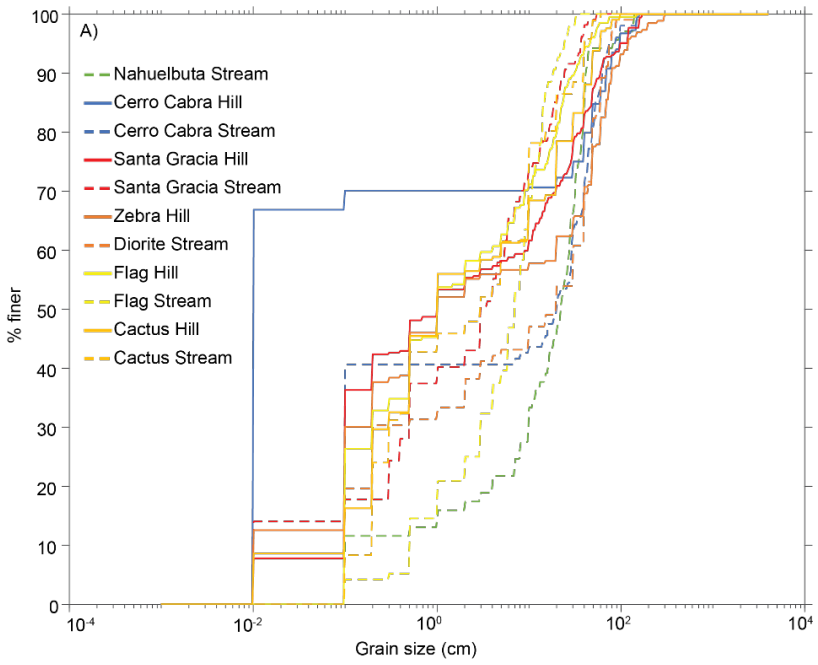

Figure 4.5. Grain size distribution function for hillslopes and streams, for each site where Wolman pebble counts were conducted, color coded by catchment.

4.4.3 Basin attributes

The six catchments investigated in this study show strong positive relationships between catchment upstream area (area) and relief and between area and D50 sediment grain size, and weak positive relationships between area and k_{sn}, area and the fine sediment denudation rate, basin average slope and k_{sn}, and between fine sediment denudation rate and both relief and D50.

Table 4.4. Average basin characteristics of all six catchments based on DEMs.

Basin	Field site	Catchment upstream area (km^2)	Mean basin slope (°)	Normalized channel steepness (k_{sn})*	Basin relief (m)
Nahuelbuta Stream	Nahuelbuta	5.437	12.24	2.01	322.17
La Campana Stream	La Campana	6.352	18.41	7.82	1192
Santa Gracia Stream	Santa Gracia	0.857	21.14	4.83	304.85
Diorite Stream	Santa Gracia	0.162	16.27	2.62	174.46
Cactus Stream	Santa Gracia	0.043	20.61	3.02	84.65
Flag Stream	Santa Gracia	0.046	15.01	3.44	91.21

* Based on a reference concavity (ϑ_{ref}) of 0.3.

4.5 Discussion

4.5.1 Impacts of self-shielding and enhanced erosion of stream boulders on ^{10}Be concentrations

In the larger streams of our field sites (Nahuelbuta Stream, La Campana Stream, and Santa Gracia Stream; Figure 4.1), ^{10}Be concentrations decline with stream sediment size (Table 4.1; Figure 4.4). This could result from two processes: first, the large stream boulders could have rotated during transport from hillslopes or within the channel, which would lower the average surficial ^{10}Be concentration due to self-shielding, and second, the boulders could be weathering and eroding more rapidly in the stream compared to finer sediment. Both sets of processes likely impact boulders in our field sites. However, there may be differences in the importance of these processes depending on the boulder size and the field site.

Larger boulders (>1 m in diameter) are likely to experience higher degrees of self-shielding due to the attenuation of cosmogenic rays (Gosse and Phillips, 2001; Mackey and Lamb, 2013). However, smaller boulders are more easily transported on both hillslopes and in streams and therefore may experience higher erosion rates due to abrasion during transport (Paola et al., 1992; Attal and Lavé, 2006, 2009; Carretier and Regard, 2011; Sklar et al., 2020). In Nahuelbuta, where precipitation (Meyer-Christoffer et al., 2015), runoff (van Dongen, 2021) and chemical weathering (Schaller and Ehlers, 2022) are higher than in the other field sites, stream flow velocity and thus shear stress due to moving water are likely also higher and should increase abrasion by transported sediment, in agreement with the relatively low ^{10}Be concentrations of Nahuelbuta's stream boulders. Within La Campana's channel, the relatively low ^{10}Be concentration for the sample of very large stream boulders (~134 cm) compared to smaller stream boulders suggests that some sampled surfaces experienced self-shielding.

In Santa Gracia Stream, the stream boulder sample consists of smaller grain sizes (~38 cm; Table 4.1) that are likely less affected by self-shielding. Therefore, its low ^{10}Be concentration could be due to infrequent yet geomorphologically impactful floods that may heavily abrade stream boulders (Molnar et al., 2006; Rossi et al., 2016; Deal et al., 2017). In contrast, in all three of Santa Gracia's small catchments (Flag Stream, Diorite Stream and Cactus Stream), stream sediment ^{10}Be concentrations increase with size (Figure 4.4). High ^{10}Be concentrations for stream boulders and larger clasts in these smaller catchments may be a result of reduced stream power due to a combination of lower channel slopes and a smaller upstream area (Table 4.4). Alternatively, the contrast in ^{10}Be concentrations between stream sediment in Santa Gracia's catchments could be due to lithological differences. Santa Gracia Stream and Diorite Stream overly two different diorite plutons (Lodes et al., submitted; see section 4.2), while Cactus Stream and Flag Stream overly a monzogranite pluton. Hillslope boulder and soil denudation rates are generally higher for the diorite underlying Santa Gracia Stream than for the other two rock types (Lodes et al., submitted), in agreement with the lower ^{10}Be concentrations for the boulders in Santa Gracia Stream.

4.5.2 ^{10}Be concentrations and grain sizes of hillslope boulders versus stream boulders

In Nahuelbuta and Santa Gracia Stream, modelled hillslope boulder ^{10}Be concentrations are higher than measured stream boulder ^{10}Be concentrations, whereas in La Campana and on Flag Hill, the opposite trend is observed (Table 4.2; Figure 4.4). Because self-shielding is incorporated into the modelled hillslope boulder concentrations, we can directly compare modelled hillslope boulder ^{10}Be concentrations to measured stream boulder ^{10}Be concentrations. Therefore, we assume that lower concentrations for stream boulders in Nahuelbuta Stream and Santa Gracia Stream compared to adjacent hillslope boulders are not due to rotation and self-shielding in the stream channel, but rather are due to enhanced weathering and erosion in the channel, as described in section 4.6.1. In addition, modelled hillslope boulders with a larger initial radius (2 or 3 m) experience decreasing ^{10}Be concentrations as they exhume (Table 4.2) that more closely match stream boulder concentrations. Therefore, modelled and measured boulder concentrations in Nahuelbuta and Santa Gracia Stream are consistent with relatively longer hillslope residence times and relatively shorter stream channel residence times.

Modelled boulder ^{10}Be concentrations on Flag Hill and measured boulder ^{10}Be concentrations in Flag Stream are both relatively high (Figure 4.4), and therefore likely reflect long hillslope residence times and even longer stream channel residence times, in agreement with a long average modelled exposure duration (>220 kyr; Table 4.2). However, in La Campana, patterns in ^{10}Be concentration and grain size are likely related to steep hillslope angles and channel gradients. Lodes et al. (2023) attributed very low measured ^{10}Be concentrations of hillslope boulders in La Campana to recent exhumation, overturning, and shallow landsliding on La Campana's steep hillslopes, and predicted that in La Campana, hillslope boulders are delivered to stream channels relatively rapidly, but have longer residence times within the channel. Similarly, as larger modelled hillslope boulder concentrations decrease in ^{10}Be concentration with percent exhumation, boulders that are transported to streams before they are fully exhumed on hillslopes have higher concentrations that more closely match the concentrations of La Campana's stream boulders. In addition, average modelled hillslope boulder exposure durations for La

Campana are only ~23 kyr (Table 4.2), nearly an order of magnitude lower than the other field sites.

Results from grain size distributions from Wolman pebble counts on hillslopes and in stream channels in La Campana and Santa Gracia (Table 4.3; Figure 4.5) align well with our analysis of measured and modelled ^{10}Be concentrations from hillslope and stream boulders. In La Campana, grain sizes are generally larger in the channel than on hillslopes (both D50 and D84 grain sizes), indicating that in La Campana, the largest grains quickly enter the streams without spending long periods of time in the weathering zone. In contrast, in Santa Gracia, D50 is larger in the streams while D84 is larger on the hillslopes. Together with ^{10}Be data, these results indicate that in Santa Gracia, generally lower hillslope denudation rates cause boulders to exhume more slowly and spend longer periods of time in the weathering zone (Lodes et al., 2023), which allows them to reduce in size on the hillslope until they are transportable by the lower slope angles and lower runoff.

4.5.3 Boulders as thresholds for channel incision

To understand the mechanisms by which infrequently mobile stream boulders affect channel slope and landscape morphology, we must consider the ability of stream boulders to act as thresholds for channel incision. Boulders and large grains in stream channels can act as erosional thresholds that limit the erodibility of the riverbed and cause a non-linear dependence of river incision on discharge (Sklar and Dietrich, 2004; Turowski et al., 2007; DiBiase and Whipple, 2011; Lague, 2014; Scherler et al., 2017). Therefore, discharge variability and grain size can dictate the magnitude of erosional thresholds and erodibility in a channel.

Van Dongen (2021) conducted a modelling study in which the authors investigated the roles of discharge variability and erosional thresholds on channel incision in the humid-temperate region surrounding Nahuelbuta, the mediterranean region surrounding La Campana, and the semi-arid region surrounding Santa Gracia. Overall, the authors found that for a given erosional threshold, Nahuelbuta's region has the highest erosional efficiency, whereas Santa Gracia's region has the lowest erosional efficiency, the highest sensitivity to erosional thresholds, and the lowest transport capacity for large grains (van

Dongen, 2021). River incision processes are likely to be highly stochastic in Santa Gracia due to its semi-arid climate and higher discharge variability, only occurring during rare and large flood events (e.g., Vargas et al., 2000, 2006; Aguilar et al., 2014, 2015; Carretier et al., 2018; van Dongen, 2021), whereas in Nahuelbuta, due to lower discharge variability, river incision likely occurs more frequently and at lower magnitudes (Tucker and Bras, 2000; Lague, 2014; Perron, 2017; Scherler et al., 2017; van Dongen, 2021).

These results are generally in agreement with the ^{10}Be measurements of stream boulders in this study and suggest that boulders have shorter residence times in streams in the humid-temperate Nahuelbuta, and longer residence times in streams in smaller catchments within semi-arid Santa Gracia (Diorite Stream, Cactus Stream and Flag Stream). The shorter residence times of stream boulders in Santa Gracia Stream may be due to the higher erodibility of the underlying dioritic lithology, or the abrasive effect of infrequent storms. In La Campana, large hillslope boulders rapidly delivered to channels may shield the channel bed from erosion, causing channels to steepen maintain equilibrium (e.g., Shobe et al., 2016; Table 4.4). In contrast, in combination with shorter stream boulder channel residence times, the lower channel steepness value for Nahuelbuta suggests relatively rapid transport of boulders and sediment within the channel due to high runoff.

4.6 Expectations for ^{14}C results

Because ^{10}Be accumulates on the surface of boulders during their residence both on the hillslope and in the channel, it is difficult to account for nuclide accumulation in the channel alone. For this reason, we sent stream boulder samples for measurement of ^{14}C, a nuclide with a shorter half-life (5700 ± 30 years; www.nndc.bnl.gov, National Nuclear Data Center) compared to the 1.4 Myr half-life of ^{10}Be. Ratios of ^{14}C apparent erosion rates to ^{10}Be apparent erosion rates (^{14}C ε_{app}/^{10}Be ε_{app}) can be used to investigate transience in eroding landscapes and infer the timing and magnitude of changes in erosion rate (Hippe et al., 2013a; Mudd, 2016). ^{14}C concentrations adjust to a change in erosion rates more rapidly than ^{10}Be concentrations, which creates an offset in the apparent ^{14}C and ^{10}Be erosion rates (^{14}C ε_{app}/^{10}Be $\varepsilon_{app} \neq 1$) that is largest for events younger than ~25 ka (Hippe, 2017). For example, all else equal, in slowly eroding landscapes such as Nahuelbuta and Santa Gracia a

doubling of erosion rates would cause ^{14}C ε_{app}/^{10}Be ε_{app} to increase by a factor of >1.5 in the first 20 kyr following the event, while a halving of erosion rates would cause ^{14}C ε_{app}/^{10}Be ε_{app} to decrease by a similar magnitude (Hippe, 2017). For the more rapidly eroding La Campana, a similar increase on erosion would cause ^{14}C ε_{app}/^{10}Be ε_{app} to increase by a factor of ~1.3, and vice versa (Hippe, 2017).

Since we have not yet received ^{14}C results, here we discuss expected results and their implications. Based on a comparison between measured stream boulder ^{10}Be concentrations to modelled hillslope boulder ^{10}Be concentrations, we predicted that in Nahuelbuta and Santa Gracia Stream, boulders spend relatively longer periods on adjacent hillslopes and relatively shorter periods in the stream channel, whereas the opposite is true for La Campana. Therefore, all else equal, we would expect ^{14}C ε_{app}/^{10}Be ε_{app} to be >1 for boulder samples in Nahuelbuta Stream and Santa Gracia Stream, and <1 for the boulders in La Campana Stream. However, if the stream boulders were exhumed from depth, ^{14}C concentrations would also be affected: as the ratio of the muonic contribution to total in situ ^{14}C surface production is much higher than the muonic contribution to ^{10}Be surface production (Borchers et al., 2016), and because muonic process dominate nuclide production at depth, a high ratio of ^{14}C concentration to ^{10}Be concentration can indicate that the sampled material has been recently exhumed from depth. We expect that such a scenario is most plausible for La Campana, where slopes are steeper and where landsliding has been observed (van Dongen et al., 2019; Terweh et al., 2021) but is also possible for Nahuelbuta, where potential evidence for shallow landsliding has been observed by Terweh et al. (2021).

4.7 Conclusions

Boulders in stream channels can play a large role in dictating landscape morphology by shielding the channel bed and reducing denudation rates, whereby longer residence times in a stream channel will result in a greater effect on the landscape morphology (Sklar and Dietrich, 2004; 2006; Shobe et al 2016; Dibiase et al., 2018). In this study, we estimated relative residence times of boulders in streams in three climate zones along the Chilean Coastal Cordillera, using ^{10}Be cosmogenic radionuclide analysis, modelling of hillslope ^{10}Be

concentrations, and grain size surveys. We found that ^{10}Be concentrations for stream boulders are lowest in the humid-temperate Nahuelbuta and in the larger catchment in semi-arid Santa Gracia, intermediate in the mediterranean climate of La Campana, and highest in Santa Gracia's smaller catchments. In the larger catchment of each field area, sediment size has a negative relationship with ^{10}Be concentration such that the largest boulders have the lowest concentrations, likely due to a combination of self-shielding, enhanced erosion, and chemical weathering in the stream channel. In contrast, in Santa Gracia's very small catchments Santa Gracia, the largest grains have the highest ^{10}Be concentrations, likely due to low transportation rates due to low runoff and upstream area. However, differences in stream boulder concentrations between sites within Santa Gracia may also be due to lithological differences.

Higher modelled hillslope boulder ^{10}Be concentrations compared to measured stream boulder concentrations for Nahuelbuta Stream and Santa Gracia Stream indicate that enhanced erosion in the stream channel, rather than self-shielding, is the cause for relatively lower stream boulder concentrations. In contrast, in La Campana, lower modelled ^{10}Be concentrations for hillslope boulders relative to stream boulders are likely due to recent exhumation and rapid transport of hillslope boulders and relatively longer residence times in the channel. Similarly, in La Campana, grain sizes are larger for stream boulders compared to hillslope boulders, whereas in Santa Gracia, the largest boulders are on hillslopes.

In general, we predict that stream boulders have the longest in-channel residence times in Santa Gracia and the shortest in-channel residence times in Nahuelbuta. In Santa Gracia, boulders have the highest potential to act as erosional thresholds due to limited precipitation and runoff; however, In La Campana, boulders may have a larger effect on the landscape due to feedbacks whereby channels steepen due to the presence of boulders, causing further influx of boulders from hillslopes to channels. In Nahuelbuta, we predict that stream boulders have the smallest effect on channel morphology due to the higher erosional efficiency in Nahuelbuta and low normalized channel steepness values.

4.8 Acknowledgements

This work was supported by the German Science Foundation (DFG) priority research program SPP-1803 “EarthShape: Earth Surface Shaping by Biota” (grant SCHE 1676/4-2 to D. S.). We are very grateful to the Earthshape management, Friedhelm von Blanckenburg and Todd Ehlers, and the Earthshape coordinators Kirstin Übernickel and Leandro Paulino. We also thank the Chilean National Park Service (CONAF) for providing access to the sample locations and on-site support of our research. We also thank Renee van Dongen and Iris Eder for her help in the field, David Scheer and Cathrin Schulz for their help in the laboratory, and Steven A. Binnie and Stefan Heinze from Cologne University for conducting AMS measurements.

Chapter 5

Influence of lithology and biota on stream erosivity and drainage density in a semi-arid landscape, Central Chile

Emma Lodes[1], Dirk Scherler[1,2], Hella Wittmann1, Anja M. Schleicher[1], Jessica A. Stammeier[1], Martín Andrés Loyola Lafuente[3], and Paulina Grigusova[4]

[1]GFZ German Research Centre for Geosciences, Telegrafenberg, 14473 Potsdam, Germany

[2]Freie Universität Berlin, Institute of Geographical Sciences, 12249 Berlin, Germany

[3]University of Chile, Departamento de Ingeniería y Suelos, 8330111 Santiago, Chile

[4]Philipps-Universität Marburg, Faculty of Geography, 35037 Marburg, Germany

Submitted for publication in (Journal of Geophysical Research: Earth Surface)

Abstract

The efficiencies of advective stream incision and diffusive soil transport processes are known to vary with rock type but are notoriously difficult to quantify. Here, we present a comprehensive analysis of a catchment in semi-arid Central Chile, where landscapes with different drainage densities, but equal tectonic and climatic conditions, have formed on three granitoid plutons (a monzogranite and two diorites). We combined topographic analysis of a 1-m DEM with 10Be-derived denudation rates to estimate stream erosivity and soil diffusivity in the different landscapes. We find that the higher drainage density in the monzogranite is primarily due to higher stream erosivity, whereas soil diffusivity is similar between rock types. Remote sensing data confirm field observations of higher vegetation cover in the diorites, especially with regard to deeper-rooted shrubs. Based on geochemical and compositional analyses, we link these differences to a relatively lower abundance of plant-essential elements in the monzogranite bedrock. We suggest that this results in less infiltration and more runoff in the monzogranite. However, measured infiltration rates are similar between rock types, which we explain by recent soil compaction due to intensive goat farming. In addition, the monzogranite's composition and crystal grain size supports more intense physical weathering and leads to a smaller observed hillslope grain size, which increases its erodibility. We conclude that subtle differences in composition and grain size can have a significant impact on stream erosivity and drainage density.

5.1 Introduction

Drainage density is a fundamental feature of landscapes (e.g., Melton, 1957; Perron et al., 2009; Sangireddy et al., 2016) that results from the combination of different erosional processes. Although the specific processes and landscape characteristics that control drainage density have been the subject of numerous studies in recent decades, they are still not fully understood. In general, drainage density is controlled by the competition between diffusive hillslope processes and advective fluvial incision processes: if advective processes increase compared to diffusive processes, the drainage density increases (Gilbert, 1909;

Smith and Bretherton, 1972; Perron et al., 2008; 2009; Sweeny et al., 2015). At a first order, advective processes require sufficient concentrated surface runoff to move the available sediment and incise. Therefore, runoff and substrate erodibility are key factors in setting drainage density. Runoff is inversely correlated with the rate of rainwater infiltration into the soil or bedrock, and lower infiltration capacity – or higher runoff – in a landscape is associated with higher drainage density, all else equal (e.g., Melton, 1957; Carlston, 1963; Litwin et al. 2022). Arid landscapes tend to have less infiltration and therefore flashier discharge responses to rainfall events, whereas vegetation in more humid landscapes increases evapotranspiration and infiltration, thereby reducing runoff (Ibarra et al., 2019). As a result, more arid and sparsely vegetated landscapes tend to have higher drainage densities (e.g., Perron, 2009; Sangireddy et al., 2016). Alternatively, if runoff is held constant, channel incision requires removable sediment, which can be achieved with less resistant rock types, which generally have a denser drainage network (e.g., Wilson, 1971), or with smaller sediment grain sizes that are easier to move (e.g., Paola et al., 1992). Vegetation can also reduce erodibility by strengthening the soil surface with root networks, thus raising the threshold for fluvial incision, and lowering the drainage density (Prosser and Dietrich, 1995).

Given the importance of infiltration capacity and erodibility in setting drainage density, bedrock lithology ought to be important, but there is no consensus. Some works suggested that less permeable rocks (e.g., claystone versus sandstone) are associated with higher drainage density (Strahler, 1956; Wilson, 1971; Eccker, 1984; Kelson and Wells, 1989), while other studies have found no significant correlation between drainage density and rock type (i.e., Sangireddy et al, 2016). In addition to rock type, other lithological properties may be important. For example, bedrock with a high fracture density can experience high infiltration rates (St. Claire et al., 2015; Lebedeva and Brantley, 2017), and rocks with an abundance of clay-producing minerals may be overlain by clay-rich soil with a higher water holding capacity (Anovitz et al., 2021). In fact, even subtle differences between granitoid mineralogical and geochemical composition can lead to differences in weathering and erosion rates (e.g., Eggleton et al., 2017), and in vegetation cover and ecosystem resilience and productivity (Hahm et al., 2013; Callahan et al., 2022).

In this study, we aim to assess the influence of lithology on drainage density in a semi-arid landscape in central Chile. The Private Reserve Santa Gracia is located in a catchment that is drained by a small, intermittent tributary of the Santa Gracia River (Figure 5.1). The bedrock in Santa Gracia consists of three granitoid plutons of similar ages, a monzogranite and two diorites, which experience the same climate and underwent the same tectonic history, but have visually differing drainage densities. We hypothesize that seemingly subtle differences in bedrock lithology cause disparate drainage densities through their influence on runoff and erodibility, which are set by infiltration, weathering, vegetation cover, and grain size. To test this hypothesis, for each of the three rock types we measured drainage density and solved for advection and diffusion using topographic metrics and a non-linear diffusion-advection equation; we measured vegetation cover and hillslope sediment grain size; we established the bedrock geochemistry and mineralogy; we performed a series of chemical extractions to obtain plant-available elements; we measured the porosity, permeability, hydraulic conductivity, and infiltration rates; and we calculated denudation rates using cosmogenic ^{10}Be. In this setting, where tectonic uplift and climate are constant, we explore our hypothesis as well as the connections between the above parameters that are all theoretically related to drainage density.

5.2 Theoretical background

In order to explore the potential effect of runoff and other parameters on drainage density in regions of contrasting rock types, we follow the approach outlined by Perron et al. (2009). The starting point is to consider the evolution of topography as described by a non-linear advection-diffusion equation (Perron et al., 2008):

$$\frac{\partial z}{\partial t} = D\nabla^2 z - KA^m|\nabla z| + U \qquad (5.1),$$

where z is elevation, t is time, A is area, U is uplift rate, D is soil diffusivity, and K and m are constants related to river incision. The first term on the right side of Eq. (5.1) describes hillslope erosion by diffusive soil creep, which is assumed to be linearly related to local slope

(Culling, 1960; Kirkby, 1971), and the second term describes river incision according to the stream power model (e.g., Whipple and Tucker, 1999; Lague, 2014) and assuming a linear dependence on local slope. By non-dimensionalizing Eq. (5.1), Perron et al. (2008, 2009) solved for a characteristic length scale, L_c, at which the timescales for advection and diffusion are equal:

$$L_c = \left(\frac{D}{K}\right)^{\frac{1}{2m+1}} \quad (5.2).$$

The length scale, L_c, has been shown to be proportional to valley spacing, which is inversely proportional to drainage density: the smaller the valley spacing, the higher the drainage density. Based on numerical landscape evolution models, Perron et al. (2008) demonstrated that L_c^2 is approximately equal (within a factor of ~1-3) to the drainage area at channel head locations. To calculate L_c, we need to estimate the ratio D/K and the parameter m, which can be done with high-resolution topographic data (see section 5.4). On hilltops, where the contributing area (A) and the local slope ($|\nabla z|$) approach zero, the contribution of river incision to erosion is negligible. Together with an assumption of topographic steady state, where uplift equals erosion ($\partial z/\partial t = 0$), Eq. (5.1) can be rearranged to:

$$\frac{U}{D} \approx -\nabla^2 z_h \quad (5.3),$$

with $\nabla^2 z_h$ being the Laplacian of elevation (curvature) on hilltops. Again, under the assumption of topographic steady state ($\partial z/\partial t = 0$), equations (5.1) and (5.3) can be combined and rearranged to:

$$\frac{|\nabla z|}{\nabla^2 z - \nabla^2 z_h} = S^* = \frac{D}{K} A^{-m} \quad (5.4),$$

where S^* is the slope function that is equal to the local slope divided by the difference between local curvature, $\nabla^2 z$, and hilltop curvature $\nabla^2 z_h$. Based on Eq. (5.4), the ratio D/K and the exponent m can be estimated from measurements of S^* and A from high-resolution topography.

The coefficient of river incision, *K*, is related to runoff, substrate erodibility and the distribution of stream power across the channel bed (DiBiase and Whipple, 2011). Parameters that increase the value of *K* include increased runoff, smaller sediment grain size, or weaker bedrock, all of which increase incision and sediment transport in streams. The soil diffusivity, *D*, describes the efficiency of creep-like diffusive transport processes (e.g., Culling, 1963) and is thus related to processes that support soil creep such as frost heave and the swelling of clays. To better constrain the mechanistic controls on variations in *D/K*, we measured as many of the above listed parameters as possible for all three plutons using field data and remote sensing. To capture runoff and infiltration, we measured infiltration rates in the field and bedrock porosity, permeability, and hydraulic conductivity in the lab. We obtained vegetation cover estimates through field surveys and remote sensing, and hillslope grain size distributions though field surveys. To measure the degree of weathering for each pluton, we determined the geochemistry and mineralogy through x-ray fluorescence, x-ray diffraction, and thin section analysis of bedrock samples, as well as by sequential chemical extraction of reactive and exchangeable (plant-available) elements from soils.

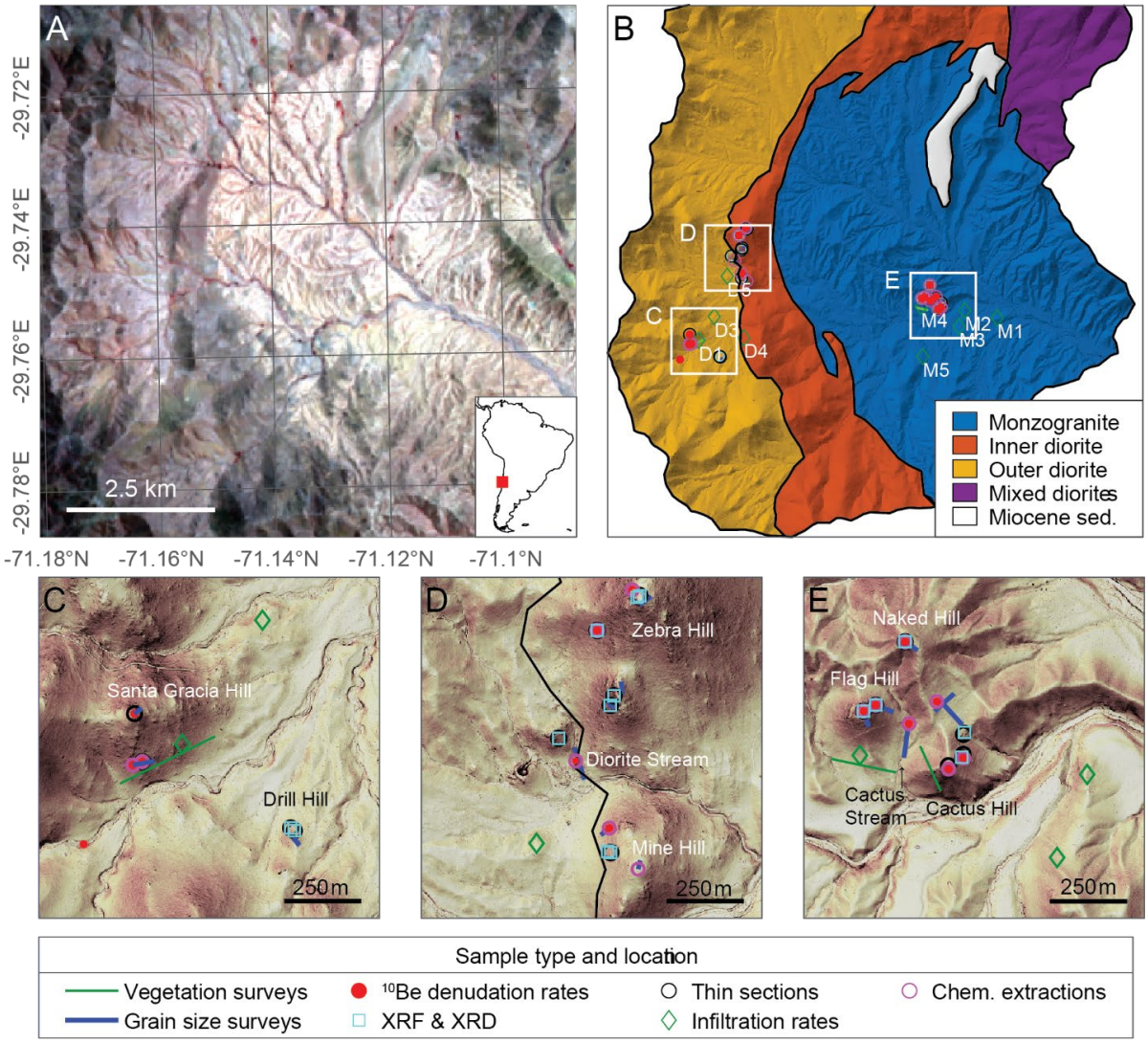

Figure 5.1. A) False color Landsat 9 satellite image of Santa Gracia with inset showing Santa Gracia's location on the South American continent. The band combination is 5-4-3 to highlight lithological contrast. B) Simplified geologic map of Santa Gracia overlying a hillshade image (based on a 1-m resolution LiDAR DEM), and showing the locations of boxes C, D and E. Lithological units are based on geological maps from the Servicio Nacional de Geologia y Minera (Sernageomin, 2003), manually adjusted with the satellite image in A. C-E) Detail panels (slope-colored hillshade images) where most samples were collected, of C) the outer diorite, D) the inner diorite, and E) the monzogranite, showing sampling locations and grain size and vegetation survey transects. Hills where ^{10}Be samples were taken are named (Flag Hill, Naked Hill and Cactus Hill in the monzogranite and Santa Gracia Hill, Zebra Hill and Mine Hill in the diorite). Samples used for bedrock porosity, permeability, and hydraulic conductivity laboratory measurements are a subset of the XRF and XRD samples.

5.3 Field site

Private Reserve Santa Gracia (~29.8°S, 71.0°W; hereon referred to as Santa Gracia) is a ~100 km^2 sized catchment located in Central Chile with a mean elevation of 714 m and a total relief of 1037 m (Figure 5.1). Santa Gracia has a semi-arid climate with a mean annual precipitation rate of 88 mm yr^{-1} (Meyer-Christoffer et al., 2015). Field surveys and leaf area index measurements by Bernhard et al. (2018) show ~30-40% vegetation cover, consisting of various species of shrubs and cacti categorized as Mediterranean desert scrub (Luebert and Pliscoff, 2006; Bernhard et al., 2018). The site is presently occupied by goat farms, and therefore the ground surface is disturbed by grazing. The landscape is composed of mainly upward convex hillslopes characteristic of diffusive erosional processes, although hillslopes sometimes shallow towards channels (Figure 5.1C-E). Landslide activity has not been observed (Terweh et al., 2021). Relatively low uplift rates of <0.1 mm $year^{-1}$ for the coastal area near Santa Gracia were reported by Melnick (2016), based on modeled coastal elevation profiles.

According to the Servicio Nacional de Geologia y Minera (Sernageomin, 2003), the pluton in the center of the catchment (Figure 5.1B) is a medium grained (crystal size of 1-5mm in diameter), biotite-amphibole monzogranite with a biotite K-Ar crystallization age of 100±3 Ma (Aguirre and Egert, 1970). The outer pluton that surrounds the monzogranite is a fine to medium grained, pyroxene-amphibole and pyroxene-olivine diorite with a biotite K-Ar crystallization age of 111±3 Ma (Emparan and Pineda, 2000). Mostly in the southwestern part of the catchment, and in between these two larger plutons is a narrow band of bedrock consisting of a third pluton (Figure 5.1B), which is a medium to coarse grained, quartz-rich diorite with an amphibole K-Ar crystallization age of 110±5 Ma (Emparan and Pineda, 2000). Finally, in the northeastern part of the catchment consists of a mixture of mostly the two diorite rock types, along with small patches of monzogranite. We call this complicated area "the mixed diorite." We did not collect any samples or conduct field measurements in this area, but we did analyze the mixed diorite's topography. We focus this work on the inner and outer diorite and the monzogranite, where we do have samples. From here on, the two dioritic plutons are grouped together and referred to as "the diorites." If one of the two is specifically discussed, they are referred to as "outer diorite" and "inner diorite." The center

pluton will be referred to as “the monzogranite.” Krone et al. (2021) measured fracture spacing and orientation in a borehole in the outer diorite of Santa Gracia, and recorded NW- to NE- trending fracture plane orientations, and fracture spacing of less than 1 meter. The fracture orientations are consistent with the Atacama Fault System, which is one of the largest tectonic structures in the northern Coastal Cordillera, stretching from 20°S to 30°S, and consists of a set of steeply dipping, N-S oriented strike slip faults formed during the Late Jurassic and Early Cretaceous. Therefore, the degree of fracturing in the different plutons is expected to be similar.

In the outer diorite, van Dongen et al. (2019) reported an *in situ* ^{10}Be-derived catchment average denudation rate of 9.21 ± 0.84 m Myr^{-1}. Adjacent to the sampled stream and also in the outer diorite, on a south-facing, 25° slope with a mixed soil layer depth of 45 cm, Schaller et al. (2018) reported *in situ* ^{10}Be-derived soil denudation rates of 16.3 m Myr^{-1} (“Santa Gracia Hill”; Figure 5.1C). On the same slope, Lodes et al. (2023) estimated slightly higher soil (~21 m Myr^{-1}) and lower boulder (~12 m Myr^{-1}) denudation rates, based on measured *in situ* ^{10}Be concentrations and a boulder exhumation model. On a north-facing, 15° slope with a mixed soil layer depth of 25 cm in the outer diorite, Schaller et al. (2018) reported an *in situ*-derived denudation rate of 10.5 m Myr^{-1}. Bernhard et al. (2018) reported that soils underlain by diorite in Santa Gracia have low soil organic matter (~1%) and total organic carbon (0.4%), a bulk density of 1500 kg m^{-3}, a pH of 6.3, and a subangular blocky structure, with soil depth increasing from the ridge to the toeslope. Based on body wave tomography surveys, Trichandi et al. (2022) estimated a mean weathering front depth of 27 m in the outer diorite, as well as some variation in saprolite thickness corresponding to minor topographic changes.

5.4 Methods

5.4.1 Topographic analysis

We used topographic analysis to quantify the drainage density and the *D/K* ratio across the Santa Gracia catchment. Topographic analyses were conducted with MATLAB and the TopoToolbox v2 (Schwanghart and Scherler, 2014), and are based on a one-meter resolution LiDAR digital elevation model (DEM), showing bare ground returns only (Kügler et

al., 2022). We identified channel head locations and calculated a drainage network using GeoNet 2.2 (Passalaqua et al., 2010; Sangireddy et al., 2016), a computational tool for automatically extracting channel heads and networks from high resolution DEMs. The GeoNet workflow consists of three main steps outlined in Passalaqua et al. (2010) and Sangireddy et al. (2016). First, non-linear filtering of DEM elevation data is performed to remove small scale variability; here we used 50 filtering iterations. Second, a quantile-quantile plot of curvature is used to identify the convergent features on the landscape (we used a threshold for curvature of 1 m), and a "skeleton" of likely channelized pixels is created that represents a first estimate of the channel network. The skeleton is refined by the user-defined skeleton thinning parameter, or threshold area, which we set to 30 m^2. Finally, the channel heads and stream network are extracted: channel heads are identified using the skeleton's connected components information, the geodesic distance, and a search box the size of the median hillslope length (our search box was 10 m), and channel centerlines are extracted based on a gradient descent on the geodesic distance from channel heads to the basin outlet. To calculate drainage density (channel head density) for each rock type separately, we measured the total length of all streams (number of channel heads) and divided by the area according to the mapped outcropping area.

Based on the streams in the different rock types, we obtained estimates of the channel steepness (k_s) and concavity (ϑ), by fitting the slope and upstream area data to the equation (e.g., Whipple et al., 2013):

$$S = k_s A^{-\theta} \tag{5.5}.$$

To derive the normalized channel steepness (k_{sn}), we fixed q to a reference concavity value, q_{ref}, which we based on the average concavities and m/n ratios between rock types. To measure channel widths, we divided the GeoNet-derived stream network into 100 m segments and measured the width of the stream channel at the midpoint of each segment using high-resolution satellite imagery and a slope map from the 1-m resolution DEM to identify channels. For comparison between the different rock types, we calculated channel width indices k_w (Turowski et al., 2008; Lague, 2014), by fitting a power law relationship between channel width (W) and upstream area for each rock type:

$$W = k_w A^{\omega} \quad (5.6).$$

Because the constant of proportionality (k_w) and the power law exponent ω covary, we furthermore fixed the exponent to the average exponent obtained from free fits for each rock type and thus obtained normalized channel width indices, k_{wn}.

Following the approach outlined in Perron et al. (2009), we calculated $|\nabla z|$ and $\nabla^2 z$ by fitting a second order polynomial surface to circular moving windows with a radius of 7 m. We estimated $\nabla^2 z_h$ as the mean $\nabla^2 z$ value for areas where the product $A\ |\nabla z| < 1$ m^2. The *D/K* ratio and parameter *m* were then estimated by least-squares regression of $\log_{10}$-transformed values of *S** and *A* using Eq. (5.4), and L_c was calculated with Eq. (5.2). We conducted the above steps for topographic data within circular areas of 500-m radius that are distributed in a hexagonal grid across the catchment area. Thereby, we obtained spatially distributed estimates of *D/K*, *m*, and L_c. We compared these estimates to the different rock units as well as maps of local relief (elevation range) calculated within a 500-m radius moving window. To allow for comparison of *D/K* ratios amongst the different rock types, we chose a common *m* value that corresponds to the mean value across the entire area. This step is needed as *D/K* and *m* covary.

5.4.2 Field measurements

Grain size. To quantify grain size distributions and how these change across the landscape, we conducted Wolman pebble counts (Wolman, 1954) with 1-meter intervals between measurements, in locations where we collected samples (Figure 5.1). We conducted separate grain size counts for ridges, hillslopes, and stream channels. Bedrock was noted separately in the pebble count, and grains < 2 mm were not distinguished any further. In total, we made 906 sediment grain size measurements in the monzogranite along transects in 9 different localities, and 1325 measurements in the diorites (6 localities in the inner diorite, 3 in the outer diorite, and one in a stream bed containing grains from both diorites). We also analyzed the grain sizes of surficial soil samples (38.5 kilograms from the monzogranite and 26.3 kilograms from the diorites), by sieving and recording the weights of the >1 mm, 0.25-1 mm, and <0.25 mm grain size fractions for each rock type.

Rill and vegetation density. We assessed the extent of small-scale surface runoff and sediment transport in each rock type by walking contour-parallel transects in the vicinity of samples collected for *in situ* ^{10}Be analysis and recording the GPS position of initiation points of rills we crossed. For a field-based manual determination of the density of vegetation in each rock type, we walked transects along hillslopes and recorded the abundance of cacti and shrubs (without specifying the species) at every meter (one pace) (Figure 5.1; Figure 5.2).

Infiltration rates. To measure infiltration rates in each rock type, we used a minidisk infiltrometer, which is a manually operated device used to measure hydraulic conductivity. At each of nine measurement sites (five in the monzogranite and four in the diorites), we first removed leaf litter to ensure an undisturbed and direct measurement of water entering the soil. We also added a fine layer of locally sourced sand that served as a uniform interface of contact between the equipment and the variably rough ground surface (Angulo-Jaramillo et al., 2000). Subsequently, we filled the bubbling chamber with water and selected supply tensions (or suction settings) of 1, 2, 4 and 6 cm. For each tension, we measured the infiltration over a period of 10 minutes, recording the readings of the water reservoir every 30 seconds. Finally, we processed the data according to the method described by Zhang (1997), which considers the geometry of the wetting bulb as a function of the textural class of the soil.

Samples. To estimate denudation rates in each rock type, we collected samples for *in situ* and meteoric ^{10}Be cosmogenic radionuclide analysis. For *in situ* ^{10}Be, we collected samples from boulders, soil and stream sediment in each rock type to supplement existing *in situ* ^{10}Be data from the inner and outer diorites presented in Schaller et al. (2018), van Dongen et al. (2019), and Lodes et al. (2023). For each boulder sample, we amalgamated rock chips collected from the top surface of at least 10 different boulders (~25 cm^2 and <2 cm thick) in an area ~20 m × 20 m (Figure 5.2). Topsoil samples were also collected by amalgamation in the area surrounding the sampled boulders, and stream sediment samples were collected by scooping stream sediment from inside channels, which were dry at the time of sampling (Figure 5.2). For meteoric ^{10}Be, we collected only two stream sediment samples, one from Diorite Stream in the diorite and one from Cactus Hill stream in the

monzogranite (Appendix 5A). To obtain information on bedrock geochemistry and weathering intensities, we collected bedrock samples for x-ray fluorescence (XRF), x-ray diffraction (XRD) and thin section analysis, as well as porosity, permeability, and hydraulic conductivity measurements. The bedrock samples were taken from the largest boulders or most intact bedrock we could find in the same areas (hilltops and hillslopes) where we collected samples for *in situ* ^{10}Be. Finally, we collected soil samples and stream sediment for extraction of exchangeable and reactive elements from the same soils that we sampled for *in situ* ^{10}Be, positioned on hillslopes and in streambeds.

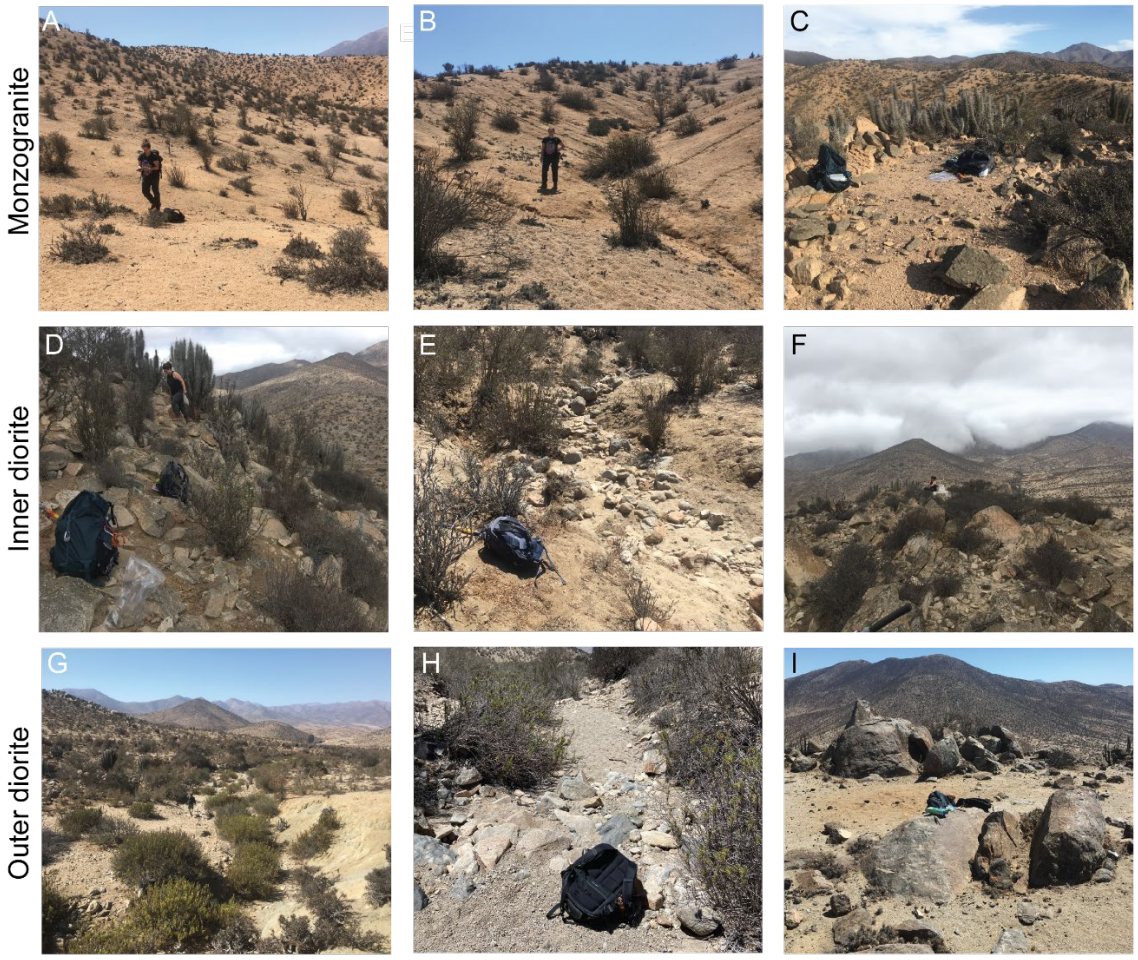

Figure 5.2. Field photos of landscapes in all three rock types. The top row (A, B and C) shows photos of the monzogranite, the middle row (D, E and F) shows the inner diorite and the bottom row (G, H and I) shows the outer diorite. The left column (A, D and G) shows photos of typical vegetation cover, the middle column (B, E and H) shows typical stream channels, and the right column (C, F and I) shows typical boulders.

5.4.3 Compositional analysis and measurement of rock properties

In the laboratory, we performed compositional analyses (XRF, XRD, point counting of thin sections, and sequential chemical extractions), and measured bedrock material properties (porosity, permeability, and hydraulic conductivity). XRF analysis was performed to obtain the bedrock geochemistry (major oxides) of samples collected from both lithologies, and XRD and thin section analyses were performed to obtain information on mineral assemblages from bedrock samples from both lithologies. Chemical extractions were performed according to Wittmann et al. (2012) on soil and stream sediment samples to obtain reactive and mineral bound fractions of elements, which we used to calculate proxies for weathering intensity and meteoric denudation rates (von Blanckenburg et al., 2012; Wittmann et al., 2015), and the concentrations of exchangeable elements, which we used to evaluate the relative amount of available plant nutrients in the soils of each rock type (e.g., Uhlig et al., 2020). Porosity, permeability, and hydraulic conductivity measurements were made on bedrock cores to better understand the ability of each rock type to transmit or retain water. Details on the laboratory procedures can be found in the Supplemental information.

We also calculated weathering intensity for two stream sediments (one stream in the monzogranite and one stream that drains both diorites), using the reactive and mineral-bound phases of ^{9}Be, and the following equation:

$$f_{reac} = \frac{1}{(\frac{9Be_{min}}{9Be_{reac}} + 1)} \quad (5.7),$$

where f_{reac} is the weathering intensity calculated from the reactive ($^{9}Be_{reac}$) and mineral-bound ($^{9}Be_{min}$) concentrations of ^{9}Be. When bedrock weathers, ^{9}Be is initially present in the dissolved form, while a fraction remains bound in the primary minerals of soils and sediment. From the dissolved phase, reactive phases (e.g. Fe-Mn-oxy-hydroxides) co-precipitate onto sediment particles that are then transported with sediment (von Blanckenburg et al., 2012). When normalized by the mineral-bound fraction, the reactive and dissolved fractions can be used as a proxy for weathering intensity. In settings where pH values of river water or soil solutions exceed a value of 5, retentivity of Be onto the reactive

phase is high, and hence the dissolved fraction must not be determined. In Santa Gracia, the soil pH is ~6.3 (Bernhard et al., 2018). Therefore, weathering intensity can be calculated using Eq. (5.7).

In addition, we used XRF results to calculate chemical index of alternation (CIA) values for each sample, which are indicative of the degree of weathering for a given bedrock sample (Nesbitt and Young, 1982). The CIA is based on the fact that feldspar minerals dominate the earth's crust, and that the elements calcium, sodium and potassium are removed from feldspars by aggressive soil solutions so that the proportion of alumina to alkalis typically increases in the weathering product. We calculated CIA values using molecular proportions of XRF-derived oxides and the following formula (Nesbitt and Young, 1982):

$$CIA = \frac{Al_2O_3}{(Al_2O_3 + CaO + Na_2O + K_2O)} \times 100 \quad (5.8).$$

5.4.4 ^{10}Be denudation rate calculations

We measured *in situ* ^{10}Be concentrations for 13 new samples from the monzogranite (four soil samples, four boulder samples, three soil samples and two stream sediment samples), four samples from the inner diorite (two soil samples and two amalgamated boulder samples), and one stream sediment sample that is mixed between both diorites. In addition, we analyzed meteoric ^{10}Be and ^{9}Be concentrations for two stream sediment samples, one from the monzogranite and one from the diorite. We compared these data with 10 samples from the outer diorite published in Lodes et al. (2023).

For *in situ* ^{10}Be analysis, we dried, crushed, and sieved samples for quartz mineral separation to 250-500 µm particle size, or to 250-1000 µm if the 250-500 µm sample fraction wasn't sufficient. We isolated ~10 g of pure quartz from each sample using standard physical and chemical separation methods, spiked each sample with 150 µg of our in-house "phenakite" ^{9}Be carrier, and dissolved the quartz in concentrated hydrofluoric acid in order to extract beryllium. To obtain meteoric ^{10}Be and ^{9}Be concentrations, we took aliquots

before ^{9}Be carrier addition from all leachates produced during sequential chemical extractions and from the final decomposed silicate residue (see supplementary methods). We set these aliquots aside for stable ^{9}Be and other elemental analysis, and respective meteoric Be aliquots were spiked with 160 µg of ^{9}Be carrier. From here on, separation of ^{10}Be for both *in situ* and meteoric samples was carried out according to the simplified separation scheme of von Blanckenburg et al. (2004), by carrying out anion and cation column separation and alkaline precipitation. ^{10}Be/^{9}Be ratios were measured by accelerator mass spectrometry at the University of Cologne, Germany (Dewald et al., 2013). Sample ratios were normalized to standards KN01-6-2 and KN01-5-3 with ratios of 5.35×10^{-13} and 6.32×10^{-12}, respectively. Final *in situ* ^{10}Be concentrations were corrected by process blanks with an average ^{10}Be/^{9}Be ratio of $(1.70 \pm 0.16) \times 10^{-14}$, and meteoric ^{10}Be concentrations using a ^{10}Be/^{9}Be ratio of $(2.51 \pm 0.13) \times 10^{-15}$, respectively.

Denudation rates for *in situ* samples were calculated differently depending on the sample type. We obtained local hillslope denudation rates from hillslope soil, clast and small boulder samples using the Cronus online calculator v. 2.3 (Balco, 2008). From stream sediment samples we obtained catchment-average denudation rates using the Matlab functions of the Cronus online calculator v. 2.3 in conjunction with the TopoToolbox v2 (Schwanghart and Scherler, 2014). For our single new large boulder sample, we used a model described in detail in Lodes et al. (2023) that determines boulder and soil denudation rates from the ^{10}Be concentration of boulder tops and their protrusion height above the surrounding soil. Lodes et al. (2023) provide boulder and soil denudation rates based on 10 diorite samples. In the monzogranite, large boulders are rare and we were able to apply the model for only one new monzogranite boulder sample. Details on meteoric denudation rate calculations are provided in Appendix 5A.

5.4.5 Remote-sensing derived vegetation cover

The classification of catchment-wide vegetation for Santa Gracia was conducted in a two-step procedure using field data of a vegetation survey, a one-meter resolution WorldView-2 (WV) and cloud-free Landsat-8 OLI images. In the first step, a supervised land surface classification was performed with the WV image for a subregion of the Santa Gracia catchment. This classification was used as training data to derive the fractional cover of

vegetation for the entire catchment with a Landsat scene. The high-resolution WV image segmentation was conducted using a random forest (RF) classification (Grigusova et al., 2023). The main classes considered for Santa Gracia were bare soil, rocks, grass/herbs, shrubs, cacti and trees. Beyond the topographically corrected WV spectral bands, a vegetation index (NDVI), the DEM, a DSM (digital surface model; an elevation model that captures all land surface features including vegetation), as well as slope and roughness were used as predictors. Topographic predictors were calculated from 1-m resolution LiDAR data using the function Terrain in R. Landcover data of 100 field polygons per class were used for the training of the RF model. The quality of the random forest model was assessed by a Leave-One-Out cross validation, and the accuracy of the RF classification was 0.81. In the second step, the WV classification is aggregated to the Landsat resolution of 30 m which results in the fractional cover of each class per Landsat pixel for the classified subregion. The data are used as endmembers for spectral unmixing of the entire Landsat scene using the Multiple Endmember Spectral Mixture Analysis (MESMA) approach (Franc et al. 2005, Zhuo et al. 2018; RSToolbox R-package). MESMA was applied using a non-negative least square (NNLS) solver method with 1000 iterations and 0 tolerance. The result was the fractional cover (0-1) of the landcover classes per 30-m Landsat pixel for the entire catchment.

5.5 Results

In the following, some results describe the inner, outer, and mixed diorite areas combined, and for others we were able to differentiate between the diorite sub-categories due to having too few samples in one of the two diorites in some cases. When all three areas of diorite bedrock are combined in the analysis, we will simply write “the diorites”.

5.5.1 Topographic analysis

Table 5.1. Summary of results from topographic analysis.

Metric	Unit	Monzogranite	Inner diorite	Outer diorite	Mixed diorite
Values for drainage network/hillslopes across entire area per rock type					
Drainage density	km^{-1}	16.0	5.9	9.9	7.7
Channel head density	km^{-2}	113.3	31.6	66.0	67.3
Median channel head upstream area	m^2	36.4	128.1	88.4	105.2
ϑ	-	0.17	0.29	0.32	0.28
k_s	$m^{2\vartheta}$	0.57	3.43	4.47	4.18
k_{sn}	$m^{0.48}$	0.79	1.10	1.11	1.76

k_{wn}	$m^{0.7}$	0.44	0.48	0.46	0.5
Median hillslope angle	degree	14	16	17	22
Mean ± std. dev. based on values from 500-m radius circular patches					
Hilltop Laplacian ($\nabla^2 z_h$)	m^{-1} ($\times 10^{-3}$)	-20.9 ± 6.1	-18.1 ± 3.8	-19.7 ± 5.6	25.0 ± 7.2
m^*	-	0.24 ± 0.04	0.23 ± 0.04	0.26 ± 0.07	0.25 ± 0.06
D/K^*	m^{2m+1}	21.27 ± 6.21	28.86 ± 15.16	55.71 ± 73.76	51.75 ± 37.74
L_c^*	m	7.67 ± 1.10	9.41 ± 1.93	10.74 ± 3.97	11.62 ± 3.75
D/K^{**}	m^{2m+1}	20.44 ± 4.14	28.90 ± 5.18	31.98 ± 11.22	36.11 ± 10.71
L_c^{**}	m	7.65 ± 1.04	9.67 ± 1.20	10.27 ± 2.35	11.18 ± 2.25
Local relief	m	126.99 ± 44.11	192.18 ± 37.48	220.72 ± 74.70	267.52 ± 63.74

* Calculated with a variable *m* parameter. ** Calculated with the *m* parameter fixed to 0.24

5.5.1.1 Drainage density and slope-area relationships

In the field, we had observed that the monzogranite has a more dissected landscape than the diorites, and our field surveys and topographic analysis support this initial observation. During our field survey of rill initiation points, we observed an average of 0.24 rills per meter in the monzogranite (~800 m survey), and 0.15 rills per meter in the outer diorite (~1500 m survey). The drainage networks derived with GeoNet are shown in Figure 5.3A. Distinguishing by rock type, we found that the monzogranite has the highest drainage density at 16 km^{-1}, and the highest density of channel heads at 113 km^{-2}, while the inner diorite has the lowest drainage density at 5.9 km^{-1} and 31.6 channel heads per km^2 (Table 5.1). The outer diorite has an intermediate drainage density at 9.9 km^{-1} and 66 channel heads per km^2, and the area of mixed diorite lithologies has a drainage density at 7.7 m^{-1} and a channel head density of 67 km^{-2} (Table 5.1). Median upstream area values of GeoNet-derived channel heads are lowest for the monzogranite at 36.44 m^2, and higher for the diorites at 128.13, 88.39, and 105.18 m^2 for the inner, outer and mixed diorite lithologies, respectively.

Slope-area plots show that the diorites have generally steeper slopes than the monzogranite for upstream drainage areas <1 km^2, in particular the area with mixed diorite lithology (Figure 5.3B). In addition, the streams in the diorites have mean concavity (q) values ranging from 0.28 to 0.32, whereas the streams in the monzogranite have a mean concavity value of 0.17, i.e., they are generally straighter. The upstream rollover to constant slope angles in the slope-area plot, typically interpreted as the transition from fluvial to

colluvial domains (Willgoose et al., 1991), occurs at approximately 10^3-10^4 m^2 in the diorites and at 10^2-10^3 m^2 in the monzogranite. Median hillslope angles increase from 14.0° in the monzogranite to ~16-17° in the inner and outer diorites and 22.3° in the mixed diorite (Figure 5.3C).

We calculated normalized channel steepness values (k_{sn}) based on a reference concavity value, q_{ref} = 0.24. Although measured q values vary between the monzogranite and the diorites (Figure 5.3B, Table 5.1), the average value is ~0.27. The average m value that we obtained from solving Eq. (5.4) with the morphological data, is 0.24. If we stay with our initial assumption of n=1 (see section 5.2), this yields m/n ratios of 0.24, similar to the average q value. Although the n value is unconstrained, for rather gentle sloping and slowly eroding soil-covered landscapes, n=1 usually provides good fits to published erosion rate data (Montgomery and Brandon, 2002; Kirby and Whipple, 2012). As already indicated in Figure 5.3B, the k_{sn} values are similar for the inner and outer diorites, but lower for the monzogranite and higher for the mixed diorite (Table 5.1).

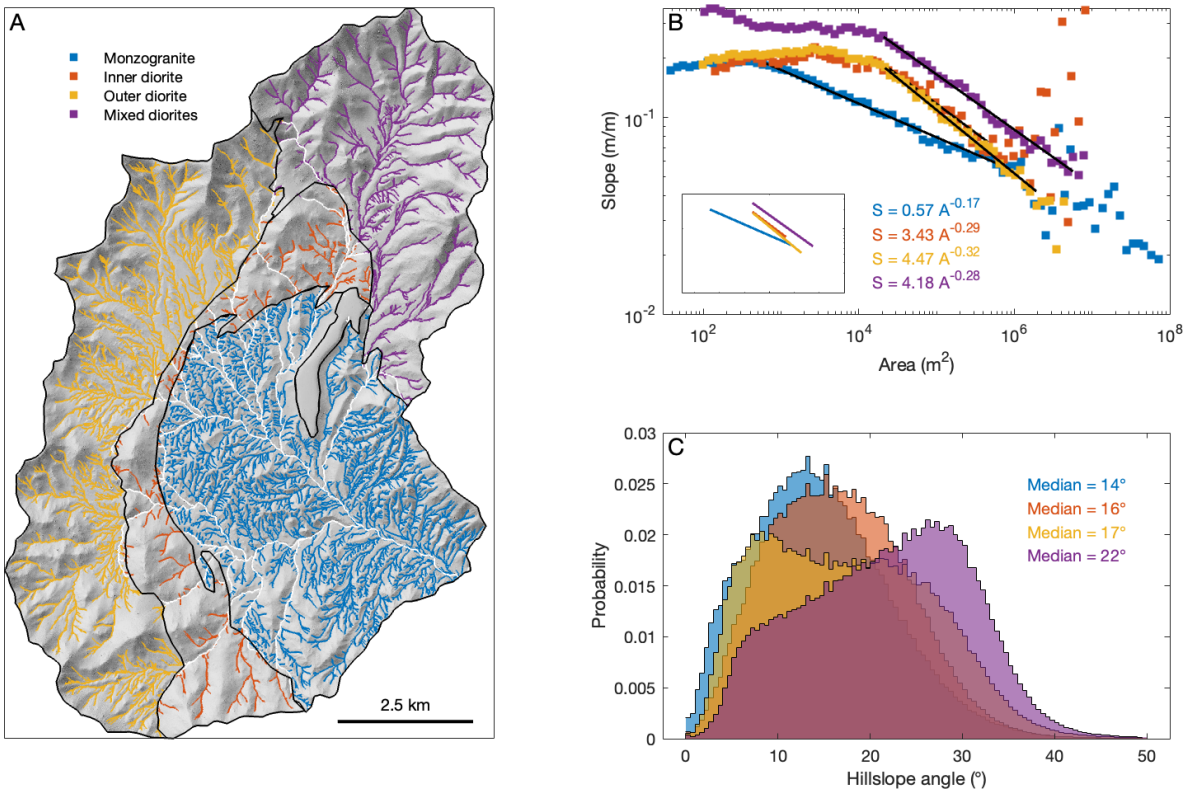

Figure 5.3. A) drainage network derived with GeoNet 2.2 (Passalacqua et al., 2010; Sangireddy et al., 2016) from a 1-m LIDAR DEM. White streams have multiple rock types in their source areas. Outlined elongated area in the northern part of the monzogranite are

presumably Miocene sediments (see Figure 5.1 A and B). B) Slope-area plot of the channels shown in A. Inset provides a simplified form of the slope-area plot showing only the fitted lines. C) Probability density plot of hillslope angles.

5.5.1.2 D/K ratios and Lc

Based on the GeoNet-derived stream networks, we calculated values of *D/K*, L_c and *m* as described in section 4.1. *D/K* and L_c values vary systematically with and without a fixed value for *m* (Figure S5.1). However, when *m* is fixed to the mean value 0.24, *D/K* and thus L_c are confined to narrow ranges and systematic differences across the landscape are clearly visible (Figure 5.4A). With a fixed value for *m*, the monzogranite has generally lower *D/K* values whereas the diorites have generally higher ones, except for the somewhat abnormal low-relief areas that are found west of the monzogranite, approximately in the central part of the outer diorite (Figure 5.4A). Accordingly, the monzogranite has the lowest mean *D/K* value, ~20, whereas the inner and outer diorites have *D/K* values of ~30 and the mixed diorite has a *D/K* value of ~36 (Table 5.1). Whereas the four rock types show some clustering of L_c, it is also apparent that a larger spread of L_c values in the diorites compared to the monzogranite is linked to greater variability in local relief (Figure 5.5). Nevertheless, with a fixed *m*, the mean ($\pm$ 1σ) L_c is 7.67 $\pm$ 1.10 m for the monzogranite, 9.41 $\pm$ 1.93 m for the inner diorite and 10.74 ± 3.97 m for the outer diorite, and 11.62 ± 3.75 m for the mixed diorite (Table 5.1).

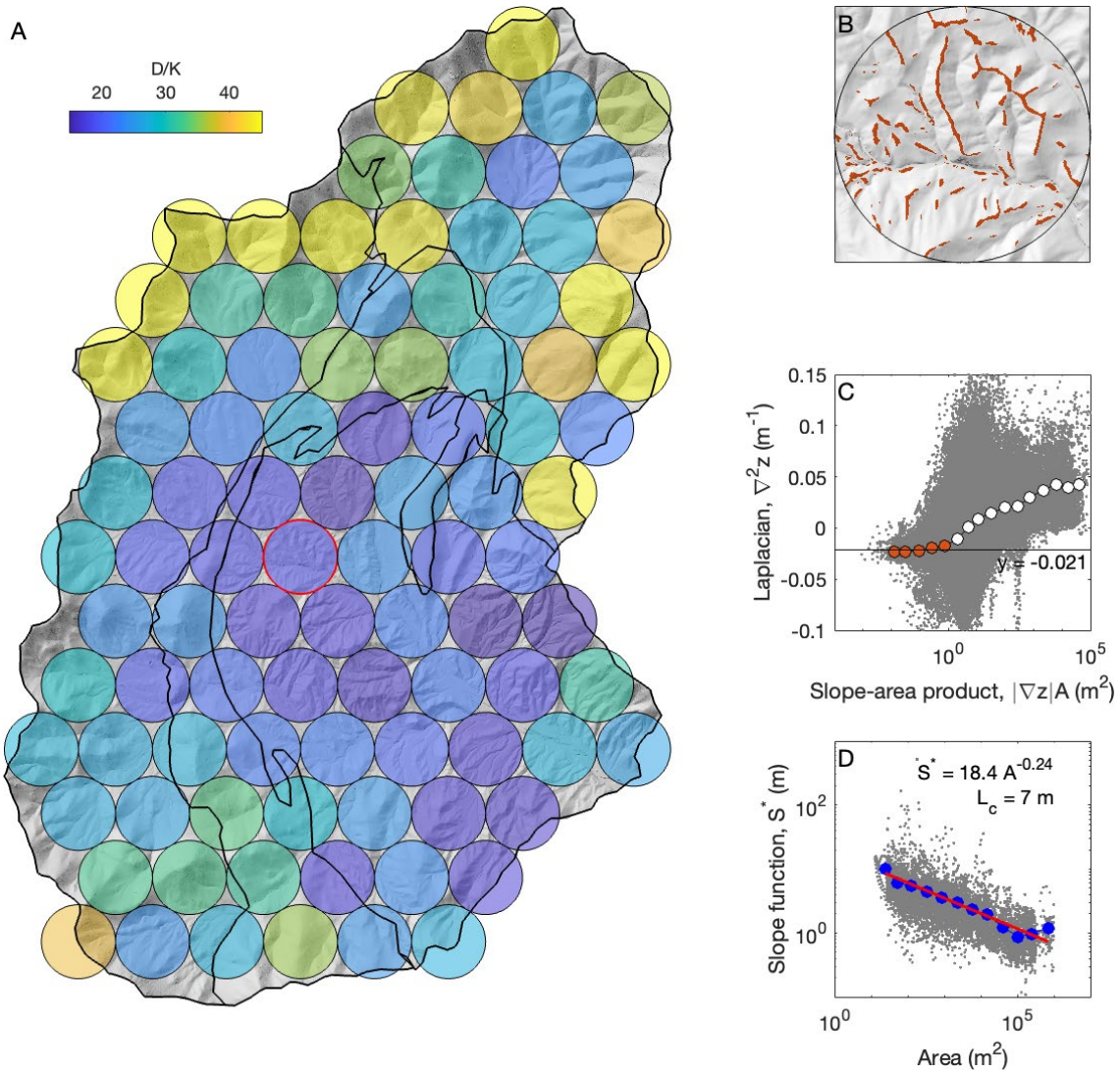

Figure 5.4. A) Map of the Santa Gracia catchment showing spatial variations in the *D/K* ratio, determined for circular patches of 500-m radius. Black lines follow lithological boundaries. Red-rimmed circle indicates the example from the monzogranite shown in B-D. B) Hillshade image with hilltops colored in red. C) Scatter plot of the Laplacian of elevation against the slope-area product. Circles represent the means of log transformed data within logarithmically spaced bins, and red circles represent the red-shaded hilltops in B used to calculate the Laplacian of elevation on hilltops ($-\nabla^2 z_h$). The Laplacian is roughly constant on hilltops where drainage area and slope are small, which is consistent with equilibrium topography as shown in Perron et al. (2009). D) Log-log plot of the slope function *S** (see Eq. 5.4) against drainage areas for stream profiles from the area of the monzogranite shown in A. The line is a least-squares fit to the binned data.

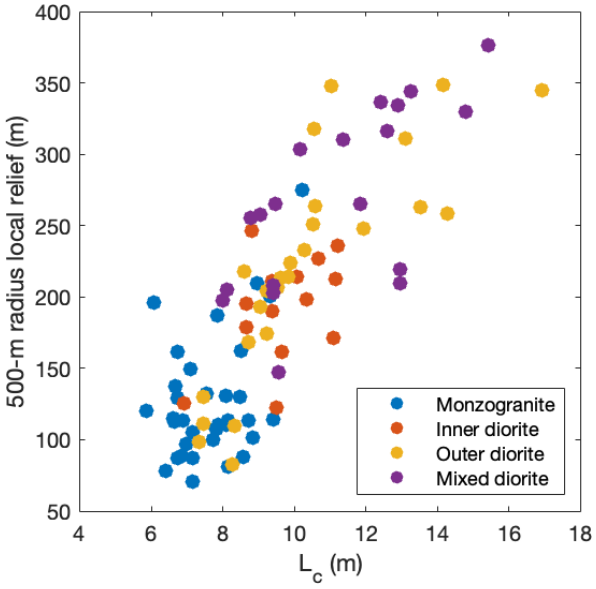

Figure 5.5. L_c (the characteristic length scale at which the timescales for advection and diffusion are equal), plotted against local relief for all three rock types and the mixed diorite category. Each point represents a circle from Figure 5.4A.

5.5.1.3 Channel width

Stream channel widths measured in all three rock types are plotted against upstream contributing area in Figure 5.6. Generally, measured streams in Santa Gracia are narrow and short, and have a small upstream contributing area; over half of the channels are less than 5 m wide and many are narrower than 1 m, and upstream areas are all less than 1 km^2. As expected, there is a positive trend between channel width and upstream area for linear fits with and without a constrained slope value. However, there is considerable scatter in the relationship between channel width and upstream area for all rock types; channel widths range by two orders of magnitude for the monzogranite and one order of magnitude for the diorites. In addition, there are relatively few data points for the inner diorite because of its smaller area and lower drainage density. To calculate normalized channel width indices (k_{wn}; Table 5.1), we fixed the exponent to the average of all unconstrained exponents (0.14; Figure 5.6). Resulting channel width indices indicate similar channel widths between rock types, with values of 0.44, 0.48, 0.46, and 0.5 for the monzogranite, inner diorite, outer diorite and mixed diorite respectively (Table 5.1). Overall, we interpret channel widths to be relatively similar between rock types.

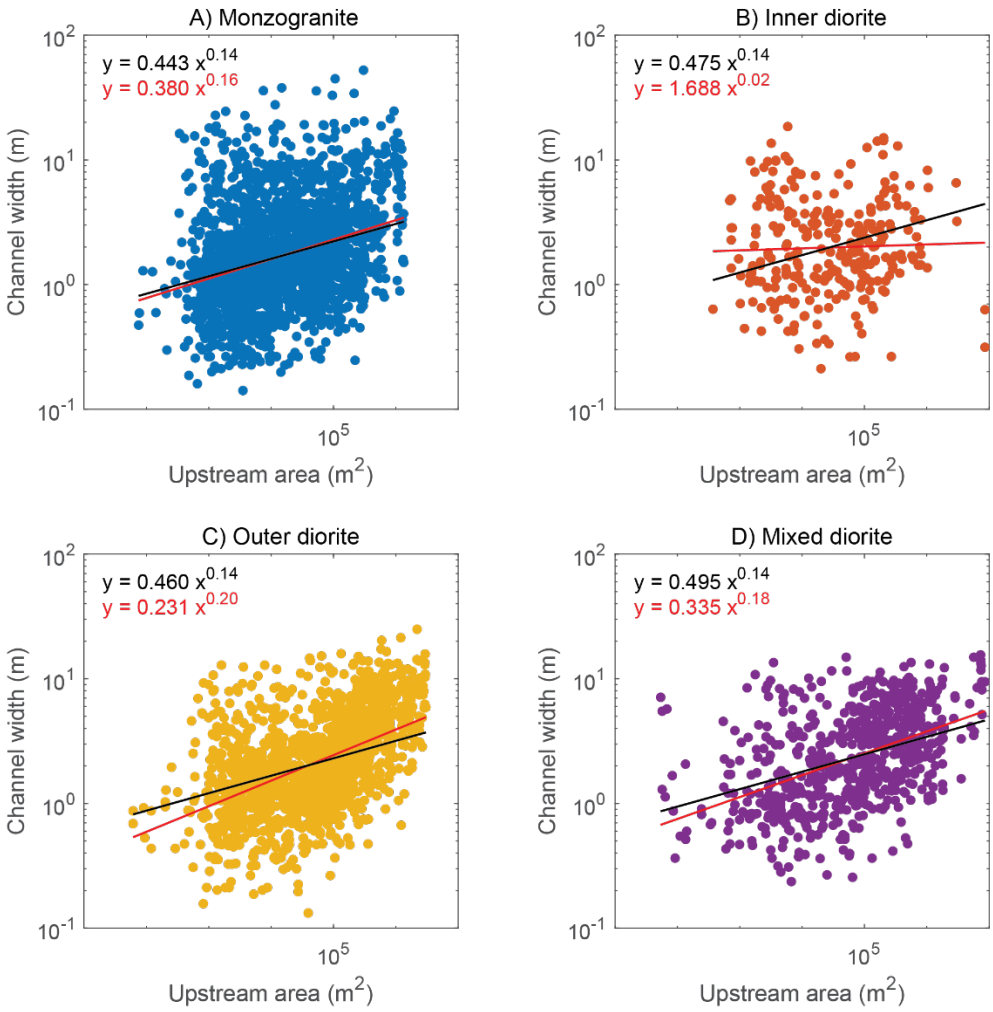

Figure 5.6. Channel widths plotted against upstream area for all three rock types including the mixed diorite area from Figure 5.1. The red lines and equations are fits with an unconstrained scaling exponent, and black lines and equations are fits with the scaling exponent fixed to 0.14, the mean of the unconstrained exponents.

5.5.2 Vegetation density

In our field surveys of vegetation (Figure 5.1, Figure 5.2), we recorded ~1.17 observations of vegetation (mostly cacti and shrubs, undifferentiated) per meter on a SSE-facing hillslope in the outer diorite, over ~350-meter survey. We recorded ~0.39 observations of vegetation per meter on a south-facing slope in the monzogranite over a ~208-meter survey, and ~0.54 observations of vegetation per meter on a WSW-facing slope

in the monzogranite over a ~198-meter survey. We did not conduct a vegetation survey in the inner diorite; however, remote sensing analysis encapsulates all three rock types. Remote sensing analysis supports our observation that vegetation density is higher in the diorites, but also shows that the distribution of vegetation is more complex and varies by species (Figure 5.7). The density of shrubs is higher in the diorites (Figure 5.7A), while the density of grass and herbs appears somewhat higher in the monzogranite (Figure 5.7B). Differences between the inner and outer diorites are difficult to resolve in the images, although the density of shrubs appears slightly higher in the inner diorite as compared to the outer diorite, with the opposite trend for grasses and herbs. The density of cacti appears to be roughly equal across rock types, with a slightly higher density in the monzogranite (Figure 5.7C).

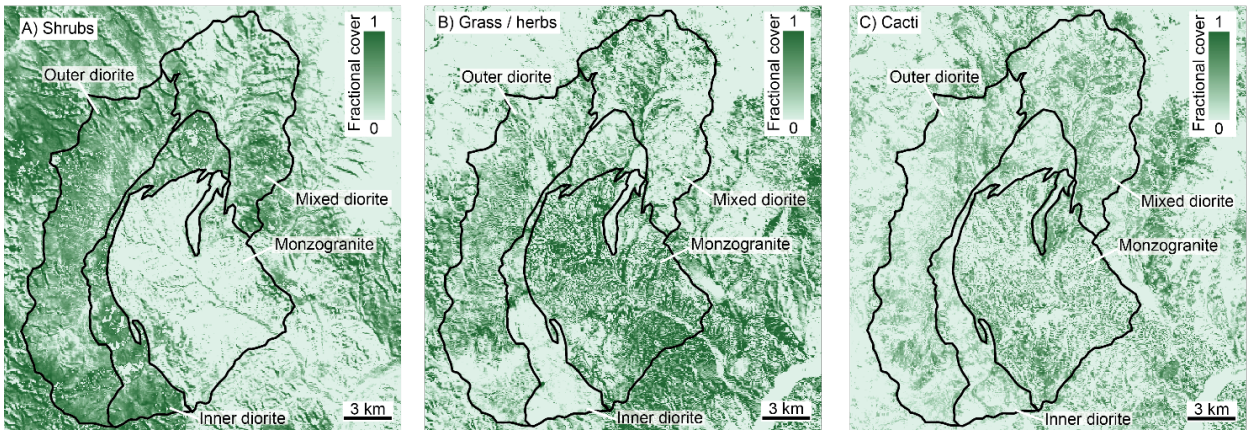

Figure 5.7. LANDSAT-based, pixel-wise fractional projective cover map for all landcover types. A) shrubs, B) grass and herbs, and C) cacti. The monzogranite area is indicated by the black outline and the diorite area lies above and to the left of the monzogranite.

5.5.3 Grain size measurements

Results from Wolman pebble counts show that, on average, the monzogranite has a smaller grain size for both hillslopes and stream channels than the diorites, and between the inner and outer diorite, the inner diorite has a larger grain size (Figure 5.8, Table 5.2 and Table 5.3). For all rock types, streams have the largest average grain size. The monzogranite has a mean hillslope grain size of just under 9 cm and a mean stream channel grain size of

just over 9 cm; the inner and outer diorites have mean hillslope grain sizes of nearly 29 cm and of 21 cm, respectively, and the stream channel shared by both diorites has a mean grain size of 27 cm. Mean, standard deviation, D16, D50 and D84 values are listed in Table 5.2. Testing with ANOVA shows that all three rock types have mean hillslope grain sizes that are significantly different from each (p-value of 8.65×10^{-22}), and the monzogranite and diorite streams have significantly different mean grain sizes (p-value of 3.31×10^{-16}). In contrast, surficial soil samples from the monzogranite have slightly larger grain size than the diorites, where 44% (by weight) of the combined monzogranite hillslope soil samples and 64% of monzogranite stream sediment has a grain size of over 1 mm in diameter, while only around one third of the inner and outer diorites have an average grain size of over 1 mm (Table 5.2). The diorites have similar soil grain size. Together, these data also show that most of the surficial sediment overlying the monzogranite falls within a narrower window of grain sizes, while the diorites have coarser and a larger spread of grain sizes.

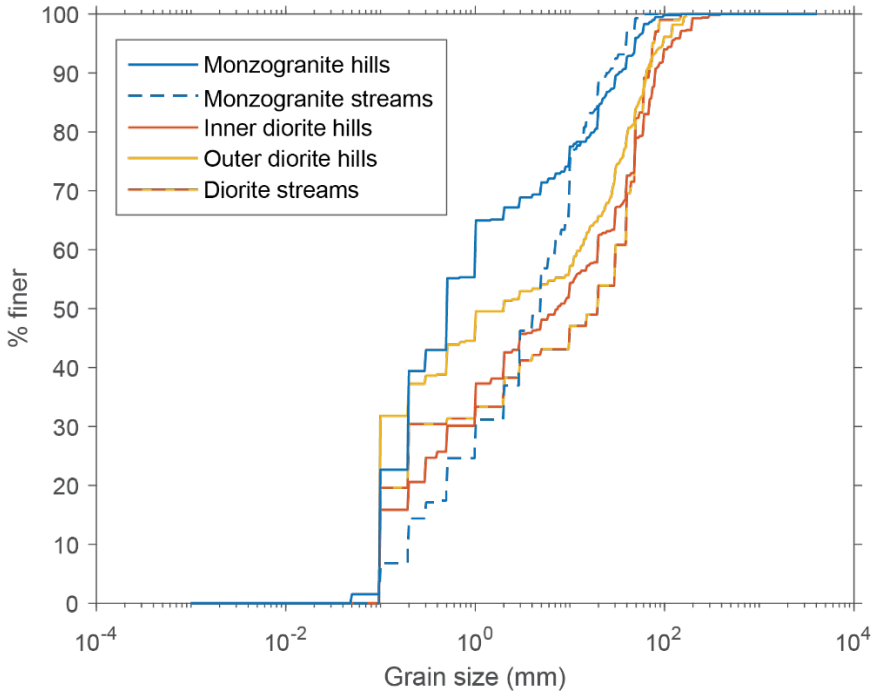

Figure 5.8. Sediment grain size cumulative distribution functions from grain size surveys of surficial sediment along hillslopes and streambeds in all rock types.

Table 5.2. Sediment and soil grain size data.

Grain size category	Monzogranite hillslope	Monzogranite stream	Inner diorite hillslope	Outer diorite hillslope	Diorite stream*
Sediment grain size data from Wolman pebble counts					
D16 (cm)	0.1	0.3	0.1	0.1	0.1
D50 (cm)	0.5	5.0	4.0	1.0	20.0
D84 (cm)	20.0	19.3	60.0	50.0	59.2
Mean (cm)	9.0	9.1	28.7	21.0	27.1
Standard deviation (cm)	17.8	12.2	47.2	33.9	29.7
Soil grain size sample from sieved bulk soil samples#					
>1mm	44%	64%	35%	33%	28%
0.25-0.5 mm	27%	22%	31%	35%	52%
<0.25 mm	29%	14%	34%	32%	20%

* The diorite stream contains sediment from hillslopes within both the inner and outer diorite. # Values shown are the percent of the total weight of the sample that falls into the grain size category shown on the left

Table 5.3. Summary of field and laboratory data.

		Monzogranite (M)	Diorite (combined) (D)	Inner diorite (ID)	Outer diorite (OD)	
Method	Unit	Mean / result	Mean / result	Mean / result	Mean / result	Significantly different means?*
Grain size (hillslope)	cm	8.96 ± 17.82	25.73 ± 42.79	28.67 ± 47.24	20.97 ± 33.92	Yes, ID largest, M smallest
Grain size (streams)	cm	9.08 ± 12.17	27.06 ± 29.68	--	--	Yes, D largest, M smallest
Bedrock porosity	%	1.00 ± 0.53	1.26 ± 0.59	1.31 ± 0.71	1.17 ± 0.33	No
Bedrock permeability	mD	1.65 ± 2.37	2.08 ± 4.12	0.50 ± 0.85	5.24 ± 6.60	No
Bedrock hydraulic conductivity	$m\ d^{-1}$ ($\times 10^{-3}$)	1.51 ± 2.17	1.91 ± 3.77	0.461 ± 0.775	4.80 ± 6.04	No
Soil infiltration rate (k_{sat})	$cm\ hr^{-1}$	11 ± 5.86	7.92 ± 2.06	6.9	8.26 ± 2.39	No
Crystal grain size	mm	1.08 ± 0.25	0.59 ± 0.14	0.56 ± 0.14	0.63 ± 0.14	Yes, M larger than D
Mineral point counting (bedrock)	Dominant minerals	+ Quartz, potassium feldspar	--	+ Plagioclase feldspar, amphibole, pyroxene, biotite	Composition between M and ID	N/A
XRD (bedrock)	Dominant minerals	+ Quartz, potassium feldspar	--	+ Plagioclase feldspar, amphibole, pyroxene	Composition between M and ID	N/A
XRF (bedrock)	Major oxides	+ SiO_2, K_2O	--	+ P_2O_5, CaO, MgO, Al_2O_3, TiO_2	Composition between M and ID	Yes, only significant results shown here
CIA (bedrock)	Percent	50.47 ± 1.20	45.16 ± 3.08	43.92 ± 2.41	48.88 ± 1.16	N/A
f_{reac}	fraction	0.26	0.06	--	--	N/A

*Significant differences were evaluated with ANOVA and multiple comparison tests.

5.5.4 Hydrological properties

Porosity, permeability, and hydraulic conductivity measurements conducted on bedrock samples from all three rock types show that the outer diorite consistently shows slightly higher values, while values for the monzogranite and inner diorite are similar (Figure 5.9A-C; Table 5.3). However, testing with ANOVA shows that there is no significant difference between the means of any of the three rock types. One diorite sample (SG34) has anomalously high permeability and hydraulic conductivity values, possibly due to the existence of a fracture, and thus is treated as an outlier. The spread of data for the outer diorite is larger, but only consists of three data points.

Minidisk infiltrometer measurements resulted in similar saturated hydraulic conductivities (a proxy for infiltration rate) for soils overlying the monzogranite and both diorites combined (Figure 5.9D; Table S5.1). Similarly, there is no significant difference between mean saturated hydraulic conductivities for any of the three rock types. Values for the diorites are combined in Figure 5.9 due to few measurement sites. Of the four measurement sites in the diorites, only one, G4, is within the inner diorite. G4 yielded a saturated hydraulic conductivity of 6.9 cm hr^{-1}, while the mean saturated hydraulic conductivity for the outer diorite sites is slightly higher at 8.26 cm hr^{-1} (Table 5.3). Two field sites for the monzogranite (M1 and M3; see Figure 5.1) yielded higher hydraulic conductivities than the other three, resulting in a slightly higher overall infiltration rate for the monzogranite (11 cm hr^{-1}). In contrast, the diorites' hydraulic conductivity measurements were less variable between sample sites.

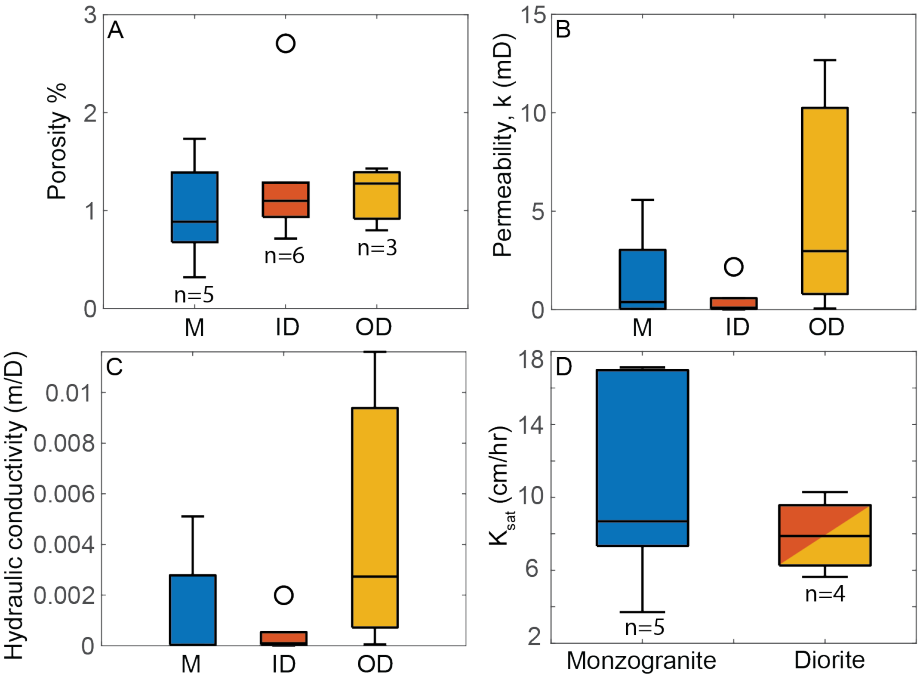

Figure 5.9. Results from hydraulic property measurements of the monzogranite and diorite rock types. A) Porosity, B) permeability, and C) hydraulic conductivity results for the monzogranite (M), inner diorite (ID) and outer diorite (OD) from bedrock cores. The number of samples measured for porosity, permeability and hydraulic conductivity is the same. D) Saturated hydraulic conductivity (K_{sat}), a proxy for infiltration rate, for the monzogranite and diorites. Box plots show the median (central mark), 25th percentile (bottom of the box) and 75th percentile (top of the box). The whiskers extend to the most extreme datapoints not considered outliers; outliers are indicated by open black circles.

5.5.5 Bedrock and soil composition, and weathering intensity

Point counting, XRD and XRF. Mineral point counting results show that, on average, the diorites have higher percentages of mafic minerals such as amphibole, pyroxene, and biotite, as well as plagioclase feldspar, while the monzogranite has higher amounts of quartz and potassium feldspars (Figure 5.10A; Figure 5.11). The outer diorite generally has a composition that lies between that of the inner diorite and the monzogranite; the inner diorite has more plagioclase feldspar and less orthoclase and quartz than the outer diorite, and pyroxene was identified in only the inner diorite. All rock types are altered, and many feldspar grains have been altered to secondary clays or micas, especially in the center. This is more common in the potassium feldspar in the monzogranite. Several of the thin sections

from the monzogranite have larger (>1 mm) crystal grains, mostly quartz and feldspar, floating in a matrix of fine-grained quartz and feldspar, occasionally also with secondary clays or micas. Excluding any fine-grained matrix, on average the crystal grain size (diameter) of the monzogranite is the largest, with an average diameter of 1.08 mm, as opposed to 0.59 mm for the inner diorite and 0.63 mm for the outer diorite. XRD measurements (Figure 5.10B) show differences between rock types that mostly align with point counting results compositionally; however, XRD measurements yield higher percentages of muscovite, sericite and clays, and lower percentages of orthoclase. For the monzogranite, a portion of the muscovite/sericite/clay and quartz percentage estimated by XRD could have been counted as "matrix" during point counting, leading to an underestimation of these categories in point counting results. In addition, due to the high degree of weathering in the samples, orthoclase may have been overestimated during thin section point counting.

XRF measurements of major oxides and trace elements show variation between the monzogranite, inner diorite and outer diorite compatible with their lithologies, and support expected values based on their mineralogical differences (Figure 5.10C, Table S5.2). Results (averaged across multiple samples, see Table 5.3 for values) from ANOVA and multiple comparison tests show that there are statistically significant differences between the means of the monzogranite and inner diorite and between the inner and outer diorite for K_2O, P_2O_3, CaO, and TiO_2, and between the monzogranite and inner diorite for SiO_2, MgO and Al_2O_3. Of the above listed oxides, the monzogranite has the highest values for SiO_2 and K_2O and the lowest values for P_2O_5, CaO, MgO, Al_2O_3 and TiO_2, as expected by the monzogranite's more felsic mineralogy. The inner diorite shows the opposite trend, with the lowest values of SiO_2 and K_2O and the highest values for P_2O_5, CaO, MgO, Al_2O_3 and TiO_2. In no case is there a significant difference between the monzogranite and the outer diorite; this may be partially due to the small sample size for XRF measurements for the outer diorite (3 samples). Based on Eq. (5.8), we also obtained CIA values (averaged across all samples for each rock type) of 50.47 for the monzogranite, 43.92 for the inner diorite, and 48.88 for the outer diorite (Tables 3 and S5.2), indicating that the monzogranite has experienced the highest degree of weathering, followed by the outer diorite, and that the

inner diorite is the least weathered. These values are similar to typical values for granites and granodiorites, which range from ~45-50 (Nesbitt and Young, 1982).

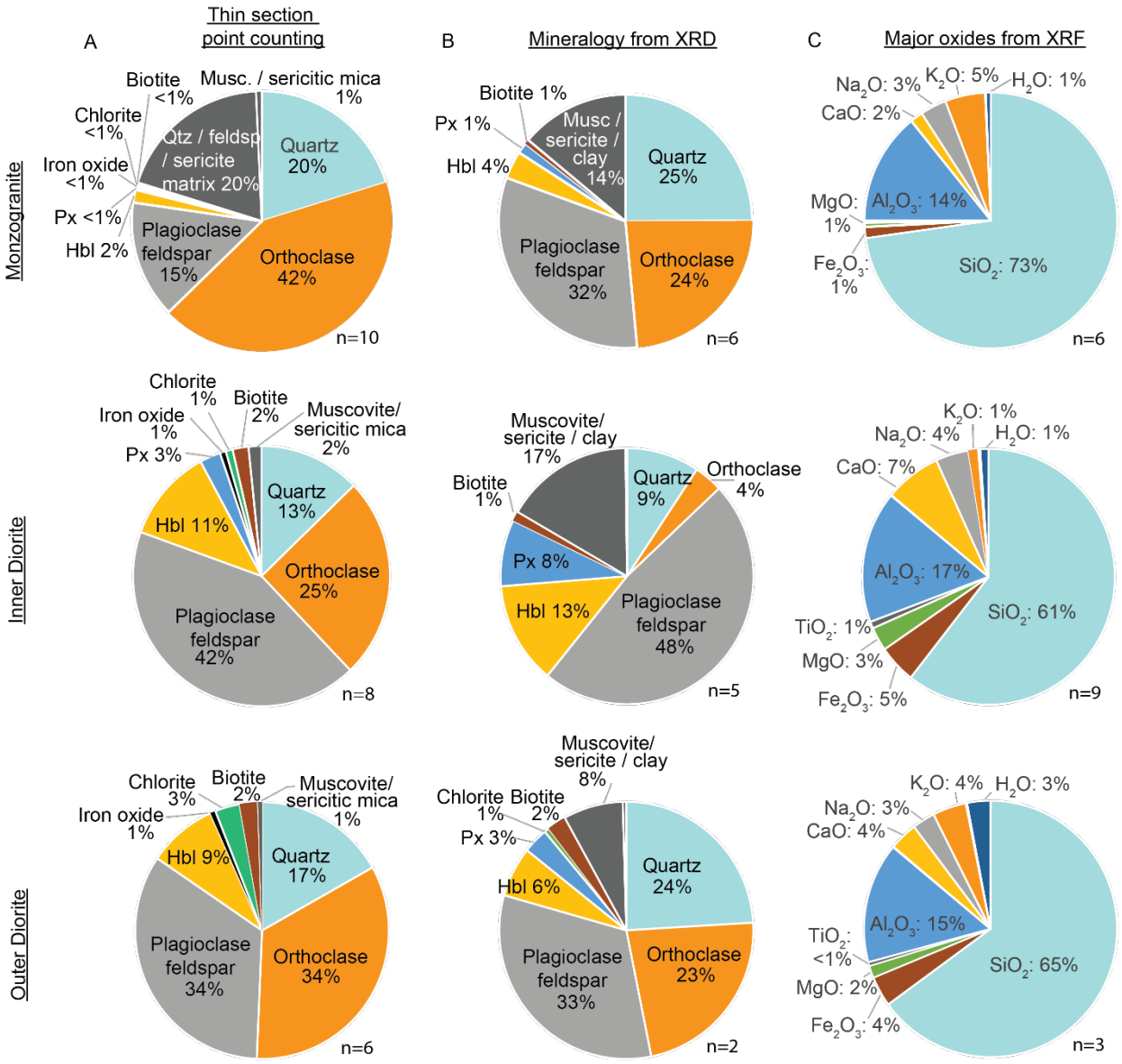

Figure 5.10. Bedrock compositional results for the monzogranite (top row), inner diorite (middle row), and outer diorite (bottom row): A) thin section point counting; B) mineralogy from XRD; C) major oxides from XRF. Px = pyroxene; Hbl = Hornblende; Musc = muscovite; Qtz = quartz; Feldsp = feldspar. Results from all measured elements are provided in Table 5.3.

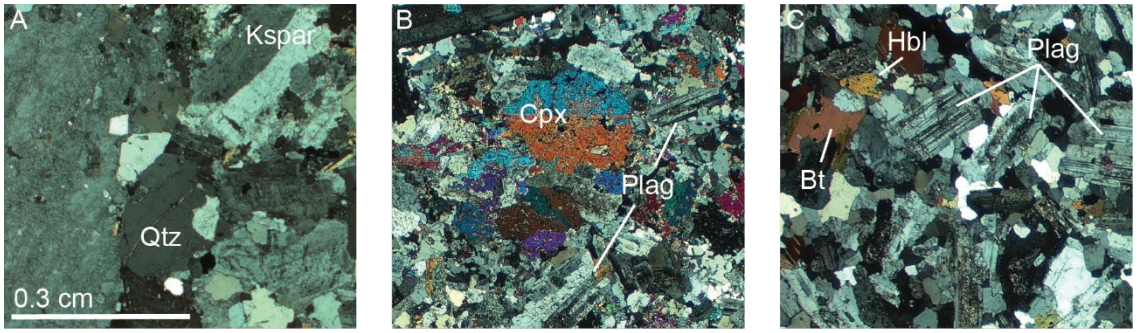

Figure 5.11. Typical thin section photomicrographs from each rock type, using the same scale. A) Monzogranite (sample EL20-SG3 from Cactus Hill), B) Inner diorite (sample EL20-SG43 from Zebra Hill), C) Outer diorite (sample EL20-SG33 from Drill Hill). Kspar = potassium feldspar / orthoclase, Qtz = quartz, Cpx = clinopyroxene, Plag = plagioclase feldspar, Bt = biotite, and Hbl = hornblende.

Sequential chemical extractions. Weathering intensity (f_{reac}) obtained from the reactive and mineral-bound concentrations of ^{9}Be measured from stream sediment samples (Eq. 5.7) is relatively higher for the monzogranite, with a value of 0.26, and lower for the diorite, with a value of 0.06. Together with the higher CIA values for the monzogranite, these proxies indicate a higher degree of weathering intensity for the monzogranite relative to the diorites (Table 5.3).

In contrast, exchangeable (plant-available, e.g., Uhlig et al., 2020) element concentrations of the plant-essential nutrients calcium, iron, potassium, and magnesium are slightly higher for the diorite than for the monzogranite (Table S5.3). Although we were unable to measure phosphorus in the sequential chemical extractions from our soil samples, XRF results from bulk bedrock show that the diorite has double the amount of phosphorus oxide compared to the monzogranite (2% vs. 1%).

5.5.6 In situ ^{10}Be-derived denudation rates

Our new ^{10}Be concentrations are similar between rock types, suggesting similar denudation rates, because of the limited relief in the catchment and therefore the similar production rates (Table S5.4). When considering calculated denudation rates, we hereon

include previously published denudation rates from Lodes et al. (2023) (7 samples from the outer diorite and 3 samples from the inner diorite). Denudation rates are shown in Figure 5.12. In general, denudation rates are similar between the monzogranite (~3-12 m Myr^{-1}) and the inner diorite (~3-9 m Myr^{-1}) and are slightly higher for the outer diorite (~8-21 m Myr^{-1}). In the monzogranite, we calculated denudation rates for hillslope soil, sediment, and small clast samples ranging from ~5-12 m Myr^{-1}, and a similar, and slightly lower range of denudation rates for boulders of ~3-12 m Myr^{-1}. The only sample consisting of very large boulders from the monzogranite (protruding ~1m) contributed the low denudation rate of ~3-5 m Myr^{-1}, while the other boulder samples have denudation rates ranging from 7-12 m Myr^{-1}. The denudation rates for the two stream sediment samples from the monzogranite range from 6 to 13 m Myr^{-1}. In the diorites, considering data from Lodes et al. (2023), denudation rates for soil and sediment range from 6.5-9 m Myr^{-1} for the inner diorite and from 12-21 m Myr^{-1} for the outer diorite, while denudation rates for hillslope boulders range from 3-5 m Myr^{-1} for the inner diorite and from 10-20 m Myr^{-1} for the outer diorite. Meteoric denudation rates are included in Appendix 5A.

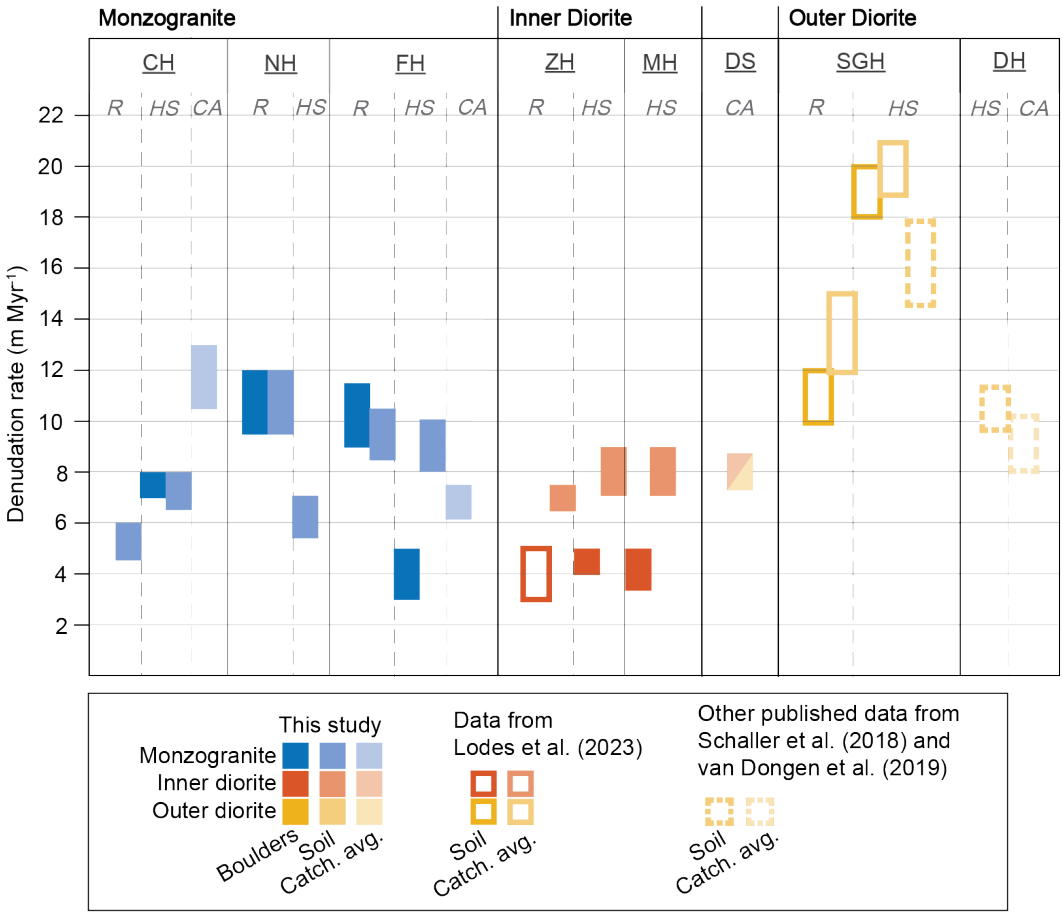

Figure 5.12. Overview data from this study and previously published in situ denudation rates. Data from this study are shown by solid symbols and previously published data are shown by hollow and dashed symbols as indicated in the legend. Soil pit data is from Schaller et al. (2018), and catchment average data is from van Dongen et al. (2019). Data are shown as a range with the error included in vertical extent of the symbol for simplicity and to match results from Lodes et al. (2023). Denudation rates for each location within a field site are separated by thin gray bars, and locations are labeled at the top of the chart. CH = Cactus Hill, NH = Naked Hill, FH = Flag Hill, ZH = Zebra Hill, MH = Mine Hill, DS = Diorite Stream, SGH = Santa Gracia Hill, and DH = Drill Hill. DS contains sediment from hillslopes in both the inner and outer diorites. R = sample from a ridge, HS = sample from a hillslope, and CA = catchment average sample from stream sediment. In the legend, Catch. Avg. = catchment average.

5.6 Discussion

5.6.1 Morphological differences due to rock type

5.6.1.1 Drainage density and channel heads

As predicted by our field observations, the monzogranite has a significantly higher drainage density than the diorites. Between the diorites, the inner and mixed diorite areas have slightly lower drainage densities than the outer diorite; however, in contrast, the inner diorite has a slightly lower L_c value than the outer diorite (Table 5.1). As a result, we consider drainage density values and other topographic metrics to be relatively similar between the inner, outer, and mixed diorite areas, but different from the monzogranite. Our drainage density results are within the range of published drainage densities that were calculated in a similar way, from catchments with similar climates and lithologies. For example, Sangireddy et al. (2016) published a large dataset of drainage density values for sites with variable climate, vegetation cover, and lithology, also calculated using GeoNet. These authors did not find any significant correlation between drainage density and lithology; instead, they reported a negative correlation between drainage density and vegetation cover, and a negative correlation between drainage density and precipitation that changes to a positive correlation at MAP >1000 mm yr^{-1}. However, the range of values for plutonic rocks in Sangireddy et al. (2016) is similar to the range we observe, even though climate is constant in our case, whereas the plutonic landscapes in Sangireddy et al. (2016)

have MAP that ranges from 150-650 mm yr^{-1}. Our drainage density values are also within the range of those measured by Perron et al. (2009), who measured valley spacing in five field sites across different climate zones with unconsolidated and sedimentary bedrock lithology (Figure 5.13).

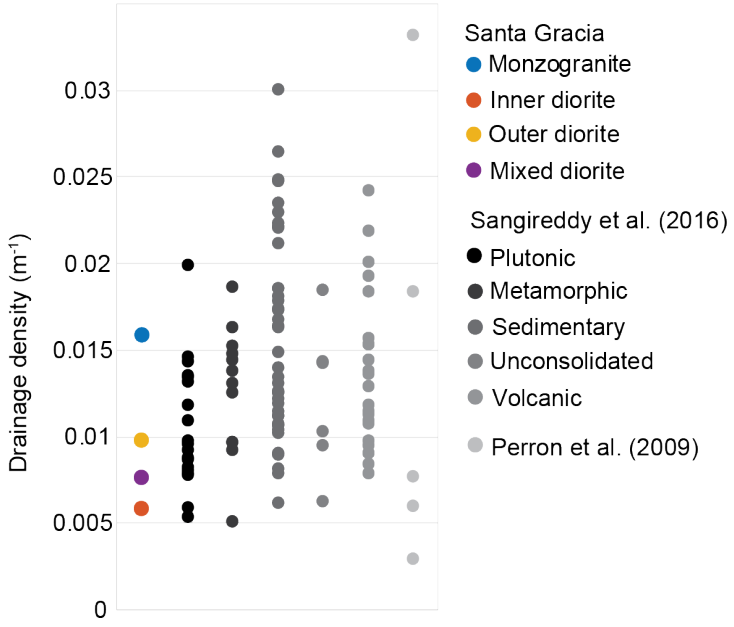

Figure 5.13. Comparison of drainage density value from this work to previously published values from Sangireddy et al. (2016) and Perron et al. (2009), chosen because they were calculated in a similar way.

A landscapes' drainage density is intimately linked to the density of channel heads, or, similarly, the drainage area at channel head locations. Our analysis yielded several estimates of this area. First, inflection point in slope area plots (Figure 5.3B), which represent the point of transition from diffusion-dominated hillslope processes to runoff-dominated fluvial processes (Willgoose et al., 1991; Tucker and Bras, 1998) or the point where the two processes are equally effective in transporting sediment (Howard, 1997), occur at a smaller drainage area for the monzogranite (10^2-10^3 m^2) and larger drainage area for the diorites (10^3-10^4 m^2). Second, the median upstream area of the GeoNet-derived channel heads is also smaller for the monzogranite at 36.4 m^2, and larger for the inner, outer and mixed diorites at 128.1, 88.4 and 105.2 m^2. Finally, the square of the characteristic length scale L_c (Eq. 5.2; L_c^2), which is approximately equivalent to the drainage

area at which the transition from diffusive hillslope to fluvial incision processes occurs, is lower for the monzogranite at 58.50 m^2 and higher for the inner, outer, and mixed diorites at 93.56 m^2, 105.57 m^2 and 125.02 m^2 respectively. Although each of these approaches gives slightly different values, the pattern remains the same, where the monzogranite always has the smallest upstream area. We note that these differences in drainage density and channel head density/drainage area come along with lower *D/K* for the monzogranite (Eq. 5.2) compared to the diorites, but it is not yet clear if this is due to rock type-related differences in *D* or *K* or both.

5.6.1.2 Channel steepness, concavity, and width

The normalized channel steepness index (k_{sn}; Table 5.1) has been shown to increase with uplift rate (Kirby and Whipple, 2012; Kirby et al., 2003, 2007; Tarboton et al., 1989) and decrease with erodibility (Hack and Hack, 1957; Hack, 1973; Cyr et al., 2014). The k_{sn} value for the monzogranite (0.79) is much lower than the values for the diorites, which range from 1.10 to 1.76 (Table 5.1). As uplift rates are equal between rock types in Santa Gracia, differences in k_{sn} must indicate that the monzogranite bedrock experiences higher runoff or is more erodible.

Concavity indices for all three rock types in Santa Gracia are positive, indicating concave-up channel longitudinal profiles. However, at values of ~0.2-0.3, they are relatively low, indicating that all three rock types have relatively straight channels, but are within the range of published values for other semi-arid and arid landscapes (Harel et al., 2016). The monzogranite channels are even less concave than the diorites (Table 5.1), suggesting a potential lithological control on concavity. There are several possible reasons for relatively straight channels in Santa Gracia; however, it is more difficult to interpret the differences in concavity between the rock types. In general, relatively straight channels have been observed in steep headwater catchments subject to debris flows (Seidl and Dietrich, 1992; Stock and Dietrich, 2003), but this explanation can be ruled out for Santa Gracia. Alternatively, in the tool-cover model of Turowski et al. (2021), concavity depends on the relationship between fluvial bedload and catchment size. If the bedload fraction remains constant along flow, which is expected for crystalline rock with rare floods and little abrasion (which we assume is the case for all rock types in Santa Gracia), concavity values

are lower (Turowski et al., 2021). Finally, river incision models predict that when uplift and lithology are uniform along the channel (as is the case in Santa Gracia), the concavity index is strongly influenced by relative rates of downstream increase in discharge versus channel width (Whipple, 2004; Whipple and Tucker, 1999), as well as incision thresholds (Lague et al., 2005; Tucker, 1999). Therefore, differences in concavity between rock types in Santa Gracia may point at differences in either discharge-channel width relationships, or possibly resistance to incision (erodibility).

Channel width (Figure 5.6) plays a large role in dictating the energy expenditure of flowing water on its bed (Bagnold, 1977). At a given discharge, narrower channels focus more erosive energy onto a smaller area of the channel, facilitating more rapid downward incision, and are typically associated with areas of increased slope or uplift rate (e.g., Duvall et al., 2004; Fisher et al., 2013). As a result, we would expect to observe slightly narrower channels in the diorites, where channel and hillslope angles are slightly steeper. Uplift rates are the same in all rock types in Santa Gracia; however, there must be some underlying differences in the diorites that cause the steepening of hillslopes and channels, and that could (in theory) also cause channels to narrow. This could be a lower degree of erodibility for the diorites, or lower surface runoff due to vegetation-induced infiltration (see section 5.6.4.1). However, normalized channel width values (k_{wn}) are similar between all rock types (Table 5.1). Therefore, we can rule out channel width as a result of increased erosional efficiency in Santa Gracia. It is possible that characteristics of the diorites that could narrow channel widths and increase slopes, such as higher infiltration rate or lower erodibility, are compensated for by the steepening of hillslopes and channels alone, and therefore channel widths need not adjust. In addition, the similarity in channel widths between rock types in Santa Gracia indicates that the differences in concavity are not due to the relationship between discharge and channel width but are rather due to differences in erodibility between rock types.

5.6.2 Spatial patterns in denudation rates

In Figure 5.12, we show *in situ* denudation rates for our new samples together with published ^{10}Be-derived denudation rates for the diorites, which consist of boulder and soil denudation rates from Lodes et al. (2023), catchment average denudation rates from van

Dongen et al. (2019) and soil denudation rates from Schaller et al. (2018). Generally, denudation rates are similar between all rock types in Santa Gracia; however, between denudation rates, there exist some variations between sample types. In the diorites, where larger boulders exist, boulder denudation rates are lower than soil denudation rates, whereas in the monzogranite, where boulders are sparse and smaller, the smaller boulders that we sampled tend to have similar denudation rates to the surrounding soil.

Overall, denudation rates range from ~3-13 m Myr^{-1} in the monzogranite, from ~3-15 m Myr^{-1} in the inner diorite, and from ~8-21 m Myr^{-1} in the outer diorite. Denudation rates from Santa Gracia Hill in the outer diorite are somewhat higher and more variable in between the ridge and hillslopes compared to denudation rates from Drill Hill in the same rock unit, where catchment average and soil pit denudation rates are ~8-10.5 m Myr^{-1}, after van Dongen et al. (2019) and Schaller et al. (2018). These values are similar to denudation rates from the monzogranite and inner diorite, and to the catchment average denudation rate of the Diorite Stream (~8 m Myr^{-1}), which drains both the inner and outer diorite. Considering only *in situ* catchment average denudation rates, we find that all rock types show similar ranges in denudation rates that together center around ~9 m Myr^{-1}. In summary, we consider denudation rates to be similar between the different rock types, with Santa Gracia Hill depicting a locally elevated denudation rate that is likely not representative for the outer diorite as a whole. Subtle deviations of boulder and soil denudation rates are likely related to the effect of grain size on surface residence times (Lodes et al., 2023). Furthermore, the similarity between our denudation rates and the lack of major knickpoints in the drainage network supports our assumption that the landscape in Santa Gracia is approximately in equilibrium with the tectonic forcing. Finally, our results are consistent with findings from Howard (1997) and Tucker and Bras (1998) that drainage density is independent of denudation rate.

5.6.3 Estimates of soil diffusivity (*D*) and stream erosivity (*K*)

The results from our morphological analysis together with our denudation rate estimates allow us to obtain further constraints on the actual values of *D* and *K*. Based on the stream power model and combined with an assumed uniform denudation rate of 9 m Myr^{-1}, we can estimate *K* from $E = K\, k_{sn}^{n}$ (e.g., Ouimet et al., 2009), and thus *D* from our

morphology-derived *D/K* ratios. As a result, we obtained pronounced differences in stream erosivity *K*, but rather similar soil diffusivities *D* between the monzogranite and the diorites. In particular, the inner and outer diorites are surprisingly similar in *K*, with values that are distinctly lower than in the monzogranite. The mixed diorite on the other hand has both lower *K* and *D* values than all other rock types. These results indicate that the differences in drainage density that we observe between the monzogranite and the diorites are mostly related to differences in stream erosivity, and not to differences in soil diffusivity.

Table 5.4. Calculations of diffusion and advection parameters

Rock type	q_{ref}	k_{sn} ($m^{0.48}$)	E (m Myr^{-1})	D/K (m^{2m+1})	D (m^2s^{-1})	$K = E/k_{sn}$ ($m^{-2m+1}s^{-1}$)
Monzogranite	0.24	0.7872	9	41	468.75	11.43
Inner diorite	0.24	1.1048	9	57	464.34	8.15
Outer diorite	0.24	1.1061	9	63	512.61	8.14
Mixed diorite	0.24	1.7565	9	71	363.79	5.12

5.6.4 Measured parameters that can influence stream erosivity in Santa Gracia

In the remainder of the discussion, we will use results from our field and laboratory data to constrain the processes and landscape characteristics that could explain the different stream erosivity (*K*) values in the rock types. We break these into two categories: first, parameters that influence runoff, where lower infiltration results in higher runoff and will increase *K* (e.g., Kirkby, 1980; Dietrich et al., 1992; Dietrich and Dunne, 1993), and second, parameters that influence substrate erodibility, where a weaker or more easily erodible substrate increases *K* (e.g., Reid, 1989; Prosser and Dietrich, 1995). Substrate erodibility is further broken into two parts, weathering extent and mineralogy, and grain size. Because the monzogranite has a higher *K* value, we would expect more runoff due to less infiltration and/or higher erodibility than in the diorites.

5.6.4.1 Infiltration capacity and vegetation cover

We measured several hydraulic properties to detect possible differences in infiltration capacity for each rock type, including infiltration rates for soils in the field, and porosity, permeability and hydraulic conductivity for bedrock cores in the lab. However, we were not able to resolve any significant differences based on our measurements for any of the hydrological properties (Figure 5.9; Table 5.3). The similar bedrock properties suggest that the unaltered bedrock behaves hydrologically similarly, which is not unexpected. Yet, the similarity of the infiltration rates was surprising to us. Although these findings may suggest that systematic differences in infiltration rates are unlikely, we are hesitant to dismiss this scenario due to the influence of vegetation, which shows some marked differences between the rock types (Figure 5.7), but where we did not conduct any infiltration measurements. Additionally, our infiltration measurements could be skewed by goat traffic (Minea et al., 2022), which is high in Santa Gracia. We conducted infiltration measurements in between plants, where goats trample on soil, which leads to soil compaction (Donovan and Monaghan, 2021), and thus reduces infiltration capacity (Cerdà et al., 1998; Gifford and Hawkins, 1978; Kidron, 2016; Proffitt et al., 1993).

In arid regions, water is the principal limiting ecological factor (Ehleringer 1985, Smith et al. 1998), and soil condition and hydrological behavior affect infiltration and moisture available to plants (Hamerlynck et al., 2002; Noy-Meir, 1973; McAuliffe, 1994). The denser shrub cover in the diorites (Figure 5.7A) could thus be interpreted as an indicator for increased soil water, as compared to the monzogranite. On the other hand, the growth and decay of roots in soil creates cavities that increase infiltration rates (Logsdon and Allmaras, 1991; Oswald et al., 2008; Zhu et al., 2022), and by intercepting rainfall and accessing soil moisture, they reduce the amount of water available for runoff (e.g., Branson and Owen, 1970; Castillo et al., 1997; Zuazo et al., 2004; Puigdefábregas et al., 2005; Bochet et al., 2006; Ibarra et al., 2019). Plant type also influences the amount of infiltration and groundwater storage. Shrubs are denser in the diorites, while cacti and grasses are relatively similar between rock types (Figure 5.7B-C). Whereas cacti and grasses have shallow root systems that extend less than 0.5 m into the subsurface (Noy-Meir, 1973; McAuliffe et al., 2022), shrubs in semi-arid Chile can have roots that extend deeper than 1 m to access

deeper soil water (Muñoz et al., 2008), as well as an extensive and dense horizontal root system (Noy-Meir, 1973). An additional cause for denser shrub cover in the diorites may be the higher concentrations of the exchangeable fraction of the plant-essential nutrients P, Ca, Fe, K and Mg as compared to the monzogranite (Table S5.3). Studies have shown that bedrock geochemistry can limit plant growth through plant essential nutrient limitations (e.g., Neff et al 2006, Morford et al 2011; Porder and Ramachandran 2012; Hahm et al., 2014; Callahan et al., 2022). Therefore, we suspect that the higher vegetation cover in the diorites is both an expression of more soil moisture and a cause for greater infiltration and less surface runoff compared to the monzogranite, aided by higher concentrations of plant-essential nutrients.

5.6.4.2 Substrate erodibility

5.6.4.2.1 Weathering extent and mineralogy

Weathering causes bedrock to disintegrate into smaller pieces that are easier to remove by concentrated surface runoff. This can be achieved either through chemical weathering, that is, the dissolution of primary minerals and conversion to secondary minerals such as clays, or through physical weathering, such as fracturing by thermal stresses (e.g., Eppes and Keanini, 2017). The mineralogical composition of the diorites (higher percentages of plagioclase feldspar, biotite, amphibole, and pyroxene; Figure 5.10) suggests that they should be subject to faster chemical weathering rates. For example, plagioclase feldspar is known to weather more rapidly than potassium feldspar (Banfield and Eggleton, 1990; Blum and Stillings, 1995; Nesbitt et al., 1997), and biotite is one of the first minerals to weather in granitic rocks. In addition, the weathering of iron-II bearing minerals, such as biotite, can initiate positive feedback by producing iron-III bearing clays and oxyhydroxides, whose crystallization inflicts pressure that can lead to cracks, increasing porosity and further weathering (e.g. Hayes et al., 2020; Anovitz et al., 2021; Hampl et al., 2022). Our data and observations from bedrock thin sections and XRD show a similar amount of weathering products (clays and oxides) in all rock types, suggesting that bedrock from all rock types has experienced a similar degree of weathering (Figure 5.10). However, calculated proxies for the degree of weathering (CIA and f_{reac}; Table 5.3) are all higher for the monzogranite, indicating a higher degree of weathering in the monzogranite's bedrock

soils and suggesting that the monzogranite experiences a higher degree of solubilization from the primary minerals.

The monzogranite's higher degree of weathering could stem from its coarse crystals and high quartz content, which may increase its vulnerability to physical weathering by solar insolation: the semi-arid climate in Santa Gracia likely causes heat-related stresses and subcritical cracking due to changes in daily temperature and stresses from solar insolation (Eppes and Keanini, 2017). Furthermore, lithologies with coarser crystal grain sizes have been shown to experience a higher degree of thermal stress than rocks with finer crystal sizes that leads to granular disaggregation and cracking along crystal grain boundaries (Gómez-Heras et al., 2006; Eppes and Griffing, 2010; Aldred et al., 2016), and matrix cracking can extend to greater depth in bedrock with coarser crystals, enhancing secondary porosity formation (Goodfellow and Hilley, 2022). In particular, quartz grains cause damage to the crystal lattice when heated and cooled due to their anisotropic coefficient of thermal expansion (Gomez-Heras et al., 2006; Hall et al., 2008; Eppes and Griffing, 2010). In summary, despite having fewer highly soluble minerals, the monzogranite's large crystal grain size and higher quartz content could ultimately increase weathering intensity, erodibility, and *K*.

5.6.4.2.2 Hillslope and stream sediment grain size

Hillslope and stream sediment grain size differences between the monzogranite and the diorites could influence erodibility and increase the *K* value of the monzogranite, as very large grains can raise thresholds for channel incision, while transportable grains can act as tools for incision (e.g., Turowski et al., 2007; Neely and DiBiase, 2023). The monzogranite has a smaller and more uniform grain size on its hillslopes and in channels, with smaller grain sizes measured with Wolman pebble counts, and a smaller quantity of very fine (<0.25 mm) sediment sieved from soil and stream sediment samples (Figure 5.8, Table 5.2, Table 5.3). Although we do not have discharge estimates for Santa Gracia, due to the low annual rainfall (88 mm yr^{-1}; Meyer-Christoffer et al., 2015), we assume that discharge is on average low in Santa Gracia, and therefore, large (i.e., >50 cm) grain sizes are probably only transported during large storms. As a result, the smaller and more uniform grains in the

monzogranite's streams may be more useful as tools for abrasion and fluvial incision (Turowski et al., 2007), thereby increasing *K*.

In addition, Turowski et al. (2023) suggested that the ratio of bedrock crystal grain size to the size of an "impactor grain" in fluvial bedload can influence erodibility by abrasion: if impactor grains are much larger than crystal grains, the impact energy is distributed over multiple crystal grain boundaries, which reduces the impact on any particular boundary, whereas if the impactor grains are smaller than the crystals, the likelihood of hitting a grain boundary diminishes. Therefore, erodibility is predicted to be higher where the crystal and impactor grain sizes are similar (Turowski et al., 2023). Since the monzogranite has smaller and more uniform sediment grain sizes, or impactor grains (about half of the sieved sediment and soil has a particle size >1 mm and half is <1 mm; Figure 5.8, Table 5.2, Table 5.3) and larger crystal grain sizes (on average, slightly over 1 mm in diameter; Table 5.3), impactor and crystal grain sizes are indeed similar, and fluvial erodibility as predicted by Turowski et al. (2023) could be higher for the monzogranite, further in alignment with its higher *K* values.

In contrast, in streams of the diorites, larger sediment grain sizes could act to move the transition to fluvial sediment transport to a lower hillslope position, due to grainsize-dependent fluvial incision thresholds and the capacity of streams to entrain and transport sediment in fluvial networks (Neely and DiBiase, 2023). Our sieved bulk soil and stream sediment samples show that the diorites also have a higher abundance of very fine (<0.25 mm) soil grains, possibly due to the smaller crystal grain size (Table 5.2; Figure 5.11); regardless, this grain size is likely too small to act as a tool to incise channel beds (e.g., Turowski et al., 2007). On the diorites' hillslopes, the relatively larger sediment grain size and longer residence time (lower denudation rates) for boulders on hillslopes in the diorites (Figure 5.12; see section 5.6.2), along with the higher abundance of deeply rooted shrubs (Figure 5.7; see section 5.6.4.1), may act together to armor hillslopes and increase hillslope roughness (DiBiase et a., 2017). Plant roots can strengthen the soil surface, thereby prevent small flows from exerting enough shear stress to erode the underlying soil, i.e., raising the threshold for fluvial incision (Prosser and Dietrich, 1995). Taken together, larger boulders and shrubs could block soil from creeping down the hillslopes in the diorites and thereby

decrease *D*. However, as our estimated soil diffusivity, that is, the efficiency with which the soil creeps down the hill, is similar between rock types (Table 5.4), it is possible that higher slope angles in the diorites (Figure 5.3C) compensate for the stabilizing vegetation cover, keeping *D* values similar between rock types.

5.6.5 Synthesis and implications for landscape evolution

In summary of the above discussion, we suggest that drainage density is higher in the monzogranite primarily due to a greater efficiency of stream incision, caused by higher runoff and greater erodibility (Figure 5.14). Our results further indicate that the monzogranite's higher runoff is a result of lower rainwater infiltration rates due to lower vegetation density, which is in turn a consequence of the relatively lower amount of plant-essential nutrients in the monzogranite bedrock compared to the diorite. The monzogranite's greater erodibility is likely in part a result of more intense physical weathering, which is due to the thermal expansion and contraction of the relatively higher abundance of quartz grains in the monzogranite, induced by solar isolation. This induces grain-by-grain erosion and leads to a small and more uniform distribution of sediment grain sizes. As a result, the monzogranite's smaller sediment grains are easier to transport by surface runoff and act as tools to incise channels. Therefore, we consider both the geochemical composition and the crystal grain size of the monzogranite and the diorites as the key factors at the beginning of a chain of processes that ultimately cause differences in drainage density.

It is important to note however, that in our reasoning, we are connecting observations that are influenced by processes that are acting on different time scales and that are likely to change with time. For example, the differences in vegetation cover between the monzogranite and the diorites could have been stronger or weaker in the past. The climate in Chile was wetter and cooler during the LGM (Starke et al., 2020; Mutz et al., 2018; Mutz and Ehlers, 2019), providing conditions which can lead to increased vegetation cover and potentially enhanced or reduced differences in vegetation density between the monzogranite and the diorites. We also acknowledge that physical characteristics measured in this study developed over different timescales. Denudation rates have integration time periods of thousands of years, the current vegetation patterns likely formed over tens to

hundreds of years, and infiltration rates are an instantaneous measurement that may change during rainstorms. Such timescale differences are difficult to bridge with the available methods.

On the other hand, the very low denudation rates in Santa Gracia (<10 m Myr^{-1}; Figure 5.12) document that the landscape (total relief of ~1 km) has evolved at a slow rate and over millions of years. Significant climatic changes typically occur on orbital time scales, like the 100-kyr cycles between glacial and interglacial periods, over which time Santa Gracia's topography changes, on average, by less than 1 m. Therefore, the topography we observe today must represent the integrated product of many climate cycles. In contrast, the bedrock composition of the monzogranite and the diorite has remained constant over the last several million years; therefore, we expect that, although the relative differences between rock types may have been stronger or weaker at certain points in the past, the differences have persisted over time and the topography we see now represents the average of these changes. We acknowledge that in other semi-arid landscapes, recent land use change and/or aridification may have caused more drastic changes in landscape morphology, such as the development of arroyos and gully erosion (e.g., Valentin et al., 2005), which could overprint and obscure any lithological influences. Intensive goat farming in Santa Gracia can also have a visible impact on the morphology if it continues long enough. The limited impact so far, is likely due to the low overall denudation rates.

Finally, although we quantified many rock properties, topographic characteristics and even surface processes that we consider relevant for stream incision and soil diffusion, our reasoning about the influence of rock type on nutrient supply, vegetation cover and its role in controlling infiltration and runoff remains rather qualitative, due to the obstacles of bridging time scales and the effects of recent land use. Nevertheless, if the causal chain that we laid out in our discussion proves to be true, it provides an example of how relatively subtle differences in rock type can have a significant impact on landscape morphology via the biota, without any difference in climate.

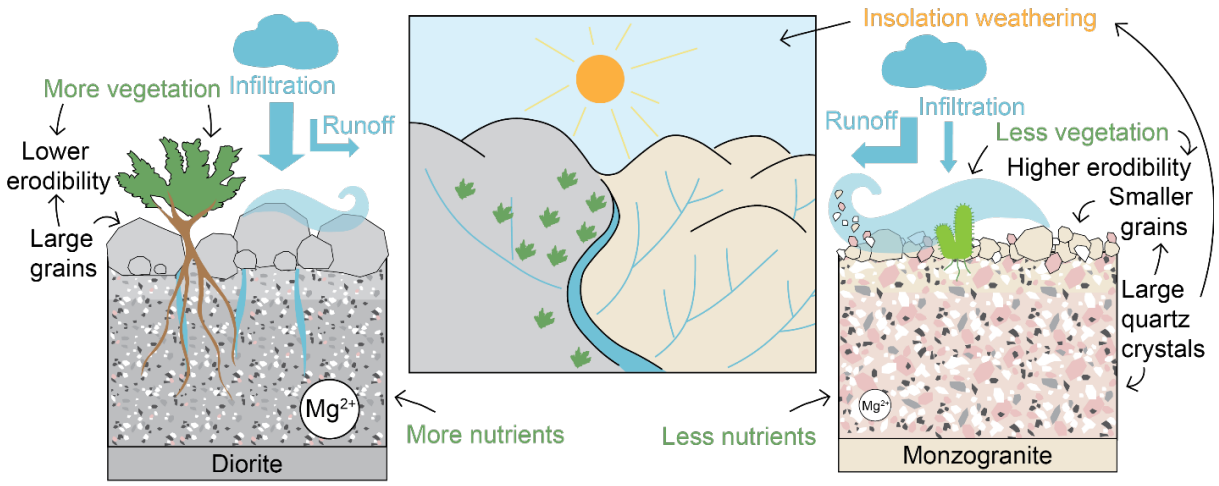

Figure 5.14. Summary figure showing how the mineralogy and geochemistry of the monzogranite and diorite bedrock influences plant growth, infiltration, weathering, and erodibility differences between the two rock types, which in turn influences the drainage density of the landscape.

5.7 Conclusions

The catchment of the Santa Gracia Preserve in central Chile hosts a suite of different plutons, a monzogranite and several diorites, that are characterized by different drainage densities. Topographic analysis of high-resolution LiDAR data shows that the significantly higher drainage density in the monzogranite corresponds to lower ratios of soil diffusivity (D) to stream erosivity (K). By combining the stream power model with ^{10}Be-derived denudation rates, we estimated values for K and D and found that the stream erosivity varies more strongly between the rock types than the soil diffusivity. After measuring parameters in Santa Gracia's rock units that relate to diffusive and advective processes such as infiltration, vegetation cover, mineralogical composition, the degree of weathering, and grain size, we deduced that the higher value of K for the monzogranite could be due to a higher amount of runoff, a higher degree of weathering, or a smaller grain size in the monzogranite, as compared to the diorites.

Although we were not able to directly detect differences in infiltration rate between the rock types, possibly related to recent soil compaction by goats, we suggest that denser vegetation cover in the diorites could lead to higher levels of infiltration, decreasing runoff in the diorites, thereby leading to a comparatively higher runoff and *K* for the monzogranite. The monzogranite bedrock and soils yield higher values for the weathering proxies CIA and f_{reac}, indicating a higher degree of weathering and therefore a higher degree of erodibility for the monzogranite, which would ease fluvial incision and raise *K*. Finally, smaller and more uniform sediment grains in the monzogranite may act as tools to incise stream beds, whereas generally larger stream sediment in the diorites may be less frequently moved and thus armor the bed, retarding incision. Together, our data suggest that subtle differences in lithology, expressed by composition and crystal grain size, can have a visible effect on drainage density through control of weatherability, surficial sediment sizes, vegetation, and infiltration.

5.8 Appendix 5A: Meteoric 10Be analysis and denudation rates

We calculated meteoric denudation rates for two stream sediment samples (one from the monzogranite, Cactus Hill stream, and one from a stream that drains both the inner and outer diorite, Diorite Stream), for which we also measured *in situ* ^{10}Be concentrations (Table A5.1). In principle, meteoric ^{10}Be/^{9}Be ratios can be used to obtain denudation rates in all rock types, because of their independence from certain minerals, in contrast to quartz-derived *in situ-produced* ^{10}Be. Despite this generally broader applicability, even to mafic and carbonate rock types, denudation data from meteoric ^{10}Be/^{9}Be is still sparse. We thus take the opportunity to compare denudation rates obtained from the meteoric method with those from the *in situ* method in quartz-bearing rocks.

Denudation rates for meteoric samples were calculated using a framework based on the ratio of meteoric ^{10}Be as atmospheric flux tracer and stable ^{9}Be that is released from rocks during weathering (von Blanckenburg et al., 2012):

$$D_{met} = \frac{\mathrm{F}_{\mathrm{met}}^{^{10}\mathrm{Be}}}{\left(\frac{^{10}\mathrm{Be}}{^{9}\mathrm{Be}}\right)_{\mathrm{reac}} \times \left[^{9}\mathrm{Be}\right]_{\mathrm{parent}}} \times f_{reac} \qquad \text{(A5.1)},$$

where D_{met} is the denudation rate (in mass/area/time), $\mathrm{F}_{\mathrm{met}}^{^{10}\mathrm{Be}}$ is the meteoric ^{10}Be depositional flux calculated for Santa Gracia (in atoms/area/year), $\left(\frac{^{10}\mathrm{Be}}{^{9}\mathrm{Be}}\right)_{\mathrm{reac}}$ is the ratio of reactive (i.e. sequentially extracted) ^{10}Be and ^{9}Be concentrations, and $[^{9}\mathrm{Be}]_{\mathrm{parent}}$ is the ^{9}Be concentration in Santa Gracia's bedrock. Two published values for $\mathrm{F}_{\mathrm{met}}^{^{10}\mathrm{Be}}$ were used, one from the global circulation model of Heikkilä and von Blanckenburg (2015), at 1.17×10^{6} atoms cm^{-2} yr^{-1}, and a value calibrated for the Atacama Desert from Wang et al. (2015), at 3.70×10^{4} atoms cm^{-2} yr^{-1}. In semi-arid environments, the depositional flux of meteoric ^{10}Be needed to calculate meteoric denudation rates is not well known (Willenbring and von Blanckenburg, 2010), hence meteoric ^{10}Be denudation rate estimates are likely subject to substantial additional unquantified uncertainty.

Because the two available, published flux values are offset from each other by two orders of magnitude, the resulting calculated denudation rates for Santa Gracia also vary by two orders of magnitude (Table A5.1). Meteoric denudation rates calculated using the global circulation model flux from Heikkilä and von Blanckenburg (2015) are 45 ± 8.89 m Myr^{-1} for the monzogranite and 107 ± 21.16 m Myr^{-1} for the diorite, whereas denudation rates calculated using the flux from Wang et al. (2015) are 1.43 ± 0.28 m Myr^{-1} for the monzogranite and 3.39 ± 0.67 m Myr^{-1} for the diorite. In contrast, *in situ* denudation rates for the same samples have intermediate values at 11.49 m Myr^{-1} for the monzogranite and 8.00 m Myr^{-1} for the diorite. Interestingly, meteoric and *in situ* denudation rates for the monzogranite and diorite show opposite patterns, where the monzogranite has a relatively higher *in situ* denudation rate and a relatively lower meteoric denudation rate, as compared to the diorite. This could be due to the differences in grain sizes used to measure the denudation rates; for in situ denudation rates, sand-sized grains are used whereas for meteoric denudation rates, clay-sized grains are used.

Table A5.1. Meteoric ^{10}Be data.

						Heikkilä and von Blanckenburg (2015)			Wang et al. (2015)		
Sample	Rock type	Be 10/9 ratio	Reactive ^{9}Be (ppm)	Mineral-bound ^{9}Be (ppm)	^{9}Be parent (ug g^{-1})	^{10}Be flux (atoms cm^{-2} yr^{-1} ×10^{5})	D rate (t/km^{2}/yr)	D rate (m Myr^{-1})	^{10}Be flux (atoms cm^{-2} yr^{-1} ×10^{5})	D rate (t/km^{2}/yr)	D rate (m Myr^{-1})
SG8	Monzogranite	4.90 ×10^{-9}	0.46 ± 0.02	1.31 ± 0.07	1.21 ± 0.07	1.17×10^{6}	113 ± 22.23	45 ± 8.89	3.70×10^{4}	3.57 ± 0.70	1.43 ± 0.28
SG45	Diorite	9.57 ×10^{-9}	0.07 ± 0.00	1.20 ± 0.06	1.21 ± 0.07	1.17×10^{6}	268 ± 52.89	107 ± 21.16	3.70×10^{4}	8.47 ± 1.67	3.39 ± 0.67

5.9 Acknowledgements

This work was supported by the German Science Foundation (DFG) priority research program SPP-1803 “EarthShape: Earth Surface Shaping by Biota” (grant SCHE 1676/4-1 and -2 to D. S.; funding of P. G. through grant BE 1780/53-1 and -2). We warmly thank the EarthShape management, Friedhelm von Blanckenburg and Todd Ehlers, and the EarthShape coordinators Kirstin Übernickel and Leandro Paulino, for their leadership and coordination. We are very grateful to the Chilean National Park Service (CONAF) for providing access to the sample locations and on-site support of our research. We also thank Isabel Wüst, Iris Eder, David Scheer, and Müge Yazici for their help in the field and in the laboratory, Laura Krone for her assistance with meteoric ^{10}Be denudation rate calculations, and Steven A. Binnie and Stefan Heinze from Cologne University for conducting AMS measurements.

5.10 Author contributions

Conceptualization: DS, EL; Methodology: EL, DS; Software: DS; Validation: EL, DS, HW, AMS, JAS, MALL, PG; Formal analysis: EL; Investigation: EL, DS, HW, AMS, JAS, MALL, PG; Writing – Original Draft Preparation: EL; Writing—Review and Editing: EL, DS, HW, AMS, JASS, PG; Visualization: EL; Supervision & Funding Acquisition: DS.

5.11 Data availability

Cosmogenic nuclide data presented in this paper will be made available as a GFZ Data Publication in accordance with FAIR principles. LiDAR data from the studied catchments is available at Krüger et al. (2022).

5.12 Supplemental information

Methods for compositional analysis. XRD and XRF analyses were done at the Elements and Minerals of the Earth Laboratory (ElMiE Lab) at the German Research Centre for Geosciences (GFZ, Potsdam). For XRF analysis, 18 bedrock samples (six from the monzogranite, nine from the inner diorite, and three from the outer diorite) were ground to <62 µm and main and trace elements were measured on fused glass beads with an XRF spectrometer (AXIOS, Malvern Panalytical, UK). Loss of ignition was determined by H_2O/CO_2 analysis using an Eltra element analyzer. Reproducibility was determined on three certified reference materials (crm) and is within the analytical precision, which is better than 2% for main elements and better than 10% for trace elements.

XRD analyses were conducted using a Malvern-PANalytical Empyrean X-ray diffractometer. 13 bulk rock samples (six from the monzogranite, six from the inner diorite and two from the outer diorite) were first crushed and powdered to a grain size of <62 µm and subsequently milled to a grain size of <10 µm using a micronizing mill (McCrone Group). The XRD operates in Bragg-Brentano geometry, with Cu-Kα radiation at 40 mA and 40 kV and a PIXel3D detector. Measurements were obtained with a step size of 0.013 °2θ from 4.6-85 °2θ, with 60 sec per step. The software package AXS DIFFRACplus EVA (version 11.0.03 by Bruker) was used to identify minerals and select peak references from the mineralogical database. Rietveld refinement for quantitative mineralogy was performed using the program BGMN and the graphical user interface Profex (version 3.10.2, Doebelin and Kleeberg, 2015) calibrated for the used diffractometer. The quality of the Rietveld fit was assessed by visually comparing the observed and calculated patterns, and by testing the result for chemical plausibility (Toby, 2006). The error of quantitative analyses is expected to be in the range of 1-3 weight %. Point counting of thin sections was performed to obtain mineral assemblages optically. We point counted minerals in 24 thin sections using a transmitted light microscope (ten from the monzogranite, eight from the inner diorite and six from the outer diorite), with 100 counts per thin section. Minerals were chosen to be identified based on intersecting lines in a 10×10 grid with 0.25 cm spacing, overlain onto a photomicrograph of each thin section. To measure the size of mineral (crystal) grains, we

measured the diameter of each mineral grain on a transect across a photomicrograph of each thin section and calculated the average diameter for each rock type.

Sequential chemical extractions. We applied sequential chemical extraction procedures to measure major elements in the exchangeable, reactive and residual mineral bound fractions of six soil samples and one stream sediment sample for the monzogranite, five soil samples from the inner diorite, two from the outer diorite, and one stream sample containing sediment from both diorites. We evaluated the inner and outer diorite samples together and compared them to the monzogranite. We performed extractions to estimate whether soils in the three rock types have differing levels of bio-available elements, and to estimate the degree of weathering in each rock type, as larger amounts of exchangeable and reactive elemental fractions in a soil sample indicate a higher degree of chemical weathering (Filgueiras et al., 2002). First, we manually dry-sieved samples to <63 μm, and used between 0.5 and 0.75 g of dried, sieved sediment for each sample. The extraction procedure applied is based on sequential extraction procedures described in Tessier et al. (1979), Wittmann et al. (2012), and Arunachalam et al. (1996), and involves five steps: 1) extraction of the ion exchangeable "Ex" fraction with ammonium acetate (1 M NH_4Ac); 2) extraction of the reactive amorphous oxy-hydroxide "Am-Ox" fraction with 0.5 M HCl ; 3) Extraction of crystalline oxides "X-Ox" with hydroxylamine-hydrochloride solution (1 M $NH_2OH \times HCl$ in 1 M HCl); 4) Decomposition of the remaining silicate residue "Min" with HF /HNO_3 mixtures. Between extraction steps, the sample residues were washed 3 to 4 times with "MilliQ" H_2O. Major element, and minor element measurements were carried out by using an optical emission, inductively-coupled plasma spectrometer (ICP-OES, model Varian 720-ES with axial optics). Aliquots were taken from leachates for meteoric ^{10}Be analysis (see main body methods). We validated the accuracy of the leach by running aliquots of San Joaquin soil (SRM 2710a), a soil reference material from the USGS (Mackey et al., 2010). To verify during measurement, we used a synthetic solution with a similar matrix to the samples.

Porosity, permeability, and hydraulic conductivity. Porosity, permeability and hydraulic conductivity were measured for 14 sample cores (5 from the monzogranite, 6 from the inner diorite and 3 from the outer diorite) taken from bedrock samples collected in

the field. Each sample core has a diameter of 3 cm and a length varying from 1.5-5 cm. Porosity was determined from the volume of the pores and the volume of the sample using the ISRM (International Society of Rock Mechanics) suggested triple weighing method, where the masses of the dry (m_{dry}) and water-saturated (m_{sat}), and submerged sample cores (m_{buoy}) are determined (ISRM, 1981). Bulk volume (V_{bulk}), pore volume (V_{pore}), and effective porosity (ϕ) were calculated from the following relations:

$$V_{bulk} = \left(m_{sat-}m_{buoy}\right) \div \rho_{fluid} \quad \text{(S5.1)},$$

$$V_{pore} = \left(m_{sat-}m_{dry}\right) \div \rho_{fluid} \quad \text{(S5.2)},$$

$$\Phi\,[\%] = \left(V_{pore} \div V_{bulk}\right) \times 100 \quad \text{(S5.3)},$$

where ρ_{fluid} denotes the density of the saturating fluid, which was determined from the buoyancy of a calibration block in the fluid at laboratory conditions. The measurements were done with a density determination kit from Sartorius in combination with a special Sartorius accuracy scale. Water permeabilities were determined by performing constant head permeability tests in a self-made standpipe at atmospheric pressure. For the tests, fully water-saturated sample cores were jacketed with PTFE ribbon and placed at the lower end of a water-filled column, whereby the height of the water head (h_1) above the lower end-face of the sample (h_2) defines the applied differential fluid pressure. The flow rate, Q, at constant pressure difference was calculated from the mass of water flowing through the sample at given time intervals. Hydraulic conductivity, k_f, was calculated from permeability, k, using Darcy's Law.

$$k = Q \times \mu_{H20} \times \frac{1}{g} \times \rho_{H20} \times \Delta h \times A \quad \text{(S5.4)},$$

$$k_f = k \times \rho_{H20} \times g \div \mu_{H20} \quad \text{(S5.5)},$$

with μ_{H2O} and ρ_{H2O} are the viscosity and density of water, Δh is the height of the fluid column, g is the acceleration of gravity, and l and A are the length and cross-sectional area of the sample, respectively.

Figure S5.1. The equivalent of Figure 5.4, but with an unconstrained *m* value. A) Hillshade images showing representative hilltops in the monzogranite (red shading); the location is shown in D by a red outline. B) An example plot of the Laplacian of elevation against the product of drainage area and slope for the area of the monzogranite shown in A. Circles represent the means of log transformed data within logarithmically spaced bins, and red circles represent the red-shaded hilltops in A used to calculate the Laplacian of elevation on hilltops ($-\boldsymbol{\nabla^2 z_h}$). The Laplacian is roughly constant on hilltops where drainage area and slope are small, which is consistent with equilibrium topography as shown in Perron et al. (2009). C) Log-log plot of the slope function *S** (see Eq. 5.4) against drainage areas for stream profiles from the area of the monzogranite shown in A, but with an unconstrained *m* value. The line is a least-squares fit to the binned data. D) Image of the Santa Gracia catchment showing all rock types (outlined in black) and the *D/K* ratio calculated with an unconstrained m value, for small sub-areas within each rock type shown by circles.

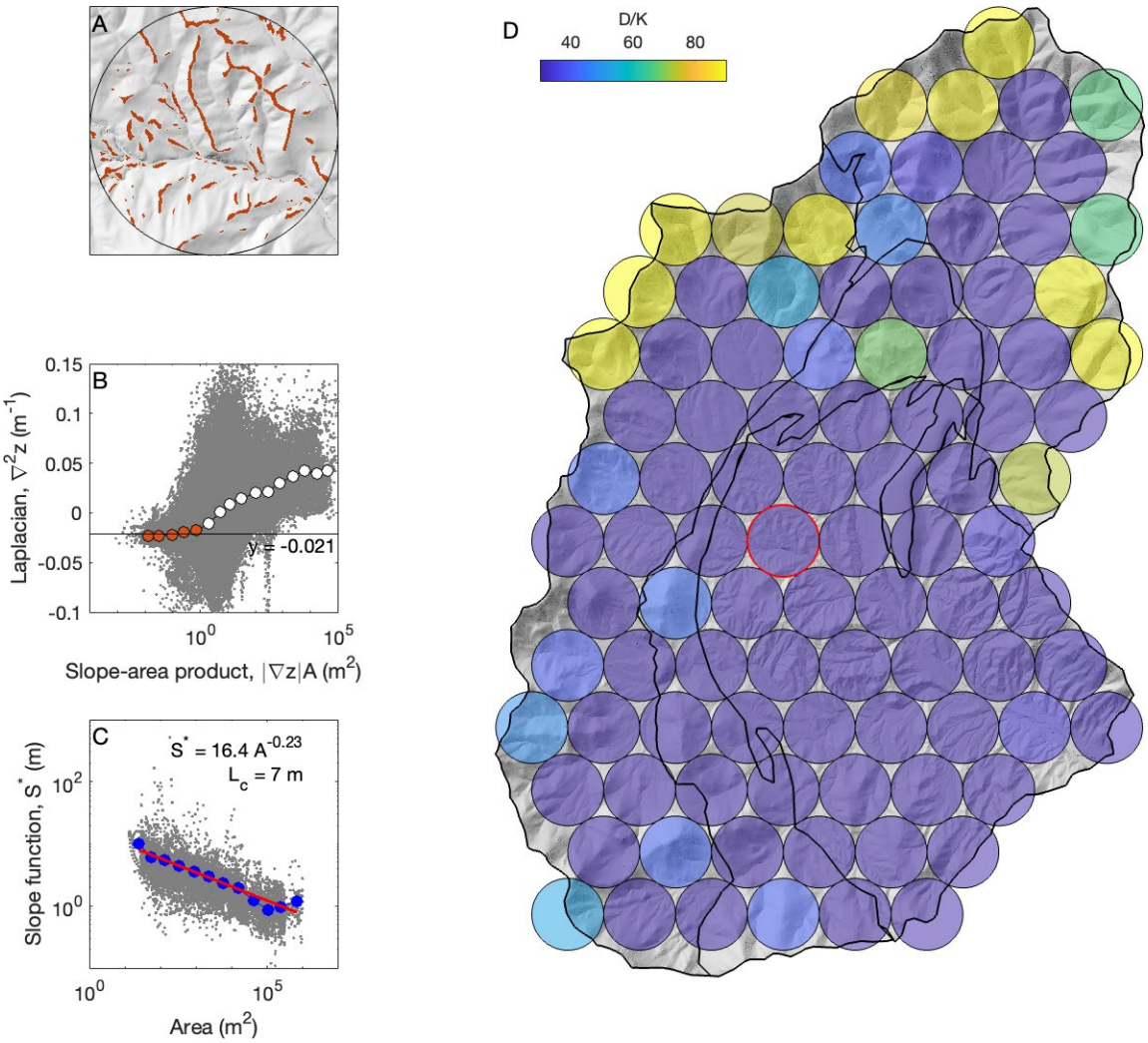

Table S5.1. Infiltraion rate data.

Sample site	Tension	Kns (cm/hr)	Kns (log(cm/mn))	Ksat (cm/hr)	Latitude (°N)	Longitude (°E)
M1	1	14.60	1.16	17.13	-29.75454	-71.11258
	2	17.00	1.23			
	4	11.38	1.06			
	6	10.26	1.01			
M2	1		0.10	8.69	-29.75336	-71.11823
	2	7.92	0.90			
	4	3.68	0.57			
	6	4.65	0.67			
M3	1	17.87	1.25	16.93	-29.75576	-71.11928
	2	13.61	1.13			
	4	12.62	1.10			
	6	12.97	1.11			
M4	1	7.05	0.85	8.54	-29.75268	-71.1258
	2	8.96	0.95			
	4	6.88	0.84			
	6	5.65	0.75			
M5	1	4.09	0.61	3.7	-29.76022	-71.12569
	2	3.85	0.59			
	4	6.07	0.78			
	6	5.29	0.72			
Monzogranite average				11.00		
Standard deviation				5.86		
Coefficient of Variation (%)				53.29		
D1	1	9.25	0.97	10.29	-29.75714	-71.16465
	2	9.93	1.00			
	4	6.26	0.80			
	6	6.64	0.82			
D3	1	4.72	0.67	5.63	-29.75358	-71.16189
	2	6.60	0.82			
	4	5.69	0.76			
	6	5.17	0.71			
D4	1	4.47	0.65	6.9	-29.75689	-71.15678
	2	7.98	0.90			
	4	5.45	0.74			
	6	3.06	0.49			
D5	1			8.85	-29.74748	-71.15949
	2	6.95	0.84			
	4	6.65	0.82			
	6	3.94	0.60			
Diorite average				7.92		
Standard deviation				2.06		
Coefficient of Variation (%)				26.05		

Table S5.2. XRF data

Sample ID	Sampling location[a]	Latitude (°N)	Longitude (°E)	SiO_2 (%)	Fe_2O_3 (%)	MgO (%)	TiO_2 (%)	Al_2O_3 (%)	MnO (%)	CaO (%)	Na_2O (%)	K_2O (%)	P_2O_5 (%)	LOI[b](%)	Sum	CIA[c]
Monzogranite																
EL20-SG3	CH ridge	-29.7514	-71.12565	70.5	2.0	0.7	0.3	15.2	0.1	2.3	3.7	4.6	0.1	0.79	100.2	50.00
EL20-SG6	CH slope	-29.75123	-71.12524	71.0	1.2	0.8	0.3	14.9	0.1	2.2	3.6	5.2	0.1	0.51	100.0	48.93
EL20-SG11	NH ridge	-29.7494	-71.12422	77.1	0.6	0.1	0.1	12.5	0.0	0.5	2.8	5.7	0.0	0.38	99.9	51.58
EL20-SG12	NH ridge	-29.7494	-71.12422	75.1	1.1	0.2	0.2	13.2	0.0	0.8	3.1	5.0	0.1	0.52	99.3	52.19
EL20-SG16	NH stream	-29.75207	-71.12229	71.3	1.8	0.7	0.3	14.8	0.1	1.8	3.5	5.2	0.1	0.74	100.1	50.20
EL20-SG18	FH slope	-29.75279	-71.1224	71.3	1.6	0.7	0.3	14.4	0.1	2.0	3.2	5.1	0.2	0.91	99.8	49.90
Inner Diorite																
EL20-SG25	DKH ridge	-29.74323	-71.15681	64.1	1.5	2.1	0.8	17.0	0.0	7.6	4.6	1.0	0.3	0.81	100.0	43.03
EL20-SG26	DKH ridge	-29.74323	-71.15681	66.7	1.3	1.9	0.7	16.9	0.0	5.3	5.2	1.1	0.3	0.81	100.1	46.58
EL20-SG29	DKH slope	-29.74351	-71.15694	64.7	1.5	2.5	0.8	16.9	0.0	6.5	4.7	0.8	0.2	0.98	99.5	45.30
EL20-SG30	DKH slope	-29.74351	-71.15694	63.2	1.3	2.4	0.8	17.6	0.0	7.9	5.5	0.6	0.2	0.80	100.2	42.26
EL20-SG31	MH slope	-29.74776	-71.15712	57.7	6.5	3.1	0.9	16.6	0.1	6.4	3.8	2.5	0.3	1.26	99.2	44.46
EL20-SG32	MH slope	-29.74779	-71.15702	50.9	14.8	5.5	1.2	14.0	0.1	7.6	3.3	1.0	0.3	1.69	100.4	40.81
EL20-SG39	ZH ridge	-29.74038	-71.15598	55.2	9.0	3.8	1.2	16.7	0.1	6.8	3.3	1.8	0.3	1.49	99.8	45.78
EL20-SG40	ZH ridge	-29.74033	-71.15589	59.7	5.6	3.4	0.6	17.4	0.1	7.0	2.9	2.1	0.2	0.95	100.0	46.73
EL20-SG43	ZH slope	-29.74132	-71.15733	62.5	2.2	2.5	0.8	16.9	0.1	9.5	4.5	0.3	0.2	0.67	100.1	40.39
Outer Diorite																
EL20-SG33	DH slope	-29.75964	-71.16108	63.3	5.2	2.1	0.7	16.2	0.1	4.4	3.1	4.1	0.2	0.00	99.3	48.14
EL20-SG34	DH slope	-29.75972	-71.16096	57.2	4.86	2.04	0.6	15.5	0.09	4.4	3.03	3.34	0.21	8.44	99.7	48.29
EL20-SG35	DEH ridge	-29.74444	-71.15868	73.6	1.41	0.42	0.2	13.7	0.03	1.9	2.58	5.43	0.05	0.45	99.8	50.23

[a]Sample locations: CH: Cactus Hill, NH: Naked Hill, FH: Flag Hill, DKH: Donkey Hill, MH: Mine Hill, DH: Drill Hill, DEH: Dino Egg Hill, ZH: Zebra Hill.
[b]LOI = Loss of ignition
[a]CIA = Chemical index of alteration

Table S5.3. Data from sequential chemical extractions. The uncertainty of all measurements is <5% based on the agreement between measurements (repeatability).

Sample	Sample type	Al 394.401	Ba 230.424	Be 31 3.107	Ca 422.673	Cu 324.754	Fe 238.204	K 766.491	Mg 279.078	Na 588.995	Sr 407.771	Zn 213.857
Exchangeable concentration (ppm)												
Monzogranite												
SG2	Soil	0.73	10.63	0.00	2178.02	0.73	1.38	440.92	274.37	93.38	13.57	0.49
SG5	Soil	0.36	7.65	0.00	1124.40	0.50	0.06	258.76	279.34	55.12	9.10	0.39
SG10	Soil	0.35	7.31	0.00	997.22	0.57	0.04	469.33	317.45	101.36	8.05	0.37
SG13	Soil	0.72	9.23	0.00	1376.74	0.68	0.25	310.31	423.80	106.27	10.27	0.44
SG14	Soil	0.35	8.37	0.00	1414.62	0.73	0.09	663.03	473.27	88.73	10.27	0.71
SG17	Soil	1.27	9.79	0.00	2311.75	1.68	2.69	374.91	317.41	109.11	15.79	1.18
SG8	Stream sediment	1.26	17.32	0.00	1949.30	0.91	1.66	208.70	472.63	130.96	18.43	0.47
Diorite												
SG23	Soil	0.51	9.57	0.00	1412.43	0.38	0.48	226.71	208.37	45.93	10.36	0.23
SG36	Soil	0.73	10.36	0.00	3601.26	0.45	1.04	940.97	399.37	59.25	18.83	0.17
SG41	Soil	0.34	11.19	0.00	1369.46	0.39	0.06	328.00	513.46	59.69	11.02	0.15
SG4	Soil	2.18	12.17	0.00	2702.35	1.92	4.65	542.60	403.32	86.32	15.41	0.51
SG6	Soil	0.37	9.98	0.00	1703.60	0.62	0.37	283.21	332.41	57.93	10.47	0.25
SG12	Soil	1.09	7.11	0.00	1887.23	0.54	1.58	388.18	214.83	56.06	12.58	0.35
SG45	Stream sediment	0.31	6.24	0.00	521.20	0.18	0.12	84.29	128.74	21.68	3.34	0.13
Reactive concentration (ppm)												
Monzogranite												
SG2	Soil	1398.67	29.11	0.29	879.04	20.42	2486.71	355.25	318.40	63.92	8.21	15.48
SG5	Soil	1527.56	35.48	0.24	1015.94	23.85	2586.82	408.38	340.22	70.47	7.29	14.80
SG10	Soil	1627.99	40.18	0.46	903.83	21.69	3509.56	636.75	413.15	76.92	7.32	13.93
SG13	Soil	1629.03	43.69	0.43	621.71	30.03	3773.46	591.52	449.55	84.58	6.68	16.14
SG14	Soil	1811.77	37.03	0.54	1241.82	42.75	3598.76	675.60	450.49	91.98	7.72	25.68
SG17	Soil	1535.86	36.89	0.32	1712.85	35.50	2614.19	450.29	413.95	73.50	12.26	29.05
SG8	Stream sediment	1354.43	42.40	0.46	1337.37	24.49	2889.75	364.42	608.10	68.16	9.71	15.27
Diorite												
SG23	Soil	1478.26	29.27	0.13	1324.72	10.78	2592.84	389.45	357.17	54.22	8.34	8.67
SG36	Soil	1737.21	25.01	0.10	4816.43	9.62	1843.29	674.05	1226.01	63.56	20.82	12.54
SG41	Soil	2004.13	27.46	0.17	3511.51	16.82	3303.38	479.70	565.25	51.50	9.00	8.41
SG4	Soil	2014.58	23.19	0.11	4945.50	30.00	2380.36	542.80	728.55	76.79	20.52	15.30
SG6	Soil	1606.77	18.23	0.11	2683.63	20.83	2402.50	365.16	560.53	55.26	9.74	10.32
SG12	Soil	1978.62	26.27	0.13	3080.94	10.92	2536.41	481.56	402.84	56.88	12.74	13.40
SG45	Stream sediment	597.08	11.71	0.07	2072.49	6.66	1171.05	140.73	209.84	39.85	5.68	4.76
Mineral bound concentration (ppm)												
Monzogranite												
SG2	Soil	92065.78	284.44	1.50	15646.28	67.38	36761.50	24260.68	9451.42	25539.75	160.59	63.68
SG5	Soil	88597.24	264.14	1.55	20271.97	66.95	54594.07	23708.46	13128.73	28573.49	163.69	70.21

SG10	Soil	93416.62	227.05	1.96	15405.46	30.18	53419.09	22350.81	12861.66	28123.07	130.64	74.90
SG13	Soil	84653.44	263.94	1.34	12236.50	40.31	50300.06	24570.68	8104.28	29821.94	129.86	57.04
SG14	Soil	87424.15	237.28	1.51	15675.17	129.66	49709.09	25347.91	10186.82	28596.32	136.12	93.95
SG17	Soil	86517.00	249.68	1.43	15782.44	123.04	43507.08	25331.93	10373.98	25076.93	147.68	75.21
SG8	Stream sediment	73658.87	226.46	1.31	14874.93	53.02	108901.62	21657.64	8915.46	25826.34	137.29	62.69
						Diorite						
SG23	Soil	70649.81	281.31	0.77	35896.11	26.72	72172.39	16180.09	20478.39	25594.46	152.79	50.21
SG36	Soil	81527.20	215.79	0.83	38376.20	51.18	64206.86	15334.17	21916.38	19769.33	274.17	79.32
SG41	Soil	48019.04	214.46	0.89	39588.48	41.83	86590.71	14365.34	15528.60	21603.32	179.32	67.36
SG4	Soil	71046.20	124.41	0.62	39920.91	120.49	37443.20	8060.31	14208.33	29003.87	197.03	26.88
SG6	Soil	73811.71	193.18	0.70	45927.47	65.33	92890.97	11613.79	24832.56	24681.93	188.88	72.89
SG12	Soil	48415.76	224.63	0.68	37657.11	30.48	83392.54	14174.59	14358.24	21439.20	129.79	52.39
SG45	Stream sediment	53706.30	151.77	0.75	43174.11	12.81	209339.50	9170.93	23432.61	18658.38	166.68	89.21

Table S5.4. In situ ^{10}Be cosmogenic nuclide sample data. Samples with an asterix next to the Sample ID are previously published in Lodes et al. (2023).

Sample ID	IGSN [a]	Sampling location [b]	Latitude (°N)	Longitude (°E)	Sample type [c]	^{10}Be conc. ±2σ (×10^5) (atoms g^{-1})	^{10}Be production rate (spallation, atoms g^{-1} yr^{-1})	Calculated denudation rate ± uncertainty (m Myr^{-1})	Method used for denudation rate calculation	Slope angle at sample location (°) [f]	Avg. boulder width / protrusion [g]	No. chips taken for sample
						Monzogranite						
EL20-SG4	GFEL1003R	CH slope	-29.75123	-71.12524	B	4.41 ± 0.20	5.02	7.28 ± 0.69	Cronus	22.48	0.37 / 0.05	13
EL20-SG9	GFEL1003L	NH ridge	-29.7494	-71.12422	B	3.20 ± 0.18	5.26	10.79 ± 1.06	Cronus	34.12	0.28 / 0.13	9
EL20-SG10	GFEL1003K	NH ridge	-29.7494	-71.12422	S	3.25 ± 0.17	5.26	10.63 ± 1.03	Cronus	34.12	N/A	N/A
EL20-SG13	GFEL1003G	NH slope	-29.75116	-71.1232	S	5.12 ± 0.24	4.95	6.11 ± 0.59	Cronus	12.89	N/A	N/A
EL20-SG2	GFEL1003T	CH ridge	-29.7514	-71.12565	S	5.89 ± 0.25	5.08	5.37 ± 0.51	Cronus	5.72	N/A	N/A
EL20-SG5	GFEL1003Q	CH slope	-29.75123	-71.12524	S	4.36 ± 0.20	5.02	7.39 ± 0.70	Cronus	22.48	N/A	N/A
EL20-SG8	GFEL1003M	CH stream	-29.75179	-71.12414	SS	2.94 ± 0.15	4.85	11.49 ± 1.08	CosmoTools	13.07	N/A	N/A
EL19-SG13	GFEL1001C	FH ridge	-29.75313	-71.12285	B	3.12 ± 0.14	4.9	10.37 ± 0.95	Cronus	10.83	0.18 / 0.06	20
EL19-SG14	GFEL1001D	FH ridge	-29.75313	-71.12285	S	3.43 ± 0.13	4.9	9.37 ± 0.84	Cronus	10.83	N/A	N/A
EL19-SG15	GFEL1001E	FH slope	-29.75282	-71.12234	B	8.93 ± 0.34	4.89	3-5	BCode	24.01	1.29 / 0.98	10
EL19-SG16	GFEL1001F	FH slope	-29.75282	-71.12234	C	3.51 ± 0.16	4.89	9.11 ± 0.85	Cronus	24.01	N/A	N/A
EL19-SG17	GFEL1001G	FH slope	-29.75282	-71.12234	S	3.97 ± 0.17	4.89	7.96 ± 0.73	Cronus	24.01	N/A	N/A
EL19-SG20	GFEL1001K	FH stream	-29.75259	-71.12159	SS	4.70 ± 0.25	4.85	6.83 ± 0.68	CosmoTools	19.96	N/A	N/A
						Inner Diorite						
EL19-SG6	GFEL10015	MH slope	-29.74708	-71.15705	S	4.24 ± 0.18	5.33	8.09 ± 0.75	Cronus	17.54	N/A	N/A
EL19-SG7	GFEL10016	MH slope	-29.74708	-71.15705	C	7.52 ± 0.31	5.33	4.3 ± 0.42	Cronus	17.54	N/A	N/A
EL20-SG36*	GFEL1002U	ZH ridge	-29.74016	-71.15613	S	5.39 ± 0.25	5.64	6.5-7.5	BCode	28.41	N/A	N/A
EL20-SG37*	GFEL1002T	ZH ridge	-29.74016	-71.15613	B	11.45 ± 0.44	5.64	3-5	BCode	28.41	1 / 0.90	10
EL20-SG38*	GFEL1002S	ZH ridge	-29.74016	-71.15613	B	7.84 ± 0.28	5.64	3-5	BCode	28.41	0.10 / 0.12	~10
EL20-SG41	GFEL1002P	ZH slope	-29.74132	-71.15733	S	2.67 ± 0.12	5.62	7-9	BCode	24.61	N/A	N/A
EL20-SG42	GFEL1002N	ZH slope	-29.74132	-71.15733	B	7.13 ± 0.30	5.62	4-5	BCode	24.61	0.3 / 0.15	~10
						Outer Diorite						
EL19-SG8*	GFEL10017	SGH ridge	-29.75623	-71.16622	B	5.93 ± 0.21	5.72	10-12	BCode	8.46	1.10 / 0.80	10
EL19-SG9*	GFEL10018	SGH ridge	-29.75623	-71.16622	B	4.69 ± 0.17	5.72	10-12	BCode	8.46	0.38 / 0.12	10
EL19-SG11*	GFEL1001A	SGH slope	-29.75763	-71.16599	B	3.55 ± 0.13	5.56	18-20	BCode	21.93	1.30 / 0.87	9
EL19-SG22*	GFEL1001M	SGH slope	-29.75772	-71.16631	B	3.85 ± 0.15	5.56	18-20	BCode	22.76	0.37 / 0.24	11
EL19-SG10*	GFEL10019	SGH ridge	-29.75623	-71.16622	S	2.57 ± 0.11	5.72	12-15	BCode	8.46	N/A	N/A
EL19-SG12*	GFEL1001B	SGH slope	-29.75763	-71.16599	S	2.38 ± 0.09	5.56	19-21	BCode	21.93	N/A	N/A
EL19-SG23*	GFEL1001N	SGH slope	-29.75772	-71.16631	S	2.09 ±0.08	5.56	19-21	BCode	22.76	N/A	N/A
						Diorite						
EL20-SG45	GFEL1002K	Diorite stream	-29.74511	-71.15813	SS	4.48 ± 0.20	5.29	8.0 ± 0.75	CosmoTools	15.66	N/A	N/A

[a]Open access metadata: http://igsn.org/[insert IGSN number here]
[b]Sample locations: CH: Cactus Hill, NH: Naked Hill, FH: Flag Hill, MH: Mine Hill, SGH: Santa Gracia Hill, ZH: Zebra Hill.
[c]Sample type abbreviations: BR: bedrock, B: boulders, S: soil, SS: stream sediment.
[d]Time constant spallation production rate scaling scheme of Lal (1991) and Stone (2000) ('St' in Balco et al., 2008), calculated taking topographic shielding into account.
[f]Local hillslope angles were calculated using a 1m DEM and an 8-connected neighbourhood method.
[g]Width and protrusion measurements (in meters) for boulders. Values are averages of >10 measurements per sample site.

Chapter 6

Final discussion

In this research, I investigated how bedrock properties interact with climate and biota to influence patterns of erosion and weathering, the locations of ridges and valleys, and overall landscape morphology in granitic landscapes. Each chapter focuses on a different property of granitic bedrock: fractures and the resulting hillslope grain size distributions in Chapter 3, grain size distributions in streams in Chapter 4, and mineralogical composition in Chapter 5. In this final discussion, I propose future work and integrate my findings to make predictions about how bedrock properties, climate, and biota can influence landscape evolution over longer timescales.

6.1 Potential future work

Chapter 3 focuses on bedrock fractures, their effect on hillslope grain size distributions and differential erosion rates, and how climate and biota interact with fractures to modulate denudation rates. Our findings suggest a control of fracture spacing and orientation on differential denudation and the locations of ridges and valleys in granitic landscapes. We assumed that areas with higher underlying fracture densities are more easily weathered and eroded due to smaller surficial grain sizes, and therefore eventually become topographic lows with deeper weathering zones. These predictions were upheld in Santa Gracia by fracture analysis in a borehole by Krone et al. (2021), who reported intensified weathering around fractured zones, geophysical surveys by Dal Bo et al. (2019), who reported increasing regolith thickness towards the toe of hillslopes, and seismic surveys reported by Trichandi et al. (2022), who reported deeper weathering zones at topographic lows. To further test this hypothesis, I conducted a grain size survey along the seismic line from Trichandi et al. (2022) and found a positive correlation between sediment grain size and elevation, which also supports our hypothesis. Similarly, a topographic stress model by Slim et al. (2014) predicts a higher potential for shear fractures at topographic lows. However, other existing models and seismic data directly contradict our hypothesis. St. Clair

et al. (2015) predict surface-parallel weathering depths in landscapes with low tectonic uplift, but deeper fracturing and weathering at topographic highs in landscapes with high tectonic uplift. According to the model by St. Clair et al. (2015), Santa Gracia's tectonic stress regime should correspond with surface parallel weathering depths, which does not align with our observations.

These discrepancies between models could be due to differences in uplift rates, topographic relief, or in the cause for fracture nucleation. To further complicate the situation, climate also plays a role in how weathering zone depth corresponds with topography (Brantley and White, 2009; Rempe and Dietrich, 2014; Braun et al., 2016). Braun et al. (2016) suggest that in orogenic environments, deeper weathering zones at topographic lows exist in climates with high precipitation rates, whereas weathering zones deepen at ridges when precipitation decreases. Along these lines, Trichandi et al. (2022) suggested that the more humid climate in Santa Gracia during the Last Glacial Maximum could be responsible for the deep weathering zones. In the future, climate change or changes in subduction dynamics along the coast of Chile could change the nature and location of fracture propagation in Santa Gracia and along the Chilean Coastal Cordillera, causing large scale shifts in the landscape morphology. For example, continued aridification in Chile (Souvignet et al., 2012; Boisier et al., 2018; Barrientos et al., 2023) could cause regolith to deepen under topographic highs, and an increase in uplift rates could cause intensified fracturing on topographic highs, allowing enhanced rainwater infiltration, chemical weathering, and denudation rates on ridges (St. Clair et al., 2015; Moon et al., 2017). Such changes could trigger a negative feedback effect in landscape morphology in which ridgelines become lower in elevation. It is possible that a spectrum exists for tectonically active landscapes, in which the morphologies of relatively low-relief settings such as Santa Gracia are controlled by pre-existing tectonic fractures that act as nuclei for deeply weathered valleys, whereas higher-relief settings develop topographic fractures at topographic highs that generate deeper regolith. However, how such fracture patterns interact with climate remains an open question. In a future study, to better predict the effects of bedrock fractures and climate on landscape morphology, it would be necessary to model the formation of fractures in accordance with the stress field in each field area, and to consider both past and future changes in both climate and tectonic setting. Such a study

could be further applied to a wider range of field areas outside of Chile, with different climate conditions and tectonic settings.

Bedrock fractures delineate the initial size of boulders that exhume on hillslopes and are subsequently transported to streams, and Chapter 4 focuses on the residence times of boulders once they reach the stream channel. Stream boulders can act as thresholds for channel incision by shielding the channel bed from erosion, which can retard the migration of knickpoints (Shobe et al., 2016) or cause channels to steepen to maintain equilibrium (e.g., Seidl et al., 1994; Thaler and Covington, 2016; Cook et al., 2018). In Nahuelbuta, thermochronological data indicates that uplift rates increased from 0.03–0.04 to over 0.2 mm $year^{-1}$ around four million years ago (Glodny et al., 2008), a shift that may be recorded by knickpoints in streams that drain a plateau. On the plateau, the large, stable boulders that we observed in Nahuelbuta's stream channels could be retarding the migration of knickpoints by shielding the channel bed from erosion (e.g., Shobe et al., 2016). To test such a hypothesis, the origin of these knickpoints and their rate of propagation must be confirmed. Further work could include mapping the locations of knickpoints and stream boulders to test whether knickpoint locations correspond to the locations of large boulders. Boulders could be mapped using, i.e., high resolution UAV imagery or structure from motion. A preliminary set of catchment average samples has already been collected from above and below knickpoints (van Dongen, personal communication), and this sample set could be expanded. Ultimately, it is clear that changes in tectonic uplift complicate relationships between climate, erosional thresholds such as large boulders, and slope. Therefore, to tease out how large boulders and climate interact to influence channel slope and landscape morphology, a further study should be conducted in a field site without tectonic uplift or large base level changes.

Chapter 5 focuses on the effects of bedrock mineralogical composition (of a monzogranite and two diorites) on drainage density, stream incision, and landscape morphology. The findings from Chapter 5 can be further applied to other landscapes with granitoid lithology, but landscapes underlain by non-granitoid rock types must be considered differently. For example, in layered rock, bedding planes form weak points that can be more easily infiltrated by rainwater that enhances chemical weathering and soil

formation, and thereby can exert some control on landscape morphology (e.g., Glade et al., 2017; Anderson et al., 2023). In addition, layers that are less susceptible to weathering and erosion will form topographic highs, and thicker bedded rock layers may contribute larger sediment to streams and cause the steepening of stream channels (e.g., Marshall and Roering, 2014; Anderson et al., 2023). In limestone landscapes, karst features cause high infiltration rates and reduce stream power erosivity; however, unlike in granitoid or other crystalline rock, rainwater infiltration in karst systems may not be retained in the regolith and therefore does not necessarily enhance vegetation growth (Ott et al., 2020). Unsurprisingly, previous studies investigating how lithology impacts drainage density on global scales have reported inconclusive or contradictory results (e.g., Perron et al., 2009; Sangireddy et al., 2016). Due to the complex interactions between lithology, tectonics, climate, weathering, erosion, and the hydrological behavior of landscapes, it is necessary to compare field sites that have very similar climatic and tectonic regimes, and to pinpoint the ways in which lithology, as well as the past and present climate and biota, have interacted to shape the landscape. Such a detailed study would be worth conducting in other fluvial landscapes where there exists a sharp contact between two different bedrock lithologies, such as sedimentary versus crystalline rock, or limestone versus sandstone.

6.2 Implications for landscape evolution over longer timescales

Over long timescales, the field sites investigated in this thesis have experienced the exhumation of heterogenous bedrock and changing climate regimes, which both force shifts in landscape morphology that must also be considered. For example, earthquakes in the Coastal Cordillera cause the formation of fractures and reactivation of faults that trigger shifts in landscape morphology (e.g., Molnar et al., 2007; Allmendinger and Gonzales, 2010; Roy et al., 2016). In addition, since bedrock fracture networks are often characterized by a distinctive and consistent dip angle, as fresh bedrock is exhumed over long time scales (millions of years), the location of fractures exposed at the surface will shift, causing a corresponding shift of ridges, valleys, and stream networks that are controlled by the fracture network and the presence and absence of fractures (Roy et al., 2016). This in turn will cause autogenic catchment dynamics and drainage divide migration (Willett et al., 2014). If fracture density increases due to the exhumation or formation of new fractures,

more rainwater will infiltrate into the fractures, which will increase chemical weathering and differential erosion, encourage vegetation growth in weathered areas, lower overland flow, and decrease drainage density (Melton, 1957; Carlston, 1963; St. Clair et al., 2015; Lebedeva and Brantley, 2017; Litwin et al. 2022).

Similarly, as fresh granitic bedrock is exhumed, plutons of different compositions will be exposed to the earth's surface. As I have shown in Chapter 5, subtle differences in granitic mineralogy can cause clear changes in vegetation cover, drainage density, and landscape morphology. When more erodible bedrock is exhumed, the density of drainage networks will likely increase (e.g., Sangireddy et al., 2016), and ridges will form over the most competent bedrock (e.g., Marshall and Roering, 2014; Eggleton et al., 2017). When bedrock with abundant plant essential elements is exhumed, more vegetation will grow and rainwater infiltration rates will increase (Hahm et al., 2019; Callahan et al., 2022), runoff rates will decrease, and therefore drainage density may decrease (e.g., Perron, 2009; Sangireddy et al., 2016). However, in combination with climate changes, bedrock with abundant plant nutrients can cause unsustainable vegetation growth during wet periods, leading to vegetation dieback during drought which may reverse this cycle (Callahan et al., 2022).

Exhumation rates are also not constant over time; as the Chilean Coastal Cordillera sits on an active subduction zone (see Chapter 2.2), tectonic uplift rates change, and the Coastal Cordillera reacts to regular earthquake cycles through uplift and subsidence (Comte and Pardo, 1991; Klotz et al., 1999; Pritchard et al., 2002; 2006; Chlieh et al., 2004). As the landscape is thrown out of equilibrium, denudation rates temporarily will not match uplift rates (e.g., Tucker and Hancock, 2010). In the event of increased uplift, knickpoints will form (Wobus et al., 2006; Whittaker and Boulton, 2012), as seen in Nahuelbuta (Glodny et al., 2008; Melnick et al., 2009). In addition, increased uplift rates cause hillslopes to steepen, and may cause the formation of additional topographically induced fractures at topographic highs or surface-parallel fractures induced by topographic unloading from rapid exhumation (Miller and Dunne, 1996; St. Clair et al. 2015; Moon et al. 2017; Lodes et al., 2023), which may lead to enhanced weathering and erosion at topographic highs in the landscape, thereby triggering an eventual reversal of topographic highs and lows.

Over these longer time scales, there are also large-scale changes in climate corresponding to the Milankovitch cycles. In this thesis, I have shown that climate influences the differences in landscape morphology and differential erosion in my study sites. However, over thousands of years, climate has and will change within each site. Chile's climate was wetter and cooler during the Last Glacial Maximum (Mutz et al., 2018; Mutz and Ehlers, 2019; Starke et al., 2020), and therefore interactions between precipitation and bedrock properties was likely more pronounced, potentially enhancing features such as differential denudation rates or drainage density. In addition, currently existing deep weathering zones at topographic lows in Santa Gracia and La Campana may have developed during a wetter climate in the past (Braun et al., 2016; Trichandi et al., 2022). The studies conducted in this thesis evaluated three landscapes during one snapshot in time, and changes in climate, bedrock lithology, and fracture density over time that influenced the present landscapes are difficult to deconvolve. In addition, the methods used in this thesis all yield results that integrate over different timescales. For example, vegetation patterns likely developed over decades and infiltration rates vary on an hourly basis, while our ^{10}Be concentrations provide us with denudation rates that integrate over several thousands of years, and in some cases encompass the end of the Last Glacial Maximum. Therefore, we cannot easily capture any temporal changes in denudation rate caused by changes in climate.

During wetter and colder periods, the semi-arid site may have experienced precipitation and vegetation cover patterns more like the mediterranean site, and the mediterranean site may have experienced conditions more like the humid-temperate site. As Chile currently experiences aridification (Souvignet et al., 2012; Boisier et al., 2018; Barrientos et al., 2023), we can estimate in the coming decades, reduced precipitation and vegetation in all sites will lead to reduced discharge and infiltration, increased drainage density, decreased differential erosion, and a lower ability to transport existing sediment in stream channels, creating cover threshold affects that may slow down channel incision initially, and eventually steepen channel slopes (e.g., DiBiase and Whipple, 2011; Shobe et al., 2016; Scherler et al, 2017). However, if the degree of climate change is relatively constant along the climate gradient, the relative differences between field sites likely have and will remain intact. Finally, as long-term denudation rates match long term uplift rates,

we can assume that the exhumation of different plutons and bedrock fracture patterns matches the timescale of measured denudation rates as well as our current and future observations of landscape morphology.

References

Aguilar, G., Carretier, S., Regard, V., Vassallo, R., Riquelme, R., & Martinod, J. (2014). Grain size-dependent 10Be concentrations in alluvial stream sediment of the Huasco Valley, a semi-arid Andes region. *Quat. Geochronol.*, 19, 163-172. https://doi.org/10.1016/j.quageo.2013.01.011

Aguilar, G., Cabré, A., Guaita, C., González, F., Ortega, F., Carretier, S., Riquelme, R., & Comte, D. (2015). Denudación por flujos de detritos durante las lluvias torrenciales de marzo de 2015 en Atacama. In *XIV Congreso Geológico Chileno*, 816–818, SERNAGEOMIN, La Serena., 2015.

Aguirre, L., & Egert, E. (1970). Cuadrangulo Lambert (La Serena), Provincia de Coquimbo. In *Carta Geologica de Chile* (No. 23, 14 p., 1 scale 1:50,000). Santiago, Chile: Instituto de Investigaciones Geologicas.

Alaska Satellite Facility Distributed Active Archive Center: ALOS PALSAR_Radiometric_Terrain_Corrected_high_res (ALPSRP191976520), includes Material © JAXA/METI 2009, ASF DAAC [dataset], https://doi.org/10.5067/Z97HFCNKR6VA, 2009.

Alaska Satellite Facility Distributed Active Archive Center: ALOS PALSAR_Radiometric_Terrain_Corrected_high_res (ALPSRP269644390), includes Material © JAXA/METI 2011, ASF DAAC [dataset], https://doi.org/10.5067/Z97HFCNKR6VA, 2011.

Alaska Satellite Facility Distributed Active Archive Center: ALOS PALSAR_Radiometric_Terrain_Corrected_high_res (ALPSRP277746590), includes Material © JAXA/METI 2011, ASF DAAC [dataset], https://doi.org/10.5067/Z97HFCNKR6VA, 2011.

Aldred, J., Eppes, M. C., Aquino, K., Deal, R., Garbini, J., Swami, S., Tuttle, A., & Xanthos, G. (2016). The influence of solar-induced thermal stresses on the mechanical weathering of rocks in humid mid-latitudes. *Earth Surface Processes and Landforms, 41*(5), 603-614.

Allmendinger, R.W., & González, G. (2010). Invited review paper: Neogene to Quaternary tectonics of the coastal Cordillera, northern Chile. *Tectonophysics*, *495*(1-2), 93-110. https://doi.org/10.1016/j.tecto.2009.04.019

Alvarez-Garreton, C., Mendoza, P. A., Boisier, J. P., Addor, N., Galleguillos, M., Zambrano-Bigiarini, M., Lara, A., Puelma, C., Cortes, G., Garreaud, R., McPhee, J., & Ayala, A. (2018). The CAMELS-CL dataset: catchment attributes and meteorology for large sample studies – Chile dataset, *Hydrol. Earth Syst. Sci.,* 22, 5817-5846. https://doi.org/10.5194/hess-22-5817-2018

Amundson, R., Richter, D. D., Humphreys, G. S., Jobbágy, E. G., & Gaillardet. J. (2007). Coupling between biota and earth materials in the critical zone, *Elements, 3* (5), 327-333. https://doi.org/10.2113/gselements.3.5.327

Anderson, S., Gasparini, N., & Johnson, J. (2023). Building a bimodal landscape: bedrock lithology and bed thickness controls on the morphology of Last Chance Canyon, New Mexico, USA. *Earth Surface Dynamics*, *11*(5), 995-1011. https://doi.org/10.5194/esurf-11-995-2023

Angermann, D., Klotz, J., & Reigber, C. (1999). Space-geodetic estimation of the Nazca-South America Euler vector. *Earth and Planetary Science Letters*, *171*(3), 329-334. https://doi.org/10.1016/S0012-821X(99)00173-9

Angulo-Jaramillo, R., Vandervaere, J., Roulier, S., Thony, J., Gaudet, J., & Vaucli, M. (2000). Field measurement of soil surface hydraulic properties by disc and ring infiltrometers: a review and recent developments. *Soil and Tillage Research, 55*(1-2), 1-29. https://doi.org/10.1016/S0167-1987(00)00098-2

Anovitz, L. M., Cheshire, M. C., Hermann, R. P., Gu, X., Sheets, J. M., Brantley, S. L., Cole, D. R., Ilton, E. S., Mildner, D. F., Gagnon, C., & Allard, L. F. (2021). Oxidation and associated pore structure modification during experimental alteration of granite. *Geochimica et Cosmochimica Acta*, 292, 532-556. https://doi.org/10.1016/j.gca.2020.08.016

Arunachalam, J., Emons, H., Krasnodebska, B., & Mohl, C. (1996). Sequential extraction studies on homogenized forest soil samples. *Science of the total environment, 181*(2), 147-159. https://doi.org/10.1016/0048-9697(95)05005-1

Attal, M., Mudd, S. M., Hurst, M. D., Weinman, B., Yoo, K., & Naylor, M. (2015). Impact of change in erosion rate and landscape steepness on hillslope and fluvial sediments grain size in the Feather River basin (Sierra Nevada, California), *Earth Surf. Dynam., 3,* 201–222. https://doi.org/10.5194/esurf-3-201-2015

Attal, M., & Lavé, J. (2006). Changes of bedload characteristics along the Marsyandi River (central Nepal): Implications for understanding hillslope sediment supply, sediment load evolution along fluvial networks, and denudation in active orogenic belts. In *Tectonics, Climate, and Landscape Evolution*, edited by S. Willett et al., Spec. Pap. Geol. Soc. Am., 398, 143–171. https://doi.org/10.1130/2006.2398(09)

Attal, M., & Lavé, J. (2009). Pebble abrasion during fluvial transport: Experimental results and implications for the evolution of the sediment load along rivers. *J. Geophys. Res*., 114, F04023. https://doi.org/10.1029/2009JF001328

Bagnold, R. A. (1977). Bed load transport by natural rivers. *Water resources research, 13*(2), 303-312. https://doi.org/10.1029/WR013i002p00303

Balco, G. (2006). Converting Al and Be isotope ratio measurements to nuclide concentrations in quartz. *Documentation—Be-10/26-Al exposure age calculator*.

Balco, G., Stone, J. O., Lifton, N. A., & Dunai, T. J. (2008). A complete and easily accessible means of calculating surface exposure ages or erosion rates from 10Be and 26Al

measurements. *Quat. Geochronol., 3*, 174-195. https://doi.org/10.1016/j.quageo.2007.12.001

Balco, G., Purvance, M. D., & Rood, D. H. (2011). Exposure dating of precariously balanced rocks. *Quaternary Geochronology*, 6(3-4), 295-303. https://doi.org/10.1016/j.quageo.2011.03.007

Banfield, J.F., & Eggleton, R.A. (1990). Analytical transmission electron microscope studies of plagioclase, muscovite, and K-feldspar weathering. *Clays and Clay Minerals*, *38*, 77-89. https://doi.org/10.1346/CCMN.1990.0380111

Barría, P., Sandoval, I. B., Guzman, C., Chadwick, C., Alvarez-Garreton, C., Díaz-Vasconcellos, R., Ocampo-Melgar, A., & Fuster, R. (2021). Water allocation under climate change: A diagnosis of the Chilean system. *Elem Sci Anth*, 9(1), 00131. https://doi.org/10.1525/elementa.2020.00131

Barrientos, G., Rubilar, R., Duarte, E., & Paredes, A. (2023). Runoff variation and progressive aridity during drought in catchments in southern-central Chile. *Hydrology Research*, *54*(12), 1590-1605. https://doi.org/10.2166/nh.2023.116

Beer, A. R., Turowski, J. M., & Kirchner, J. W. (2017). Spatial patterns of erosion in a bedrock gorge. *Journal of Geophysical Research: Earth Surface*, *122*(1), 191-214. https://doi.org/10.1002/2016JF003850

Bernhard, N., Moskwa, L. M., Schmidt, K., Oeser, R. A., Aburto, F., Bader, M. Y., Baumann, K., Von Blanckenburg, F., Boy, J., van den Brink, L., & Brucker, E. (2018). Pedogenic and microbial interrelations to regional climate and local topography: New insights from a climate gradient (arid to humid) along the Coastal Cordillera of Chile. *Catena*, 170, 335-355. https://doi.org/10.1016/j.catena.2018.06.018

Bierman, P. (1994). Using in situ produced cosmogenic isotopes to estimate rates of Landscape evolution: A review from the geomorphic perspective. *J. Geophys. Res.: Solid Earth, 99* (B7), 13885-13896. https://doi.org/10.1029/94JB00459

Bierman, P. R., & Caffee, M. W. (2002). Cosmogenic exposure and erosion history of Australian rock landforms. *Geol. Soc. Am. Bull.,* 114, 787–803. https://doi.org/10.1130/0016-7606(2002)114<0787:CEAEHO>2.0.CO;2

Blum, A. E., & Stillings, L. L. (1995). Feldspar dissolution kinetics. In *Chemical weathering rates of silicate minerals* (pp. 291-352). De Gruyter, https://doi.org/10.1515/9781501509650-009

Bochet, E., Poesen, J., & Rubio, J. L. (2006). Runoff and soil loss under individual plants of a semi-arid Mediterranean shrubland: influence of plant morphology and rainfall intensity. *Earth Surf. Process. Landforms, 31*, 536-549. https://doi.org/10.1002/esp.1351

Boisier, J. P., Alvarez-Garreton, C., Cordero, R. R., Damiani, A., Gallardo, L., Garreaud, R.D., Lambert, F., Ramallo, C., Rojas, M., & Rondanelli, R. (2018). Anthropogenic drying in central-southern Chile evidenced by long-term observations and climate model simulations. *Elem Sci Anth*, 6, 74. https://doi.org/10.1525/elementa.328

Borchers, B., Marrero, S., Balco, G., Caffee, M., Goehring, B., Lifton, N., Nishiizumi, K., Phillips, F., Schaefer, & J., Stone, J. (2016). Geological calibration of spallation production rates in the CRONUS-Earth project. *Quat. Geochronol.*, 31, 188-198. https://doi.org/10.1016/j.quageo.2015.01.009

Brantley, S. L., & White, A. F. (2009). Approaches to modeling weathered regolith. In: Oelkers, E.H. & Schott, J. (Eds.) Thermodynamics and Kinetics of Water–Rock Interaction. Berlin: De Gruyter, 435-484. https://doi.org/10.1515/9781501508462-012

Braucher, R., Merchel, S., Borgomano, J., & Bourlès, D.L. (2011). Production of cosmogenic radionuclides at great depth: A multi element approach. *Earth Planet. Sc. Lett., 309,* (1–2), 1-9. https://doi.org/10.1016/j.epsl.2011.06.036

Braun, J., Mercier, J., Guillocheau, F., & Robin, C. (2016). A simple model for regolith formation by chemical weathering. *Journal of Geophysical Research – Earth Surface, 121*(11), 2140-2171. https://doi.org/10.1002/2016JF003914

Broxton, P. D., Zeng, X., Scheftic, W., & Troch, P. A. (2014). A MODIS-based global 1-km maximum green vegetation fraction dataset. *Journal of Applied Meteorology and Climatology, 53*(8), 1996-2004. https://doi.org/10.1175/JAMC-D-13-0356.1

Buske, S., Lüth, S., Meyer, H., Patzig, R., Reichert, C., Shapiro, S., Wigger, P., & Yoon, M. (2002). Broad depth range seismic imaging of the subducted Nazca Slab, North Chile. *Tectonophysics*, *350*(4), 273-282. https://doi.org/10.1016/S0040-1951(02)00117-8

Burbank, D. W., Leland, J., Fielding, E., Anderson, R. S., Brozovic, N., Reid, M. R., & Duncan, C. (1996). Bedrock incision, rock uplift and threshold hillslopes in the northwestern Himalayas. *Nature, 379,* 505–510. https://doi.org/10.1038/379505a0

Bursztyn, N., Pederson, J. L., Tressler, C., Mackley, R. D., & Mitchell, K. J. (2015). Rock strength along a fluvial transect of the Colorado Plateau–quantifying a fundamental control on geomorphology. *Earth and Planetary Science Letters*, *429*, 90-100. https://doi.org/10.1016/j.epsl.2015.07.042

Buss, H. L., Brantley, S. L., Scatena, F. N., Bazilievskaya, E. A., Blum, A., Schulz, M., Jiménez, R., White, A. F., Rother, G., & Cole, D. (2013). Probing the deep critical zone beneath the Luquillo Experimental Forest, Puerto Rico. *Earth Surf. Proc. Land., 38*(10), 1170-1186. https://doi.org/10.1002/esp.3409

Callahan, R.P., Riebe, C.S., Pasquet, S., Ferrier, K.L., Grana, D., Sklar, L.S., Taylor, N.J., Flinchum, B.A., Hayes, J.L., Carr, B.J., & Hartsough, P.C. (2020). Subsurface weathering revealed in hillslope-integrated porosity distributions. *Geophys. Res. Lett., 47*(15), https://doi.org/10.1029/2020GL088322

Callahan, R. P., Riebe, C. S., Sklar, L. S., Pasquet, S., Ferrier, K. L., Hahm, W. J., Taylor, N. J., Grana, D., Flinchum, B. A., Hayes, J. L., & Holbrook, W. S. (2022). Forest vulnerability to drought controlled by bedrock composition. *Nature Geoscience, 15*(9), 714-719.

Carlston, C. W. (1963). Drainage density and streamflow. In *Physiographic and hydraulic studies of rivers* (Geological Survey Professional Paper 422-C). US Government Printing Office.

Carretier, S., & Regard, V. (2011). Is it possible to quantify pebble abrasion and velocity in rivers using terrestrial cosmogenic nuclides?. *Journal of Geophysical Research: Earth Surface*, 116(F4). https://doi.org/10.1029/2011JF001968

Carretier, S., Regard, V., Vassallo, R., Aguilar, G., Martinod, J., Riquelme, R., Pepin, E., Charrier, R., Hérail, G., Farías, M., Guyot, J. L., Vargas, G., & Lagane, C. (2013). Slope and climate variability control of erosion in the Andes of central Chile. *Geology, 41*(2), 195-198. https://doi.org/10.1130/G33735.1

Carretier, S., Regard, V., Vassallo, R., Aguilar, G., Martinod, J., Riquelme, R., Christophoul, F., Charrier, R., Gayer, E., Farías, M., Audin, L., & Lagane, C. (2015a). Differences in 10Be concentrations between river sand, gravel and pebbles along the western side of the central Andes. *Quat. Geochronol., 27*(April), 33-51. https://doi.org/10.1016/j.quageo.2014.12.002

Carretier, S., Tolorza, V., Rodríguez, M. P., Pepin, E., Aguilar, G., Regard, V., Martinod, J., Riquelme, R., Bonnet, S., Brichau, S., Hérail, G., Pinto, L., Farías, M., Charrier, R., & Guyot, J. L. (2015b). Erosion in the Chilean Andes between 27°S and 39°S: tectonic, climatic and geomorphic control. *Geol. Soc. London, Spec. Publ., 399*(October 2015), 401-418. https://doi.org/10.1144/SP399.16

Carretier, S., Tolorza, V., Regard, V., Aguilar, G., Bermúdez, M. A., & Martinod, J. (2018). Review of erosion dynamics along the major N-S climatic gradient in Chile and perspectives, *Geomorphology, 300*, 45-68. https://doi.org/10.1016/j.geomorph.2017.10.016

Carretier, S., Regard, V., Abdelhafiz, Y., & Plazolles, B. (2023). Modelling detrital cosmogenic nuclide concentrations during landscape evolution in Cidre v2. 0. *Geoscientific Model Development,* 16(22), 6741-6755. https://doi.org/10.5194/gmd-16-6741-2023

Castillo, V. M., Martinez-Mena, M., & Albaladejo, J. (1997), Runoff and Soil Loss Response to Vegetation Removal in a Semiarid Environment. *Soil Science Society of America Journal*, 61, 1116-1121. https://doi.org/10.2136/sssaj1997.03615995006100040018x

Cembrano, J., González, G., Arancibia, G., Ahumada, I., Olivares, V., & Herrera, V. (2005). Fault zone development and strain partitioning in an extensional strike-slip duplex: A case study from the Mesozoic Atacama fault system Northern Chile. *Tectonophysics 400*, 105-125. https://doi.org/10.1016/j.tecto.2005.02.012

Cerdà, A., Schnabel, S., Ceballos, A., & Gomez-Amelia, D. (1998). Soil hydrological response under simulated rainfall in the Dehesa land system (Extremadura, SW Spain) under drought

conditions. *Earth Surface Processes and Landforms, 23*(3), 195–209. https://doi.org/10.1002/(SICI)1096-9837(199803)23:330.CO;2-I

Chen, S. A., Michaelides, K., Grieve, S. W., & Singer, M. B. (2019). Aridity is expressed in river topography globally. *Nature*, *573*(7775), 573-577.

Chilton, K. D., & Spotila, J. A. (2020). Preservation of Valley and Ridge topography via delivery of resistant, ridge-sourced boulders to hillslopes and channels, Southern Appalachian Mountains, USA. *Geomorphology*, 365, 107263. https://doi.org/10.1016/j.geomorph.2020.107263

Chlieh, M., de Chabalier, J. B., Ruegg, J. C., Armijo, R., Dmowska, R., Campos, J., & Feigl, K. L. (2004). Crustal deformation and fault slip during the seismic cycle in the North Chile subduction zone, from GPS and InSAR observations. *Geophysical Journal International 158*, 695-711. https://doi.org/10.1111/j.1365-246X.2004.02326.x

Clair, J. St., Moon, S., Holbrook, W.S., Perron, J.T., Riebe, C.S., & Martel, S.J. (2015). Geophysical imaging reveals topographic stress control of bedrock weathering, *Geomorphology, 350* (6260). https://doi.org/10.1126/science.aab2210

Coira, B., Davidson, J., Mpodozis, C., & Ramos, V. (1982). Tectonic and magmatic evolution of the Andes of northern Argentina and Chile, *Earth Sci. Rev.*, 18, 303-332. https://doi.org/10.1016/0012-8252(82)90042-3

Collins, D. B. G., & Bras, R. L. (2010). Climatic and ecological controls of equilibrium drainage density, relief, and channel concavity in dry lands. *Water Resour. Res.,* 46, W04508. http://dx.doi.org/10.1029/2009WR008615

Comte, D., & Pardo, M. (1991). Reappraisal of great historical earthquakes in the northern Chile and southern Peru seismic gaps. *Natural Hazards 4*, 23-44.

Cook, K. L., Andermann, C., Gimbert, F., Adhikari, B. R., & Hovius, N. (2018). Glacial lake outburst floods as drivers of fluvial erosion in the Himalaya. *Science*, *362*(6410), 53-57. https://doi.org/10.1126/science.aat4981

Cyr, A. J., Granger, D. E., Olivetti, V., & Molin, P. (2014). Distinguishing between tectonic and lithologic controls on bedrock channel longitudinal profiles using cosmogenic 10Be erosion rates and channel steepness index. *Geomorphology*, 209, 27-38. https://doi.org/10.1016/j.geomorph.2013.12.010

Culling, W. E. H. (1960). Analytical theory of erosion. *J. Geol*., 68, 336-344. https://doi.org/10.1086/626663

Culling, W. E. H. (1963). Soil creep and the development of hillside slopes. *J. Geol*., 71, 127-161. https://doi.org/10.1086/626891

Cyr, A. J., Granger, D. E., Olivetti, V., & Molin, P. (2014). Distinguishing between tectonic and lithologic controls on bedrock channel longitudinal profiles using cosmogenic 10Be erosion rates and channel steepness index. *Geomorphology,* 209, 27-38. https://doi.org/10.1016/j.geomorph.2013.12.010

Dal Bo, I., Klotzsche, A., Schaller, M., Ehlers, T. A., Kaufmann, M. S., Espoz, J. P. F., Vereecken, H., & van der Kruk, J. (2019). Geophysical imaging of regolith in landscapes along a climate and vegetation gradient in the Chilean coastal cordillera. *Catena*, *180*, 146-159. https://doi.org/10.1016/j.catena.2019.04.023

Darling, A., & Whipple, K. (2015). Geomorphic constraints on the age of the western Grand Canyon. *Geosphere*, *11*(4), 958-976. https://doi.org/10.1130/GES01131.1

Deal, E. (2017). A Probabilistic Approach to Understanding the Influence of Rainfall on Landscape Evolution, Doctoral thesis, Univ. Grenoble Alpes; http://www.theses.fr/2017GREAU012.pdf.

Dewald, A., Heinze, S., Jolie, J., Zilges, A., Dunai, T., Rethemeyer, J., Melles, M., Staubwasser, M., Kuczewski, B., Richter, J., Radtke, U., von Blanckenburg, F., & Klein, M. (2013). Cologne AMS, a dedicated center for accelerator mass spectrometry in Germany. *Nucl. Instrum. Meth. B,* 294, 18-23. https://doi.org/10.1016/j.nimb.2012.04.030

Diaz, H. F., & Kiladis, G. N. (1995). Climatic variability on decadal to century timescales. In Future climates of the world: a modelling perspective. *World Survey of Climatology*, Elsevier Publ. Co., 191-244.

DiBiase, R. A., & Whipple, K. X. (2011). The influence of erosion thresholds and runoff variability on the relationships among topography, climate, and erosion rate. *Journal of Geophysical Research: Earth Surface, 116* (F4). https://doi.org/10.1029/2011JF002095

DiBiase, R. A., Lamb, M. P., Ganti, V., & Booth, A. M. (2017). Slope, grain size, and roughness controls on dry sediment transport and storage on steep hillslopes. *J. Geophys. Res.-Earth Surf.*, 122, 941–960. https://doi.org/10.1002/2016JF003970

DiBiase, R. A., Rossi, M. W., & Neely, A. B. (2018). Fracture density and grain size controls on the relief structure of bedrock landscapes. *Geology*, *46*(5), 399-402. https://doi.org/10.1130/G40006.1

DiBiase, R. A., & Whipple, K. X. (2011). The influence of erosion thresholds and runoff variability on the relationships among topography, climate, and erosion rate. *Journal of Geophysical Research: Earth Surface*, 116 (F4). https://doi.org/10.1029/2011JF002095

Dietrich, W. E., Wilson, C. J., Montgomery, D. R., McKean, J., & Bauer, R. (1992). Erosion thresholds and land surface morphology. *Geology, 20*(8), 675-679. https://doi.org/10.1130/0091-7613(1992)020<0675:ETALSM>2.3.CO;2

Dietrich, W. E., & Dunne, T. (1993). The channel head. *Channel network hydrology,* 799, 175-219.

Dietrich, W. E., Bellugi, D. G., Sklar, L. S., Stock, J. D., Heimsath, A. M., & Roering, J. J. (2003). Geomorphic transport laws for predicting landscape form and dynamics. *Geophys. Monogr. -American Geophysical Union, 135*, 103-132. https://doi.org/10.1029/135GM09

Dixon, J. L., Chadwick, O. A., & Vitousek, P. M. (2016). Climate-driven thresholds for chemical weathering in postglacial soils of New Zealand. *Journal of Geophysical Research: Earth Surface*, *121*(9), 1619-1634. https://doi.org/10.1002/2016JF003864

Doebelin, N., & Kleeberg, R. (2015). Profex : A graphical user interface for the Rietveld refinement program BGMN. *Journal of Applied Crystallography,* 48, 1573-1580. https://doi.org/10.1107/S1600576715014685

Donovan, M., & Monaghan, R. (2021). Impacts of grazing on ground cover, soil physical properties and soil loss via surface erosion: A novel geospatial modelling approach. *Journal of Environmental Management, 287*, 112206. https://doi.org/10.1016/j.jenvman.2021.112206

Drever, J. I. (1994), The effect of land plants on weathering rates of silicate minerals. *Geochim. et Cosmochim. Acta 58*, 2325-2332. https://doi.org/10.1016/0016-7037(94)90013-2

Dühnforth, M., Anderson, R. S., Ward, D., & Stock, G. M. (2010). Bedrock fracture control of glacial erosion processes and rates. *Geology, 38* (5), 423-426. https://doi.org/10.1130/G30576.1, 2010.

Duvall, A., Kirby, E., & Burbank, D. (2004). Tectonic and lithologic controls on bedrock channel profiles and processes in coastal California. *Journal of Geophysical Research: Earth Surface, 109*, F03002. http://dx.doi.org/10.1029/2003JF000086

Eccker, S. L. (1984). Effect of lithology and climate on the morphology of drainage basins in northwestern Colorado, (Doctoral dissertation). Fort Collins, CO: Colorado State University.

Eggleton, R. A. (2017). Mineralogy maketh mountains: Granitic landscapes shaped by dissolution. *Geomorphology*, 285, 363-373. https://doi.org/10.1016/j.geomorph.2017.01.016

Ehleringer, J. (1985). Annuals and perennials of warm deserts. In *Physiological ecology of North American plant communities* (pp. 162-180). Dordrecht: Springer Netherlands.

Emparan, C., & Pineda, G. (2000). Área La Serena – La Higuera. Región de Coquimbo. In *Mapas Geológicos* (No. 18, scale 1:100,000). Santiago, Chile: Servicio Nacional de Geología y Minería.

Eppes, M. C., & Griffing, D. (2010). Granular disintegration of marble in nature: A thermal-mechanical origin for a grus and corestone landscape. *Geomorphology, 117*(1-2), 170-180. https://doi.org/10.1016/j.geomorph.2009.11.028

Eppes, M. C., & Keanini, R. (2017). Mechanical weathering and rock erosion by climate-dependent subcritical cracking. *Rev. Geophys., 55*, 470–508. https://doi.org/10.1002/2017RG000557

Filgueiras, A.V., Lavilla, I., & Bendicho, C. (2002). Chemical sequential extraction for metal partitioning in environmental solid samples. *Journal of Environmental Monitoring, 4*(6), 823-857. https://doi.org/10.1039/B207574C

Fisher, G. B., Bookhagen, B., & Amos, C.B. (2013). Channel planform geometry and slopes from freely available high-spatial resolution imagery and DEM fusion: Implications for channel width scalings, erosion proxies, and fluvial signatures in tectonically active landscapes. *Geomorphology, 194*, 46-56. https://doi.org/10.1016/j.geomorph.2013.04.011

Fletcher, R.C., & Brantley, S.L. (2010). Reduction of bedrock blocks as corestones in the weathering profile: Observations and model. *Am. J. Sci., 310*(3), 131-164. https://doi.org/10.2475/03.2010.01

Flint, J. (1974). Stream gradients as a function of order magnitude and discharge. *Water Resources Research 10*, 969-973. https://doi.org/10.1029/WR010i005p00969

Franc, V., Hlaváč, V., & Navara, M. (2005). Sequential coordinate-wise algorithm for the non-negative least squares problem. In *International Conference on Computer Analysis of Images and Patterns* (pp. 407-414). Berlin, Heidelberg: Springer Berlin Heidelberg.

Garreaud, R. D., Vuille, M., Compagnucci, R., & Marengo, J. (2009). Present-day South American climate. *Palaeogeogr. Palaeoclimatol. Palaeoecol., 281*(3-4), 180-195. https://doi.org/10.1016/j.palaeo.2007.10.032

Gifford, G. F., & Hawkins, R. H. (1978). Hydrologic impact of grazing on infiltration: A critical review. *Water Resources Research, 14*(2), 305–313. https://doi.org/10.1029/wr014i002p00305

Gilbert, G. K. (1909). The convexity of hilltops. *J. Geol., 17*, 344-350.

Glade, R. C., Anderson, R. S., & Tucker, G. E. (2017). Block-controlled hillslope form and persistence of topography in rocky landscape. *Geology, 45* (4), 311-314. https://doi.org/10.1130/G38665.1

Glodny, J., Graaefe, K., & Rosenau, M. (2008). Mesozoic to Quaternary continental margin dynamics in South-Central Chile (36– 42◦ S): the apatite and zircon fission track perspective, *Int. J. Earth Sci*., 97, 1271-1291. https://doi.org/10.1007/s00531-007- 0203-1

Gómez-Heras, M., Smith, B. J., & Fort, R. (2006). Surface temperature differences between minerals in crystalline rocks: Implications for granular disaggregation of granites through thermal fatigue. *Geomorphology, 78*(3-4), 236-249. https://doi.org/10.1016/j.geomorph.2005.12.013

Goodfellow, B. W., & Hilley, G. E. (2022). Climatic and lithological controls on the structure and thickness of granitic weathering zones. *Earth and Planetary Science Letters, 600*, 117890. https://doi.org/10.1016/j.epsl.2022.117890

Gosse, J. C., & Phillips, F. M. (2001). Terrestrial in situ cosmogenic nuclides: theory and application. *Quaternary Science Reviews*, *20*(14), 1475-1560. https://doi.org/10.1016/S0277-3791(00)00171-2

Granger, D.E., & Smith, A.L. (2000). Dating buried sediments using radioactive decay and muogenic production of 26Al and 10Be. *Nuclear Instruments and Methods in Physics Research Section B: Beam Interactions with Materials and Atoms 172*(1-4), 822-826. https://doi.org/10.1016/S0168-583X(00)00087-2

Granger, D. E., Riebe, C. S., Kirchner, J. W., & Finkel, R. C. (2001). Modulation of erosion on steep granitic slopes by boulder armoring, as revealed by cosmogenic 26Al and 10Be. *Earth and Planetary Science Letters*, *186*(2), 269-281. https://doi.org/10.1016/S0012-821X(01)00236-9

Granger, D.E., & Muzikar, P.F. (2001). Dating sediment burial with in situ-produced cosmogenic nuclides: theory, techniques, and limitations. *Earth and Planetary Science Letters 188*(1-2), 269-281. https://doi.org/10.1016/S0012-821X(01)00309-0

Granger, D. E., & Riebe, C. S. (2014). Cosmogenic Nuclides in Weathering and Erosion, in: *Treatise on Geochemistry, Second Edition*, edited by: Holland, H. D., & Turekian, K. K., Elsevier, Oxford, 7, 401-436. https://doi.org/10.1016/B978-0-08-095975-7.00514-3

Grigusova, P., Larsen, A., Brandl, R., Del Río, C., Farwig, N., Kraus, D., Paulino, L., Pliscoff, P. & Bendix, J. (2023). Mammalian bioturbation amplifies rates of both hillslope sediment erosion and accumulation along the Chilean climate gradient. *Biogeosciences, 20*(15), 3367-3394. https://doi.org/10.5194/bg-20-3367-2023

Gutiérrez-Jurado, H. A., Vivoni, E. R., Bruce, J., Harrison, J., & Guan, H. (2006). Ecohydrology of root zone water fluxes and soil development in complex semiarid rangelands. *Hydrol. Process. 20*, 3289-3316. https://doi.org/10.1002/hyp.6333

Hack, J. T., & Hack, J. T. (1957). Studies of longitudinal profiles in Virginia and Maryland. *Professional Paper, 294-B. U.S. Geological Survey*, Washington D. C. 45-97.

Hack, J. T. (1973). Stream-profile analysis and stream-gradient index. *Journal of Research of the U.S. Geological Survey 1*, 421-429.

Hahm, W. J., Rempe, D. M., Dralle, D. N., Dawson, T. E., Lovill, S. M., Bryk, A. B., Bish, D. L., Schieber, J., & Dietrich, W. E. (2019). Lithologically controlled subsurface critical zone thickness and water storage capacity determine regional plant community composition. *Water Resources Research, 55*(4), 3028-3055. https://doi.org/10.1073/pnas.1315667111

Hamerlynck, E. P., McAuliffe, J. R., McDonald, E. V., & Smith, S. D. (2002). Ecological responses of two Mojave Desert shrubs to soil horizon development and soil water dynamics. *Ecology, 83*(3), 768-779. https://doi.org/10.1890/0012-9658(2002)083[0768:EROTMD]2.0.CO;2

Hampl, F. J., Schiperski, F., Byrne, J. M., Schwerdhelm, C., Kappler, A., Bryce, C., von Blanckenburg, F., & Neumann, T. (2022). The role of iron-bearing minerals for the deep weathering of a hydrothermally altered plutonic rock in semi-arid climate (Chilean Coastal Cordillera). *Chemical Geology, 604,* 120922. https://doi.org/10.1016/j.chemgeo.2022.120922

Harel, M. A., Mudd, S. M., & Attal, M. (2016). Global analysis of the stream power law parameters based on worldwide 10Be denudation rates. *Geomorphology, 268*, 184-196. https://doi.org/10.1016/j.geomorph.2016.05.035

Hartley, A. J., Chong, G., Houston, J., & Mather, A. E. (2005). 150 million years of climatic stability: Evidence from the Atacama Desert, northern Chile*. J. Geol. Soc. London., 162*(3), 421-424. https://doi.org/10.1144/0016-764904-071

Hayes, N. R., Buss, H. L., Moore, O. W., Krám, P., & Pancost, R. D. (2020). Controls on granitic weathering fronts in contrasting climates, *Chem. Geol., 535*, 119450. https://doi.org/10.1016/j.chemgeo.2019.119450

Heikkilä, U., & von Blanckenburg, F. (2015). The global distribution of Holocene meteoric 10Be fluxes from atmospheric models: Distribution maps for terrestrial Earth's surface applications. GFZ Data Services, 10.

Heimsath, A. M., Chappell, J., Dietrich, W. E., Nishiizumi, K., & Finkel, R. C. (2000). Soil production on a retreating escarpment in southeastern Australia. *Geology*, 28, 787-790. https://doi.org/10.1130/0091-7613(2000)28<787:SPOARE>2.0.CO;2

Heimsath, A. M., Chappell, J., Dietrich, W. E., Nishiizumid, K., & Finkel, R. C. (2001). Late Quaternary erosion in southeastern Australia: a field example using cosmogenic nuclides, *Quatern. Int.*, 83, 169-185. https://doi.org/10.1016/S1040-6182(01)00038-6

Heimsath, A. M., Chappell, J., Dietrich, W. E., Nishiizumid, K., & Finkel, R. C. (2012). Late Quaternary erosion in southeastern Australia: a field example using cosmogenic nuclides. *Quat. Internat., 83*, 169-185. https://doi.org/10.1016/S1040-6182(01)00038-6

Kirby, E. and Whipple, K.X.: Expression of active tectonics in erosional landscapes*, J. Struct. Geol., 44,* 54-75, https://doi.org/10.1016/j.jsg.2012.07.009, 2012.

Hippe, K., Kober, F., Ivy-Ochs, S., Lupker, M., Wacker, L., Christl, M., & Wieler, R. (2013a). Complex in Situ Cosmogenic 10Be-14C Data Suggest Mid-Holocene Climate Change on the Bolivian Altiplano. Goldschmidt 2013 Conference Abstracts.

Hippe, K. (2017). Constraining processes of landscape change with combined in situ cosmogenic 14C-10Be analysis. *Quaternary Science Reviews,* 173, 1-19. https://doi.org/10.1016/j.quascirev.2017.07.020

Houston, J. (2006). Variability of precipitation in the Atacama Desert: Its causes and hydrological impact. *Int. J. Climatol., 26*, 2181-2198. https://doi.org/10.1002/joc.1359

Howard, A. D. (1997). Badland morphology and evolution: Interpretation using a simulation model. *Earth Surface Processes and Landforms: The Journal of the British Geomorphological Group, 22*(3), 211-227. https://doi.org/10.1002/(SICI)1096-9837(199703)22:3<211::AID-ESP749>3.0.CO;2-E

Howard, A., & Kerby, G. (1983). Channels changes in badlands. *Geological Society of America Bulletin 94*, 739-752. https://doi.org/10.1130/0016-7606(1983)94<739:CCIB>2.0.CO;2

Huber, M. L., Lupker, M., Gallen, S. F., Christl, M., & Gajurel, A. P. (2020). Timing of exotic, far-traveled boulder emplacement and paleo-outburst flooding in the central Himalayas. *Earth Surface Dynamics*, *8*(3), 769-787. https://doi.org/10.5194/esurf-8-769-2020

Husen, S., Kissling, E., Flueh, E., & Asch, G., 1999. Accurate hypocentre determination in the seismogenic zone of the subducting Nazca Plate in northern Chile using a combined on-/offshore network. *Geophysical Journal International*, *138*(3), 687-701. https://doi.org/10.1046/j.1365-246x.1999.00893.x

Husen, S., Kissling, E., & Flueh, E.R. (2000). Local earthquake tomography of shallow subduction in north Chile: A combined onshore and offshore study. *Journal of Geophysical Research: Solid Earth*, *105*(B12), 28183-28198. https://doi.org/10.1029/2000JB900229

Ibarra, D. E., Rugenstein, J. K. C., Bachan, A., Baresch, A., Lau, K. V., Thomas, D. L., Lee, J. E., Boyce, C. K., & Chamberlain, C. P. (2019). Modeling the consequences of land plant evolution on silicate weathering. *Am. J. Sci*., 319, 1-43. https://doi.org/10.2475/01.2019.01

Insel, N., Poulsen, C. J., & Ehlers, T. A. (2010). Influence of the Andes Mountains on South American moisture transport, convection, and precipitation. *Climate Dynamics*, *35*, 1477-1492. https://doi.org/10.1007/s00382-009-0637-1

Jordan, T. E., Kirk-Lawlor, N.E., Blanco, N. P., Rech, J. A., & Cosentino, N. J. (2014). Landscape modification in response to repeated onset of hyperarid paleoclimate states since 14 Ma, Atacama Desert, Chile. *Bulletin*, *126*(7-8), 1016-1046. https://doi.org/10.1130/B30978.1

Kelson, K. I., & Wells, S. G. (1989). Geologic influences on fluvial hydrology and bedload transport in small mountainous watersheds, northern New Mexico, USA. *Earth surface processes and landforms, 14*(8), 671-690. https://doi.org/10.1002/esp.3290140803

Kendrick, E., Bevis, M., Robert Smalley, J., Brooks, B., Vargas, R.B., Lauría, E., & Fortes, L. P. S. (2003). The Nazca–South America Euler vector and its rate of change. *Journal of South American Earth Sciences 16*, 125-131. https://doi.org/10.1016/S0895-9811(03)00028-2

Kidron, G. J. (2016). Goat trampling affects plant establishment, runoff and sediment yields over crusted dunes. *Hydrological Processes, 30*(13), 2237-2246. https://doi.org/10.1002/hyp.10794

Kirkby, M. J. (1971). Hillslope process-response models based on the continuity equation, *Inst. Br. Geogr. Spec. Publ.,* 3, 15-30.

Kirby, E., & Whipple, K. (2001). Quantifying differential rock-uplift rates via stream profile analysis. *Geology, 29*(5), 415-418. https://doi.org/10.1130/0091-7613(2001)029<0415:QDRURV>2.0.CO;2

Kirby, E., & Whipple, K. (2012), Expression of active tectonics in erosional landscapes. *J. Structural Geology*., 44, 54-75. https://doi.org/10.1016/j.jsg.2012.07.009

Kirby, E., Whipple, K. X., Tang, W., & Chen, Z. (2003). Distribution of active rock uplift along the eastern margin of the Tibetan Plateau: Inferences from bedrock channel longitudinal profiles. *Journal of Geophysical Research: Solid Earth,* 108(B4). https://doi.org/10.1029/2001JB000861

Kirby, E., Harkins, N., Wang, E., Shi, X., Fan, C., & Burbank, D. (2007). Slip rate gradients along the eastern Kunlun fault. *Tectonics,* 26(2). https://doi.org/10.1029/2006TC002033

Klotz, J., Angermann, D., Michel, G., Porth, R., Reigber, C., Reinking, J., Viramonte, J., Perdomo, R., Rios, V., Barrientos, S., Barriga, R., & Cifuentes, O. (1999). GPS-derived deformation of the Central Andes including the 1995 Antofagasta Mw=8.0 earthquake. *Pure and Applied Geophysics 154,* 709-730.

Krone, L. V., Hampl, F. J., Schwerdhelm, C., Bryce, C., Ganzert, L., Kitte, A., Übernickel, K., Dielforder, A., Aldaz, S., Oses-Pedraza, R., & Perez, J. P. H. (2021). Deep weathering in the semi-arid Coastal Cordillera, Chile. *Sci. Rep*., 11, 1-15.

Kügler, M., Hoffmann, T. O., Beer, A. R., Übernickel, K., Ehlers, T. A., Scherler, D., & Eichel, J. (2022). (LiDAR) 3D Point Clouds and Topographic Data from the Chilean Coastal Cordillera. V. 1.0. GFZ Data Services. https://doi.org/10.5880/fidgeo.2022.002

Lague, D. (2010). Reduction of long-term bedrock incision efficiency by short-term alluvial cover intermittency. *Journal of Geophysical Research: Earth Surface*, *115*(F2). https://doi.org/10.1029/2008JF001210

Lague, D. (2014). The stream power river incision model: Evidence, theory and beyond. *Earth Surface Processes and Landforms, 39* (1), 38-61. https://doi.org/10.1002/esp.3462

Lague, D., Hovius, N., & Davy, P. (2005). Discharge, discharge variability, and the bedrock channel profile. *Journal of Geophysical Research: Earth Surface, 110*(F4). https://doi.org/10.1029/2004JF000259

Lal, D. (1991). Cosmic ray labeling of erosion surfaces: in situ nuclide production rates and erosion models. *Earth Planet. Sc. Lett*., 104, 424-439. https://doi.org/10.1016/0012-821X(91)90220-C.

Lal, D., & Peters, B. (1967). Cosmic ray produced radioactivity on the Earth. In *Kosmische Strahlung II/Cosmic Rays II* (551-612). Berlin, Heidelberg: Springer Berlin Heidelberg.

Lal, D., & Chen, J. (2005). Cosmic ray labeling of erosion surfaces II: Special cases of exposure histories of boulders, soils and beach terraces. *Earth and Planetary Science Letters*, *236*(3-4), 797-813. https://doi.org/10.1016/j.epsl.2005.05.025

Lamb, M. P., Finnegan, N. J., Scheingross, J. S., & Sklar, L. S. (2015). New insights into the mechanics of fluvial bedrock erosion through flume experiments and theory. *Geomorphology*, *244*, 33-55. https://doi.org/10.1016/j.geomorph.2015.03.003

Lamb, M. P., Dietrich, W. E., & Sklar, L. S. (2008). A model for fluvial bedrock incision by impacting suspended and bed load sediment. *Journal of Geophysical Research: Earth Surface*, *113*(F3). https://doi.org/10.1029/2007JF000915

Lebedeva, M. I., & Brantley, S. L. (2017). Weathering and erosion of fractured bedrock systems. *Earth Surf. Proc. Land., 42*, 2090-2108. https://doi.org/10.1002/esp.4177

Litwin, D. G., Tucker, G. E., Barnhart, K. R., & Harman, C. J. (2022). Groundwater affects the geomorphic and hydrologic properties of coevolved landscapes. *Journal of Geophysical Research: Earth Surface, 127*(1), p.e2021JF006239. https://doi.org/10.1029/2021JF006239

Lodes, E., Scherler, D., van Dongen, R., & Wittmann, H. (2023). The story of a summit nucleus: hillslope boulders and their effect on erosional patterns and landscape morphology in the Chilean Coastal Cordillera. *Earth Surface Dynamics, 11*(2), 305-324. https://doi.org/10.5194/esurf-11-305-2023

Lodes, E., Scherler, D., Wittmann, H., Schleicher, A., Stammeier, J., Loyola Lafuente, M, & Grigusova, P. Influence of lithology and biota on stream erosivity and drainage density in a semi-arid landscape, Central Chile [submitted].

Logsdon, S. D., & Allmaras, R. R. (1991). Maize and soybean root clustering as indicated by root mapping. *Plant Soil, 131*, 169-176. https://doi.org/10.1007/BF00009446

Luebert, F., & Pliscoff, P. (2006). Sinopsis bioclimática y vegetacional de Chile. Editorial Universitaria.

Luo, Y., Zhao, L., & Tian, J. (2019). Spatial and temporal variations of stress field in the Longmenshan fault zone after the 2008 Wenchuan, China earthquake. *Tectonophysics*, *767*, 228172. https://doi.org/10.1016/j.tecto.2019.228172

Mackey, E. A., Christopher, S. J., Lindstrom, R. M., Long, S. E., Marlow, A. F., Murphy, K. E., Paul, R. L., Popelka-Filcoff, R. S., Rabb, S. A., Sieber, J. R. & Spatz, R. O. (2010). Certification of three NIST renewal soil standard reference materials for element content: SRM 2709a San Joaquin Soil, SRM 2710a Montana Soil I, and SRM 2711a Montana Soil II. NIST Special Publication, 260(172), 1-39.

Mackey, B. H., & Lamb, M. P. (2013). Deciphering boulder mobility and erosion from cosmogenic nuclide exposure dating. *Journal of Geophysical Research: Earth Surface*, *118*(1), 184-197. https://doi.org/10.1002/jgrf.20035

Marshall, J. A., & Roering, J. J. (2014). Diagenetic variation in the Oregon Coast Range: Implications for rock strength, soil production, hillslope form, and landscape evolution. *Journal of Geophysical Research: Earth Surface*, *119*(6), 1395-1417. https://doi.org/10.1002/2013JF003004

Martel, S.J. (2011). Mechanics of curved surfaces, with application to surface-parallel cracks. *Geophys. Res. Lett., 38*(20). https://doi.org/10.1029/2011GL049354

McAuliffe, J. R. (1994). Landscape evolution, soil formation, and ecological patterns and processes in Sonoran Desert bajadas. *Ecological Monographs, 64*(2), 111-148. https://doi.org/10.2307/2937038

Melnick, D., Bookhagen, B., Strecker, M. R., & Echtler, H. P. (2009). Segmentation of megathrust rupture zones from fore-arc deformation patterns over hundreds to millions of years, Arauco peninsula, Chile. *Journal of Geophysical Research: Solid Earth*, *114*(B1). https://doi.org/10.1029/2008JB005788

Melnick, D. (2016). Rise of the central Andean coast by earthquakes straddling the Moho. *Nat. Geosci., 9*, 1-8. https://doi.org/10.1038/ngeo2683

Melton, M. A. (1957). An Analysis of the Relations Among Elements of Climate, Surface Properties, and Geomorphology. *Technical Report 11 Office of Naval Research Department of Geology*, Columbia University.

Meyer-Christoffer, A., Becker, A., Finger, P., Rudolf, B., Schneider, U., & Ziese, M. (2015). GPCC Climatology Version 2015 at 0.25◦: Monthly Land-Surface Precipitation Climatology for Every Month and the Total Year from Rain-Gauges built on GTS-based and Historic Data. https://doi.org/10.5676/DWD_GPCC/CLIM_M_V2015_025

Miller, D. J., & Dunne, T. (1996). Topographic perturbations of regional stresses and consequent bedrock fracturing. *J. Geophys. Res. 101*(B11), 25523-25536. https://doi.org/10.1029/96JB02531

Minea, G., Mititelu-Ionuș, O., Gyasi Agyei, Y., Ciobotaru, N., & Rodrigo Comino, J. (2022). Impacts of grazing by small ruminants on hillslope hydrological processes: A review of European current understanding. *Water Resources Research, 58*, e2021WR030716. https://doi.org/10.1029/2021WR030716

Molnar, P., Anderson, R. S., Kier, G., & Rose, J. (2006). Relationships among probability distributions of stream discharges in floods, climate, bed load transport, and river incision. *J. Geophys. Res. 111*, F02001. https://doi.org/10.1029/2005JF000310

Molnar, P., Anderson, R. S., & Anderson, S. P. (2007). Tectonics, fracturing of rock, and erosion. *J. Geophys. Res., 112*, F03014. https://doi.org/10.1029/2005JF000433

Montgomery, D. R., & Brandon, M. T. (2002). Topographic controls on erosion rates in tectonically active mountain ranges. *Earth and Planetary Science Letters, 201*(3-4), 481-489. https://doi.org/10.1016/S0012-821X(02)00725-2

Moon, S., Perron, J. T., Martel, S. J., Holbrook, W. S., & St. Clair, J. (2017). A model of three-dimensional topographic stresses with implications for bedrock fractures, surface processes, and landscape evolution. *Journal of Geophysical Research: Earth Surface*, *122*(4), 823-846. https://doi.org/10.1002/2016JF004155

Moreno, M. S., Klotz, J., Melnick, D., Echtler, H., & Bataille, K. (2008). Active faulting and heterogeneous deformation across a megathrust segment boundary from GPS data, south central Chile (36–39 S). *Geochemistry, Geophysics, Geosystems*, *9*(12). https://doi.org/10.1029/2008GC002198

Morford, S. L., Houlton, B. Z., & Dahlgren, R. A., (2011). Increased forest ecosystem carbon and nitrogen storage from nitrogen rich bedrock. *Nature, 477*(7362), 78-81.

Mudd, S.M. (2016). Detection of transience in eroding landscapes. *Earth Surf. Proc. Land,* 42, 24-41. https://doi.org/10.1002/esp.3923

Muñoz, M. R., Squeo, F. A., León, M. F., Tracol, Y., & Gutiérrez, J. R. (2008). Hydraulic lift in three shrub species from the Chilean coastal desert. *Journal of Arid Environments, 72*(5), 624-632. https://doi.org/10.1016/j.jaridenv.2007.09.006

Murphy, B.P. (2016). Feedbacks among chemical weathering, rock strength and erosion with implications for the climatic control of bedrock river incision (Doctoral dissertation).

Mutz, S. G., Ehlers, T. A., Werner, M., Lohmann, G., Stepanek, C., & Li, J. (2018). Estimates of late Cenozoic climate change relevant to Earth surface processes in tectonically active orogens. *Earth Surface Dynamics*, *6*(2), 271-301. https://doi.org/10.5194/esurf-6-271-2018

Mutz, S. G., & Ehlers, T. A. (2019). Detection and explanation of spatiotemporal patterns in Late Cenozoic palaeoclimate change relevant to Earth surface processes. *Earth Surface Dynamics*, *7*(3), 663-679. https://doi.org/10.5194/esurf-7-663-2019

National Nuclear Data Center, B.N.L., www.nndc.bnl.gov.

Neely, A. B., DiBiase, R. A., Corbett, L. B., Bierman, P. R., & Caffee, M. W. (2019). Bedrock fracture density controls on hillslope erodibility in steep, rocky landscapes with patchy soil cover, southern California, USA. *Earth Planet. Sc. Lett., 522,* 186-197. https://doi.org/10.1016/j.epsl.2019.06.011

Neely, A. B., & DiBiase, R. A. (2020). Drainage Area, Bedrock Fracture Spacing, and Weathering Controls on Landscape-Scale Patterns in Surface Sediment Grain Size. *J. Geophys. Res. Earth Surf., 125*, (10). https://doi.org/10.1029/2020JF005560

Neely, A. B., & DiBiase, R. A. (2023). Sediment controls on the transition from debris flow to fluvial channels in steep mountain ranges. *Earth Surface Processes and Landforms, 48*(7), 1342-1361. https://doi.org/10.1002/esp.5553

Neff, J. C., Reynolds, R., Sanford, R. L., Fernandez, D., & Lamothe, P. (2006). Controls of bedrock geochemistry on soil and plant nutrients in southeastern Utah. *Ecosystems, 9*(6), 879-893. https://doi.org/10.1007/s10021-005-0092-8

Nesbitt, H., & Young, G. M. (1982). Early Proterozoic climates and plate motions inferred from major element chemistry of lutites. *Nature, 299*(5885), 715-717.

Nesbitt, H. W., Fedo, C. M., & Young, G. M. (1997). Quartz and feldspar stability, steady and non-steady-state weathering, and petrogenesis of siliciclastic sands and muds. *The Journal of Geology, 105*(2), 173-192.

Noy-Meir, I. (1973). Desert ecosystems: environment and producers. *Annual review of ecology and systematics, 4*(1), 25-51.

Oberlander, T. M. (1972). Morphogenesis of Granitic Boulder Slopes in the Mojave Desert. *California, J. Geol., 80*, 1–20. https://doi.org/10.1086/627710

Oswald, S. E., Menon, M., Carminati, A., Vontobel, P., Lehmann, E., & Schulin, R. (2008). Quantitative imaging of infiltration, root growth, and root water uptake via neutron radiography. *Vadose Zone Journal, 7*(3),1035-1047. https://doi.org/10.2136/vzj2007.0156

Ott, R. F. (2020). How lithology impacts global topography, vegetation, and animal biodiversity: A global-scale analysis of mountainous regions. *Geophysical Research Letters*, *47*(20), https://doi.org/10.1029/2020GL088649

Oeser, R. A., Stroncik, N., Moskwa, L., Bernhard, N., Schaller, M., Canessa, R., Brink, L. Van Den, Köster, M., Brucker, E., Stock, S., Pablo, J., Godoy, R., Javier, F., Oses, R., Osses, P., Paulino, L., Seguel, O., Bader, M. Y., Boy, J., Dippold, M. A., Ehlers, T. A., Kühn, P., Kuzyakov, Y., Leinweber, P., Scholten, T., Spielvogel, S., Spohn, M., Übernickel, K., Tielbörger, K., Wagner, D., and von Blanckenburg, F. (2018). Chemistry and microbiology of the Critical

Zone along a steep climate and vegetation gradient in the Chilean Coastal Cordillera. *Catena, 170*, 183-203. https://doi.org/10.1016/j.catena.2018.06.002

Ouimet, W. B., Whipple, K. X., & Granger, D. E. (2009). Beyond threshold hillslopes: Channel adjustment to base-level fall in tectonically active mountain ranges. *Geology, 37*(7), 579-582. https://doi.org/10.1130/G30013A.1

Paola, C., Heller, P. L., & Angevine, C. L. (1992). The large-scale dynamics of grain-size variation in alluvial basins, 1: Theory. *Basin research*, 4(2), 73-90. https://doi.org/10.1111/j.1365-2117.1992.tb00145.x

Passalacqua, P., Do Trung, T., Foufoula-Georgiou, E., Sapiro, G., & Dietrich, W. E. (2010). A geometric framework for channel network extraction from lidar: Nonlinear diffusion and geodesic paths. *J. Geophys. Res. 115*, F01002. https://doi.org/10.1029/2009JF001254

Parada, M. A., Nyström, J. O., & Levi, B. (1999). Multiple sources for the Coastal Batholith of central Chile (31-34 S): geochemical and Sr–Nd isotopic evidence and tectonic implications. *Lithos*, *46*(3), 505-521. https://doi.org/10.1016/S0024-4937(98)00080-2

Parada, M. A., López-Escobar, L., Oliveros, V., Fuentes, F., Morata, D., Calderón, M., Aguirre, L., Féraud, G., Espinoza, F., Moreno, H., & Figueroa, O. (2007). *Andean magmatism*. Geological Society of London: London, England. https://doi.org/10.1144/GOCH.4

Pardo-Casas, F., & Molnar, P. (1987). Relative motion of the Nazca (Farallon) and South American plates since Late Cretaceous time. *Tectonics*, *6*(3), 233-248.

Perron, J. T., Dietrich, W. E., & Kirchner, J. W. (2008). Controls on the spacing of first-order valleys. *Journal of Geophysical Research: Earth Surface*, 113(F4). https://doi.org/10.1029/2007JF000977

Perron, J., Kirchner, J. & Dietrich, W. (2009). Formation of evenly spaced ridges and valleys. *Nature*, 460, 502-505. https://doi.org/10.1038/nature08174

Perron, J. T. (2011). Numerical methods for nonlinear hillslope transport laws. *Journal of Geophysical Research: Earth Surface*, *116*(F2). https://doi.org/10.1029/2010JF001801

Perron, J. T. (2017). Climate and the Pace of Erosional Landscape Evolution. *Annu. Rev. Earth Planet. Sci., 45*, 561-591. https://doi.org/10.1146/annurev-earth-060614- 105405

Porder, S. & Ramachandran, S. (2012). The phosphorus concentration of common rocks—a potential driver of ecosystem P status. *Plant Soil, 367*(1-2), 1–15.

Portenga, E. W., & Bierman, P. R. (2011). Understanding earth's eroding surface with 10Be. *GSA Today, 21*, 4–10. https://doi.org/10.1130/G111A.1

Pritchard, M. E., Simons, M., Rosen, P. A., Hensley, S., & Webb, F. H. (2002). Co-seismic slip from the 1995 July 30 Mw=8.1 Antofagasta, Chile, earthquake as constrained by

InSAR and GPS observations. *Geophysical Journal International 150*, 362-376. https://doi.org/10.1046/j.1365-246X.2002.01661.x

Pritchard, M., Ji, C., & Simons, M. (2006). Distribution of slip from 11 Mw N6 earthquakes in the northern Chile subduction zone. *Journal of Geophysical Research,* 111. https://doi.org/10.1029/2005JB004013

Proffitt, A. P. B., Bendotti, S., Howell, M. R., & Eastham, J. (1993). The effect of sheep trampling and grazing on soil physical properties and pasture growth for a red-brown earth. *Australian Journal of Agricultural Research, 44*(2), 317–331. https://doi.org/10.1071/ar9930317

Prosser, I. P., & Dietrich, W. E. (1995). Field experiments on erosion by overland flow and their implication for a digital terrain model of channel initiation. *Water Resources Research, 31*(11), 2867-2876. https://doi.org/10.1029/95WR02218

Puigdefábregas, J. (2005). The role of vegetation patterns in structuring runoff and sediment fluxes in drylands. *Earth Surf. Process. Landforms, 30*, 133-147. https://doi.org/10.1002/esp.1181

Raab, G., Egli, M., Norton, K., Dahms, D., Brandová, D., Christl, M., & Scarciglia, F. (2019). Climate and relief-induced controls on the temporal variability of denudation rates in a granitic upland. *Earth Surf. Proc. Land., 44*(13), 2570-2586. https://doi.org/10.1002/esp.4681

Rabassa, J., Gordillo, S., Ocampo, C., & Rivas Hurtado, P. (2008). The southernmost evidence for an interglacial transgression (Sangamon?) in South America: First record of upraised Pleistocene marine deposits in Isla Navarino (Beagle Channel, Southern Chile). *Geologica Acta 6*(2), 251-258. https://doi.org/10.1344/105.000000254

Reid, L. M. (1989). Channel incision by surface runoff in grassland catchments. University of Washington.

Rempe, D. M., & Dietrich, W. E. (2014). A bottom-up control on fresh bedrock topography under landscapes. *Proceedings of the National Academy of Sciences of the United States of America, 111*(18), 6576-6581. https://doi.org/10.1073/pnas.1404763111

Riebe, C. S., Kirchner, J. W., & Finkel, R. C. (2004). Erosional and climatic effects on long-term chemical weathering rates in granitic landscapes spanning diverse climate regimes. *Earth and Planetary Science Letters*, *224*(3-4), 547-562. https://doi.org/10.1016/j.epsl.2004.05.019

Riebe, C.S., & Granger, D.E. (2013). Quantifying effects of deep and near-surface chemical erosion on cosmogenic nuclides in soils, saprolite, and sediment. *Earth Surf. Proc. Land., 38*(5), 523-533. https://doi.org/10.1002/esp.3339

Roda-Boluda, D. C., D'Arcy, M., McDonald, J., & Whittaker, A. C. (2018). Lithological controls on hillslope sediment supply: insights from landslide activity and grain size distributions. *Earth Surf. Proc. Land., 43*, 956-977. https://doi.org/10.1002/esp.4281

Rodriguez Padilla, A. M., Oskin, M. E., Milliner, C. W., & Plesch, A. (2022). Accrual of widespread rock damage from the 2019 Ridgecrest earthquakes. *Nat. Geosci., 15*(3), 222-226.

Rossi, B. (1948). Interpretation of cosmic-ray phenomena. *Reviews of Modern Physics*, *20*(3), 537. https://doi.org/10.1103/RevModPhys.20.537

Rossi, M. W., Whipple, K. X., & Vivoni, E. R. (2016). Precipitation and evapotranspiration - controls on daily runoff variability in the contiguous United States and Puerto Rico. *J. Geophys. Res. Earth Surface 121*, 128-145. https://doi.org/10.1002/2015JF003446

Roy, S. G., Koons, P. O., Upton, P., & Tucker, G. E. (2015). The influence of crustal strength fields on the patterns and rates of fluvial incision. *J. Geophys. Res, Earth Surf., 120(*2), 275-299. https://doi.org/10.1002/2014JF003281

Roy, S. G., Tucker, G. E., Koons, P. O., Smith, S. M., & Upton, P. (2016). A fault runs through it: Modeling the influence of rock strength and grain-size distribution in a fault-damaged landscape. *J. Geophys. Res. Earth Surf. 121*. https://doi.org/10.1002/2015JF003662

Sangireddy, H., Stark, C. P., Kladzyk, A., & Passalacqua, P. (2016). GeoNet: An open source software for the automatic and objective extraction of channel heads, channel network, and channel morphology from high resolution topography data. *Environmental Modeling and Software*, 83, 58-73. https://doi.org/10.1016/j.envsoft.2016.04.026

Schaller, M., Ehlers, T. A., Lang, K. A. H., Schmid, M., & Fuentes-Espoz, J. P. (2018). Addressing the contribution of climate and vegetation cover on hillslope denudation, Chilean Coastal Cordillera (26◦–38◦S). *Earth Planet. Sc. Lett., 489*, 111-122. https://doi.org/10.1016/j.epsl.2018.02.026

Schaller, M., & Ehlers, T. A. (2022). Comparison of soil production, chemical weathering, and physical erosion rates along a climate and ecological gradient (Chile) to global observations. *Earth Surf. Dynam.,* 10, 131-150. https://doi.org/10.5194/esurf-10-131-2022

Scheingross, J. S., Brun, F., Lo, D. Y., Omerdin, K., & Lamb, M. P. (2014). Experimental evidence for fluvial bedrock incision by suspended and bedload sediment. *Geology*, *42*(6), 523-526. https://doi.org/10.1130/G35432.1

Scherler, D., DiBiase, R. A., Fisher, G. B., & Avouac, J. P. (2017). Testing monsoonal controls on bedrock river incision in the Himalaya and Eastern Tibet with a stochastic-threshold stream power model. *Journal of Geophysical Research: Earth Surface*, *122*(7), 1389-1429. https://doi.org/10.1002/2016JF004011

Scheuber, E., & Andriessen, P. A. M. (1990). The kinematic and geodynamic significance of the Atacama fault zone, northern Chile. *J. Struct. Geol. 12*, 243-257. https://doi.org/10.1016/0191-8141(90)90008-M

Scheuber, E., & Gonzalez, G. (1999). Tectonics of the Jurassic-Early Cretaceous magmatic arc of the north Chilean Coastal Cordillera (22°-26°S): A story of crustal deformation along a convergent plate boundary. *Tectonics 18*, 895-910. https://doi.org/10.1029/1999TC900024

Schmid, M., Ehlers, T. A., Werner, C., Hickler, T., & Fuentes-Espoz, J. P. (2018). Effect of changing vegetation and precipitation on denudation–Part 2: Predicted landscape response to transient climate and vegetation cover over millennial to million-year timescales. *Earth Surface Dynamics, 6*(4), 859-881. https://doi.org/10.5194/esurf-6-859-2018

Schumm, S. A. (1967). Rates of surficial rock creep on hillslopes in western Colorado. *Science*, *155*(3762), 560-562. https://doi.org/10.1126/science.155.3762.560

Schumm, S. A., & Stevens, M. A. (1973). Abrasion in place: a mechanism for rounding and size reduction of coarse sediments in rivers. *Geology*, *1*(1), 37-40.

Schwanghart, W., & Scherler, D. (2014). Short Communication: Topo Toolbox 2 – MATLAB-based software for topographic analysis and modeling in Earth surface sciences. *Earth Surf. Dynam. 2*, 1-7. https://doi.org/10.5194/esurf-2-1-2014

Scott, D. N., & Wohl, E. E. (2019). Bedrock fracture influences on geomorphic process and form across process domains and scales. *Earth Surface Processes and Landforms*, *44*(1), 27-45. https://doi.org/10.1002/esp.4473

Seidl, M. A., Dietrich, W. E., & Kirchner, J. W. (1994). Longitudinal profile development into bedrock: An analysis of Hawaiian channels. *The Journal of Geology, 102*(4), 457-474. https://doi.org/10.1086/629686

Sernageomin (2003). Mapa Geológico de Chile: versión digital, Servicio Nacional de Geología y Minería, Publicación Geológica Digital No. 4, [data set], https://portalgeomin.sernageomin.cl/service (last access: 22.01.2024).

Shobe, C. M., Tucker, G. E., & Anderson, R. S. (2016). Hillslope-derived blocks retard river incision. *Geophys. Res. Lett.,* 43, 5070-5078. https://doi.org/10.1002/2016GL069262

Shobe, C. M., Tucker, G. E., & Rossi, M. W. (2018). Variable-threshold behavior in rivers arising from hillslope-derived blocks. *Journal of Geophysical Research: Earth Surface*, *123*(8), 1931-1957. https://doi.org/10.1029/2017JF004575

Shobe, C. M., Turowski, J. M., Nativ, R., Glade, R. C., Bennett, G. L., & Dini, B. (2021). The role of infrequently mobile boulders in modulating landscape evolution and geomorphic hazards. *Earth-Science Reviews*, 220, 103717. https://doi.org/10.1016/j.earscirev.2021.103717

Sklar, L. S., & Dietrich, W. E. (2001). Sediment and rock strength controls on river incision into bedrock. *Geology*, 29, 1087-1090. https://doi.org/10.1130/0091-7613(2001)029<1087:SARSCO>2.0.CO;24

Sklar, L. S., & Dietrich, W. E. (2004). A mechanistic model for river incision into bedrock by saltating bed load. *Water Resources Research*, *40*(6). https://doi.org/10.1029/2003WR002496

Sklar, L. S., & Dietrich, W. E. (2006). The role of sediment in controlling steady-state bedrock channel slope: Implications of the saltation-abrasion incision model. *Geomorphology*, *82*(1-2), 58-83. https://doi.org/10.1016/j.geomorph.2005.08.019

Sklar, L. S., & Dietrich, W. E. (2008). Implications of the saltation–abrasion bedrock incision model for steady-state river longitudinal profile relief and concavity. *Earth Surface Processes and Landforms: The Journal of the British Geomorphological Research Group*, *33*(7), 1129-1151. https://doi.org/10.1002/esp.1689

Sklar, L. S., Riebe, C. S., Marshall, J. A., Genetti, J., Leclere, S., Lukens, C. L., & Merces, V. (2017). The problem of predicting the size distribution of sediment supplied by hillslopes to rivers. *Geomorphology, 277*, 31-49. https://doi.org/10.1016/j.geomorph.2016.05.005

Sklar, L. S., Riebe, C. S., Genetti, J., Leclere, S., & Lukens, C. E. (2020). Downvalley fining of hillslope sediment in an alpine catchment: implications for downstream fining of sediment flux in mountain rivers. *Earth Surf. Proc. Land.*, 45, 1828-1845. https://doi.org/10.1002/esp.4849

Slim, M., Perron, J. T., Martel, S. J., & Singha, K. (2014). Topographic stress and rock fracture: a two-dimensional numerical model for arbitrary topography and preliminary comparison with borehole observations. *Earth Surface Processes and Landforms*, *40*(4), 512-529. https://doi.org/10.1002/esp.3646

Small, E. E., Anderson, R. S., Repka, J. L., & Finkel, R. (1997). Erosion rates of alpine bedrock summit surfaces deduced from in situ 10Be and 26A1. *Earth Planet. Sc. Lett., 150,* 413-425. https://doi.org/10.1016/S0012-821X(97)00092-7

Smith, T. R., & Bretherton, F. P. (1972). Stability and the conservation of mass in drainage basin evolution. *Water Resources Research, 8*(6), 1506-1529, https://doi.org/10.1029/WR008i006p01506.

Smith, S. D., Devitt, D. A., Sala, A., Cleverly, J. R., & Busch, D. E. (1998). Water relations of riparian plants from warm desert regions. *Wetlands*, 18, 687-696. https://doi.org/10.1007/BF03161683

Somoza, R. (1998). Updated Nazca (Farallon)-South America relative motions during the last 40 My: implications for mountain building in the central Andean region. *Journal of South American Earth Sciences*, *11*(3), 211-215. https://doi.org/10.1016/S0895-9811(98)00012-1

Souvignet, M., Oyarzún, R., Verbist, K. M., Gaese, H., & Heinrich, J. (2012). Hydro-meteorological trends in semi-arid north-central Chile (29–32 S): Water resources implications for a fragile Andean region. *Hydrological Sciences Journal*, *57*(3), 479-495. https://doi.org/10.1080/02626667.2012.665607

Starke, J., Ehlers, T. A., & Schaller, M. (2020). Latitudinal effect of vegetation on erosion rates identified along western South America. *Science*, *367*(6484), 1358-1361. https://doi.org/10.1126/science.aaz0840

Stock, J., & Dietrich, W. E. (2003). Valley incision by debris flows: Evidence of a topographic signature. *Water Resources Research*, 39(4). https://doi.org/10.1029/2001WR001057

Stone, J.O. (2000). Air pressure and cosmogenic isotope production. *J. Geophys. Res. Solid Earth*, 105, B10, 23753-23759. https://doi.org/10.1029/2000JB900181

Strahler, A. N. (1956). Quantitative slope analysis. *Geological Society of America Bulletin 67*(5), 571-596, https://doi.org/10.1130/0016-7606(1956)67[571:QSA]2.0.CO;2

Sweeney, K. E., Roering, J. J., & Ellis, C. (2015). Experimental evidence for hillslope control of landscape scale. *Science, 349*(6243), 51-53. https://doi.org/10.1126/science.aab0017

Tarboton, D. G., Bras, R. L., & Rodriguez-Iturbe, I. (1989). Scaling and elevation in river networks. *Water Resources Research, 25*(9), 2037-2051. https://doi.org/10.1029/WR025i009p02037

Terweh, S., Hassan, M. A., Mao, L., Schrott, L., Hoffmann, T. O. (2021). Bio-climate affects hillslope and fluvial sediment grain size along the Chilean Coastal Cordillera. *Geomorphology*, 384, 107700. https://doi.org/10.1016/j.geomorph.2021.107700

Tessier, A. P. G. C., Campbell, P. G., & Bisson, M. J. A. C. (1979). Sequential extraction procedure for the speciation of particulate trace metals. *Analytical chemistry, 51*(7), 844-851.

Thaler, E. A., & Covington, M. D. (2016). The influence of sandstone caprock material on bedrock channel steepness within a tectonically passive setting: Buffalo National River Basin, Arkansas, USA. *Journal of Geophysical Research-Earth Surface, 121* (9), 1635-1650. https://doi.org/10.1002/2015JF003771

Toby, B.H. (2006). R factors in Rietveld analysis: How good is good enough? *Powder Diffraction,* 21, 67–70. https://doi.org/10.1154/1.2179804

Tofelde, S., Duesing, W., Schildgen, T. F., Wickert, A. D., Wittmann, H., Alonso, R. N., & Strecker, M. (2018). Effects of deep-seated versus shallow hillslope processes on cosmogenic 10Be concentrations in fluvial sand and gravel. *Earth Surface Processes and Landforms*, *43*(15), 3086-3098. https://doi.org/10.1002/esp.4471

Trichandi, R., Bauer, K., Ryberg, T., Scherler, D., Bataille, K., & Krawczyk, C.M. (2022). Combined seismic and borehole investigation of the deep granite weathering structure: Santa Gracia Reserve case in Chile. *Earth Surface Processes and Landforms*, *47*(14), 3302-3316. https://doi.org/10.1002/esp.5457

Tucker, G. E., & Bras, R. L. (1998). Hillslope processes, drainage density, and landscape morphology. *Water resources research, 34*(10), 2751-2764, https://doi.org/10.1029/98WR01474

Tucker, G. E., & Bras, R. L. (2000). A stochastic approach to modeling the role of rainfall variability in drainage basin evolution, *Water Resour. Res., 36*(7), 1953-1964. https://doi.org/10.1029/2000wr900065

Tucker, G. E., & Hancock, G. R. (2010). Modelling landscape evolution. *Earth Surface Processes and Landforms*, *35*(1), 28-50. https://doi.org/10.1002/esp.1952

Turowski, J. M., Lague, D., & Hovius, N. (2007). Cover effect in bedrock abrasion: A new derivation and its implications for the modeling of bedrock channel morphology. *Journal of Geophysical Research: Earth Surface*, 112(F4). https://doi.org/10.1029/2006JF000697

Turowski, J. M., Hovius, N., Meng-Long, H., Lague, D., & Men-Chiang, C. (2008). Distribution of erosion across bedrock channels. *Earth Surface Processes and Landforms: The Journal of the British Geomorphological Research Group, 33*(3), 353-363. https://doi.org/10.1002/esp.1559

Turowski, J. M., Yager, E. M., Badoux, A., Rickenmann, D., & Molnar, P. (2009). The impact of exceptional events on erosion, bedload transport and channel stability in a step-pool channel. *Earth Surface Processes and Landforms*, *34*(12), 1661-1673. https://doi.org/10.1002/esp.1855

Turowski, J. M., Pruß, G., Voigtländer, A., Ludwig, A., Landgraf, A., Kober, F., & Bonnelye, A. (2023). Geotechnical controls on erodibility in fluvial impact erosion. *Earth Surface Dynamics, 11*(5), 979-994. https://doi.org/10.5194/esurf-11-979-2023

Udden, J.A., (1914). Mechanical composition of clastic sediments. *Geol. Soc. Am. Bull*, 25, 655-744.

Uhlig, D., Amelung, W., & von Blanckenburg, F. (2020). Mineral nutrients sourced in deep regolith sustain long-term nutrition of mountainous temperate forest ecosystems. *Global Biogeochemical Cycles*, 34(9), p.e2019GB006513. https://doi.org/10.1029/2019GB006513

Valentin, C., Poesen, J., & Li, Y. (2005). Gully erosion: Impacts, factors and control. *Catena*, 63(2-3), 132-153. https://doi.org/10.1016/j.catena.2005.06.001

van Dongen, R., Scherler, D., Wittmann, H., & von Blanckenburg, F. (2019). Cosmogenic 10Be in river sediment: where grain size matters and why. *Earth Surf. Dynam*. 7, 393-410. https://doi.org/10.5194/esurf-7-393-2019

van Dongen, Renee. (2021). Discharge variability and river incision along a climate gradient in central Chile [Doctoral dissertation, Free University of Berlin], http://dx.doi.org/10.17169/refubium-32011

Vargas, G., Ortlieb, L., & Rutllant, J. (2000). Historic mudflows in Antofagasta, Chile, and their relationship to the El Niño/southern oscillation events. *Rev. Geol. Chile*, 27(2), 157-176.

Vargas, G., Rutllant, J., & Ortlieb, L. (2006). ENSO tropical-extratropical climate teleconnections and mechanisms for Holocene debris flows along the hyperarid coast of western South America (17°-24°S). *Earth Planet. Sci. Lett., 249*(3-4), 467-483. doi:10.1016/j.epsl.2006.07.022

Verdian, J. P., Sklar, L. S., Riebe, C. S., & Moore, J. R. (2021). Sediment size on talus slopes correlates with fracture spacing on bedrock cliffs: implications for predicting initial sediment size distributions on hillslopes. *Earth Surf. Dynam., 9*(4), 1073-1090. https://doi.org/10.5194/esurf-9-1073-2021

von Blanckenburg, F., Hewawasam, T., & Kubik, P. W. (2004). Cosmogenic nuclide evidence for low weathering and denudation in the wet, tropical highlands of Sri Lanka. *J. Geophys. Res*. 109, F03008. https://doi.org/10.1029/2003JF000049

von Blanckenburg, F. (2005). The control mechanisms of erosion and weathering at basin scale from cosmogenic nuclides in river sediment. *Earth and Planetary Science Letters*, *237*(3-4), 462-479. https://doi.org/10.1016/j.epsl.2005.06.030

von Blanckenburg, F., Bouchez, J., & Wittmann, H. (2012). Earth surface erosion and weathering from the 10Be (meteoric)/9Be ratio. *Earth and Planetary Science Letters*, 351, 295-305. https://doi.org/10.1016/j.epsl.2012.07.022

von Blanckenburg, F., & Willenbring, J. K. (2014). Cosmogenic nuclides: Dates and rates of Earth-surface change. *Elements*, *10*(5), 341-346. https://doi.org/10.2113/gselements.10.5.341

Wang, F., Michalski, G., Seo, J. H., Granger, D. E., Lifton, N., & Caffee, M. (2015). Beryllium-10 concentrations in the hyper-arid soils in the Atacama Desert, Chile: Implications for arid soil formation rates and El Niño driven changes in Pliocene precipitation. *Geochimica et Cosmochimica Acta,* 160, 227-242. https://doi.org/10.1016/j.gca.2015.03.008

Wentworth, C.K. (1922). A scale of grade and class terms for clastic sediments. *J. Geol.*, 30, 377-392.

Werner, C., Schmid, M., Ehlers, T. A., Pablo Fuentes-Espoz, J., Steinkamp, J. S., Forrest, M., Liakka, J., Maldonado, A., & Hickler, T. (2018). Effect of changing vegetation and precipitation on denudation - Part 1: Predicted vegetation composition and cover over the last 21 thousand years along the Coastal Cordillera of Chile. *Earth Surf. Dyn., 6*(4), 829-858. https://doi:10.5194/esurf-6-829-2018

Whipple, K. X., & Tucker, G. E. (1999). Dynamics of the stream-power river incision model: Implications for height limits of mountain ranges, landscape response timescales, and research needs. *Journal of Geophysical Research: Solid Earth*, 104(B8), 17661-17674. https://doi.org/10.1029/1999JB900120

Whipple, K. X., Hancock, G. S., & Anderson, R. S. (2000). River incision into bedrock: Mechanics and relative efficacy of plucking, abrasion, and cavitation. *Geological Society of America Bulletin*, *112*(3), 490-503. https://doi.org/10.1130/0016-7606(2000)112<490:RIIBMA>2.0.CO;2

Whipple, K. X. (2004). Bedrock rivers and the geomorphology of active orogens. *Annu. Rev. Earth Planet. Sci*., 32, 151-185. https://doi.org/10.1146/annurev.earth.32.101802.120356

Whipple, K. X., DiBiase, R. A., & Crosby, B. T. (2013). Bedrock rivers. In *Treatise on Geomorphology*, 9, edited by J. Shroder (Editor in Chief), & E. Wohl (Ed.), 50-573, Academic Press, San Diego, Calif.

White, A. F., Bullen, T. D., Schulz, M. S., Blum, A. E., Huntington, T. G., & Peters, N. E. (2001). Differential rates of feldspar weathering in granitic regoliths. *Geochimica et Cosmochimica Acta*, *65*(6), 847-869. https://doi.org/10.1016/S0016-7037(00)00577-9

White, T., Brantley, S., Banwart, S., Chorover, J., Dietrich, W., Derry, L., Lohse, K., Anderson, S., Aufdendkampe, A., Bales, R., & Kumar, P. (2015). The role of critical zone observatories in critical zone science. In *Developments in earth surface processes 19*, 15-78. Elsevier. https://doi.org/10.1016/B978-0-444-63369-9.00002-1

Whittaker, A. C., & Boulton, S. J. (2012). Tectonic and climatic controls on knickpoint retreat rates and landscape response times. *Journal of Geophysical Research: Earth Surface*, *117*(F2). https://doi.org/10.1029/2011JF002157

Willett, S. D., McCoy, S. W., Perron, J. T., Goren, L., & Chen, C. Y. (2014). Dynamic reorganization of river basins. *Science 343*(6175). https://doi.org/10.1126/science.1248765

Willenbring, J. K., & von Blanckenburg, F. (2010). Meteoric cosmogenic Beryllium-10 adsorbed to river sediment and soil: Applications for Earth-surface dynamics. *Earth-Science Reviews*, 98(1-2), 105-122. https://doi.org/10.1016/j.earscirev.2009.10.008

Willgoose, G. R., Bras, R. L., & Rodriguez-Iturbe, I. (1991). A coupled channel network growth and hillslope evolution model. *Water Resources Research*, 27, 1671–1702. https://doi.org/10.1029/91WR00935

Wilson, L. (1971). Drainage density, length ratios, and lithology in a glaciated area of southern Connecticut. *Geological Society of America Bulletin, 82*(10), 2955-2956. https://doi.org/10.1130/0016-7606(1971)82[2955:DDLRAL]2.0.CO;2

Wilson, A., Hovius, N., & Turowski, J. M. (2013). Upstream-facing convex surfaces: Bedrock bedforms produced by fluvial bedload abrasion. *Geomorphology*, *180*, 187-204. https://doi.org/10.1016/j.geomorph.2012.10.010

Wittmann, H., von Blanckenburg, F., Bouchez, J., Dannhaus, N., Naumann, R., Christl, M., & Gaillardet, J. (2012). The dependence of meteoric ^{10}Be concentrations on particle size in Amazon River bed sediment and the extraction of reactive 10Be/9Be ratios. *Chemical Geology*, 318, 126-138. https://doi.org/10.1016/j.chemgeo.2012.04.031

Wittmann, H., von Blanckenburg, F., Dannhaus, N., Bouchez, J., Gaillardet, J., Guyot, J. L., Maurice, L., Roig, H., Filizola, N., & Christl, M. (2015). A test of the cosmogenic 10Be (meteoric)/9Be proxy for simultaneously determining basin-wide erosion rates, denudation rates, and the degree of weathering in the Amazon basin. *Journal of Geophysical Research: Earth Surface*, 120(12), 2498-2528. https://doi.org/10.1002/2015JF003581

Wobus, C., Whipple, K. X., Kirby, E., Snyder, N., Johnson, J., Spyropolou, K., Crosby, B., & Sheehan, D. (2006). Tectonics from topography: Procedures, promise, and pitfalls. In *Tectonics, Climate, and Landscape Evolution* (GSA Special Papers). https://doi.org/10.1130/2006.2398(04)

Wohl, E. E., Greenbaum, N., Schick, A. P., & Baker, V. R. (1994). Controls on bedrock channel incision along Nahal Paran, Israel. *Earth Surface Processes and Landforms*, *19*(1), 1-13. https://doi.org/10.1002/esp.3290190102

Wolman, M. G. (1954). A method of sampling coarse river-bed material. *Trans. Am. Geophys. Union*., 35, 951-956. https://doi.org/10.1029/TR035i006p00951

Zernitz, E.R. (1932). Drainage patterns and their significance. *J. Geol., 40* (6), 498-521. https://doi.org/10.1086/623976

Zhang, R. (1997). Determination of soil sorptivity and hydraulic conductivity from the disk infiltrometer. *Soil Science Society of American Journal, 61*(4), 124-130. https://doi.org/10.2136/sssaj1997.03615995006100040005x

Zhu, P., Zhang, G., & Zhang, B. (2022). Soil saturated hydraulic conductivity of typical revegetated plants on steep gully slopes of Chinese Loess Plateau. *Geoderma*, 412, 115717. https://doi.org/10.1016/j.geoderma.2022.115717

Zhuo, Y., Mansouri Tehrani, A., & Brgoch, J. (2018). Predicting the band gaps of inorganic solids by machine learning. *The journal of physical chemistry letters, 9*(7), 1668-1673. https://doi.org/10.1021/acs.jpclett.8b00124

Zuazo, V. D., Martínez, J. F., & Raya, A. M. (2004). Impact of Vegetative Cover on Runoff and Soil Erosion at Hillslope Scale in Lanjaron, Spain. *The Environmentalist*, 24, 39-48. https://doi.org/10.1023/B:ENVR.0000046345.44569.35